

**PROCESS INTENSIFICATION IN THE SYNTHESIS OF ORGANIC ESTERS:  
KINETICS, SIMULATIONS AND PILOT PLANT EXPERIMENTS**

**By**

**Venkata Krishna Sai Pappu**

**A DISSERTATION**

**Submitted to  
Michigan State University  
in partial fulfillment of the requirements  
for the degree of**

**DOCTOR OF PHILOSOPHY**

**Chemical Engineering**

**2012**

## ABSTRACT

### PROCESS INTENSIFICATION IN THE SYNTHESIS OF ORGANIC ESTERS: KINETICS, SIMULATIONS AND PILOT PLANT EXPERIMENTS

By

**Venkata Krishna Sai Pappu**

Organic esters are commercially important bulk chemicals used in a gamut of industrial applications. Traditional routes for the synthesis of esters are energy intensive, involving repeated steps of reaction typically followed by distillation, signifying the need for process intensification (PI). This study focuses on the evaluation of PI concepts such as reactive distillation (RD) and distillation with external side reactors in the production of organic acid ester via esterification or transesterification reactions catalyzed by solid acid catalysts.

Integration of reaction and separation in one column using RD is a classic example of PI in chemical process development. Indirect hydration of cyclohexene to produce cyclohexanol via esterification with acetic acid was chosen to demonstrate the benefits of applying PI principles in RD. In this work, chemical equilibrium and reaction kinetics were measured using batch reactors for Amberlyst 70 catalyzed esterification of acetic acid with cyclohexene to give cyclohexyl acetate. A kinetic model that can be used in modeling reactive distillation processes was developed. The kinetic equations are written in terms of activities, with activity coefficients calculated using the NRTL model. Heat of reaction obtained from experiments is compared to predicted heat which is calculated using standard thermodynamic data. The effect of cyclohexene dimerization and initial water concentration on the activity of heterogeneous catalyst is also discussed.

Continuous pilot scale reactive distillation runs were conducted to demonstrate the technical feasibility of cyclohexyl acetate formation and to exemplify the opportunities for heat

integration in RD operation. Based on these preliminary runs, process configurations and conditions suitable for high conversions of cyclohexene are suggested. The experimental data obtained at steady state are compared with results obtained from simulations performed using the RADFRAC column module in Aspen Plus.

The concept of distillation with an external side reactor was evaluated in a process involving the transesterification of methyl stearate and 1-butanol, yielding butyl stearate. An activity-based kinetic model for this reaction using Amberlyst™ 15 as catalyst was developed. The kinetic model includes etherification reactions occurring at reaction temperatures greater than 90°C, producing butyl methyl ether and dibutyl ether. Kinetic parameters from this database were used in modeling the distillation column with external side reactors. Process simulation using Aspen Plus describes column performance as a function of operating conditions, number of side reactors utilized, requirement for a pre-reactor, location of side draws and re-entry points in the column. The column configuration that maximizes conversion of the methyl ester to its butyl counterpart is presented.

In addition to evaluation of the PI concepts, using butyric acid as a model compound, the effect of factors such as alcohol carbon chain length and type of solid acid catalyst on esterification reaction rate was investigated.

In summary, advanced process concepts for continuous production of organic esters have been examined. Chemical kinetic data from laboratory scale experiments has been used in developing computational models of these concepts using Aspen Plus. The combination of process simulations and pilot-plant experiments have identified process configurations and conditions that lead to more efficient organic esters production with potential commercial interest.

## ACKNOWLEDGEMENTS

I would like to thank Dr. Dennis J. Miller for being a great teacher and a patient mentor throughout my Ph. D. Special thanks to Dr. Carl T. Lira for his advice and support. I also wish to thank Dr. James E. Jackson, Dr. Ramani Narayan and Dr. Wei Liao for serving on my committee. I would like to thank Dr. John Prindle of Tulane University for his help with process simulations.

I wish to extend my gratitude for financial support by the U.S. Department of Energy's (DOE's) Office of Energy Efficiency and Renewable Energy (EERE) through the Industrial Technology Programs (DOE Contract No. DE-AC02-06CH11357) and also the U.S. Department of Energy Freedom Car Program (Award #DE-FC2607NT42378) administered through the National Energy Technology Laboratory in Morgantown, West Virginia.

Special thanks to Dr. Lars Peereboom for his help and support. Thanks to Dr. Aspi Kolah for working with me on the reactive distillation unit. Thanks to Dr. Alvaro Orjuela, Dr. Abu Hassan, Dr. Xi Hong, Aaron Oberg, Tyler Jordison, Arathi Santanakrishnan and Annie Lown for being friendly and helpful lab mates. Also, I thank undergraduate students Omar Mcgiveron, Victor Kanyi, Abraham Yanez, Evan Muller and Alex Smith for their assistance. I want to extend my appreciation to William Andres Chasoy Rojas and Fernando Lenis for working with me on pilot plant runs.

# TABLE OF CONTENTS

LIST OF TABLES .....	viii
LIST OF FIGURES .....	x
KEY TO SYMBOLS AND ABBREVIATIONS .....	xxi
Chapter 1: Introduction .....	1
1.1. ADVANCED PI TECHNIQUES .....	2
1.1.1. Reactive Distillation.....	2
1.1.2. Distillation with external side reactor (DSR).....	6
1.2. RESEARCH APPROACH AND OUTLINE .....	7
1.2.1. Cyclohexyl acetate – an intermediate in cyclohexanol production .....	8
1.2.2. Butyl stearate – a model compound for potential biodiesel constituents.....	11
1.2.3. Butyric acid esterification: The effect of alcohol carbon chain length and type of catalyst on the rate of esterification reaction .....	12
1.3. REFERENCES .....	14
Chapter 2: Cyclohexyl acetate production from cyclohexene and acetic acid: Reaction kinetics and chemical equilibrium.....	19
2.1. SUMMARY .....	19
2.2. INTRODUCTION .....	19
2.3. MATERIALS AND METHODS .....	22
2.4. RESULTS AND DISCUSSION.....	24
2.4.1. Reaction studies .....	24
2.4.2. Pseudo-Homogeneous (PH) kinetic model.....	28
2.4.3. Kinetic model comparison with experiments .....	31
2.4.4. Effect of cyclohexene dimerization on activity of Amberlyst 70 .....	35
2.4.5. Effect of water on the activity of Amberlyst 70 .....	37
2.5. CONCLUSION.....	39
2.6. APPENDIX A.....	42
2.7. REFERENCES .....	69
Chapter 3: Cyclohexyl acetate production using reactive distillation: Pilot plant experiments and simulations .....	72
3.1. SUMMARY.....	72
3.2. INTRODUCTION .....	72
3.3. MATERIALS AND METHODS .....	74

3.3.1 Reactive distillation column configuration and operating procedure .....	75
3.4. RESULTS AND DISCUSSION.....	80
3.4.1. Heat Integration Runs .....	82
3.4.2. Energy balance for Runs 9a & 9b .....	83
3.4.3. Simulation of RD column .....	87
3.4.4. Comparison of simulation and experimental results.....	89
3.4.5. Effect of feed stage on CHE conversion.....	93
3.4.6. Effect of heat loss on CHE conversion .....	94
3.4.7. Effect of heat addition on CHE conversion .....	95
3.4.8. Effect of heat transfer between catalytic sections.....	95
3.5. CONCLUSIONS .....	97
3.6. APPENDIX B .....	99
3.7. REFERENCES .....	103

Chapter 4: A Kinetic Model of the Amberlyst-15 Catalyzed Transesterification of Methyl Stearate with n-Butanol.....	105
4.1. SUMMARY .....	105
4.2. INTRODUCTION .....	105
4.3. MATERIALS AND METHODS .....	107
4.3.1. Materials .....	107
4.3.2. Reactors.....	107
4.3.3. Procedure .....	108
4.3.4. Analysis.....	108
4.4. RESULTS AND DISCUSSION.....	109
4.4.1. Experimental evaluation of mass transfer resistances.....	109
4.4.2. Kinetic model.....	111
4.4.3. Results.....	117
4.4.4. Discussion.....	123
4.5. CONCLUSION.....	125
4.6. APPENDIX C .....	127
4.7. REFERENCES .....	141

Chapter 5: Butyl stearate production using distillation column with external side reactors: Process concept, simulation and analysis .....	143
5.1. SUMMARY .....	143
5.2. INTRODUCTION .....	143
5.3. DISTILLATION WITH EXTERNAL SIDE REACTOR CONCEPT (D-SRC).....	145
5.3.1. MS transesterification reaction .....	148
5.3.2. Boiling point ranking .....	148
5.3.3. Simulation methodology.....	149
5.4. RESULTS .....	153
5.4.1. Cases 1&2: Three PFRs in series.....	153
5.4.2. Cases 3: Distillation with three external reactors.....	155
5.4.3. Case 4: Distillation with two external reactors and pre-reactor.....	155
5.5. CONCLUSION.....	158

5.6. REFERENCES .....	160
Chapter 6: Butyric acid esterification over solid acid catalysts: The effect of alcohol carbon chain length and a kinetic model for Amberlyst 70 catalyzed esterification with 2-ethylhexanol .....	162
6.1. SUMMARY.....	162
6.2. INTRODUCTION .....	162
6.3. MATERIALS AND METHODS .....	164
6.3.1. Preparation of 4-Heptanol.....	165
6.3.2. Preparation of 2-ethylhexyl butyrate (2-EHB) .....	165
6.3.3. Batch experiments.....	165
6.3.4. Sample analysis.....	166
6.4. RESULTS AND DISCUSSION.....	167
6.4.1. Esterification of BA with different alcohols .....	167
6.4.2. BA esterification kinetics with 2-EHA .....	171
6.4.3. Kinetic model for Amberlyst 70-catalyzed and auto-catalyzed esterification.....	175
6.4.4. Effect of butyrate esters on biodiesel cloud point.....	177
6.5. CONCLUSIONS .....	178
6.6. APPENDIX D.....	181
6.7. REFERENCES .....	207
Chapter 7: Conclusions, significance and recommendations for future work .....	210
7.1. REACTIVE DISTILLATION IN CYCLOHEXYL ACETATE PRODUCTION .....	210
7.2. DISTILLATION WITH SIDE REACTOR CONCEPT EVALUATION .....	212
7.3. BUTYRIC ACID ESTERIFICATION WITH A SERIES OF ALCOHOLS .....	213

## LIST OF TABLES

Table 2.1a: Standard Enthalpies and Standard Gibbs Energies of Formation (1 atm, 298K) .....	28
Table 2.1b: Standard Enthalpies and Standard Gibbs Energies of Reaction at 298K .....	28
Table 2.2: Summary of reaction kinetic parameters .....	31
Table A.2a: Component molecular weight and density information .....	43
Table A.2b: Component individual weight and volume measurement.....	44
Table A.3.1 Summary of batch experiments with Amberlyst 70 as catalyst .....	45
Table A.6.2: NRTL parameters used in Aspen simulations <sup>a</sup> .....	67
Table 3.1: Characteristics of pilot plant reactive distillation column .....	78
Table 3.2: Summary of reaction conditions in pilot plant runs.....	84
Table 3.3a: Energy balance from experimental material balance .....	85
Table 3.3b: Energy balance from ideal material balance.....	85
Table 3.4a: Ideal vs. Experimental material balance for Run 9a .....	86
Table 3.4b: Ideal vs. Experimental material balance for Run 9b.....	86
Table 3.5: RD column parameters used in process simulations .....	87
Table 3.6: Modified kinetic parameters used in process simulations .....	88

Table B.1.1: Reboiler duty calculation .....	99
Table B.2.1: Condenser duty calculation .....	100
Table B.3.1: Standard heat of formation from DIPPR database .....	101
Table 4.1: Kinetic model parameters .....	116
Table 4.2: Summary of experimental conditions and calculated mole fraction differences for MS .....	117
Table 4.3: Comparison of transesterification forward rate constants at 363 K .....	124
Table C.2.1: UNIFAC group identification of the components.....	131
Table C.2.2: UNIFAC group interaction parameters.....	132
Table C.3.1: Summary of experimental conditions and calculated errors .....	133
Table 5.1: Simulation results for cases 1 and 2. ....	154
Table 5.2a: Simulation results for cases 3 and 4.....	155
Table 5.2b:Column properties and conditions from simulation of Cases 3 and 4.....	157
Table 6.1: Optimized kinetic model parameters with 95% confidence limits .....	178
Table D.1.1: Data for Figure D.1.2 determined from kinetic rate measurements in this work and corresponding steric substituent constants taken from Newman [26]. ....	183
Table D.4.1: Summary of experiments and reaction conditions.....	186

## LIST OF FIGURES

Figure 1.1: Principle of the choice of equipment from Schoenmakers et al.[27]. For interpretation of the references to color in this and all other figures, the reader is referred to the electronic version of this dissertation. ....	4
Figure 1.2: An outline of research approach.....	8
Figure 1.3: Major production routes for cyclohexanol and its end uses.....	10
Figure 2.1: Reaction network for cyclohexanol production from cyclohexene.....	20
Figure 2.2: Cyclohexene esterification with acetic acid .....	22
Figure 2.3: Effect of catalyst loading on initial cyclohexene esterification rate. Reaction conditions: Temperature: 363 K, Initial mole ratio CHE:AA = 1:3. ....	25
Figure 2.4: Chemical equilibrium constant $K_a$ (▲) and the best fit of experimental data (solid line), compared with estimation based on Eq. (2.2) and thermodynamic data (dashed line). (■) - $K_a$ for Runs 30-33. ....	27
Figure 2.5: Experimental and predicted mole fraction profiles of CHE esterification. (▲)- AA; (×)- CHA; (■)- CHE; (◆)- CHX. Continuous lines represent the predicted mole fraction profiles. a) Run 16: Temperature 373 K; initial mole ratio CHE:AA = 1:3; CHE:CHX = 5:1; catalyst loading 0.02 kgcat/kg soln. b) Run 17: Temperature 383 K; initial mole ratio CHE:AA = 1:3; CHE:CHX = 5:1; catalyst loading 0.02 kgcat/kg soln. c) Run 18: Temperature 393 K; initial mole ratio CHE:AA = 1:3; CHE:CHX = 5:1; catalyst loading 0.02 kgcat/kg soln. ....	32
Figure 2.6: Experimental and predicted mole fraction profiles of CHE esterification. (▲)- AA; (×)- CHA; (■)- CHE; Continuous lines represent the predicted mole fraction profiles. a) Run 9: Temperature 363 K; initial mole ratio CHE:AA = 1:1; catalyst loading 0.02 kgcat/kg soln. b) Run 10: Temperature 363 K; initial mole ratio CHE:AA = 1:3; catalyst loading 0.02 kgcat/kg soln. c) Run 11: Temperature 363 K; initial mole ratio CHE:AA = 1:5; catalyst loading 0.02 kgcat/kg soln. ....	34

Figure 2.7: Cyclohexene dimer formation during esterification reaction. Straight line represents the best fit for side product formation. (■) Acetic acid; (▲) Cyclohexyl acetate; (◆) Cyclohexene; (×) Cyclohexene dimer. Reaction conditions: Temperature 403 K, Initial mole ratio CHE to AA = 3:1 and catalyst loading 0.02 kgcat/kg soln..... 36

Figure 2.8: Effect of initial water concentration on reaction rate. Reaction conditions: Temperature 363 K, Initial mole ratio CHE to AA = 1:1 and catalyst loading 0.02 kg cat/kg soln. .... 39

Figure A.1a: Effect of agitation speed on reaction rate. (□)-400 rpm; (×)-550 rpm; (Δ)-800 rpm; (▲)-1160 rpm; Reaction conditions: Temperature 363 K; initial mole ratio CHE:AA = 1:1; catalyst loading 0.02 kgcat/kg soln. .... 42

Figure A.1b: Effect of catalyst particle size on reaction rate. (▲)- $d_p < 150\mu\text{m}$ ; (■)- $250 < d_p < 590\mu\text{m}$ ; (□)- $d_p > 590\mu\text{m}$ . Reaction conditions: Temperature 363 K; initial mole ratio CHE :AA = 1:1; catalyst loading 0.02 kgcat/kg soln. .... 43

Figure A.2: Parity plot for verification of additivity of volumes assumption ..... 44

Figure A.3.1: Experimental and predicted mole fraction profiles of CHE esterification for Run 1. (▲)- AA; (×)- CHA; (■)- CHE. .... 47

Figure A.3.2: Experimental and predicted mole fraction profiles of CHE esterification for Run 2. (▲)- AA; (×)- CHA; (■)- CHE. .... 47

Figure A.3.3: Experimental and predicted mole fraction profiles of CHE esterification for Run 3. (▲)- AA; (×)- CHA; (■)- CHE. .... 48

Figure A.3.4: Experimental and predicted mole fraction profiles of CHE esterification for Run 4. (▲)- AA; (×)- CHA; (■)- CHE. .... 48

Figure A.3.5: Experimental and predicted mole fraction profiles of CHE esterification for Run 5. (▲)- AA; (×)- CHA; (■)- CHE. .... 49

Figure A.3.6: Experimental and predicted mole fraction profiles of CHE esterification for Run 6. (▲)- AA; (×)- CHA; (■)- CHE. .... 49

Figure A.3.7: Experimental and predicted mole fraction profiles of CHE esterification for Run 7. (▲)- AA; (×)- CHA; (■)- CHE. ....	50
Figure A.3.8: Experimental and predicted mole fraction profiles of CHE esterification for Run 8. (▲)- AA; (×)- CHA; (■)- CHE. ....	50
Figure A.3.9: Experimental and predicted mole fraction profiles of CHE esterification for Run 12. (▲)- AA; (×)- CHA; (■)- CHE. ....	51
Figure A.3.10: Experimental and predicted mole fraction profiles of CHE esterification for Run 13. (▲)- AA; (×)- CHA; (■)- CHE. ....	51
Figure A.3.11: Experimental and predicted mole fraction profiles of CHE esterification for Run 14. (▲)- AA; (×)- CHA; (■)- CHE. ....	52
Figure A.3.12: Experimental and predicted mole fraction profiles of CHE esterification for Run 15. (▲)- AA; (×)- CHA; (■)- CHE. ....	52
Figure A.3.13: Experimental and predicted mole fraction profiles of CHE esterification for Run 19. (▲)- AA; (×)- CHA; (■)- CHE. ....	53
Figure A.3.14: Experimental and predicted mole fraction profiles of CHE esterification for Run 20. (▲)- AA; (×)- CHA; (■)- CHE. ....	53
Figure A.3.15: Experimental and predicted mole fraction profiles of CHE esterification for Run 21. (▲)- AA; (×)- CHA; (■)- CHE. ....	54
Figure A.3.16: Experimental and predicted mole fraction profiles of CHE esterification for Run 22. (▲)- AA; (×)- CHA; (■)- CHE. ....	54
Figure A.3.17: Experimental and predicted mole fraction profiles of CHE esterification for Run 23. (▲)- AA; (×)- CHA; (■)- CHE. ....	55
Figure A.3.18: Experimental and predicted mole fraction profiles of CHE esterification for Run 24. (▲)- AA; (×)- CHA; (■)- CHE. ....	55
Figure A.3.19: Experimental and predicted mole fraction profiles of CHE esterification for Run 25. (▲)- AA; (×)- CHA; (■)- CHE. ....	56

Figure A.3.20: Experimental mole fraction profiles of CHE esterification for Run 26. (▲) CHA; (■) AA; (◆) CHE;(×) CHE oligomers. Straight line represents the best fit for side product formation.....	56
Figure A.3.21: Experimental mole fraction profiles of CHE esterification for Run 28. (▲) CHA; (■) AA; (◆) CHE; (×) CHE oligomers. Straight line represents the best fit for side product formation.....	57
Figure A.3.22: Experimental mole fraction profiles of CHE esterification for Run 29. (▲) CHA; (■) AA; (◆) CHE; (×) CHE oligomers. Straight line represents the best fit for side product formation.....	57
Figure A.3.23: Experimental mole fraction profiles for Run 30. (▲) AA; (■) CHA (◆) CHE....	58
Figure A.3.24: Experimental mole fraction profiles for Run 31. (▲) AA; (■) CHA (◆) CHE....	58
Figure A.3.25: Experimental mole fraction profiles for Run 32. (▲) AA; (■) CHA (◆) CHE....	59
Figure A.3.26: Experimental mole fraction profiles for Run 33. (▲) AA; (■) CHA (◆) CHE....	59
Figure A.4.1: Chromatogram for CHE dimer identification.....	60
Figure A.4.2: Mass spectra for 1-cyclohexyl cyclohexene.....	61
Figure A.4.3: Mass spectra for 3-cyclohexyl cyclohexene.....	62
Figure A.4.4: Mass spectra for 1,1'-oxybis cyclohexane .....	63
Figure A.5.1: calibration plot for Cyclohexene (CHE).....	65
Figure A.5.2: calibration plot for Acetic acid (AA).....	65
Figure A.5.3: calibration plot for Cyclohexyl acetate (CHA) .....	66
Figure 3.1: A schematic of pilot scale RD column.....	77

Figure 3.2: Temperature profile for Run 4.....	82
Figure 3.3a: Temperature profile Run 9a. (♦)- Experimental; (■) – simulation assuming heat loss on Stage 13; (▲) – simulation assuming heat loss uniformly across Stages 2-13. ....	91
Figure 3.3b: Composition profile of Run 9a. (×)-CHE; (♦)- CHE simulated; (□)- CHA; (■)- CHA simulated; (Δ)-AA; (▲)- AA simulated .....	91
Figure 3.4a: Temperature profile Run 9b. (♦)- Experimental; (■) – simulation.....	92
Figure 3.4b: Composition profile of Run 9b. (×)-CHE; (♦)- CHE simulated; (□)- CHA; (■)- CHA simulated; (Δ)- AA; (▲)- AA simulated. ....	92
Figure 3.5: Effect of feed stage on CHE conversion for Run 9a. (♦)- Changing CHE feed stage (■) – Changing AA feed stage .....	93
Figure 3.6: Effect of heat loss on CHE conversion for Run 9a. ....	94
Figure 3.7: Effect of heat addition to stages in catalytic section on CHE conversion for Run 9a.....	96
Figure 3.8: Effect of heat transfer between stages in catalytic section on CHE conversion for Run 9a.....	96
Figure 4.1. Effect of agitation speed on conversion rate of MS. Reaction conditions: BuOH:MS molar feed ratio = 20:1; catalyst loading = 5.6 wt%; reaction temperature = 363 K. (□ - 300 rpm; ■ - 900 rpm; ▲ - 1060; × - 1230 rpm; + - 1460 rpm). ....	109
Figure 4.2. Effect of catalyst particle size on conversion rate of MS. Reaction conditions: BuOH:MS molar feed ratio = 20:1; Amberlyst 15 catalyst loading = 5.6 wt% or equivalent of 10.25 meq H <sup>+</sup> ; reaction temperature = 363 K. (□ - 60-250 μm; ■ -250-500 μm; ▲ - > 500 μm). ....	110
Figure 4.3a. Initial MS transesterification rate vs. catalyst loading (wt%). BuOH:MS molar feed ratio = 20:1. (×) – 373 K; (■) – 363 K. Solid line represents best fit of the data. ....	119
Figure 4.3b. Effect of catalyst loading (wt%) on the conversion rate of MS. Reaction conditions: BuOH:MS molar feed ratio = 20:1; reaction temperature = 363 K. (-■- - 5.6 wt%; -▲- - 2.8 wt%; -●- - 1.4 wt%). ....	119

Figure 4.4a. Mole fraction profiles of species present in MS transesterification reactions at 363 K. Reaction conditions: BuOH:MS molar feed ratio = 20:1; catalyst loading = 4.8 wt%. (-□- - MS; -■- - BS; -▲- - MeOH; -×- - DBE; +- - BME; -○- - W). ..... 121

Figure 4.4b. Mole fraction profiles of species present in MS transesterification reactions at 373 K. Reaction conditions: BuOH:MS molar feed ratio = 20:1; catalyst loading = 4.8 wt%; (-□- - MS; -■- - BS; -▲- - MeOH; -×- - DBE; +- - BME; -○- - W). ..... 121

Figure 4.5. Effect of temperature on the conversion rate of MS. Reaction conditions: BuOH:MS molar feed ratio = 20:1; catalyst loading = 5.6 wt%. (×) -343 K ; (■) - 353 K; (▲) -363 K. .. 122

Figure 4.6. Effect of BuOH:MS molar feed ratio on MS conversion. Reaction conditions: Temperature = 363 K; catalyst loading = 4.8 wt%. (-▲- - 5:1; -■- - 10:1; -×- - 20:1). ..... 123

Figure C.1.1: Calibration plot for Methyl stearate (MS) ..... 128

Figure C.1.2: Calibration plot for 1-Butanol (BuOH) ..... 128

Figure C.1.3: Calibration plot for Butyl stearate (BS)..... 129

Figure C.1.4: Calibration plot for Methanol (MeOH) ..... 129

Figure C.1.5: Calibration plot for Dibutyl ether (DBE)..... 130

Figure C.1.6.:Calibration plot for Butyl methyl ether (BME) ..... 130

Figure C.3.1: Mole fraction profiles of species present in MS transesterification reactions at 70°C. Reaction conditions: initial mole ratio MS to BuOH = 1:20; catalyst loading = 5.6 wt%; (-□- -MS;-■- - BS;-▲- -MeOH;-×- -DBE;+- -BME; -○- -W). ..... 134

Figure C.3.2: Mole fraction profiles of species present in MS transesterification reactions at 80°C. Reaction conditions: initial mole ratio MS to BuOH = 1:20; catalyst loading = 5.6 wt%; (-□- -MS;-■- - BS;-▲- -MeOH;-×- -DBE;+- -BME; -○- -W). ..... 134

Figure C.3.3: Mole fraction profiles of species present in MS transesterification reactions at 90°C. Reaction conditions: initial mole ratio MS to BuOH = 1:20; catalyst loading = 5.6 wt%; (-□- -MS;-■- - BS;-▲- -MeOH;-×- -DBE;+- -BME; -○- -W). ..... 135

Figure C.3.4: Mole fraction profiles of species present in MS transesterification reactions at 90°C. Reaction conditions: initial mole ratio MS to BuOH = 1:20; catalyst loading = 2.8 wt%; (-□- -MS; -■- -BS; -▲- -MeOH; -×- -DBE; -+- -BME; -○- -W). ..... 135

Figure C.3.5: Mole fraction profiles of species present in MS transesterification reactions at 90°C. Reaction conditions: initial mole ratio MS to BuOH = 1:20; catalyst loading = 1.4 wt%; (-□- -MS; -■- -BS; -▲- -MeOH; -×- -DBE; -+- -BME; -○- -W). ..... 136

Figure C.3.6: Mole fraction profiles of species present in MS transesterification reactions at 90°C. Reaction conditions: initial mole ratio MS to BuOH = 1:10; catalyst loading = 4.8 wt%; (-□- -MS; -■- -BS; -▲- -MeOH; -×- -DBE; -+- -BME; -○- -W). ..... 136

Figure C.3.7: Mole fraction profiles of species present in MS transesterification reactions at 90°C. Reaction conditions: initial mole ratio MS to BuOH = 1:10; catalyst loading = 4.8 wt%; (-□- -MS; -■- -BS; -▲- -MeOH; -×- -DBE; -+- -BME; -○- -W). ..... 137

Figure C.3.8: Mole fraction profiles of species present in MS transesterification reactions at 90°C. Reaction conditions: initial mole ratio MS to BuOH = 1:5; catalyst loading = 4.8 wt%; (-□- -MS; -■- -BS; -▲- -MeOH; -×- -DBE; -+- -BME; -○- -W). ..... 137

Figure C.3.9: Mole fraction profiles of species present in MS transesterification reactions at 90°C. Reaction conditions: initial mole ratio MS to BuOH = 1:30; catalyst loading = 4.8 wt%; (-□- -MS; -■- -BS; -▲- -MeOH; -×- -DBE; -+- -BME; -○- -W). ..... 138

Figure C.3.10: Mole fraction profiles of species present in MS transesterification reactions at 90°C. Reaction conditions: initial mole ratio MS to BuOH = 1:20; catalyst loading = 4.8 wt%; (-□- -MS; -■- -BS; -▲- -MeOH; -×- -DBE; -+- -BME; -○- -W). ..... 138

Figure C.3.11: Mole fraction profiles of species present in MS transesterification reactions at 100°C. Reaction conditions: initial mole ratio MS to BuOH = 1:20; catalyst loading = 2.8 wt%; (-□- -MS; -■- -BS; -▲- -MeOH; -×- -DBE; -+- -BME; -○- -W). ..... 139

Figure C.3.12: Mole fraction profiles of species present in MS transesterification reactions at 100°C. Reaction conditions: initial mole ratio MS to BuOH = 1:20; catalyst loading = 5.6 wt%; (-□- -MS; -■- -BS; -▲- -MeOH; -×- -DBE; -+- -BME; -○- -W). ..... 139

Figure 5.1: Schematic of distillation column with external side reactors and flow diagram for Case 3..... 147

Figure 5.2: Simulation methodology for D-SRC evaluation. ....	150
Figure 5.3: Effect of reactor PFR reaction temperature on MS conversion and BuOH selectivity towards BS. (■)- BS selectivity; (◆) - MS conversion. Reaction conditions: Feed mole ratio of BuOH to MS = 2; Catalyst weight in reactor= 20 kg; Pressure = 3 atm. ....	153
Figure 5.4a: Flow diagram representing cases 1a and 1b. ....	154
Figure 5.4b: Flow diagram representing case 2. ....	154
Figure 5.5: Flow diagram representing cases 4a, 4b and 4c. ....	156
Figure 6.1. Effect of increasing linear alcohol carbon number on esterification rate of butyric acid. a) (TON); b) $k_{TON}$ (Eq.6.2). (■) – Amberlyst 70 ;(◆) - p-TSA; Reaction conditions: 3:1 alcohol:acid molar feed ratio, 0.01 kg cat/kg soln, 60°C. ....	169
Figure 6.2: Esterification rate of butyric acid with primary alcohols. (□) – Amberlyst 70;(◇) - Amberlyst BD20; (○) – Amberlyst 15; (Δ) - Amberlyst 36; Reaction conditions: 3:1 alcohol:acid feed molar ratio, 0.01 kg cat/kg soln, 60°C. ....	171
Figure 6.3: Initial BA esterification rate vs. catalyst loading; (◆)-120°C; (■)-130°C; Reaction conditions: 2-EHA:BA feed molar ratio = 6:1. Solid lines represent best fit of the data. ....	173
Figure 6.4: Mole fraction profiles of reaction components; (◆) – BA; (▲) – 2EHB; (×) – W; Reaction conditions: 6:1 2-EHA:BA molar feed ratio, 0.01 kg cat/kg soln, 130°C. Continuous lines represent predicted mole fraction profiles from kinetic model. ....	176
Figure 6.5: Comparison of cloud points between canola biodiesel, #2 Diesel and canola biodiesel with butyric acid esters. ....	178
Figure D.1.1: Verification of Taft Equation - polar effect; (◇) - p-TSA; (Δ) -Amberlyst 70. ...	182
Figure D.1.2: Verification of Taft Equation (steric effect) catalyzed esterification of butyric acid with linear alcohols; (◆) – p-TSA; (■) – Amberlyst 70. ....	183
Figure D.2.1: Effect of alcohol chain branching on butyric acid esterification rate. Reaction conditions: 3:1 alcohol:BA feed molar ratio, 0.01 kg Amberlyst 70/kg soln, 60°C. ....	184

Figure D.3.1: (a) Effect of agitation speed on conversion rate of butyric acid: ( $\Delta$ ) -100rpm; ( $\blacklozenge$ ) - 530 rpm; ( $\square$ ) - 850 rpm. (b) Effect of catalyst particle size on conversion rate of butyric acid: (+) - 300-500 $\mu\text{m}$ ; ( $\times$ ) - 250-500  $\mu\text{m}$ ; ( $\square$ ) - 150-250  $\mu\text{m}$ . Reaction conditions: 1:1 BA:2-EHA molar feed ratio, 0.01 kg Amberlyst 70/kg soln., 110°C. .... 185

Figure D.4.1: Mole fraction profiles of reaction components for Run 1; ( $\blacklozenge$ ) – BA; ( $\blacktriangle$ ) – 2EHB; ( $\times$ ) – W. Continuous lines represent predicted mole fraction profiles from kinetic model. .... 187

Figure D.4.2: Mole fraction profiles of reaction components for Run 2; ( $\blacklozenge$ ) – BA; ( $\blacktriangle$ ) – 2EHB; ( $\times$ ) – W. Continuous lines represent predicted mole fraction profiles from kinetic model. .... 187

Figure D.4.3: Mole fraction profiles of reaction components for Run 3; ( $\blacklozenge$ ) – BA; ( $\blacktriangle$ ) – 2EHB; ( $\times$ ) – W. Continuous lines represent predicted mole fraction profiles from kinetic model. .... 188

Figure D.4.4: Mole fraction profiles of reaction components for Run 5; ( $\blacklozenge$ ) – BA; ( $\blacktriangle$ ) – 2EHB; ( $\times$ ) – W. Continuous lines represent predicted mole fraction profiles from kinetic model. .... 188

Figure D.4.5: Mole fraction profiles of reaction components for Run 6; ( $\blacklozenge$ ) – BA; ( $\blacktriangle$ ) – 2EHB; ( $\times$ ) – W. Continuous lines represent predicted mole fraction profiles from kinetic model. .... 189

Figure D.4.6: Mole fraction profiles of reaction components for Run 7; ( $\blacklozenge$ ) – BA; ( $\blacktriangle$ ) – 2EHB; ( $\times$ ) – W. Continuous lines represent predicted mole fraction profiles from kinetic model. .... 189

Figure D.4.7: Mole fraction profiles of reaction components for Run 8; ( $\blacklozenge$ ) – BA; ( $\blacktriangle$ ) – 2EHB; ( $\times$ ) – W. Continuous lines represent predicted mole fraction profiles from kinetic model. .... 190

Figure D.4.8: Mole fraction profiles of reaction components for Run 9; ( $\blacklozenge$ ) – BA; ( $\blacktriangle$ ) – 2EHB; ( $\times$ ) – W. Continuous lines represent predicted mole fraction profiles from kinetic model. .... 190

Figure D.4.9: Mole fraction profiles of reaction components for Run 10; ( $\blacklozenge$ ) – BA; ( $\blacktriangle$ ) – 2EHB; ( $\times$ ) – W. Continuous lines represent predicted mole fraction profiles from kinetic model. .... 191

Figure D.4.10: Mole fraction profiles of reaction components for Run 11; ( $\blacklozenge$ ) – BA; ( $\blacktriangle$ ) – 2EHB; ( $\times$ ) – W. Continuous lines represent predicted mole fraction profiles from kinetic model ..... 191

Figure D.4.11: Mole fraction profiles of reaction components for Run 12; (◆) – BA; (▲) – 2EHB; (×) – W. Continuous lines represent predicted mole fraction profiles from kinetic model. .... 192

Figure D.4.12: Mole fraction profiles of reaction components for Run 13; (◆) – BA; (▲) – 2EHB; (×) – W. Continuous lines represent predicted mole fraction profiles from kinetic model. .... 192

Figure D.4.13: Mole fraction profiles of reaction components for Run 14; (◆) – BA; (▲) – 2EHB; (×) – W. Continuous lines represent predicted mole fraction profiles from kinetic model. .... 193

Figure D.4.14: Mole fraction profiles of reaction components for Run 15; (◆) – BA; (▲) – 2EHB; (×) – W. Continuous lines represent predicted mole fraction profiles from kinetic model. .... 193

Figure D.4.15: Mole fraction profiles of reaction components for Run 16; (◆) – BA; (▲) – 2EHB; (×) – W. Continuous lines represent predicted mole fraction profiles from kinetic model. .... 194

Figure D.4.16: Mole fraction profiles of reaction components for Run 17; (◆) – BA; (▲) – 2EHB; (×) – W. Continuous lines represent predicted mole fraction profiles from kinetic model. .... 194

Figure D.4.17: Mole fraction profiles of reaction components for Run 18; (◆) – BA; (▲) – 2EHB; (×) – W. Continuous lines represent predicted mole fraction profiles from kinetic model. .... 195

Figure D.4.18: Mole fraction profiles of reaction components for Run 19; (◆) – BA; (▲) – 2EHB; (×) – W. Continuous lines represent predicted mole fraction profiles from kinetic model. .... 195

Figure D.4.19: Mole fraction profiles of reaction components for Run 20; (◆) – BA; (▲) – 2EHB; (×) – W. Continuous lines represent predicted mole fraction profiles from kinetic model. .... 196

Figure D.5.1: Calibration plot for Butyric acid (BA) ..... 197

Figure D.5.2: Calibration plot for 1-Butanol (BuOH) ..... 198

Figure D.5.3: Calibration plot for Butyl butyrate (BB) .....	198
Figure D.5.4: Calibration plot for Ethanol (EtOH).....	199
Figure D.5.5: Calibration plot for Ethyl butyrate (EB).....	199
Figure D.5.6: Calibration plot for isopropanol (IPA). .....	200
Figure D.5.7: Calibration plot for isopropyl butyrate (IPB). .....	200
Figure D.5.8: Calibration plot for Methanol (MeOH). .....	201
Figure D.5.9: Calibration plot for Methyl butyrate (MB).....	201
Figure D.5.10: Calibration plot for 1-Propanol (PrOH). .....	202
Figure D.5.11: Calibration plot for Propyl butyrate (PB).....	202
Figure D.5.12: Calibration plot for Sec-Butanol (S-BuOH).....	203
Figure D.5.13: Calibration plot for tert-Butanol (t-BuOH). .....	203
Figure D.5.14: Calibration plot for Butyric acid (BA) .....	204
Figure D.5.15: Calibration plot for 2-Ethylhexyl butyrate (2-EHB). .....	204
Figure D.5.16: Calibration plot for 2-Ethylhexanol (2-EHA). .....	205

## KEY TO SYMBOLS AND ABBREVIATIONS

$a_i$	Activity of species of $i$ in solution
AA	Acetic acid
BA	Butyric acid
BME	Butyl methyl ether
BS	Butyl stearate
BuOH	1-butanol
CHA	Cyclohexyl acetate
CHE	Cyclohexene
CHX	Cyclohexane
DBE	Dibutyl ether
D-SRC	Distillation with external side reactor concept
2-EHA	2-Ethylhexanol
2EHB	2-Ethylhexyl butyrate
$E_f$	Energy of activation for forward esterification reaction, kJ/kmol
$F_{\min}^2$	Absolute sum of mean square differences
IE	Ion exchange capacity of solid acid catalyst (Equivalents/kg cat)
$k_f^0$	Pre-exponential factor for forward reaction rate constant
$k_f$	Forward reaction rate constant
$K_a$	Equilibrium constant

$k_{TON}$	Turnover number normalized to actual alcohol and acid concentrations ( $m^6/kmol$ alcohol/ $kmol H^+$ /hr)
$k_{f,auto}^0$	Pre-exponential factor of forward reaction rate constant in auto-catalyzed esterification reaction (1/min)
$k_{f,auto}$	Forward reaction rate constant in auto-catalyzed esterification reaction (1/min)
MeOH	Methanol
MS	Methyl stearate
$(MV)_{tot}$	Total molar volume of the solution ( $m^3/kmol$ )
$n_{runs}$	Number of data points
NaCl	Sodium Chloride
NaOH	Sodium hydroxide
$N_i^{predicted}$	Moles of $i^{th}$ component predicted by kinetic model
$N_i^{experimental}$	Experimentally determined moles of $i^{th}$ component
$r_{CHE}$	Initial reaction rate of Cyclohexene (kmol/hr)
$N_i$	Moles of $i^{th}$ component in liquid phase
p-TSA	Para toluene sulfonic acid
$r_i$	Reaction rate of $i^{th}$ component ( $kmol/m^3/min$ )
$-r_{BA}$	Initial reaction rate of butyric acid determined from mole fraction profile (1/min)

$(-r_{BA})_{ini}$	Initial reaction rate of butyric acid determined from mole fraction profile (1/min)
TON	Turnover number (kmol limiting reactant/kmol $H^+$ /hr)
V	Volume of solution ( $m^3$ )
W	Water
$W_{cat}$	Catalyst concentration (kg catalyst/kg solution)
$W_{sol}$	Weight of solution (kg)
$x_j$	Mole fraction of species j in solution
$\Delta_R H^o$	Standard enthalpy of reaction in liquid state, kJ/mol
$\Delta H_{v,j}$	Heat of vaporization for species, kJ/mol
$\Delta g_r^o$	Standard Gibbs energy of reaction
$\Delta g_f^o$	Gibbs energy of formation
$\Delta h_f^o$	Standard enthalpy of formation kJ/mol
$\Delta h_r^o$	Standard enthalpy of reaction kJ/mol
W	Water
$W_{cat}$	Catalyst concentration (kg cat/kg soln)
$x_{i,exp}$	Experimentally determined mole fraction of $i^{th}$ component
$x_{i,cal}$	Mole fraction of $i^{th}$ component calculated using pseudo-homogeneous model

*Greek Letters*

$\gamma_i$       Liquid phase activity coefficient

$\nu_i$       Stoichiometric coefficient of  $i^{\text{th}}$  component in solution

*Subscripts*

$i$       Species in solution

## Chapter 1: Introduction

Organic esters are an important class of commercial chemicals with the general formula  $\text{RCOOR}'$ , where R and R' can be either the same or different aliphatic, aromatic or heterocyclic groups [1]. The most common methods for organic ester synthesis by acid catalysis are [2-4]: a) direct addition of carboxylic acid to alcohol with the elimination of water b) transesterification of an ester by alcohol and c) direct addition of olefin to carboxylic acid. Esters derived from carboxylic acids are used as solvents, plasticizers, and food flavors [5]. They find application in perfumery and are precursors in making a wide range of detergents [6], agrochemicals, and pharmaceuticals. Diesters of carboxylic acids can be used as fuel components that improve cold flow properties of biodiesel fuel [7, 8], and fatty acid methyl esters are used as biodiesel fuel [9, 10]. Conventional routes for ester production use homogeneous catalysts such as sulfuric acid [11] and p-toluene sulfonic acid [12]. Heterogeneous catalysts such as cation exchange resins [6, 13, 14] are replacing corrosive homogeneous catalysts in organic ester synthesis due to their eco-friendly nature and ease of separation from the reaction mixture.

The chemical industry is one of the largest energy consuming sectors in the world. In 2008, the industrial sector accounted for 38% of the global energy use of 505 quadrillion Btu, 22% of which was consumed for chemicals processing. Energy also represents 60% of the chemical industry's operating costs [15]. Most organic esters are high production volume chemicals, produced at levels greater than 1000 MT per year by at least one member country in Organization for Economic Cooperation and Development (OECD) [16].

Esterification and transesterification reactions, which are used to produce organic esters, are limited by chemical equilibrium. Unit operations such as distillation are required to separate

the ester (or co-product water) and thus drive the reaction to completion, making these processes highly energy intensive. Because of the growing demand for esters, there is an urgent need for alternative chemical processing technologies with lower energy intensity to produce esters more economically.

Process intensification (PI) provides an opportunity to use engineering principles to simplify processes, improve energy efficiency and decrease waste production, energy intensity and operational costs. It helps in developing a sustainable processing technology [17-19]. PI can be achieved by combining functions or phenomena in an operation, adding or enhancing targeted functions in a process and/or by using alternative energy sources to enhance performance.

A brief introduction to two PI concepts, namely reactive distillation and distillation with external side reactors is given in Section 1.1. These concepts were evaluated in this study to decrease energy intensity in esterification and transesterification processes to produce organic esters of commercial importance.

## **1.1. Advanced PI techniques**

### **1.1.1. Reactive Distillation**

Reactive distillation represents a successful example of process intensification by integrating chemical reaction and physical separation into a single unit operation. Use of RD to produce high purity methyl acetate was a pioneering commercial application of PI to improve energy efficiency and lower capital costs. Eastman chemicals' methyl acetate RD process was patented in 1984[20]. In the last three decades, RD was used in the commercial production of methyl tertiary butyl ether (MTBE), ethyl tertiary butyl ether (ETBE), and tertiary amyl methyl ether (TAME) [21] as gasoline oxygenate additives. With growing concerns regarding ground water pollution in the USA, MTBE is now being replaced with ETBE and TAME [22]. Apart

from its use in traditional processes such as esterification and etherification, RD has also been successfully applied as a PI technique for reactions such as desulfurization, selective hydrogenation, dimerization and isomerization [23, 24]. According to Harmsen [23], CDTECH and Sulzer Chemtech are the two major industrial scale technology suppliers for processes involving RD operations. In 2006, CDTECH alone had licensed 146 commercial applications of RD. Over 200 licensed commercial applications of RD are reported worldwide [23]. This shows emerging interest in applying RD as a potential PI technique within the chemical industry.

RD offers the following advantages over conventional processes [25, 26]

- reduces capital investment and operational costs
- has scope for improving thermodynamic efficiency by utilizing heat of reaction for liquid evaporation
- drives the reaction towards completion by removing the volatile product thereby overcoming conversion limitations related to chemical equilibrium
- improves desired product selectivity by removing or maintaining low concentration of reactants or products in the column that lead to side reaction
- gives better control over the reactor system (by avoiding hot spots in the reactor)

In literature, certain guidelines to choose a reaction system for RD based on reaction kinetics and relative volatilities of components are available [27, 28]. Figure 1.1 shows a qualitative graphical method to identify reactive systems that can be considered for RD. Areas for RD, distillation with side reactor configuration and evaporator connected to a reactor configuration are shown. For reactions with moderate to fast reaction rate, RD is suggested. For very slow reactions with low to medium relative volatilities, distillation with an external side reactor is suggested.

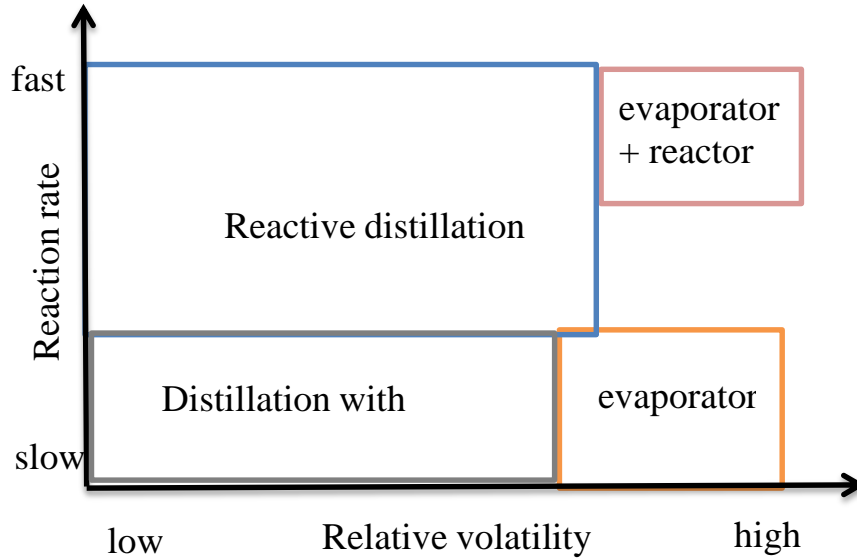


Figure 1.1: Principle of the choice of equipment from Schoenmakers et al.[27]. For interpretation of the references to color in this and all other figures, the reader is referred to the electronic version of this dissertation.

#### 1.1.1.1. Heat integration in RD column

To enhance energy efficiency, the heat of reaction needs to be taken into account during the conceptual stages of RD column design [29]. Internal heat integration improves thermodynamic efficiency of the RD process by using the heat of reaction for separation operation in RD column. This internal heat utilization can be quantified as the thermal effect of a reaction ( $\xi$ ), a dimensional number first introduced by Sundmacher et al.,[26]. It is defined as the ratio between the heat of reaction and mean heat of vaporization.

$$\xi = \frac{(\Delta_R H^o)^L}{\sum_{j=1}^N (x_j \Delta H_{v,j})^L} \quad \text{where } j=1, N \text{ number of components in the reaction} \quad (1.1)$$

Based on  $\xi$ , Sun et al [30] divided the RD columns into the following three broad categories:

- Reactions involving high thermal effect ( $\xi > 1.0$ ) where internal heat integration must be considered
- Reactions with moderate thermal effect ( $0.05 \leq \xi \leq 1.0$ ) where balance between internal mass and heat integration is needed
- Reactions with negligible thermal effect ( $0 \leq \xi < 0.05$ ) where there is no heat utilization but higher conversions can be achieved by vaporizing the products thus affecting the kinetic equilibrium

While considering the RD process for reactions involving moderate thermal effect ( $0.05 \leq \xi \leq 1.0$ ), both internal mass and heat integration need to be evaluated during conceptual stages of RD design. The synergy between mass and heat integration has a significant effect on process intensification. A systematic methodology for internal heat integration for reactions with  $\xi > 1.0$  is proposed in literature [29]. Detailed simulation studies of reactive distillation processes with internal heat integration showed substantial improvements in energy efficiency besides reduced capital investment [29, 31-35]. Huang et al., [29] studied methyl acetate production from methanol and acetic acid (a reaction with moderate thermal effect  $\xi = 0.79$  at 330K) using RD and showed that simultaneous mass and heat integration can reduce heat duties of condenser and reboiler by 3.68% and 4.52% respectively compared to a basic process design. It is important to note that the reduction in energy consumption is only a result of increasing thermodynamic efficiency in one RD column. In a system with a RD column followed by a distillation column as in the transesterification methyl acetate with n-butanol, thermal coupling of RD with a side stripper column to separate methanol and methyl acetate results in 14.% decrease in energy consumption [36].

This study will focus on the simulation and pilot plant operation of a RD column involving a reaction with moderate thermal effect. In addition to internal mass and heat integration, the focus of this work is to study the effect of external heat integration on the energy efficiency of RD column.

#### *1.1.1.2. Alternative to RD technique*

Reactive distillation is not always advantageous in organic ester synthesis. It is ineffective for chemical systems in which temperatures favorable for reaction and that for separation based on vapor-liquid equilibrium are not complementary. Another hardware issue that mitigates RD use is catalyst deactivation or the need for changing catalyst in RD. It is cumbersome to change heterogeneous catalyst packing from a RD column; this inflexibility adds to the operating cost of the process. In chemical systems with very low reaction rate, high catalyst hold up is required to achieve higher conversions. But high catalyst hold up in RD affects separation efficiency by minimizing interfacial area between vapor and liquid. These challenges in operational and hardware configurations can be overcome by using a distillation column with external side reactors (herein DSR).

#### **1.1.2. Distillation with external side reactor (DSR)**

The concept of DSR as an alternative to RD was first proposed in literature by Schoenmakers et al. [37]. Baur et al. [38] identified the complexities associated with DSR and suggested an algorithm to determine optimum side reactor/column configuration. They studied the methyl acetate process using DSR and concluded that it can match the methyl acetate yield obtained using a reactive column. Bisowarno et al. [39] applied the DSR concept to ethyl tert-butyl ether (ETBE) production. Ouni et al. [40] compared DSR and RD configurations for tert-

amyl methyl ether (TAME) production and isobutylene dimerization. Ojeda Nava et al.[41] also studied TAME production using the DSR concept. They concluded that by optimizing design parameters for DSR, it can compete with RD both in terms of energy efficiency and process economics. Ding et al. [42] presented an optimization study for benzyl chloride production using DSR. Kaymak et al.[28, 43, 44] identified that for RD to be economically attractive for any reaction system, the temperature range suitable for chemical reaction to be compatible with the temperature range suitable for vapor-liquid equilibrium. Their study is a quantitative representation of the equipment choice guideline shown in Figure 1.1. They evaluated DSR for a generic exothermic reaction where relative volatilities of components were assumed.

## **1.2. Research approach and outline**

In this research, for a defined process concept to produce organic esters, a comprehensive literature review was carried out. In addition, a study on chemical thermodynamics of the process under consideration was also conducted. Batch reactor experiments were carried out to characterize reaction kinetics of the system. These kinetic parameters were used in the process simulation software, Aspen Plus. Non-ideality of the reaction system was taken into account during kinetics characterization and process simulation. The simulation model thus developed was used to evaluate process configurations that result in energy efficient production routes. An outline of research approach followed in this work is presented in Figure 1.2. This research approach was followed for evaluating PI techniques, RD and DSR in the production of cyclohexyl acetate and butyl stearate respectively. The process simulation model was experimentally verified using pilot plant experiments only in the case of cyclohexyl acetate production.

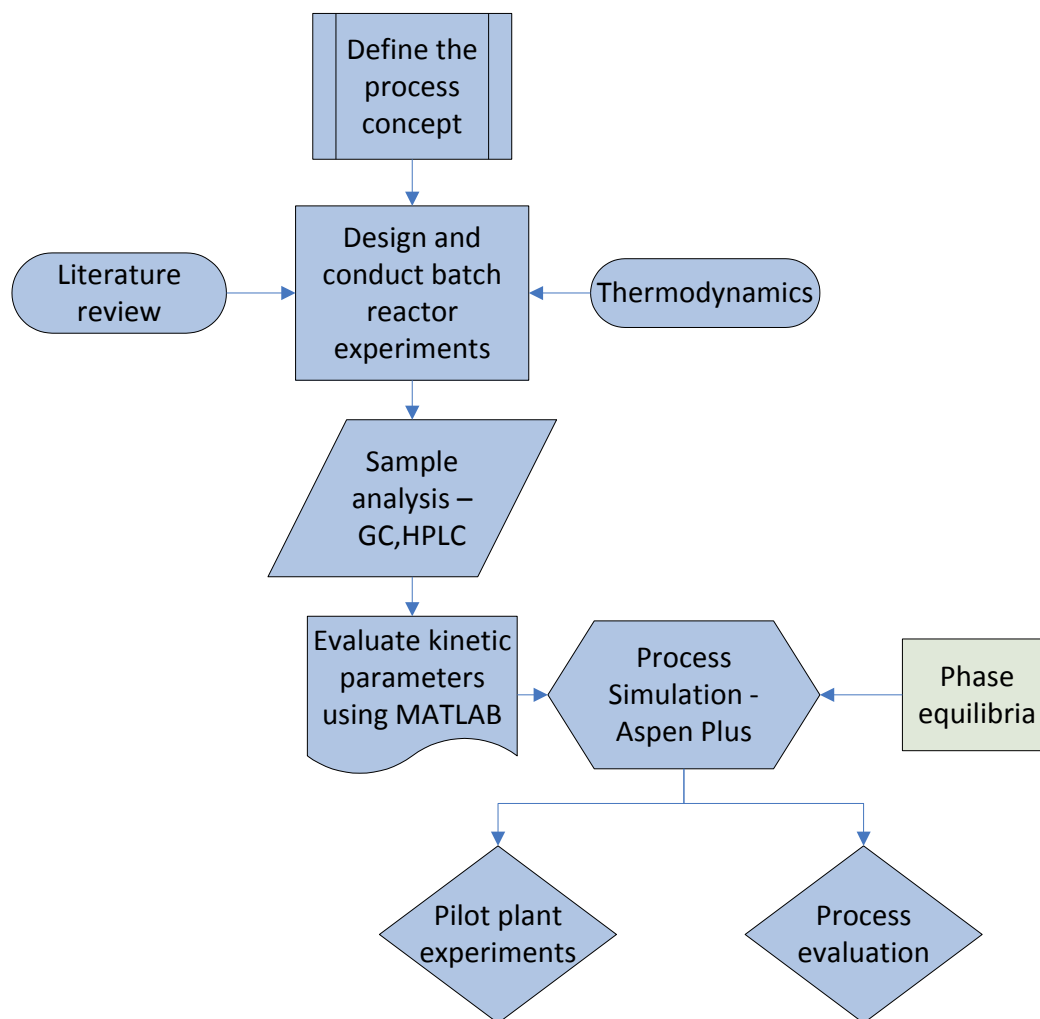


Figure 1.2: An outline of research approach.

### 1.2.1. Cyclohexyl acetate – an intermediate in cyclohexanol production

Cyclohexanol is an industrially important chemical produced in large scale worldwide, particularly as an intermediate in the production of nylon [45]. Major production routes for producing nylon starting from naphtha, coal or natural gas are presented in Figure 1.3. It is to be noted here that the benzene production route from natural gas shown in Figure 1.3 is not yet a commercial process. Catalysts that can be used for direct conversion of natural gas to petrochemicals have been reported in literature [46]. This route is included in the Figure 1.3 to make it more comprehensive.

The conventional route to cyclohexanol is via partial oxidation of cyclohexane, but this route gives low selectivity with substantial byproduct formation and large recycle streams. Hydrogenation of phenol with a metal catalyst is another commercial route to produce cyclohexanol and cyclohexanone (Ketone-Alcohol oil or KA oil), and yields as high as 95% at 100% conversion can be achieved by this route. Though efficient, this route is energy intensive because three moles of hydrogen are required for every mole of cyclohexanol formed. An alternative route to produce cyclohexanol has been commercialized by Asahi chemicals [47]. This route involves partial hydrogenation of benzene to cyclohexene and cyclohexane separation of cyclohexene from benzene and cyclohexane by successive extractive distillations, and direct hydration of cyclohexene to cyclohexanol using a HZSM-5 type zeolite catalyst. The first step in this process offers the advantage of less hydrogen consumption than the phenol route. The second step involves high energy consumption to separate the close boiling mixture of benzene, cyclohexane and cyclohexene by extractive distillation. The third step suffers from the drawback of very low equilibrium conversion (~14%) [45]. This third step is also very energy intensive, as the reaction is carried out in a slurry reactor followed by distillation for external separation.

All of the commercial processes discussed above have one common disadvantage: reaction must be followed by an energy-intensive separation step. There thus exists an opportunity in cyclohexanol production offer for process intensification [48]; reactive distillation (RD) can combine reaction with separation, leading to a process with potentially lower energy consumption.

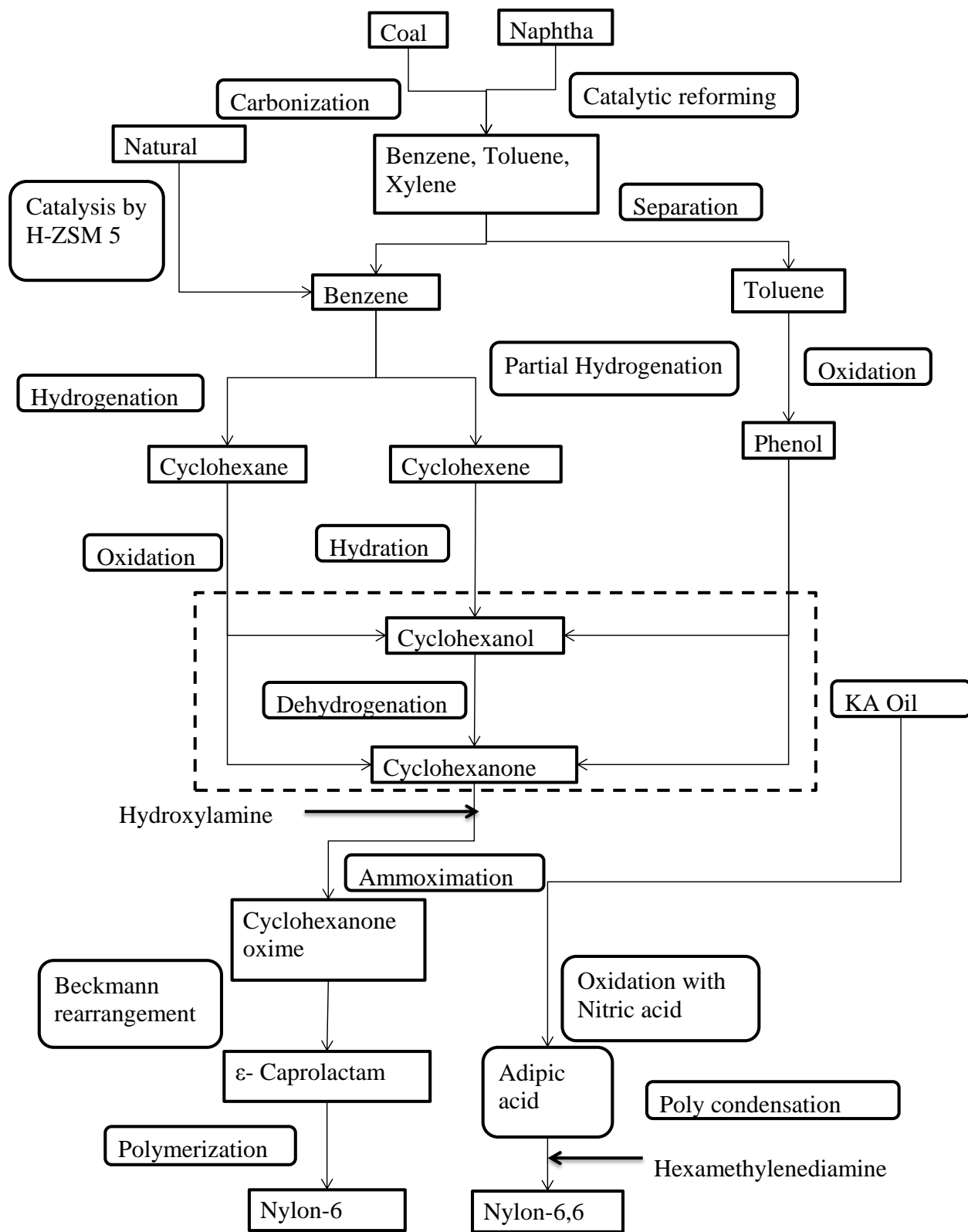


Figure 1.3: Major production routes for cyclohexanol and its end uses

The reaction of cyclohexene with a carboxylic acid to form cyclohexyl ester with subsequent hydrolysis of the ester is an attractive cyclohexene hydration route to cyclohexanol for nylon-6,6 production. The use of RD to produce cyclohexyl formate and subsequent hydration to cyclohexanol has been reported in the literature [49, 50]. In this work, acetic acid is used as the reactive entrainer instead of formic acid, because the latter is toxic and decomposes into carbon monoxide and water at higher temperatures. Cyclohexene esterification with acetic acid is a moderately fast reaction. Therefore, RD is an apt choice for this reaction system (Figure 1.1). In addition to chemical kinetics and pilot scale experiments, insight into the effect of heat addition and heat transfer between the reactive stages on cyclohexene conversion in RD column using process simulations is also presented.

Chapters 2 and 3 in this study describe the use of RD technique to produce cyclohexyl acetate. In Chapter 2, the chemical reaction kinetics and equilibrium dependence on temperature of Amberlyst 70 catalyzed esterification of acetic acid with cyclohexene are described. This chapter also deals with the effect of cyclohexene dimerization and initial water concentration on the activity of the heterogeneous Amberlyst 70 catalyst.

In Chapter 3, pilot plant-scale RD experiments of cyclohexene esterification with acetic acid are described. Based on preliminary pilot-plant runs, process configuration and conditions suitable for high conversions of cyclohexene are suggested, and initial investigations into heat integration for this reaction system are reported. This experimental data was also used to develop a simulation model using the process design software -Aspen Plus.

### **1.2.2. Butyl stearate – a model compound for potential biodiesel constituents**

Fatty acid butyl esters can be used as potential biodiesel constituents. Butyl stearate was chosen as a model compound to represent fatty acid butyl esters. A process concept to produce

butyl stearate from methyl stearate by transesterification with 1-butanol was chosen to evaluate DSR as a potential PI technique. In Chapter 4, the chemical reaction kinetics of Amberlyst 15 catalyzed transesterification of methyl stearate with 1-butanol along with etherification side reaction is described. Using this kinetics in the Aspen Plus process design software, a model to evaluate the concept of distillation with an external side reactor was simulated. In Chapter 5, the details of these simulations are described.

### **1.2.3. Butyric acid esterification: The effect of alcohol carbon chain length and type of catalyst on the rate of esterification reaction**

In addition to evaluation of PI concepts, the effect of factors such as alcohol carbon chain length and type of solid acid catalyst on esterification reaction rate was investigated. Butyric acid, a carboxylic acid that can potentially be obtained from fermentation processes was chosen as a model compound in this study. The effect of increasing alcohol carbon chain length and branching on esterification rate is presented. Four strong cation exchange resins, Amberlyst 15, Amberlyst 36, Amberlyst BD 20, and Amberlyst 70, were examined along with p-toluene sulfonic acid as a homogeneous catalyst. For all catalysts, the decrease in turnover number (TON) with increasing carbon chain length of the alcohol is described in terms of steric hindrance and alcohol polarity. Detailed kinetics of butyric acid esterification with 2-ethylhexanol using Amberlyst 70 catalyst were studied in a batch reactor. In Chapter 6, an activity-based, pseudo-homogeneous kinetic model that includes autocatalysis by butyric acid is presented for the Amberlyst 70 ion exchange resin catalyst.

## **REFERENCES**

### 1.3. References

1. Riemenschneider, W. and H.M. Bolt, *Esters, Organic*. Ullmann's Encyclopedia of Industrial Chemistry. 2000: Wiley-VCH Verlag GmbH & Co. KGaA.
2. Yadav, G.D. and P.H. Mehta, *Heterogeneous Catalysis in Esterification Reactions: Preparation of Phenethyl Acetate and Cyclohexyl Acetate by Using a Variety of Solid Acidic Catalysts*. Industrial & Engineering Chemistry Research, 1994. **33**(9): p. 2198-2208.
3. Michael A. Ogliaruso, J.F.W., Saul Patai, Zvi Rappoport, *Synthesis of Carboxylic Acids, Esters and their Derivatives*. 1991, New York: John Wiley.
4. Yadav, G.D. and P.K. Goel, *Selective synthesis of perfumery grade cyclohexyl esters from cyclohexene and carboxylic acids over ion exchange resins: an example of 100% atom economy*. Green Chemistry, 2000. **2**(2): p. 71-78.
5. Armstrong, D.W. and H. Yamazaki, *Natural flavours production: a biotechnological approach*. Trends in Biotechnology, 1986. **4**(10): p. 264-268.
6. Harmer, M.A. and Q. Sun, *Solid acid catalysis using ion-exchange resins*. Applied Catalysis A: General, 2001. **221**(1-2): p. 45-62.
7. Miller, D.J., et al., *Process for producing mixed esters of fatty acids as biofuels*. 2008: Patent application, 12/313,343, USA.
8. Moser, B., et al., *Diesters from Oleic Acid: Synthesis, Low Temperature Properties, and Oxidation Stability*. Journal of the American Oil Chemists' Society, 2007. **84**(7): p. 675-680.
9. Knothe, G., Krahl, J., Van Gerpen, J., Eds., *The Biodiesel Handbook*. 2005, Champaign, IL: AOCS Press.
10. Wang, P.S., M.E. Tat, and J. Van Gerpen, *The production of fatty acid isopropyl esters and their use as a diesel engine fuel*. Journal of the American Oil Chemists Society, 2005. **82**(11): p. 845-849.

11. Grob, S. and H. Hasse, *Reaction Kinetics of the Homogeneously Catalyzed Esterification of 1-Butanol with Acetic Acid in a Wide Range of Initial Compositions*. *Industrial & Engineering Chemistry Research*, 2006. **45**(6): p. 1869-1874.
12. de Jong, M.C., et al., *Reaction kinetics of the esterification of myristic acid with isopropanol and n-propanol using p-toluene sulphonic acid as catalyst*. *Applied Catalysis A: General*, 2009. **365**(1): p. 141-147.
13. Lundquist, E.G., *Catalyzed esterification process* 1995: USA.
14. Sharma, M.M., *Some novel aspects of cationic ion-exchange resins as catalysts*. *Reactive and Functional Polymers*, 1995. **26**(1-3): p. 3-23.
15. Vincent, K.R., *International Energy Outlook 2011*, U.S.E.I. Administration, 2011: Washington, DC.
16. *The 2004 OECD List of High Production Volume Chemicals*, E.D. OECD, 2004: Paris.
17. Stankiewicz, A.I. and J.A. Moulijn, *Process intensification: Transforming chemical engineering*. *Chemical Engineering Progress*, 2000. **96**(1): p. 22-34.
18. Schembecker, G. and S. Tlatlik, *Process synthesis for reactive separations*. *Chemical Engineering and Processing*, 2003. **42**(3): p. 179-189.
19. Lutze, P., R. Gani, and J.M. Woodley, *Process intensification: A perspective on process synthesis*. *Chemical Engineering and Processing: Process Intensification*, 2010. **49**(6): p. 547-558.
20. Victor H. Agreda; Lee R. Partin, b.o.K., Tenn, *Reactive distillation process for the production of methyl acetate*, U.S. Patent, Editor. 1984, Eastman Kodak Company, Rochester, N.Y.: USA.
21. Sharma, M.M. and S.M. Mahajani, *Industrial Applications of Reactive Distillation*, in *Reactive Distillation*. 2003, Wiley-VCH Verlag GmbH & Co. KGaA. p. 1-29.
22. Winterberg, M., et al., *Methyl Tert-Butyl Ether*, in *Ullmann's Encyclopedia of Industrial Chemistry*. 2000, Wiley-VCH Verlag GmbH & Co. KGaA.

23. Harmsen, G.J., *Reactive distillation: The front-runner of industrial process intensification: A full review of commercial applications, research, scale-up, design and operation*. Chemical Engineering and Processing, 2007. **46**(9): p. 774-780.
24. *Reactive Distillation: Status and Future Directions*, ed. K. Sundmacher and A. Kienle. 2002: Wiley-VCH Verlag GmbH & Co. KGaA.
25. Taylor, R. and R. Krishna, *Modelling reactive distillation*. Chemical Engineering Science, 2000. **55**(22): p. 5183-5229.
26. Sundmacher, K.A.I., L.K. Rihko, and U. Hoffmann, *Classification of reactive distillation processes by dimensionless numbers*. Chemical Engineering Communications, 1994. **127**(1): p. 151-167.
27. Schoenmakers, H.G. and B. Bessling, *Reactive and catalytic distillation from an industrial perspective*. Chemical Engineering and Processing: Process Intensification, 2003. **42**(3): p. 145-155.
28. Kaymak, D.B., W.L. Luyben, and Smith, *Effect of Relative Volatility on the Quantitative Comparison of Reactive Distillation and Conventional Multi-unit Systems*. Industrial & Engineering Chemistry Research, 2004. **43**(12): p. 3151-3162.
29. Huang, K., et al., *Reactive distillation design with considerations of heats of reaction*. AIChE Journal, 2006. **52**(7): p. 2518-2534.
30. Sun, J., K. Huang, and S. Wang, *Deepening Internal Mass Integration in Design of Reactive Distillation Columns, 1: Principle and Procedure*. Industrial & Engineering Chemistry Research, 2009. **48**(4): p. 2034-2048.
31. Huang, K., S.-J. Wang, and W. Ding, *Towards further internal heat integration in design of reactive distillation columns--Part III: Application to a MTBE reactive distillation column*. Chemical Engineering Science, 2008. **63**(8): p. 2119-2134.
32. Zhu, F., et al., *Towards further internal heat integration in design of reactive distillation columns--Part IV: Application to a high-purity ethylene glycol reactive distillation column*. Chemical Engineering Science, 2009. **64**(15): p. 3498-3509.

33. Kumar, M.V.P. and N. Kaistha, *Internal Heat Integration and Controllability of Double Feed Reactive Distillation Columns, 1. Effect of Feed Tray Location*. Industrial & Engineering Chemistry Research, 2008. **47**(19): p. 7294-7303.
34. Pavan Kumar, M.V. and N. Kaistha, *Internal Heat Integration and Controllability of Double Feed Reactive Distillation Columns, 2. Effect of Catalyst Redistribution*. Industrial & Engineering Chemistry Research, 2008. **47**(19): p. 7304-7311.
35. Huang, K., et al., *A fundamental principle and systematic procedures for process intensification in reactive distillation columns*. Chemical Engineering and Processing: Process Intensification. **49**(3): p. 294-311.
36. Wang, S.-J., D.S.H. Wong, and S.-W. Yu, *Design and control of transesterification reactive distillation with thermal coupling*. Computers & Chemical Engineering, 2008. **32**(12): p. 3030-3037.
37. Schoenmakers, H. and W. Buehler, *Distillation column with external reactors - an alternative to the reaction column*. Chem.-Ing.-Tech., 1982. **54**(2): p. 163.
38. Baur, R. and R. Krishna, *Distillation column with reactive pump arounds: an alternative to reactive distillation*. Chem. Eng. Process., 2003. **43**(3): p. 435-445.
39. Bisowarno, B.H., Y.-C. Tian, and M.O. TadÃ©, *Application of side reactors on ETBE reactive distillation*. Chemical Engineering Journal, 2004. **99**(1): p. 35-43.
40. Ouni, T., et al., *Enhancing productivity of side reactor configuration through optimizing the reaction conditions*. Chem. Eng. Res. Des., 2004. **82**(A2): p. 167-174.
41. Ojeda Nava, J.A., R. Baur, and R. Krishna, *Combining Distillation and Heterogeneous Catalytic Reactors*. Chemical Engineering Research and Design, 2004. **82**(2): p. 160-166.
42. Ding, L.-H., et al., *Optimum Design and Analysis Based on Independent Reaction Amount for Distillation Column with Side Reactors: Production of Benzyl Chloride*. Ind. Eng. Chem. Res., 2011. **50**(19): p. 11143-11152.
43. Kaymak, D.B. and W.L. Luyben, *Design of Distillation Columns with External Side Reactors*. Industrial & Engineering Chemistry Research, 2004. **43**(25): p. 8049-8056.

44. Kaymak, D.B. and W.L. Luyben, *Optimum Design of a Column/Side Reactor Process*. Ind. Eng. Chem. Res., 2007. **46**(15): p. 5175-5185.
45. Musser, M.T., *Cyclohexanol and Cyclohexanone*. Ullmann's Encyclopedia of Industrial Chemistry. 2000: Wiley-VCH Verlag GmbH & Co. KGaA.
46. Aboul-Gheit, A.K., et al., *Direct Conversion of Natural Gas to Petrochemicals Using Monofunctional Mo/SiO<sub>2</sub> and H-ZSM-5 Zeolite Catalysts and Bifunctional Mo/H-ZSM-5 Zeolite Catalyst*. Petroleum Science and Technology. **30**(9): p. 893-903.
47. Osamu Mitsui, Y.F., *Process for producing cyclic alcohol*. 1986, Asahi Kasei Kogyo Kabushiki Kaisha: USA.
48. Freund, H. and K. Sundmacher, *Process Intensification, 1. Fundamentals and Molecular Level*, in *Ullmann's Encyclopedia of Industrial Chemistry*. 2011, Wiley-VCH Verlag GmbH & Co. KGaA.
49. Steyer, F. and K. Sundmacher, *Cyclohexanol Production via Esterification of Cyclohexene with Formic Acid and Subsequent Hydration of the Ester Reaction Kinetics*. Industrial & Engineering Chemistry Research, 2007. **46**(4): p. 1099-1104.
50. Steyer, F., H.r. Freund, and K. Sundmacher, *A Novel Reactive Distillation Process for the Indirect Hydration of Cyclohexene to Cyclohexanol Using a Reactive Entrainer*. Industrial & Engineering Chemistry Research, 2008. **47**(23): p. 9581-9587.

## **Chapter 2: Cyclohexyl acetate production from cyclohexene and acetic acid: Reaction kinetics and chemical equilibrium**

### **2.1. Summary**

The reaction of cyclohexene with acetic acid to form cyclohexyl acetate with subsequent hydrolysis of the ester is an attractive cyclohexene hydration route to cyclohexanol for nylon-6,6 production. In this work, the chemical reaction kinetics and equilibrium state of Amberlyst 70 catalyzed esterification of acetic acid with cyclohexene were measured in batch reactions. Reactions were conducted over a temperature range of 343-403 K, initial mole ratios of acetic acid:cyclohexene between 1: 5 and 5:1, and at catalyst loadings of 1 to 4wt% of feed. An activity-based kinetic model is presented with activity coefficients calculated using the NRTL model. Heat of reaction obtained from experiments is compared to the predicted heat calculated using standard thermodynamic data. Effects of cyclohexene dimerization and initial water concentration on the activity of heterogeneous catalyst are also discussed. The kinetic model is useful for simulating cyclohexanol production in processes such as reactive distillation.

### **2.2. Introduction**

Cyclohexanol is an industrially important chemical produced in large scale worldwide, particularly as an intermediate in the production of nylon-6,6 [1]. A novel approach using reactive distillation (herein, RD) to produce cyclohexanol from cyclohexene (herein, CHE) produced in benzene hydrogenation is via indirect hydration [2-4]. In versions of this process reported, formic acid is used as reactive entrainer - CHE is esterified with formic acid to produce cyclohexyl formate in a first RD column, and the ester thus obtained can be hydrolyzed in a second RD column to give cyclohexanol and formic acid, which can be recycled to the first

column. Apart from safety and energy efficiency, this method offers the additional key advantage of separating cyclohexane (herein, CHX) from CHE. CHX does not participate in the esterification reaction and can be collected as a top product from the first RD column, thus eliminating the extractive distillation step required to separate the mixture of CHE and CHX. Detailed reaction kinetics and vapor-liquid and liquid-liquid equilibrium data describing CHE esterification with formic acid and cyclohexyl formate hydrolysis is reported in literature [5-10]. In this study, acetic acid (herein, AA) is used as reactive entrainer to produce cyclohexanol from CHE. The reaction scheme is shown in Figure 2.1. The production of cyclohexyl acetate (herein, CHA) via esterification CHE with AA, which can be an intermediate in the production of cyclohexanol is the focus of this study.

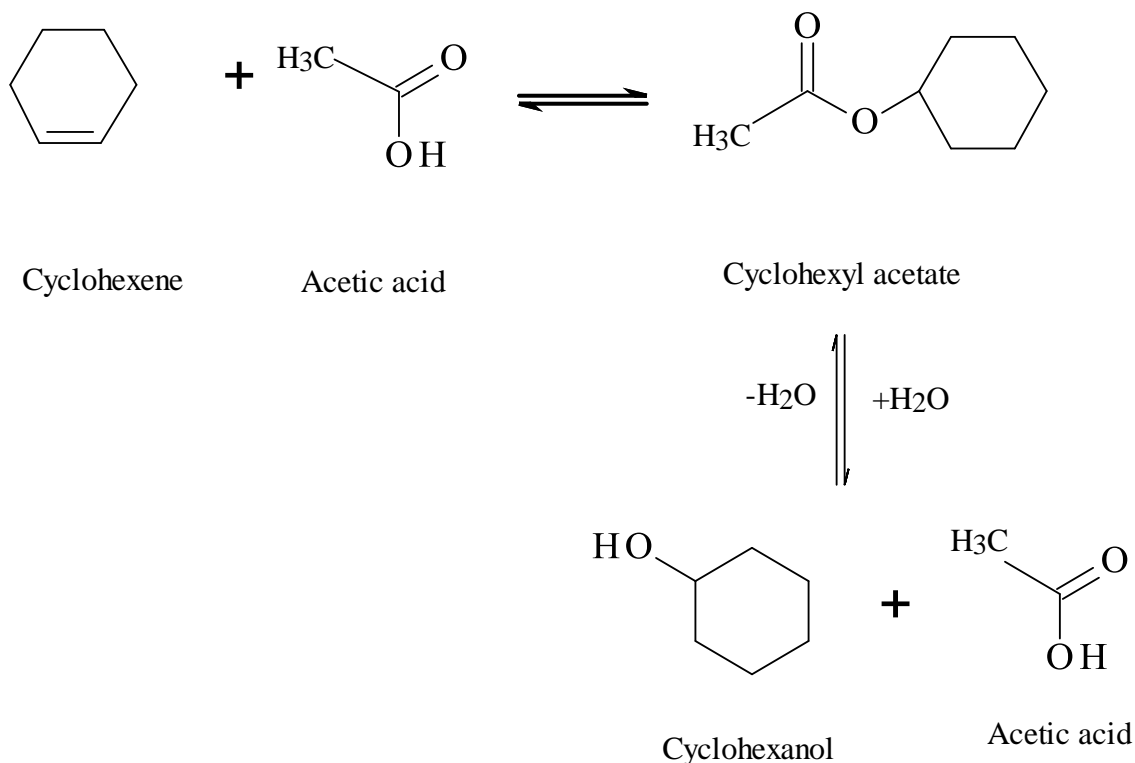


Figure 2.1: Reaction network for cyclohexanol production from cyclohexene

Esterification kinetics of CHE with acetic acid, acrylic acid, and methacrylic acid using solid acid catalysts are reported in the literature [4, 11]. Chakrabarti et al.[11] studied this reaction between 70-90°C using Amberlyst 15 catalyst, assuming that the reaction was irreversible in the temperature range studied. However, olefin esterification with carboxylic acids is an equilibrium limited reaction [12], so their kinetics are incomplete in this sense. Also, strong cation exchange resin catalyst Amberlyst 70 has been shown to be superior to more commonly used Amberlyst 15 in terms of high temperature stability and turn over frequency [13-15].

Therefore, a systematic kinetic study of CHE esterification with AA catalyzed by Amberlyst 70 has been conducted to determine reaction conditions desirable for the esterification reaction. Effects of temperature, catalyst loading and initial mole ratio of acetic acid to cyclohexene on reaction were investigated. AA is used as the reactive entrainer instead of formic acid because the latter is toxic and decomposes at higher temperatures to carbon monoxide and water. The reaction scheme is shown in Figure 2.2;

The side reaction involving CHE dimerization has been shown by Ronchin et al. [16], who studied alkylation kinetics of phenol with CHE using styrene divinylbenzene sulfonic resins treated with nitric acid and sulfuric acid, to be the only significant oligomerization reaction that affects the overall kinetics. Yadav et al. [15] studied esterification of CHE with carboxylic acids to make perfumery-grade esters in the presence of ion exchange resins. In the presence of CHX and short reaction times at 373 K, they found negligible amounts of dimer formation [17]. For production of cyclohexyl acetate (here in , CHA) using reactive distillation , further study of CHE dimerization is important because when CHE is fed to the lower part of the column, the presence of catalyst at high temperatures can lead to CHE oligomerization. Thus

oligomerization and the subsequent effect of oligomers on ion exchange resin catalyst are examined here.

Effects of water on catalyst activity were also studied. This study gives an insight into the desirable operating conditions for reactive distillation column operation.

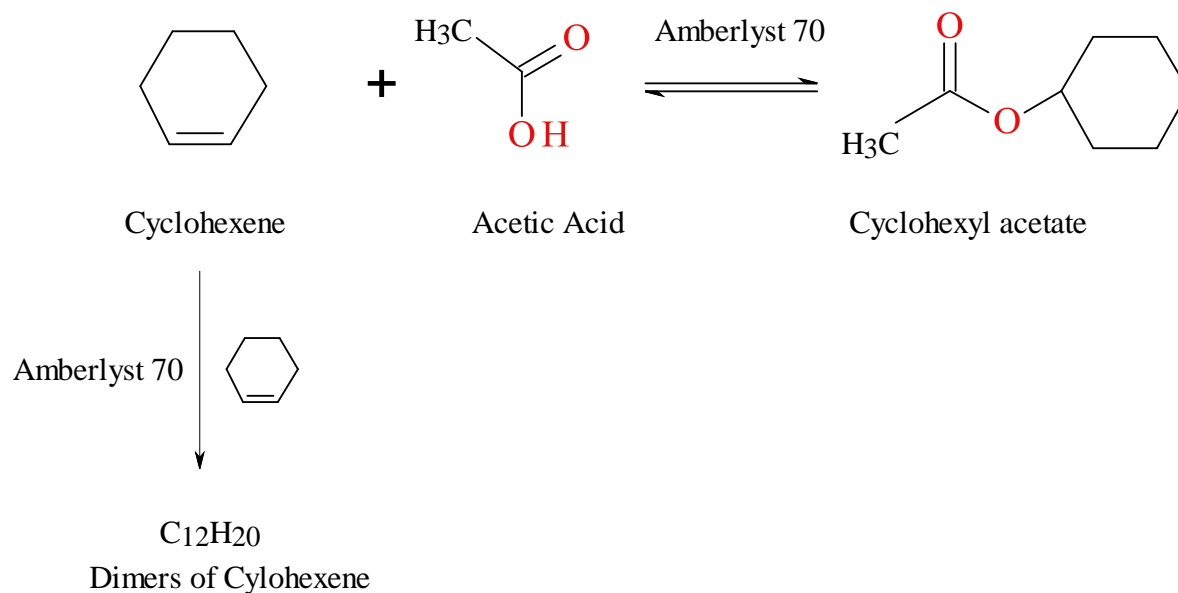


Figure 2.2: Cyclohexene esterification with acetic acid

### 2.3. Materials and Methods

The starting materials used in this work, cyclohexene (>99%), cyclohexyl acetate (>99%) and 1,4 dioxane (>99%), were obtained from Sigma-Aldrich. Glacial acetic acid (>99.7%) was purchased from VWR Scientific, and 1-butanol was obtained from Mallinckrodt-Baker, Inc. Amberlyst 70 ion exchange resin was purchased from the Dow Chemical Company. The ion-exchange resin catalyst was washed with deionized water and then with ethanol until the supernatant liquid was colorless and then dried overnight at 373 K under vacuum before use in experiments. The ion exchange capacity of the resin catalyst was determined by titration as  $2.6 \pm 0.2$  eq/kg, a value in reasonable agreement with the value of 2.55 eq/kg reported by the manufacturer [18].

Batch reactions for kinetic study were performed in a Parr 5000 multi-reactor system equipped with temperature control ( $\pm 0.2^\circ\text{C}$ ) and stirring speed control (0-1400 rpm). In a typical experiment, measured quantities of CHE and AA along with Amberlyst 70 catalyst were charged into the reactor. Stirring of the reactors was kept at 800 rpm. The reactor was sealed and heating was then initiated. Zero reaction time was taken at the point that the desired reaction temperature was reached even though a small amount of reaction takes place during heating. Approximately one-milliliter samples were taken at specified intervals over a period of 3 hours of the reaction via use of a syringe attached to a sample port. Equilibrium samples were collected after 24 hours of reaction. Samples were passed through a  $2\mu\text{m}$  filter attached to the end of the sample port to separate sample solution from the catalyst.

Samples were analyzed using a HP-5890 Series II gas chromatograph equipped with a flame ionization detector (FID). A 30m length, 0.53mm ID,  $1.0\mu\text{m}$  film thickness Aquawax-DA column was used to separate the components. Oven temperature maintained initially at  $40^\circ\text{C}$  for 1.0 min, increased at  $20^\circ\text{C}/\text{min}$  to  $250^\circ\text{C}$ , and then maintained at that temperature for an additional 2.0 min. Injector and detector temperatures were maintained at  $250^\circ\text{C}$  and  $300^\circ\text{C}$  respectively. 1,4-Dioxane was used as internal standard. To identify cyclohexene dimers, a Varian CP-3800 gas chromatograph equipped with Saturn 2000 mass spectrometer was used. A fused silica capillary column SLB<sup>TM</sup>-5ms:30m  $\times$  0.25mm  $\times$   $0.25\mu\text{m}$  film thickness was used to separate the components. Water content in the reactants was analyzed using Hydranal-coulomat E solution in a coulometric AQ-2100 Karl-Fisher titrator.

To determine the effect of water and dimerization reaction on esterification of CHE with AA, turn over number (TON,  $\text{kmol CHE}/\text{kmol H}^+/\text{hr}$ ) was calculated from the observed initial reaction rate of cyclohexene ( $-r_{\text{CHE}}$ ) as follows:

$$TON = \frac{-r_{CHE}}{W_{cat} * (IE) * W_{sol}} \quad (2.1)$$

## 2.4. Results and Discussion

### 2.4.1. Reaction studies

#### 2.4.1.1. Reusability of catalyst

The TON calculated for repeated use of Amberlyst 70 at 363 K and an initial mole ratio of CHE to AA at 1:1, varied between 8.9 and 9.2 kmol CHE/kmol H<sup>+</sup>/hr. This initial result suggests that Amberlyst 70 is an effective catalyst for this reaction. A control experiment with only CHE and AA at 363 K and no catalyst showed no reaction over 24 hours. Therefore auto-catalysis of this reaction was assumed negligible at the conditions studied.

#### 2.4.1.2 Mass transfer considerations

The development of an accurate kinetic model requires that external and internal mass transfer resistances be minimized in reaction. To ensure that there were no external mass transfer resistances in CHE esterification with AA, the reaction was carried out at several different agitation speeds while keeping all other conditions the same. Figure A.1a in Appendix A shows that there is no significant effect of speed of agitation on the mole fraction of CHE over the entire range of stirring rates. All further reactions were carried out at 800 rpm. Internal mass transfer resistances were evaluated using different particle sizes of Amberlyst 70 obtained by grinding the resin into finer particles and screening for three different size fractions. These three fractions were evaluated under identical reaction conditions. Figure A.1b shows no significant

difference in CHE mole fraction profile for the different catalyst particle sizes, indicating that intra-particle diffusion resistances are negligible for Amberlyst 70-catalyzed esterification.

Preliminary experiments at identical reaction conditions (800 rpm, 363 K, 1:1 cyclohexene: acetic acid) with increasing catalyst loading were conducted: a linear increase in initial reaction rate of CHE was observed with increasing catalyst loading as shown in Figure 2.3 ( $R^2=0.96$ ) showing the intrinsic nature of kinetic data collected in this study.

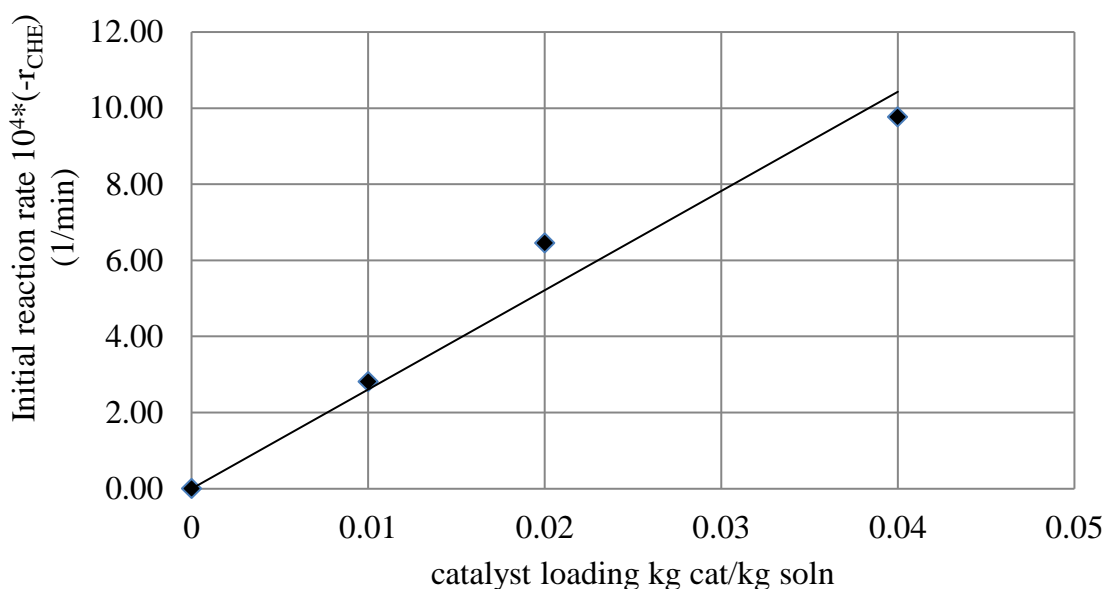


Figure 2.3: Effect of catalyst loading on initial cyclohexene esterification rate. Reaction conditions: Temperature: 363 K, Initial mole ratio CHE:AA = 1:3.

#### 2.4.1.3. Chemical equilibrium constant

The mole fraction-based equilibrium constants ( $K_x$ ) were determined by analysis of reaction samples taken after 24 hours of reaction time, a period sufficient for the esterification reaction to closely approach equilibrium. The activity-based equilibrium constant,  $K_a$ , was calculated from  $K_x$  via inclusion of activity coefficients of the species in the mixture as determined by the NRTL model (Eq. 2.2).

$$K_a = \prod a_i^{\nu_i} = K_x K_\gamma = \prod x_i^{\nu_i} * \prod \gamma_i^{\nu_i} \quad (2.2)$$

In Figure 2.4, the natural logarithm of  $K_a$  obtained in this way was plotted against the inverse of absolute temperature. In order to verify the values of  $K_a$  obtained for reactions starting with CHE and AA, four additional experiments (Runs 30-33, Appendix A, Table A.3.1) starting with CHA and AA were conducted. As shown in Figure 2.4,  $K_a$  obtained for these experiments (reverse reaction) is in agreement with that obtained from experiments starting with CHE and AA (forward reaction). In Runs 30-33, high initial mole ratio of AA to CHA was maintained to avoid CHE oligomerization which affects kinetic equilibrium.

Along with the experimental data, values of  $K_a$  calculated from standard thermodynamic properties of individual reactants and products, obtained from the NIST database and DIPPR database [19] (Table 2.1a) were included in Figure 2.4. The standard Gibbs energy of reaction and equilibrium constant at 298 K are related as follows:

$$\ln K_a(T^o) = -\frac{\Delta g_r^o}{RT^o} \quad (2.3)$$

The value of  $\Delta g_r^o$  at standard temperature was computed using the heat capacity of components involved in the reaction [20]. As can be seen in Figure 2.3, the heat of reaction estimated from the slope of the regression of experimental data is similar to that obtained from standard thermodynamic data. It is to be noted that the value of  $\Delta g_r^o$  depends on standard Gibbs energy of formation obtained from literature. A small error in standard data will lead to an error in estimated value of  $\Delta g_r^o$ . The uncertainties on  $\Delta g_f^o$  for components involved in the reaction

are given in Table 2.1a. Based on these uncertainties,  $\Delta g_r^o$  for the reaction is between -24.03 and 34.83. Therefore, the value for  $\Delta g_r^o$  (-9.34 KJ/mol) obtained from linear regression (Table 2.1b) is acceptable and within the expected range.

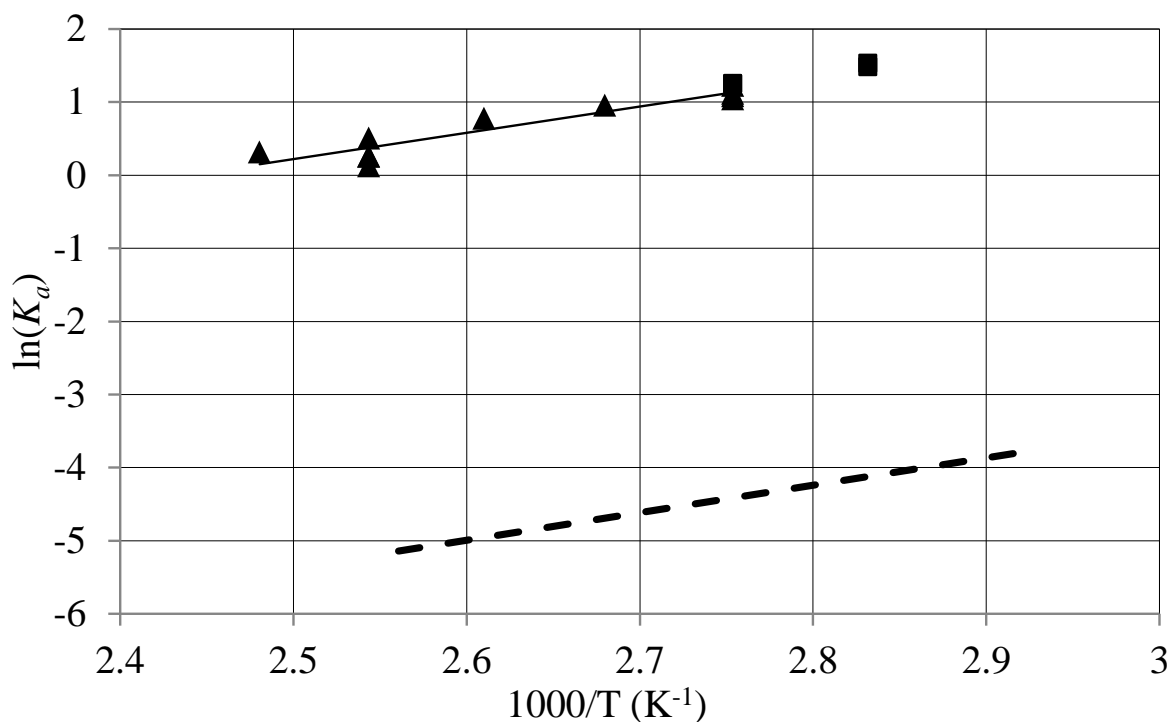


Figure 2.4: Chemical equilibrium constant  $K_a$  (▲) and the best fit of experimental data (solid line), compared with estimation based on Eq. (2.2) and thermodynamic data (dashed line). (■) -  $K_a$  for Runs 30-33.

Measured values of  $K_a$  were then used to calculate thermodynamic properties of the reaction and were compared to that obtained using standard thermodynamic and heat capacity data of individual components, given in Table 2.1b. The value of  $K_a$  decreases with increasing temperature, showing the moderate exothermicity of the reaction. The temperature dependence of the equilibrium constant which describes the best fit of the experimentally obtained equilibrium constants can be expressed as follows:

$$K_a = \exp(3600.5/T - 8.7819) \quad (R^2 = 0.88) \quad (2.4)$$

The heat of reaction obtained from experimental data is very close to that obtained from standard thermodynamic data (Table 2.1b), showing the consistency of data used in this study.

Table 2.1a: Standard Enthalpies and Standard Gibbs Energies of Formation (1 atm, 298K)

Component	$\Delta h_f^o$ (kJ/mol)	$\Delta g_f^o$ (kJ/mol)	Uncertainty in $\Delta g_f^o$ (kJ/mol)
Cyclohexene	-38.22	103	$\pm 10.3$
Acetic acid	-484.5	-389	$\pm 11.67$
Cyclohexyl acetate	-553.4	-280.6	$\pm 28.06$

Table 2.1b: Standard Enthalpies and Standard Gibbs Energies of Reaction at 298K

Component	$\Delta h_r^o$ (kJ/mol)	$\Delta g_r^o$ (kJ/mol)
From heats of formation (Table 2.1a)	-30.68	-24 to +34.8
From linear regression of experimental data	-29.93	-8.17

#### 2.4.2. Pseudo-Homogeneous (PH) kinetic model

Since the effects of mass transfer are negligible, a pseudo-homogeneous kinetic model can be applied to this system according to Helfferich [21]. To account for the thermodynamic non-ideality of the liquid solution in which reaction takes place, activity is used as a measure of species concentration instead of mole fraction, with activity coefficients calculated using NRTL model for binary components [22]. Although somewhat more complex to develop, activity-based models generally provides a more accurate representation of species evolution during reaction.

Cyclohexene (CHE) esterification with acetic acid (AA) to give cyclohexyl acetate (CHA) can be represented by a single, reversible second order reaction.



The rate constant for the reverse reaction can be represented as  $k_r = k_f/K_a$ , where  $K_a$  is the equilibrium constant for esterification reaction.

The design equation for batch reactor is as follows,

$$\frac{dN_i}{dt} = r_i V \quad (2.6)$$

where  $r_i$  has units of  $\text{kmol/m}^3/\text{min}$ . In this reaction, two moles react to form only one mole of product, thus decreasing the total number of moles in the system and also the total volume of the system. Volume changes in the system were accounted for by assuming additivity of individual volumes. To validate this assumption, known weights of CHE, AA and CHA were mixed and resulting total volume was measured. Correlation between computed volume using Eq (2.7) measured volumes is linear as shown in Figure A.2.

$$V = \sum \frac{N_i}{\rho_i}, \text{ where } \rho_i \text{ is the molar density} \quad (2.7)$$

The pseudo-homogeneous rate law for any species  $i$ , in terms of mole fractions can be written as,

$$\frac{r_i}{\nu_i} = W_{cat} k_f \left( x_{CHE} x_{AA} - \frac{x_{CHA}}{K_x} \right) \quad (2.8)$$

By taking nonideality of the system into account, reaction rate can be written as

$$\frac{r_i}{\nu_i} = W_{cat} k_f \left( a_{CHE} a_{AA} - \frac{a_{CHA}}{K_a} \right); a_i = \gamma_i x_i \quad (2.9)$$

The temperature dependence of the rate constants can be expressed by the Arrhenius equation.

$$k_f = k_f^o \exp\left(-\frac{E_f}{RT}\right) \quad (2.10)$$

Two kinetic parameters  $k_f^o$  and  $E_f$  have to be determined to describe the reaction system.

#### 2.4.2.1 Parameter evaluation

A second order Runge-Kutta method, ODE23 in MATLAB 7.0, was used to numerically integrate the differential equations describing the formation and consumption of each species in the system. Liquid phase mole fractions of all species were calculated over the course of each reaction using an initial set of kinetic parameters and were compared to the experimental data. Kinetic parameters were then optimized by minimizing the root mean square error between experimental and calculated mole profiles in liquid phase ( $N_i$ ) in all experiments according to Eq. (2.11) below. A total of 25 experiments (Runs 1-25) containing 175 data points were fitted to the kinetic rate expressions. A summary on reaction conditions of all the experiments and corresponding molefraction profile comparison between experimental and predicted is given in Appendix A.3.

$$F_{\min}^2 = \sum_{runs} \sum_{species} \frac{(N_i^{predicted} - N_i^{experimental})^2}{n_{runs}} \quad (2.11)$$

The kinetic parameters that result in the lowest root mean square error of 1.45 for an activity based pseudo-homogeneous models are given in Table 2.2. The calibration plots used in

quantification of components are presented in Appendix A.5. The NRTL parameters used to calculate activity coefficients provided by Smith et al [22] are presented in Appendix A.6.

During kinetic parameter evaluation, the change in total weight of solution in each experiment due to removal of small quantities as samples was not taken into account. In a typical experiment, it was observed that  $W_{\text{cat}}$  increased by 6% by the end of the experiment as a result of sample removal. Therefore, in this study,  $W_{\text{cat}}$  was changed by  $\pm 6\%$  and new kinetic parameters were evaluated. It was observed that this change in  $W_{\text{cat}}$  did not change the  $F_{\text{min}}$  and also the resulting kinetic parameters were within  $\pm 1\%$  the results reported here. Therefore, in all further studies, it is assumed that  $W_{\text{cat}}$  is constant throughout the reaction.

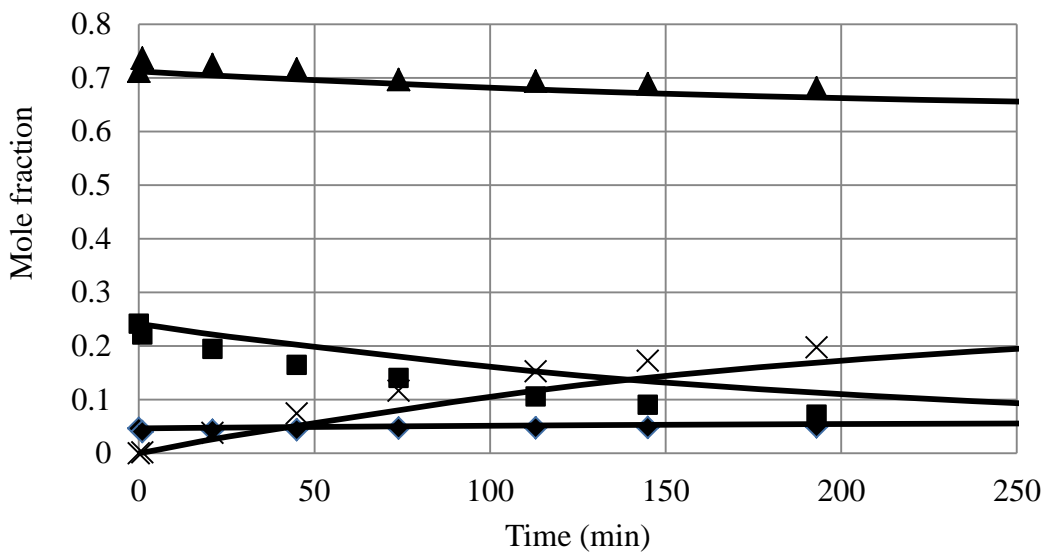
Table 2.2: Summary of reaction kinetic parameters

Parameter	Value	Units
$k_0$	3.34E+12	$(\text{kmol.kg soln})/(\text{kg cat.min.m}^3)$
$E_f$	88100	kJ/kmol

### 2.4.3. Kinetic model comparison with experiments

In this reaction system, as described in Section 2.4.2, the total number of moles is not constant. Therefore, understanding stoichiometry of the system from mole fraction profiles can be challenging in that molefraction of AA remains constant while AA is consumed. Even though this can be overcome by showing the change in absolute moles of each component in the system with time for all experiments, only mole fraction profiles are presented to keep uniformity among all chapters in this work.

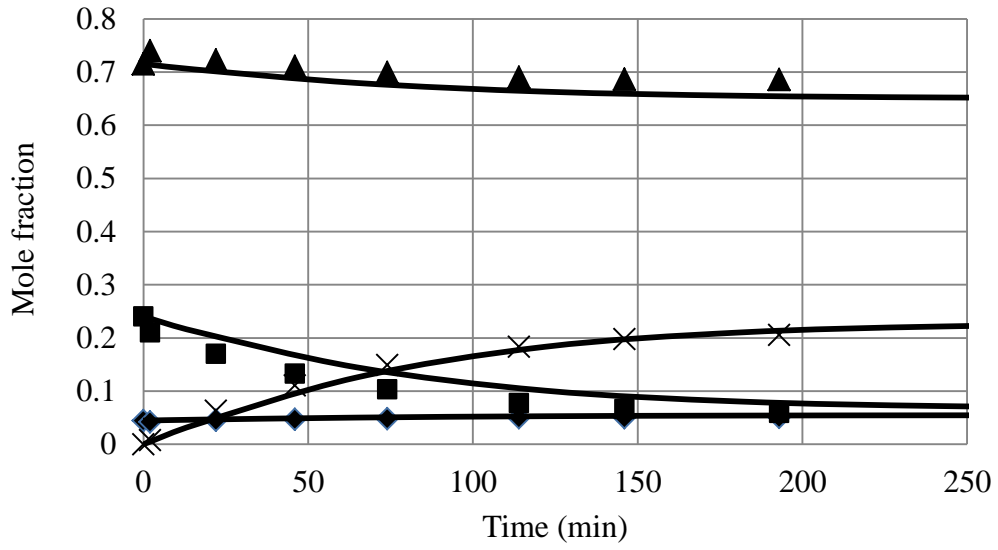
The plots in Figure 2.5 show the mole fraction profiles for experiments conducted at temperatures from 373 to 393 K, keeping all other conditions the same. The model properly predicts the increase in esterification rate with temperature, as well as the concentration of the inert component in the reaction, CHX.



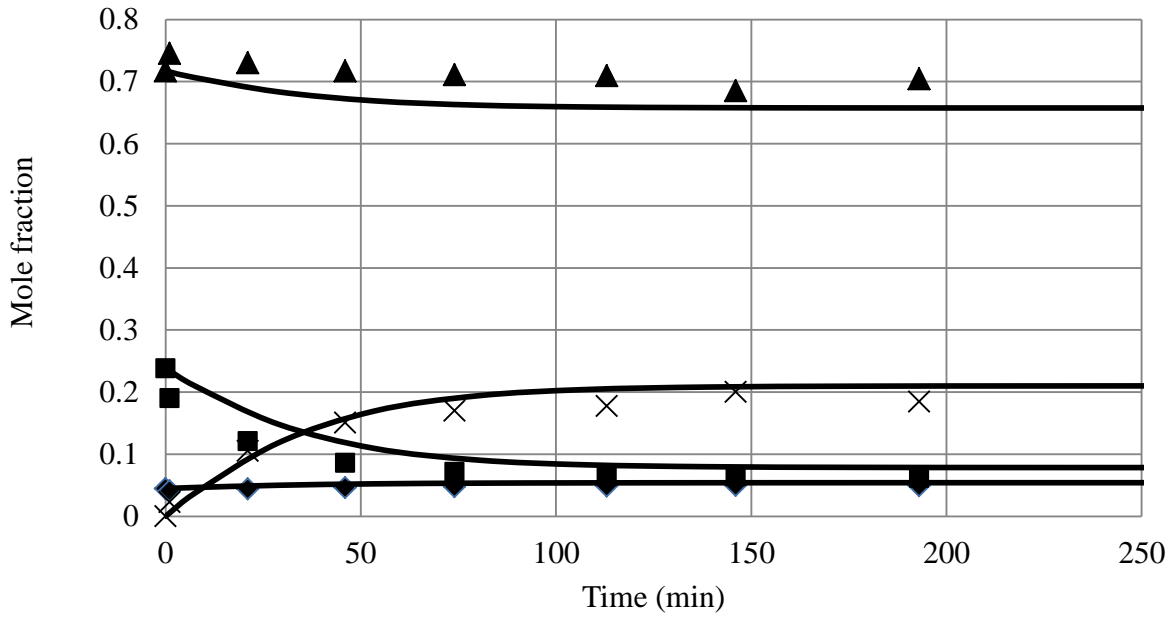
2.5(a)

Figure 2.5: Experimental and predicted mole fraction profiles of CHE esterification. (▲)- AA; (×)- CHA; (■)- CHE; (◆)- CHX. Continuous lines represent the predicted mole fraction profiles. a) Run 16: Temperature 373 K; initial mole ratio CHE:AA = 1:3; CHE:CHX = 5:1; catalyst loading 0.02 kgcat/kg soln. b) Run 17: Temperature 383 K; initial mole ratio CHE:AA = 1:3; CHE:CHX = 5:1; catalyst loading 0.02 kgcat/kg soln. c) Run 18: Temperature 393 K; initial mole ratio CHE:AA = 1:3; CHE:CHX = 5:1; catalyst loading 0.02 kgcat/kg soln.

Figure 2.5 (cont'd)

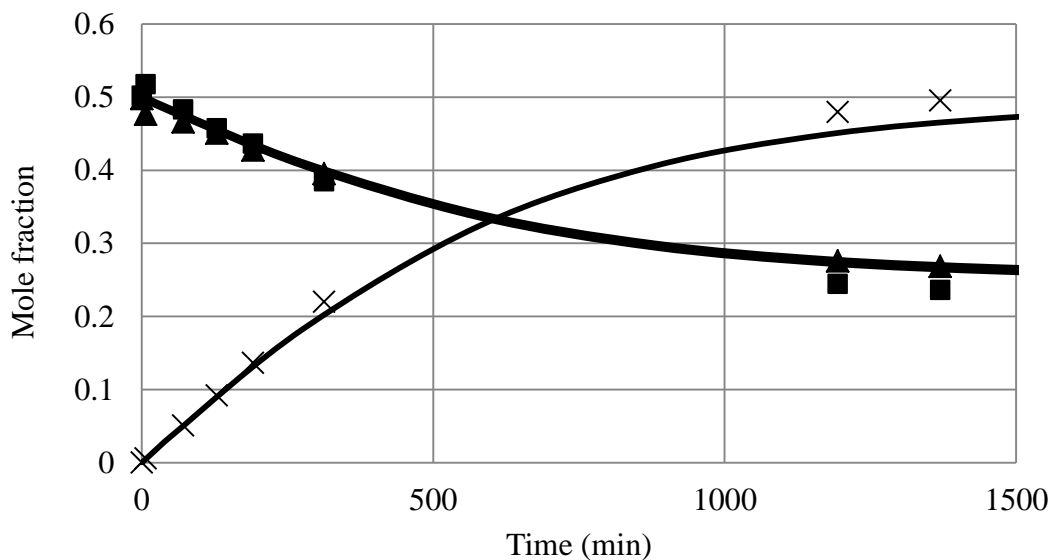


2.5(b)



2.5(c)

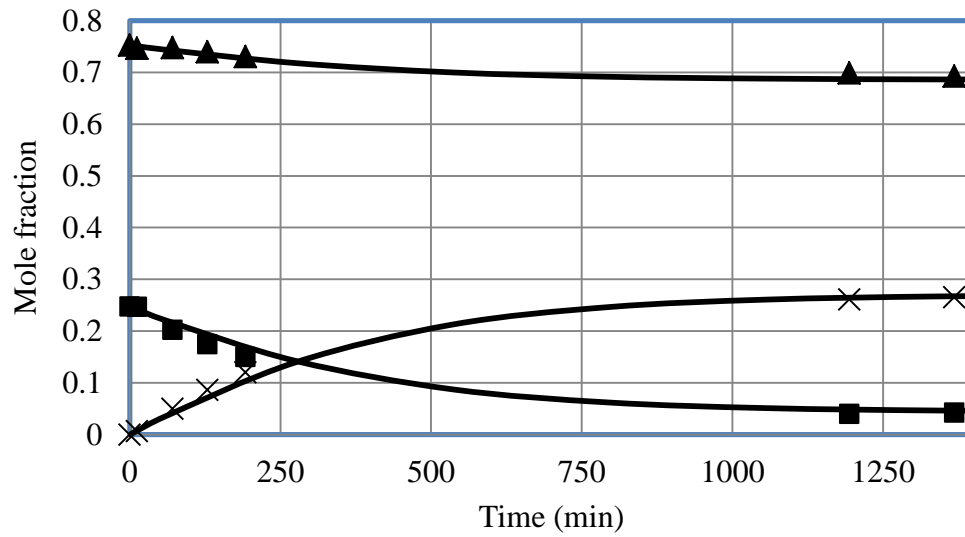
Figure 2.6 shows the predicted mole fraction profiles along with the experimental data at different mole ratios of CHE to AA from 1:1 to 1:5. It is to be noted that this model does not take into account CHE dimerization that occurs at temperatures above 373 K. The reaction conditions that are more suitable for the side reaction and its effect on the solid acid catalysis discussed in the next section.



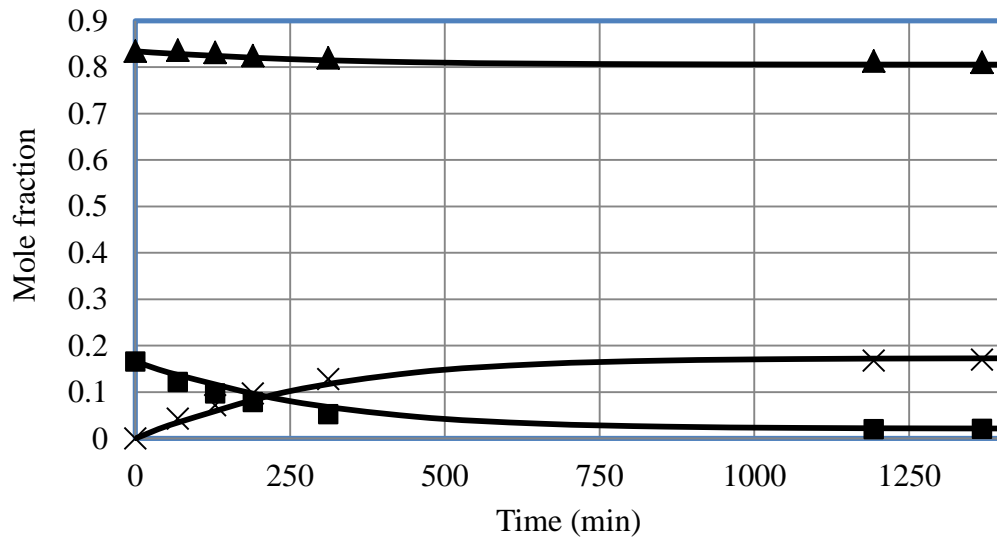
2.6(a)

Figure 2.6: Experimental and predicted mole fraction profiles of CHE esterification. (▲)- AA; (×)- CHA; (■)- CHE; Continuous lines represent the predicted mole fraction profiles. a) Run 9: Temperature 363 K; initial mole ratio CHE:AA = 1:1; catalyst loading 0.02 kgcat/kg soln. b) Run 10: Temperature 363 K; initial mole ratio CHE:AA = 1:3; catalyst loading 0.02 kgcat/kg soln. c) Run 11: Temperature 363 K; initial mole ratio CHE:AA = 1:5; catalyst loading 0.02 kgcat/kg soln.

Figure 2.6 (cont'd)



2.6(b)



2.6(c)

#### 2.4.4. Effect of cyclohexene dimerization on activity of Amberlyst 70

In addition to experiments for kinetic parameter evaluation, batch experiments with higher initial CHE concentrations were carried out (Run 26-29) and side products were

quantified by stoichiometry. Initial mole ratio of CHE:AA was maintained at 5:1 and 3:1 and temperature was maintained at 373 K and 403K in these experiments. It is assumed that CHE oligomerization is an irreversible reaction. Figure 2.7 shows the mole profile of components in the reaction mixture including the side products for Run 27. Oligomer formation follows a straight line, justifying the assumption of an irreversible reaction.

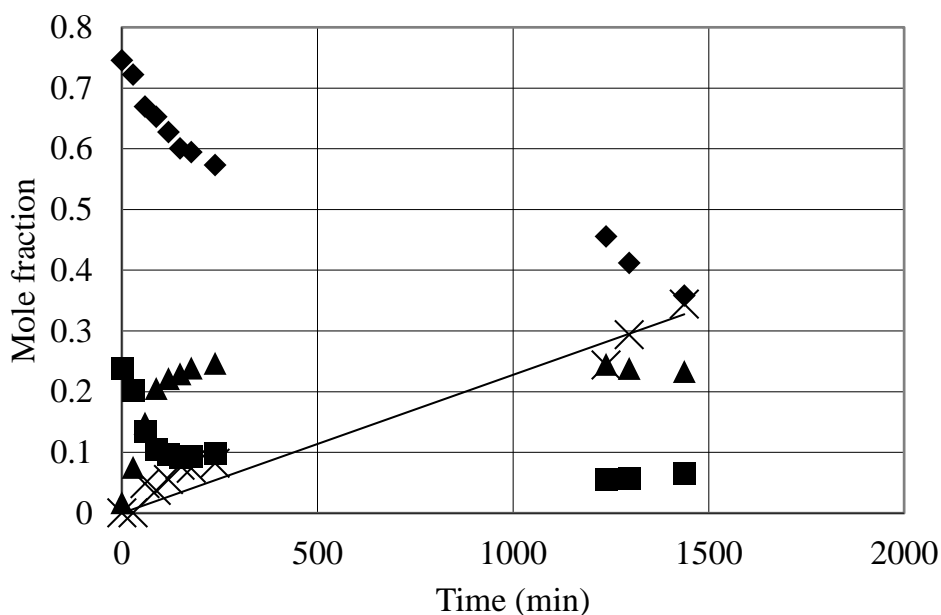


Figure 2.7: Cyclohexene dimer formation during esterification reaction. Straight line represents the best fit for side product formation. (■) Acetic acid; (▲) Cyclohexyl acetate; (◆) Cyclohexene; (×) Cyclohexene dimer. Reaction conditions: Temperature 403 K, Initial mole ratio CHE to AA = 3:1 and catalyst loading 0.02 kgcat/kg soln.

To determine whether oligomers of CHE deposit inside the pores of the catalyst and deactivate it, a control batch experiment with known amount of Amberlyst 70 catalyst at 403 K and cyclohexene was carried out for 72 hours. A sample taken after 48 hours from this reaction was analyzed by mass spectrometer to identify the oligomers. It was found that CHE dimers, 1-

cyclohexyl-cyclohexene and 3-cyclohexyl-cyclohexene, along with 1,1'-oxybis-cyclohexane (Dicyclohexyl ether), were the major products from this reaction. Trace amounts of water present inside the pores of Amberlyst 70 and 85 ppm of water in the feed CHE catalyst must be responsible for the formation of dicyclohexyl ether. A chromatogram showing retention time of dimers along with their chemical structures and corresponding mass spectra are given in Appendix A.4. This result is in agreement with observations found in literature, that CHE dimerization is the predominant reaction in oligomerization of CHE [14].

After the reaction, the catalyst was washed with ethanol and dried at 378 K under vacuum for 12 hours. It was observed that the catalyst weight increased by 15%, evidence to polymer deposition in the pores of Amberlyst 70 catalyst. The activity of this catalyst determined by titration was 1.8 eq/kg compared to 2.4 eq/kg of fresh catalyst. This catalyst, upon testing in esterification at 363 K and an initial mole ratio of CHE to AA 1:1, showed a slightly decreased TON (8.2 kmol CHE/kmol H<sup>+</sup>/hr) compared to the TON of 9.2 kmol CHE/kmol H<sup>+</sup>/hr when fresh. A negligible amount of CHE oligomers were observed in batch reactor experiments at 353 and 363 K with 1:5 initial mole ratio of AA to CHE (Runs 28, 29). Therefore, it can be concluded that CHE dimerization reaction occurs at very high mole ratios of CHE and at higher reaction temperatures. For this reason, while considering reactive distillation for the production of CHA from CHE and AA, care must be taken to avoid reaction conditions in the column that suit CHE dimerization reaction which deactivates the catalyst.

#### **2.4.5. Effect of water on the activity of Amberlyst 70**

The esterification of AA with CHE is in theory a water-free reaction. However, glacial acetic acid and cyclohexene used in the batch experiments in this study contain 620 and 85 ppm of water, respectively. Since water molecules are involved in competitive adsorption onto the

active sites on catalyst along with the reactants, it is important to study the effect of water on the catalytic activity of Amberlyst 70 for this reaction.

Six batch reactions with increasing initial water concentration were carried out and TON for each reaction was calculated using Eq 2.1. As seen in Figure 2.8, the TON decreases rapidly with increasing initial water concentration on from 0.01M to 0.07M. For reactions catalyzed by strong ion exchange resins like Amberlyst 70, small amounts of water are preferentially adsorbed onto  $-\text{SO}_3\text{H}$  groups. This competitive adsorption decreases the strength and number of acid sites available for the desired reaction. This is responsible for drastic decrease in TON. At higher concentrations of water, according to Gates et al.[23], reaction is catalyzed by hydrated protons and reaction rate becomes constant with increasing water concentration. This is in agreement with the results shown in Figure 2.8: as the water concentration is raised from 0.07M to 0.13M, the TON is almost a constant. For reactive distillation, it is thus desirable that water content in the reactants is as low as possible for CHA production from CHE and an overhead decanter along with condenser is recommended for removal of water.

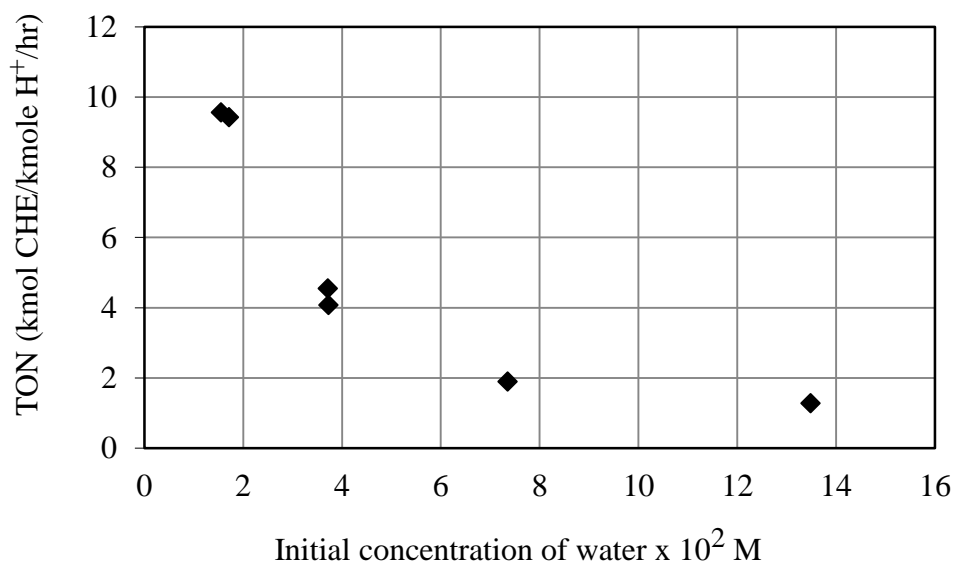


Figure 2.8: Effect of initial water concentration on reaction rate. Reaction conditions: Temperature 363 K, Initial mole ratio CHE to AA = 1:1 and catalyst loading 0.02 kg cat/kg soln.

## 2.5. Conclusion

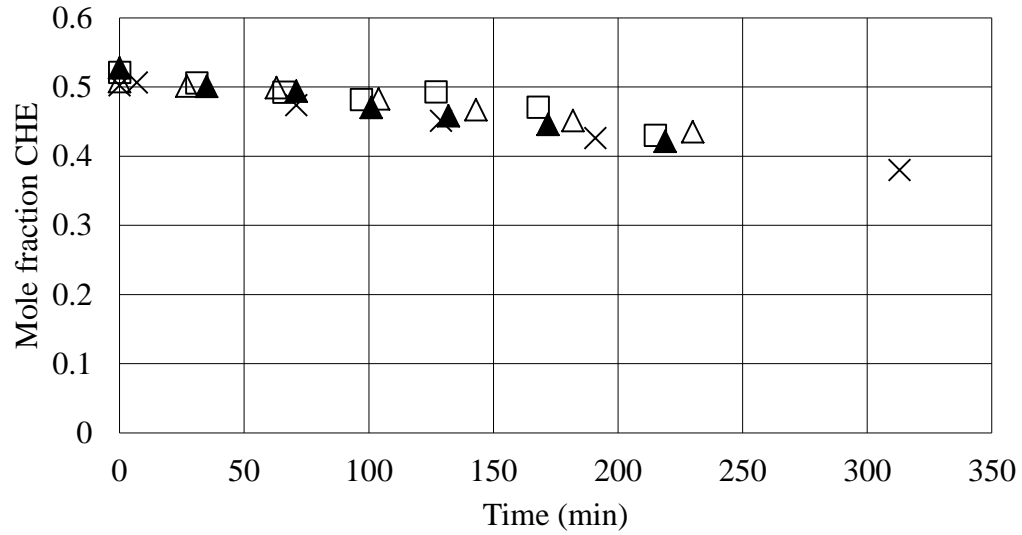
The kinetics of Amberlyst 70– catalyzed kinetics of CHE with AA was studied in a stirred batch reactor under kinetically controlled reaction conditions. Experimental mole fraction profiles were fitted to a second-order, activity-based, pseudo-homogeneous kinetic model. The dependence of the esterification equilibrium constant on temperature was also examined. The model reasonably predicts esterification rate over the temperature range of 343-403 K. Effect of dimerization of CHE and initial water concentration on reaction rate and activity of the catalyst were studied and reaction conditions that minimize side product formation were identified. This information can be useful in designing continuous processes like reactive distillation for CHA production.



## **APPENDIX A**

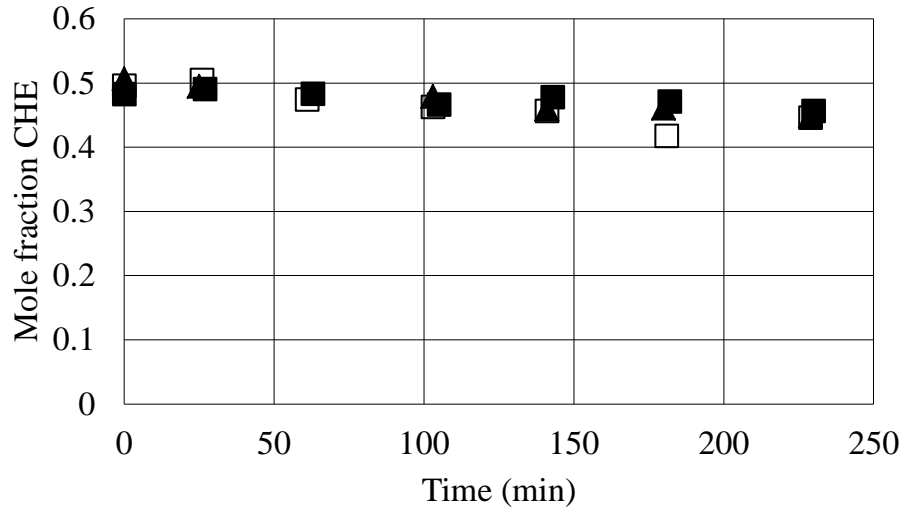
## 2.6. Appendix A

### A.1: Internal and external mass transfer resistance



(a)

Figure A.1a: Effect of agitation speed on reaction rate. (□)-400 rpm; (×)-550 rpm; (Δ)-800 rpm; (▲)-1160 rpm; Reaction conditions: Temperature 363 K; initial mole ratio CHE:AA = 1:1; catalyst loading 0.02 kgcat/kg soln.



(b)

Figure A.1b: Effect of catalyst particle size on reaction rate. (▲)- $d_p < 150 \mu\text{m}$ ; (■)- $250 < d_p < 590 \mu\text{m}$ ; (□)- $d_p > 590 \mu\text{m}$ . Reaction conditions: Temperature 363 K; initial mole ratio CHE :AA = 1:1; catalyst loading 0.02 kgcat/kg soln.

*A.2: The additivity of volumes assumption:*

Theoretical and measured volumes from Table A.2b were used in a parity plot to verify the additivity of volumes assumption is shown in Figure A.2. The measured volumes were only 1.5% higher than theoretical volume (from best fit of the data  $R^2=0.98$ ). This difference is small enough that additivity of volumes can be assumed.

Table A.2a: Component molecular weight and density information

component	Molecular weight kg/kmol	density kg/L	Molar density kmol/L
CHE	82.14	0.811	0.00987
AA	60.05	1.049	0.01746
CHA	142.2	0.97	0.00682

Table A.2b: Component individual weight and volume measurement

weight CHE (gm)	weight AA (gm)	weight CHA (gm)	Volume Theoretical Eq.(2.7)	Volume measured	error %
10.00	4.99	5.01	22.2	22.6	1.5
5.03	10.00	5.01	20.9	21.4	2.3
5.04	5.02	10.01	21.3	21.6	1.3
12.01	5.01	3.01	22.6	23	1.3
3.00	12.01	5.00	20.2	20.6	1.4
5.10	3.01	12.02	21.5	21.7	0.7
7.01	7.00	5.99	21.4	21.8	1.4
8.02	8.09	4.02	21.7	22.2	2.0
4.01	8.04	8.00	20.8	21.1	1.1
8.09	4.03	7.99	22.0	22.3	1.1

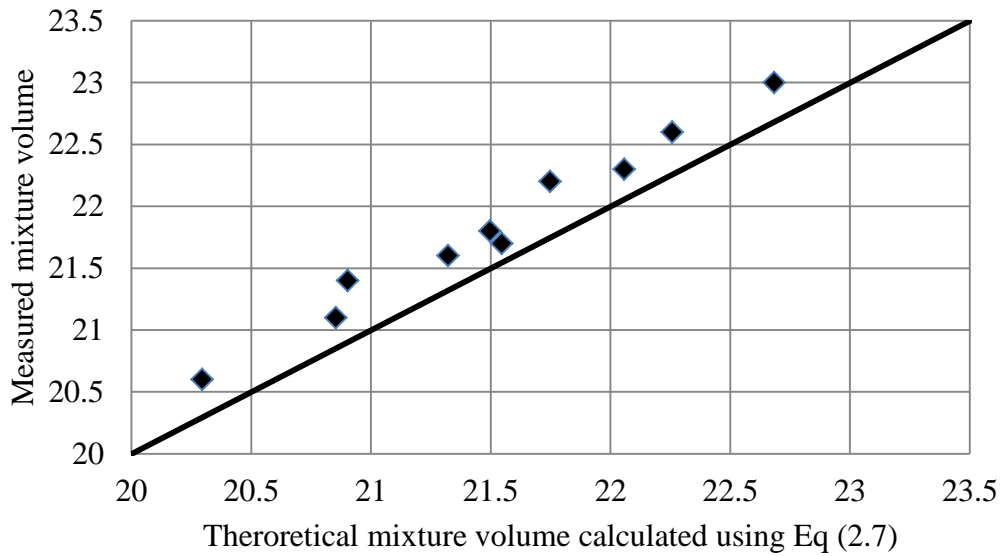


Figure A.2: Parity plot for verification of additivity of volumes assumption

### A.3: Summary of batch reactor experiments

In this section a summary of all batch reactor experiments used to characterize reaction kinetics of CHE esterification with AA is presented. Table A.3.1 shows the reaction conditions of the batch experiments. In Figures A.3.1 to A.3.22 continuous lines represent predicted mole fraction profiles and data points represent experimental data.

Table A.3.1 Summary of batch experiments with Amberlyst 70 as catalyst

Run	Temperature (K)	Mass % of catalyst $W_{cat}$	Duration (hr)	Initial mole ratio AA :CHE	Initial mole ratio CHE: CHX	Total initial moles	Total initial volume (cc)	Figure number
1	373.15	2	21	4		0.88	58	A.3.1
2	383.15	2	21	4		0.88	58	A.3.2
3	393.15	2	21	4		0.88	58	A.3.3
4	403.15	2	21	4		0.88	58	A.3.4
5	393.15	2	23	1		0.78	62	A.3.5
6	393.15	2	4	3		0.88	60.2	A.3.6
7	393.15	2	24	5		0.91	58.5	A.3.7
8	393.15	4	24	4		0.88	58	A.3.8
9	363.15	2	48	1		0.78	61.5	2.6a
10	363.15	2	48	3		0.89	60.3	2.6b
11	363.15	2	23	5		0.92	59.5	2.6c
12	363.15	1	23	3		0.89	60.3	A.3.9
13	363.15	4	23	3		0.89	60.3	A.3.10
14	353.15	2	5	3		0.89	60.3	A.3.11
15	343.15	2	5	3		0.89	60.3	A.3.12

Table A.3.1 (cont'd)

16	373.15	2	3.5	3	5	0.83	58.6	2.5a
17	383.15	2	3.5	3	5	0.83	58.2	2.5b
18	393.15	2	3.5	3	5	0.83	58	2.5c
19	403.15	2	3.5	3	5	0.83	58.1	A.3.13
20	393.15	2	3.5	1.2	5	0.77	61.8	A.3.14
21	393.15	2	3.5	5	5	0.86	57	A.3.15
22	363.15	2	3.5	0.2		0.70	58	A.3.16
23	363.15	2	24	0.35		0.74	58	A.3.17
24	353.15	2	72	0.2		0.70	58	A.3.18
25	353.15	2	72	0.33		0.73	58	A.3.19
26	403.15	2	24	0.2		0.7	58	A.3.20
27	403.15	2	24	0.33		0.732	58	2.7
28	373.15	2	72	0.2		0.7	58	A.3.21
29	373.15	2	72	0.33		0.731	58	A.3.22
Run	Temperature (K)	Mass % of catalyst $W_{cat}$	Duration (hr)	Initial mole ratio AA :CHA	Initial mole ratio CHE: CHX	Total initial moles	Total initial volume (cc)	Figure number
30	363.15	2.8	94	3		0.71	56.7	A.3.23
31	363.15	2.8	94	3		0.71	56.7	A.3.24
32	353.15	2.8	94	1.8		0.64	56.8	A.3.25
33	353.15	2.8	72	1.8		0.64	56.8	A.3.26

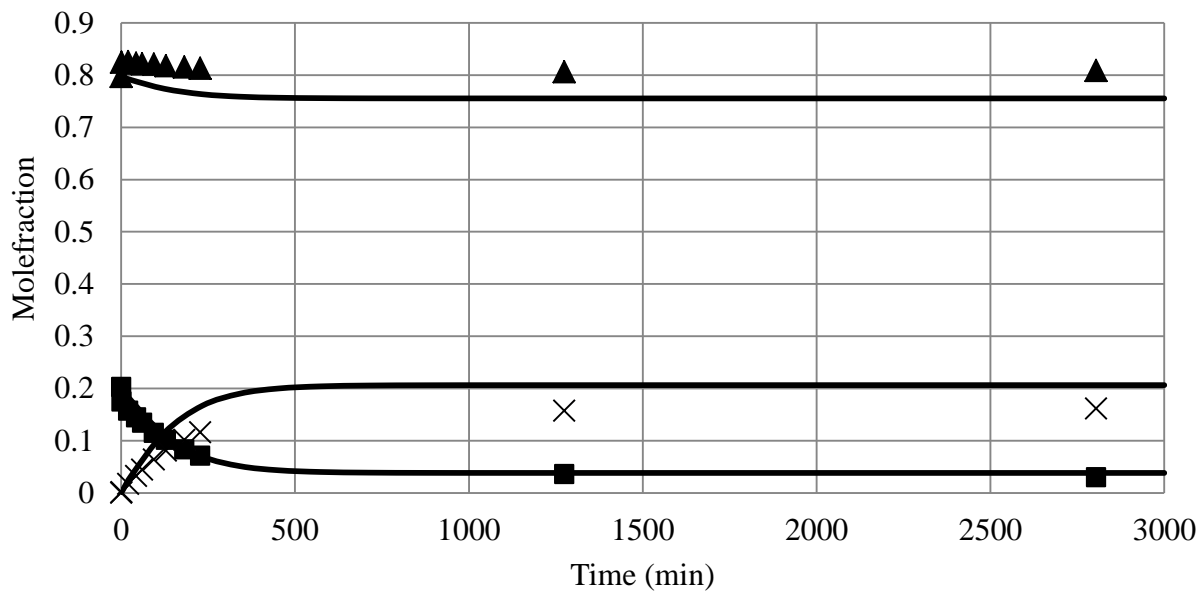


Figure A.3.1: Experimental and predicted mole fraction profiles of CHE esterification for Run1. (▲)- AA; (×)- CHA; (■)- CHE.

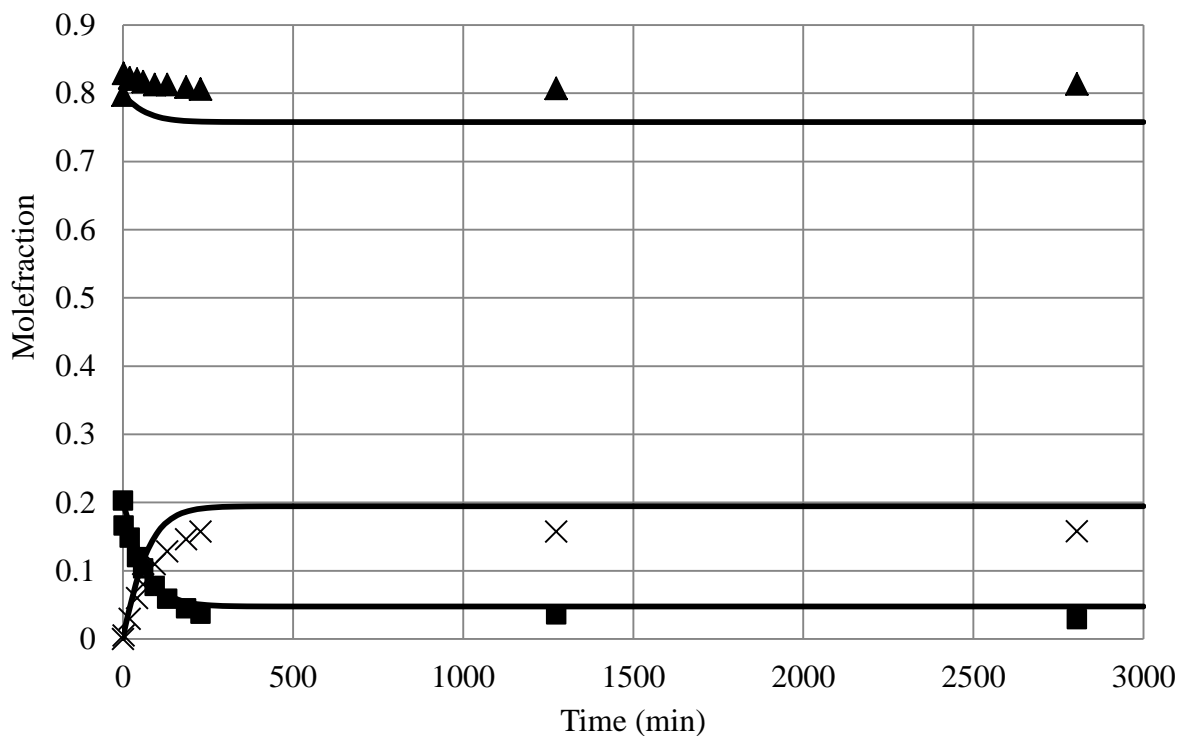


Figure A.3.2: Experimental and predicted mole fraction profiles of CHE esterification for Run 2. (▲)- AA; (×)- CHA; (■)- CHE.

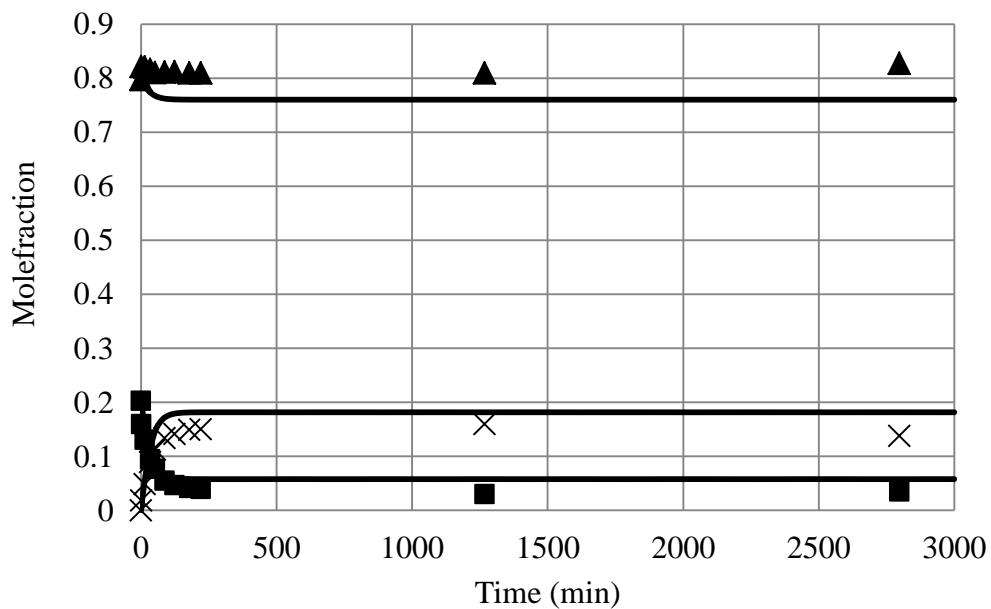


Figure A.3.3: Experimental and predicted mole fraction profiles of CHE esterification for Run 3. (▲)- AA; (×)- CHA; (■)- CHE.

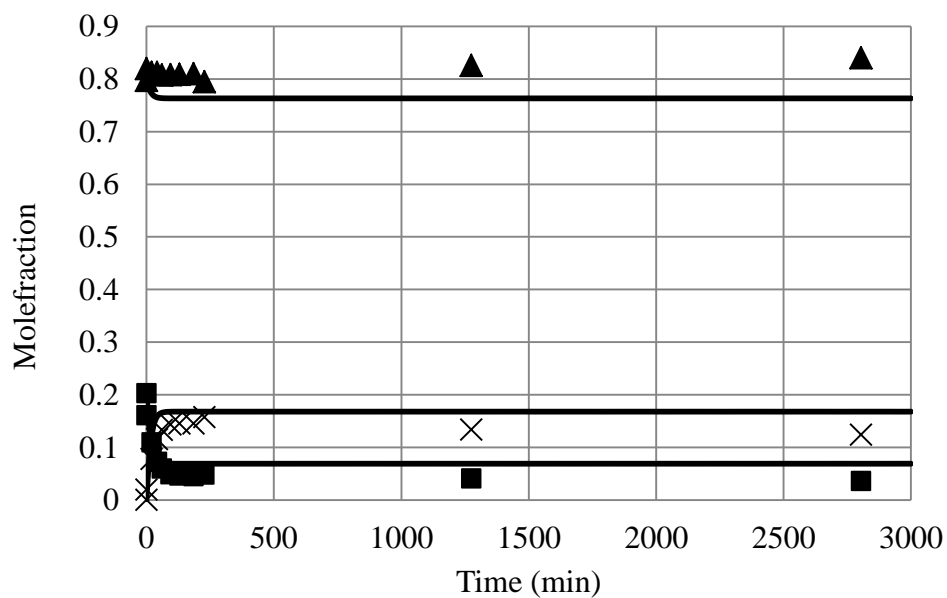


Figure A.3.4: Experimental and predicted mole fraction profiles of CHE esterification for Run 4. (▲)- AA; (×)- CHA; (■)- CHE.

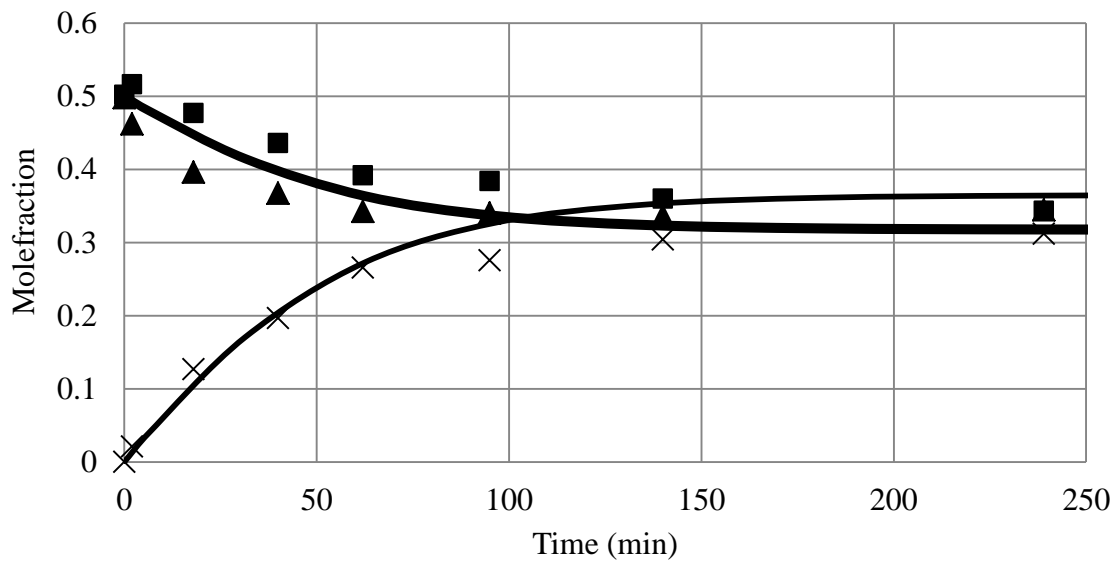


Figure A.3.5: Experimental and predicted mole fraction profiles of CHE esterification for Run 5. (▲)- AA; (×)- CHA; (■)- CHE.

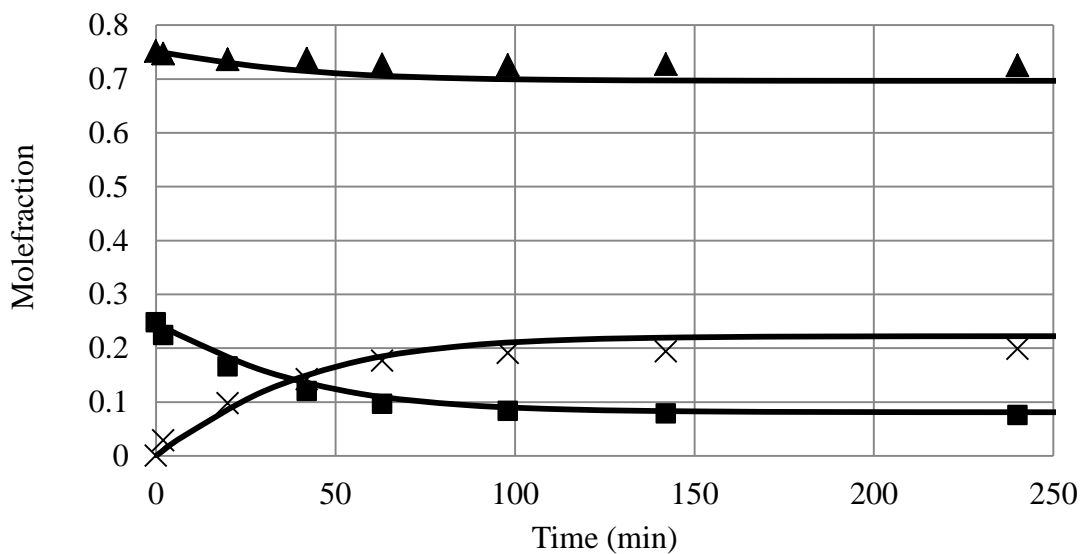


Figure A.3.6: Experimental and predicted mole fraction profiles of CHE esterification for Run 6. (▲)- AA; (×)- CHA; (■)- CHE.

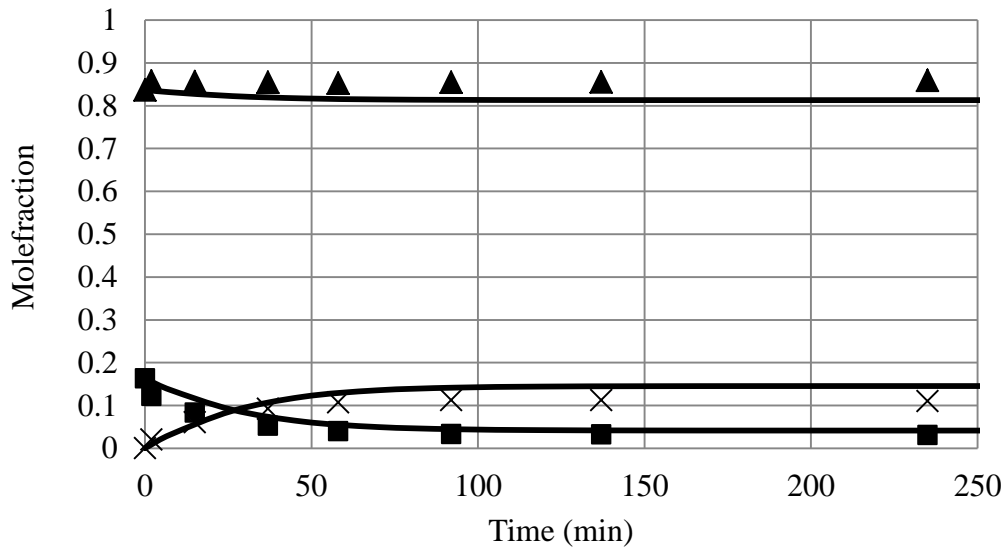


Figure A.3.7: Experimental and predicted mole fraction profiles of CHE esterification for Run 7. (▲)- AA; (×)- CHA; (■)- CHE.

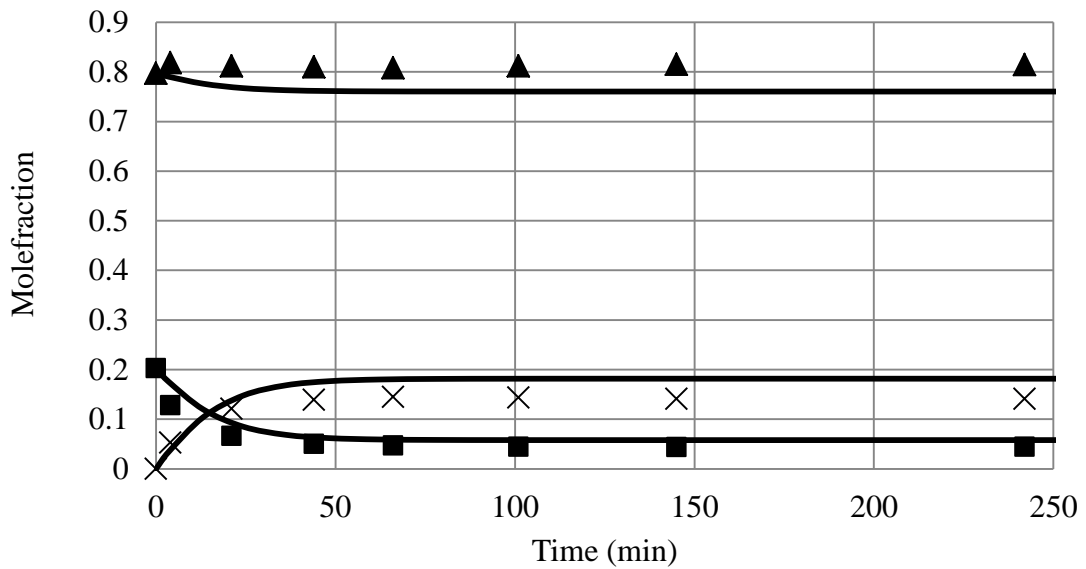


Figure A.3.8: Experimental and predicted mole fraction profiles of CHE esterification for Run 8. (▲)- AA; (×)- CHA; (■)- CHE.

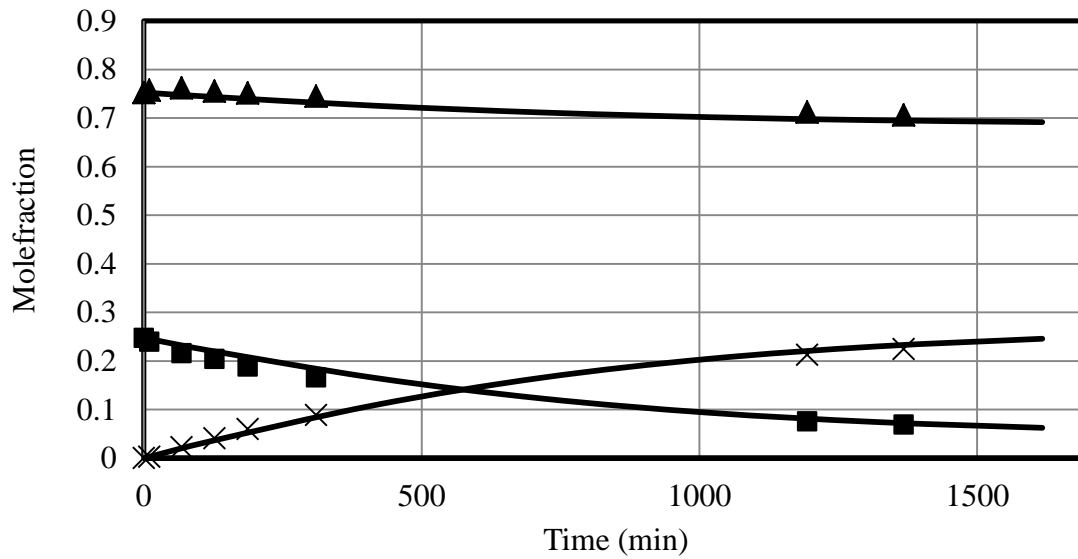


Figure A.3.9: Experimental and predicted mole fraction profiles of CHE esterification for Run 12. (▲)- AA; (×)- CHA; (■)- CHE.

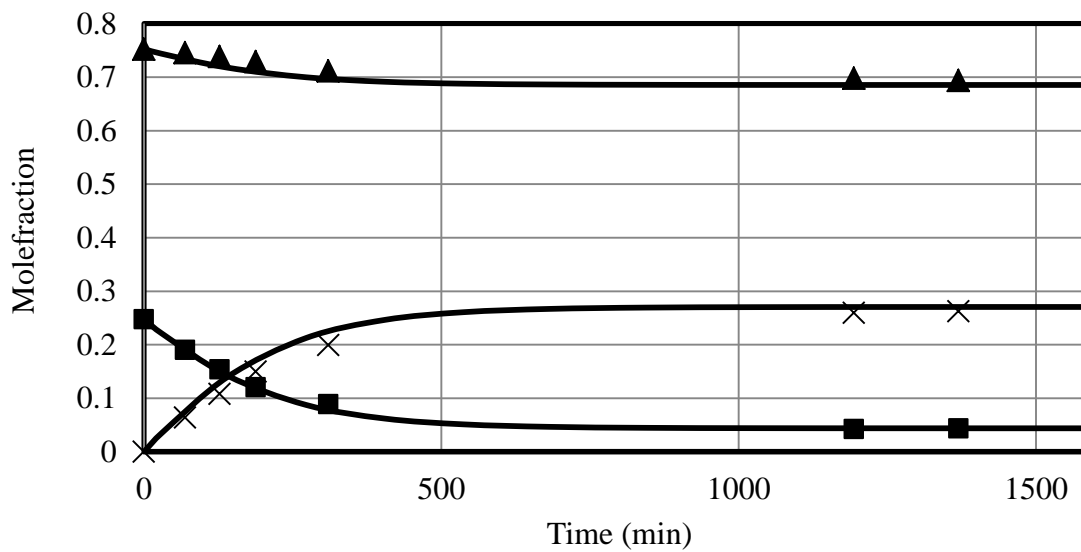


Figure A.3.10: Experimental and predicted mole fraction profiles of CHE esterification for Run 13. (▲)- AA; (×)- CHA; (■)- CHE.

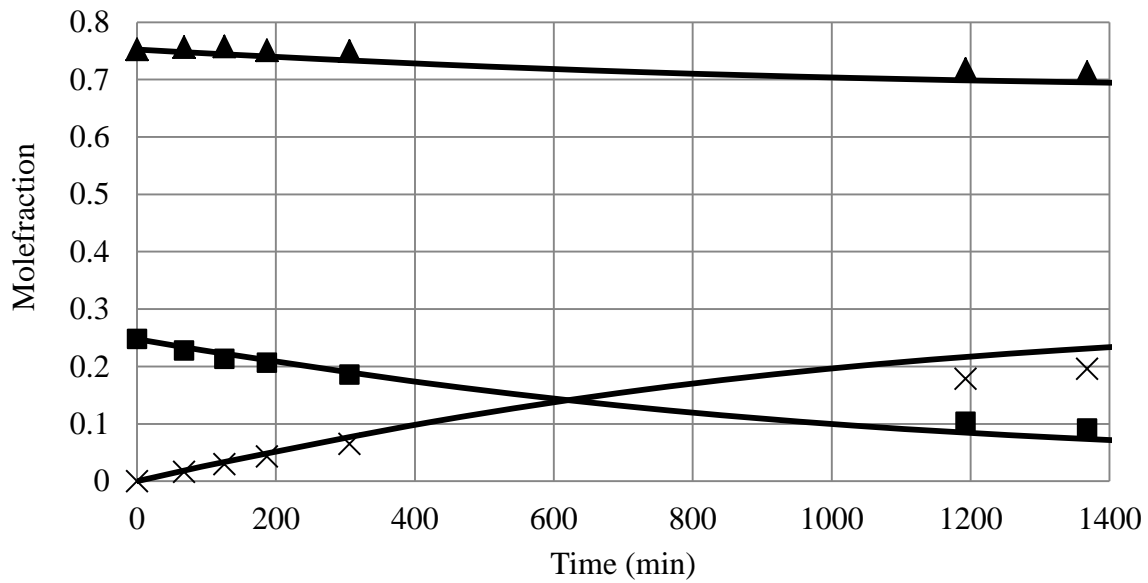


Figure A.3.11: Experimental and predicted mole fraction profiles of CHE esterification for Run 14. (▲)- AA; (×)- CHA; (■)- CHE.

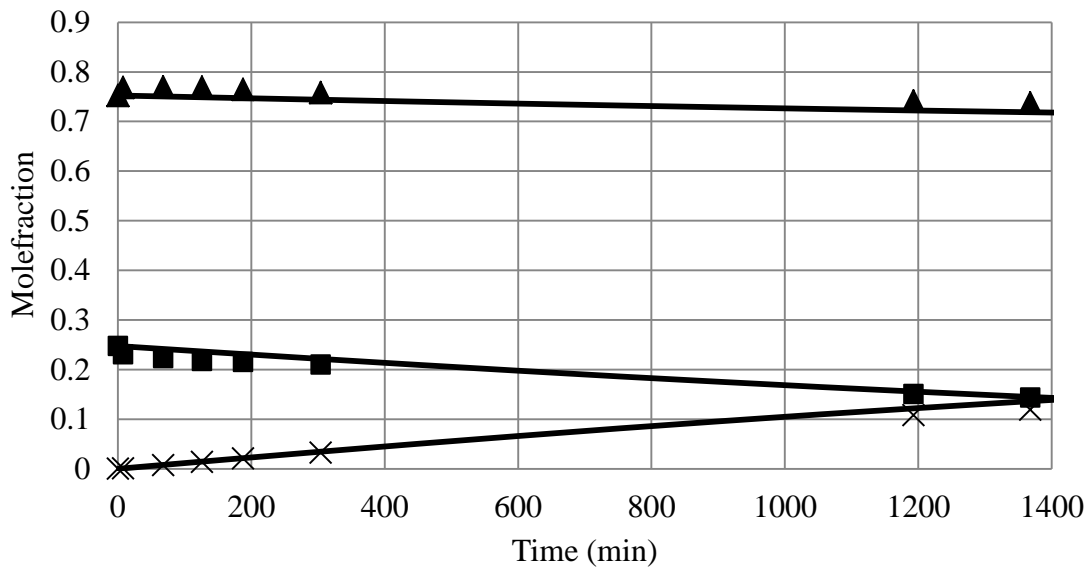


Figure A.3.12: Experimental and predicted mole fraction profiles of CHE esterification for Run 15. (▲)- AA; (×)- CHA; (■)- CHE.

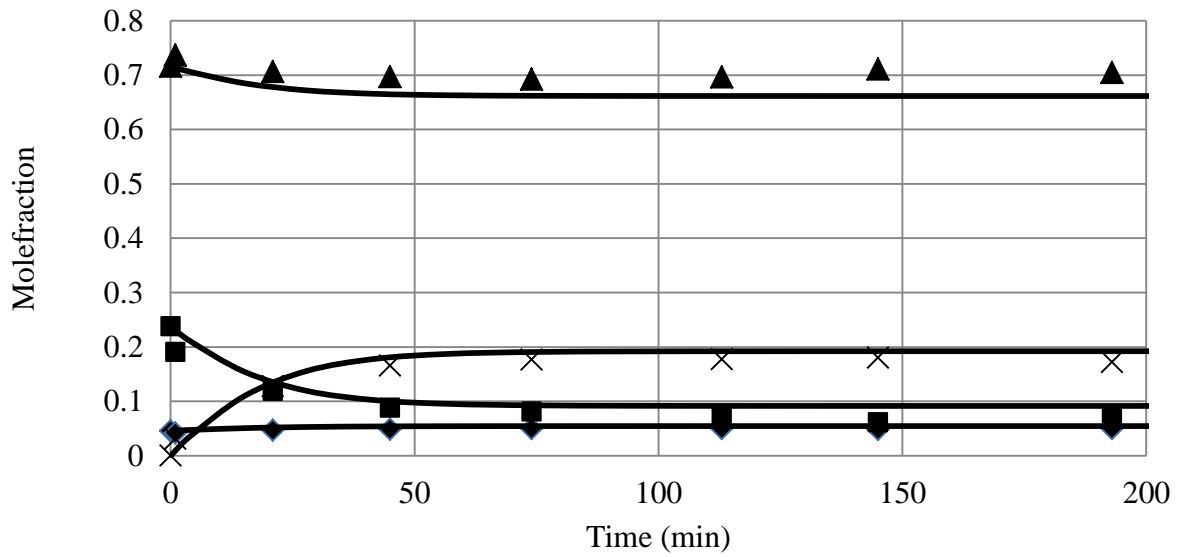


Figure A.3.13: Experimental and predicted mole fraction profiles of CHE esterification for Run 19. (▲)- AA; (×)- CHA; (■)- CHE.

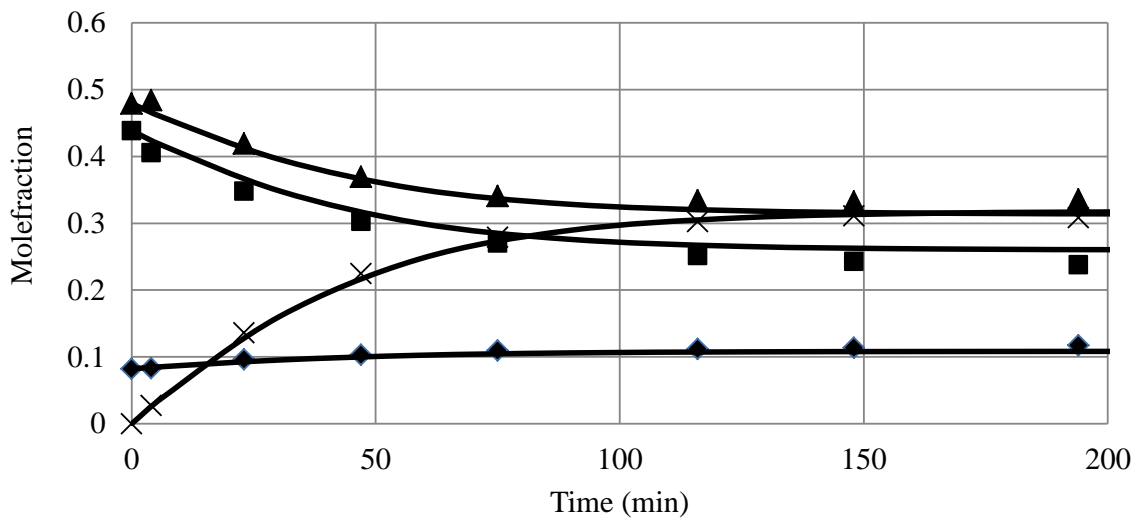


Figure A.3.14: Experimental and predicted mole fraction profiles of CHE esterification for Run 20. (▲)- AA; (×)- CHA; (■)- CHE.

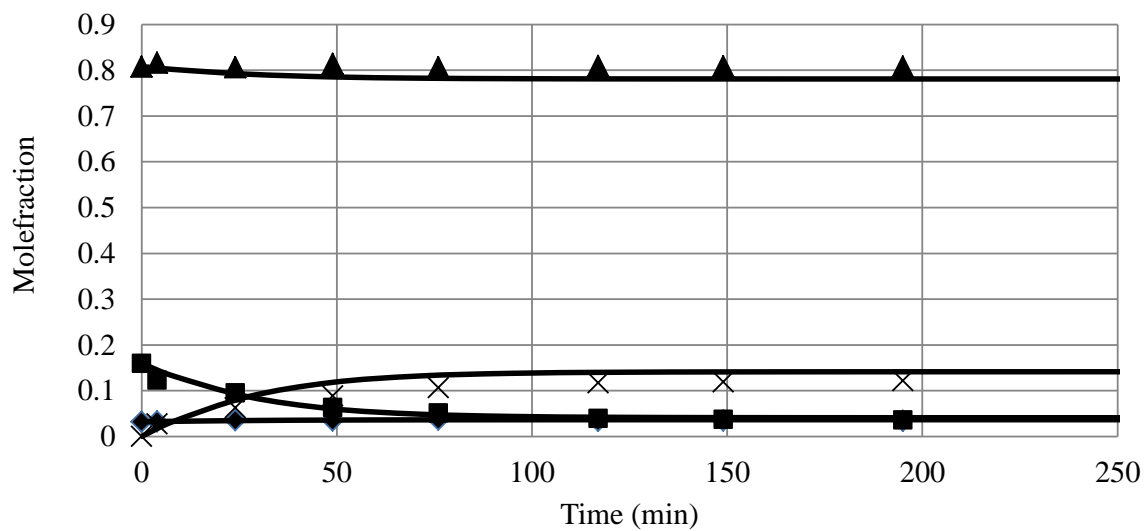


Figure A.3.15: Experimental and predicted mole fraction profiles of CHE esterification for Run 21. (▲)- AA; (×)- CHA; (■)- CHE.

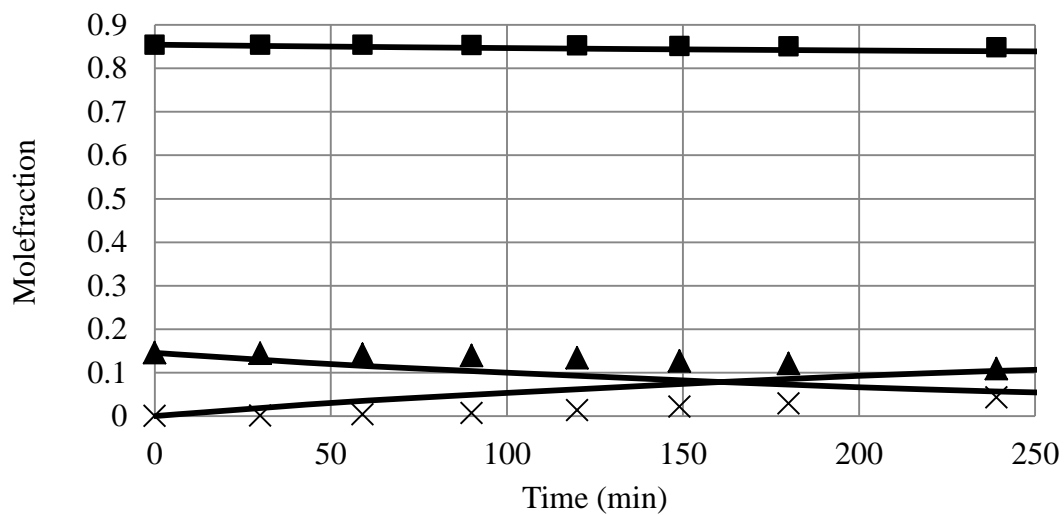


Figure A.3.16: Experimental and predicted mole fraction profiles of CHE esterification for Run 22. (▲)- AA; (×)- CHA; (■)- CHE.

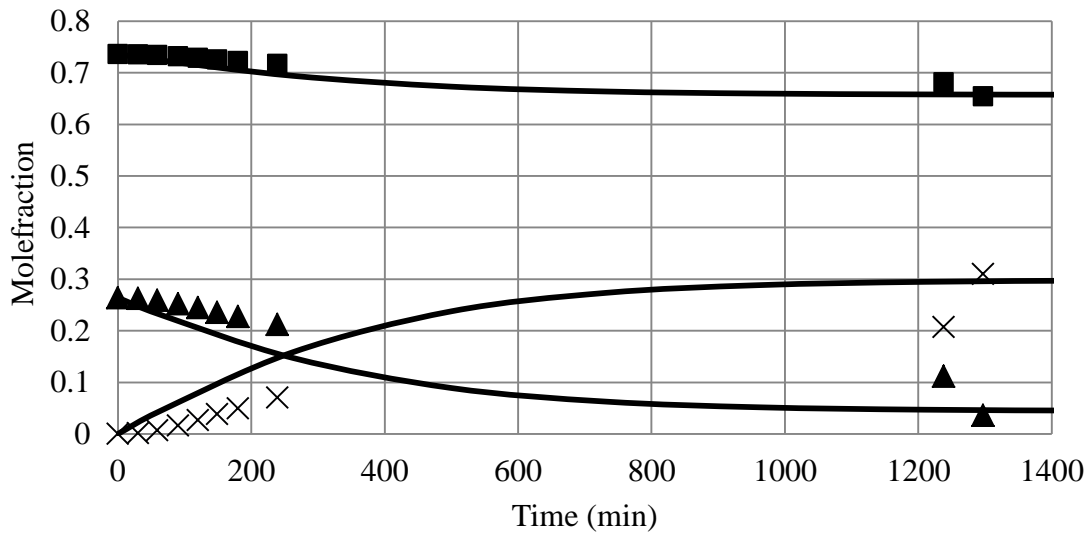


Figure A.3.17: Experimental and predicted mole fraction profiles of CHE esterification for Run 23. (▲)- AA; (×)- CHA; (■)- CHE.

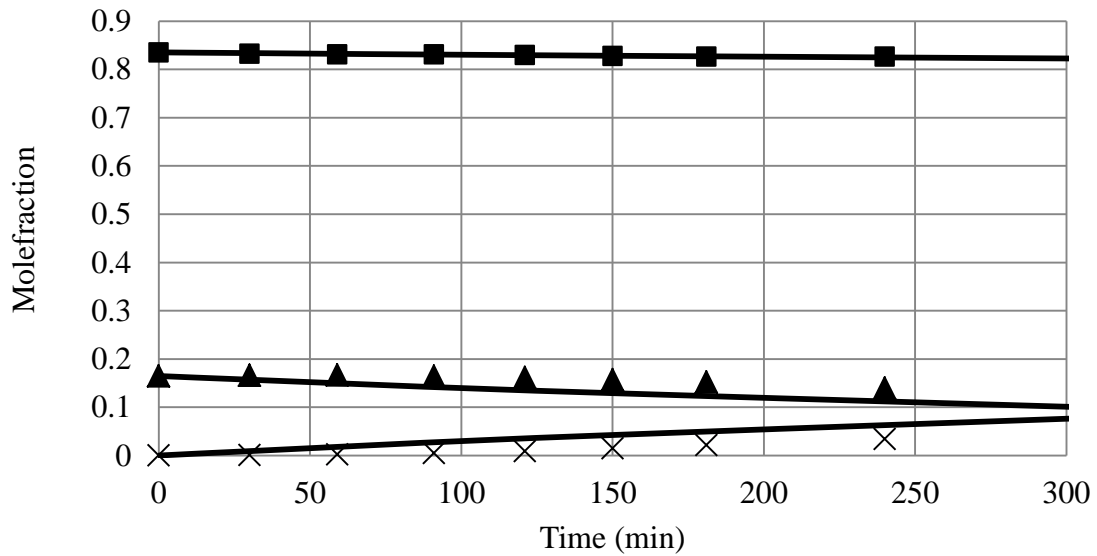


Figure A.3.18: Experimental and predicted mole fraction profiles of CHE esterification for Run 24. (▲)- AA; (×)- CHA; (■)- CHE.

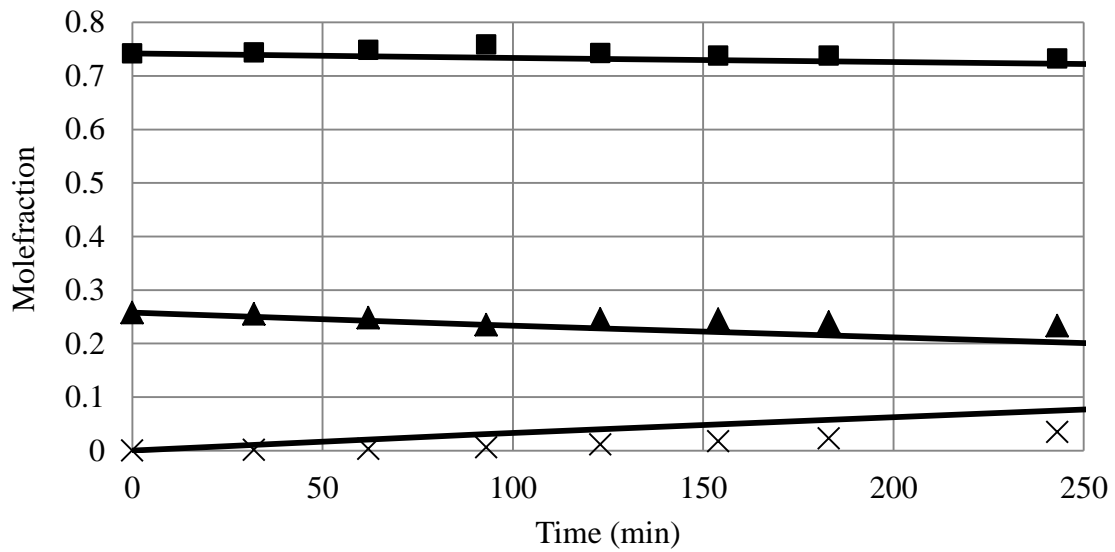


Figure A.3.19: Experimental and predicted mole fraction profiles of CHE esterification for Run 25. (▲)- AA; (×)- CHA; (■)- CHE.

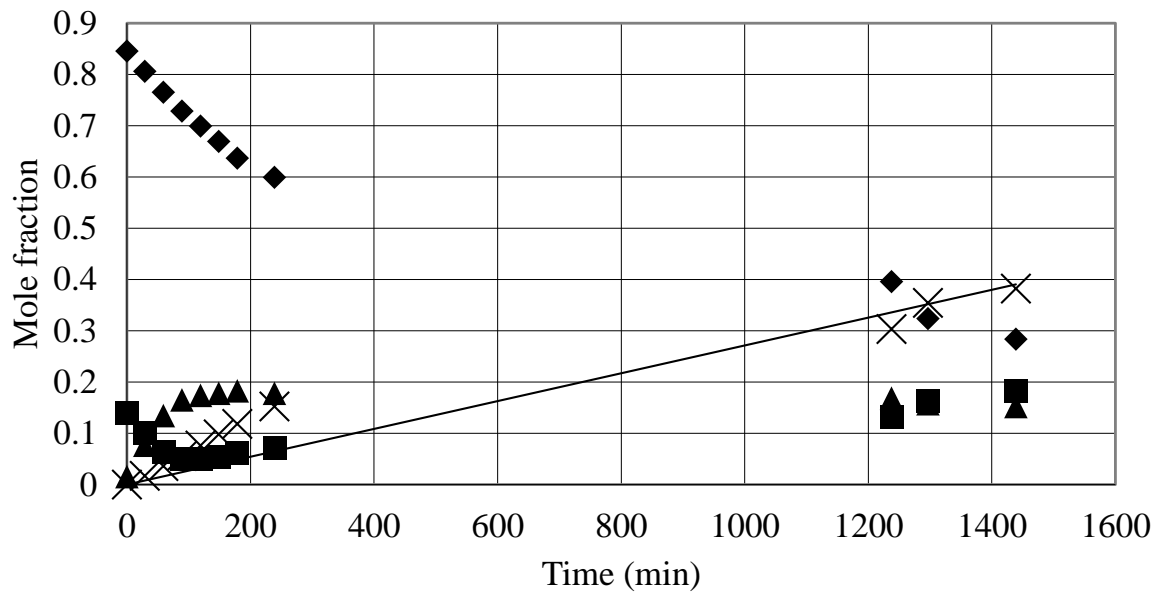


Figure A.3.20: Experimental mole fraction profiles of CHE esterification for Run 26. (▲) CHA; (■) AA; (◆) CHE; (×) CHE oligomers. Straight line represents the best fit for side product formation.

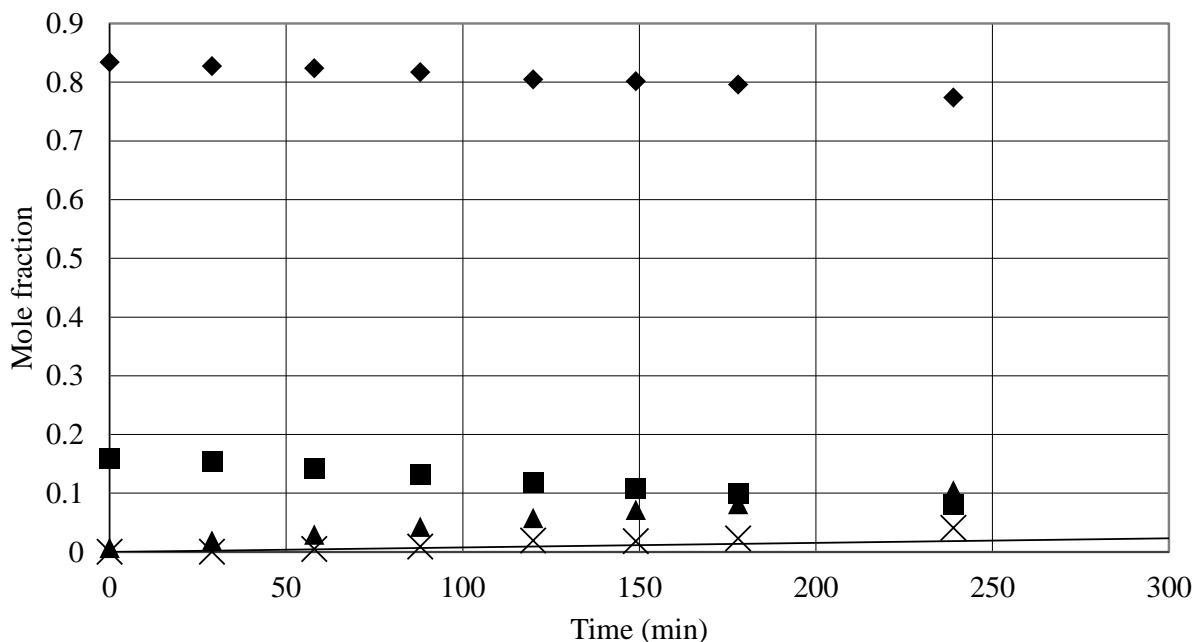


Figure A.3.21: Experimental mole fraction profiles of CHE esterification for Run 28. (▲) CHA; (■) AA; (♦) CHE; (×) CHE oligomers. Straight line represents the best fit for side product formation.

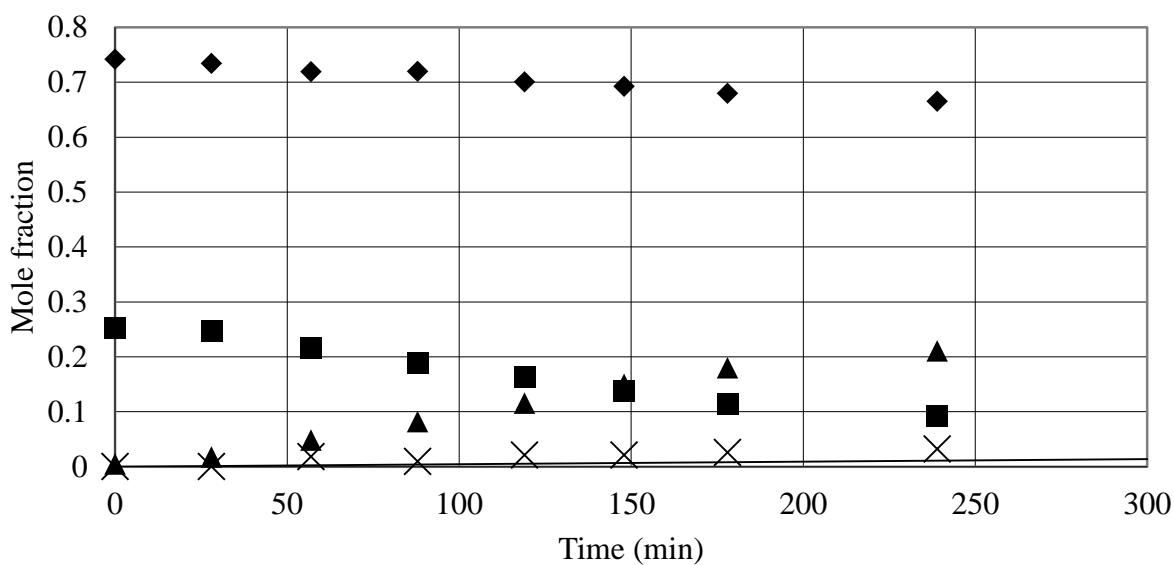


Figure A.3.22: Experimental mole fraction profiles of CHE esterification for Run 29. (▲) CHA; (■) AA; (♦) CHE; (×) CHE oligomers. Straight line represents the best fit for side product formation.

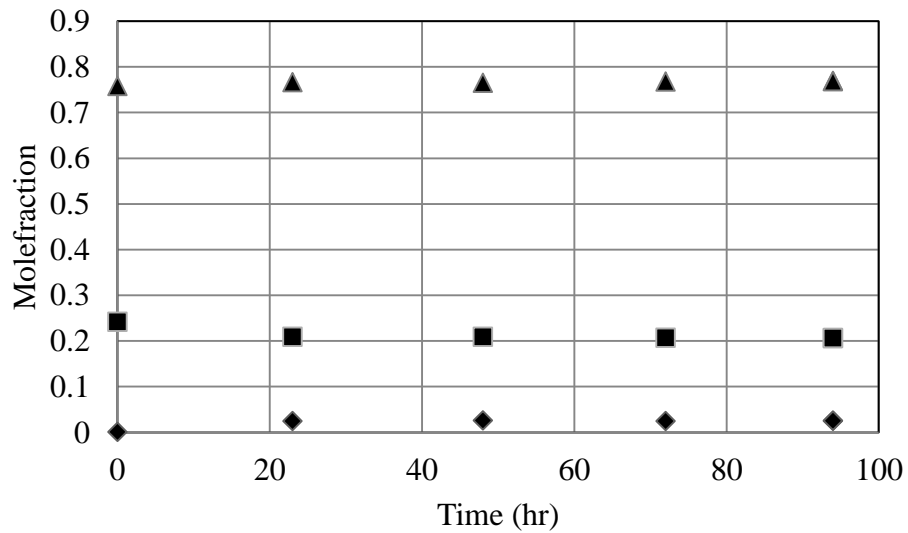


Figure A.3.23: Experimental mole fraction profiles for Run 30. (▲) AA; (■) CHA (◆) CHE.

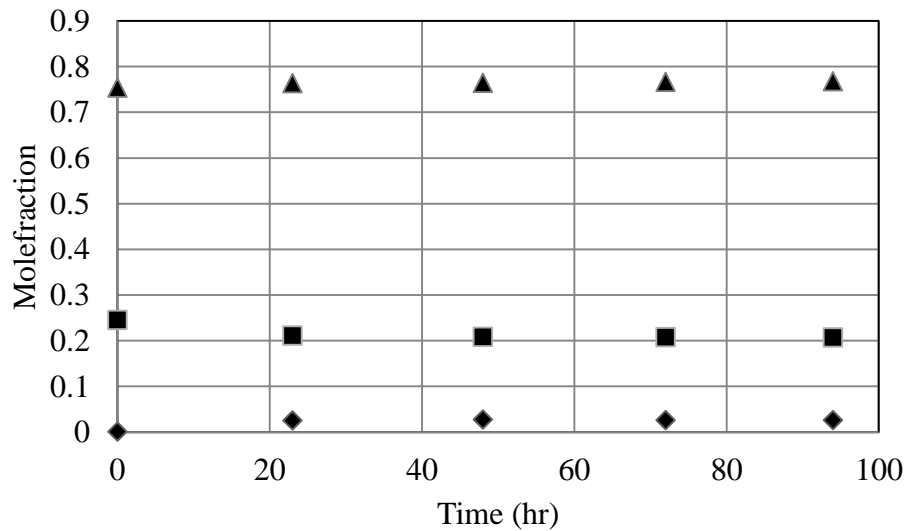


Figure A.3.24: Experimental mole fraction profiles for Run 31. (▲) AA; (■) CHA (◆) CHE.

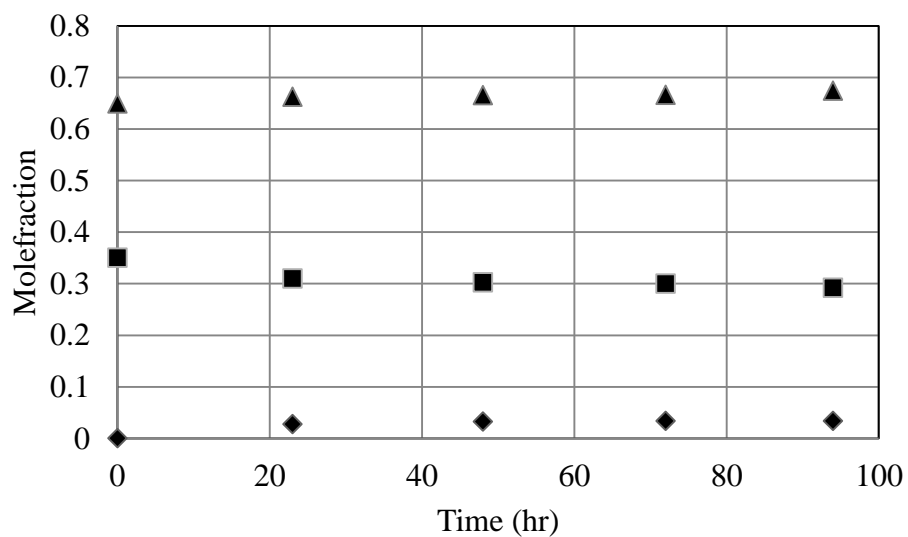


Figure A.3.25: Experimental mole fraction profiles for Run 32. (▲) AA; (■) CHA (◆) CHE.

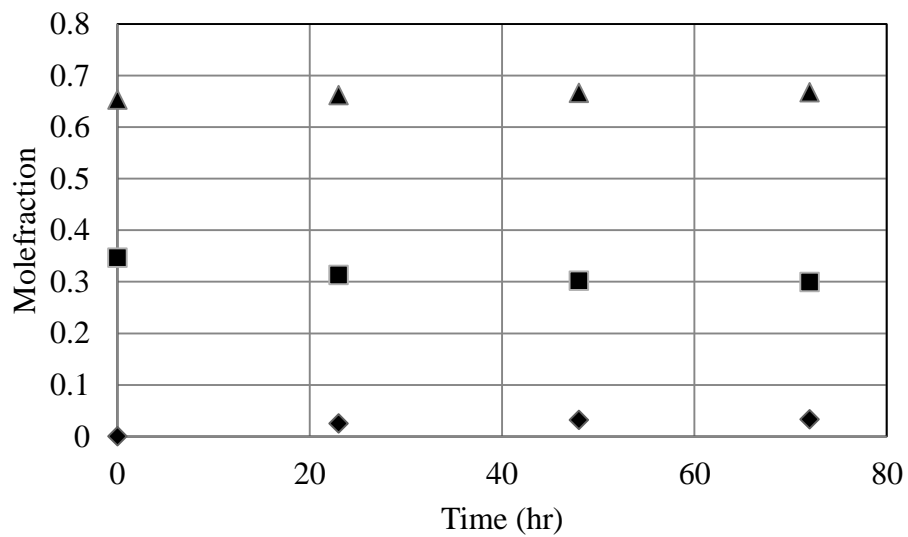


Figure A.3.26: Experimental mole fraction profiles for Run 33. (▲) AA; (■) CHA (◆) CHE.

### A.3: Identification of Cyclohexene oligomers

Figure A.4.1 shows retention time of CHE dimer peaks along with their structures in a gas chromatogram. Figures A.4.2, A.4.3 and A.4.4 show the mass spectra for 1-cyclohexyl cyclohexene, 3-cyclohexyl cyclohexene and 1,1'-oxybis cyclohexane respectively. It is to be noted here that mass spectrometry was used only for identification of CHE dimers.

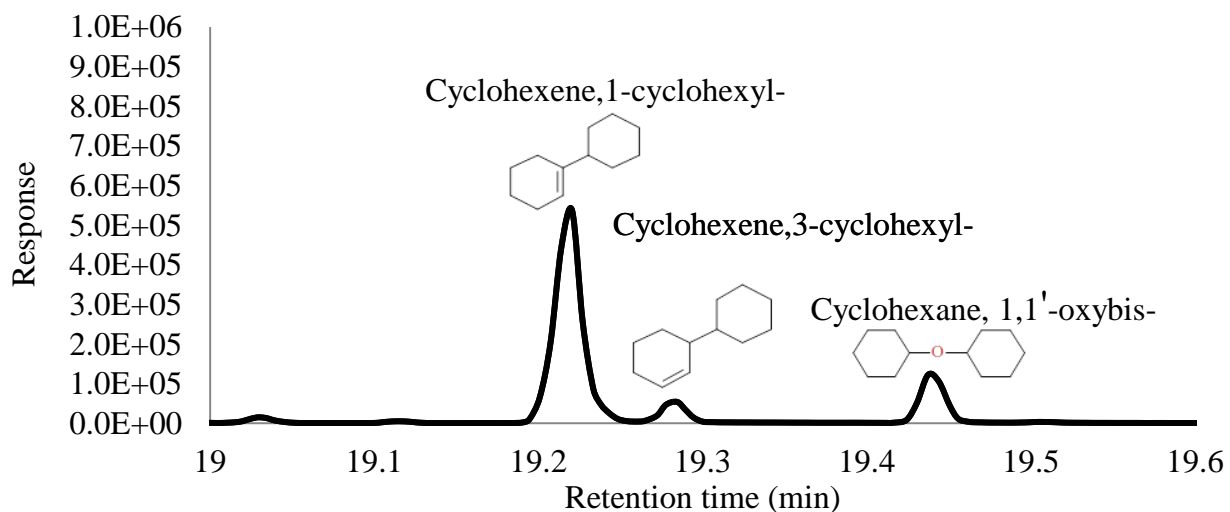


Figure A.4.1: Chromatogram for CHE dimer identification

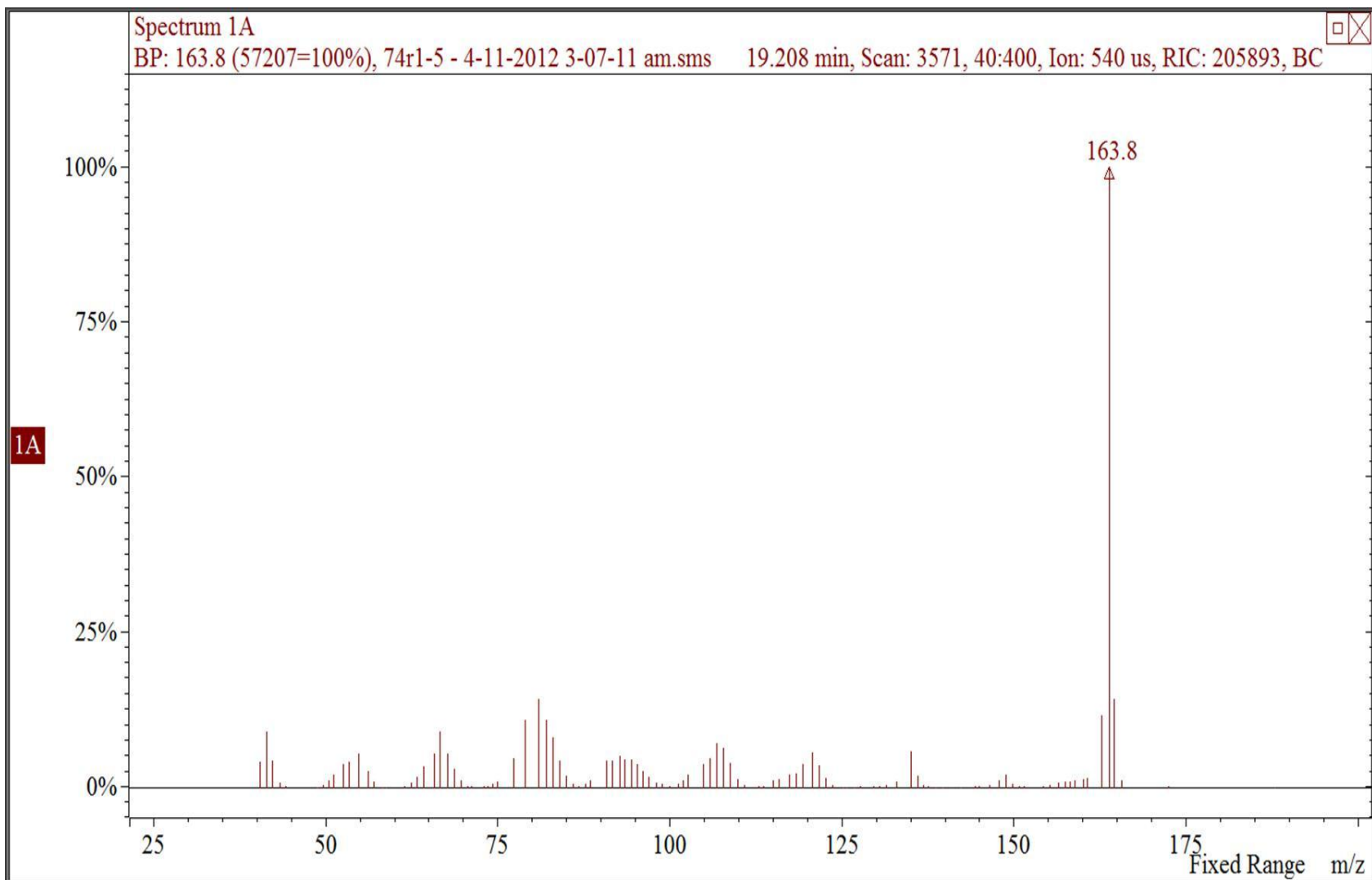


Figure A.4.2: Mass spectra for 1-cyclohexyl cyclohexene

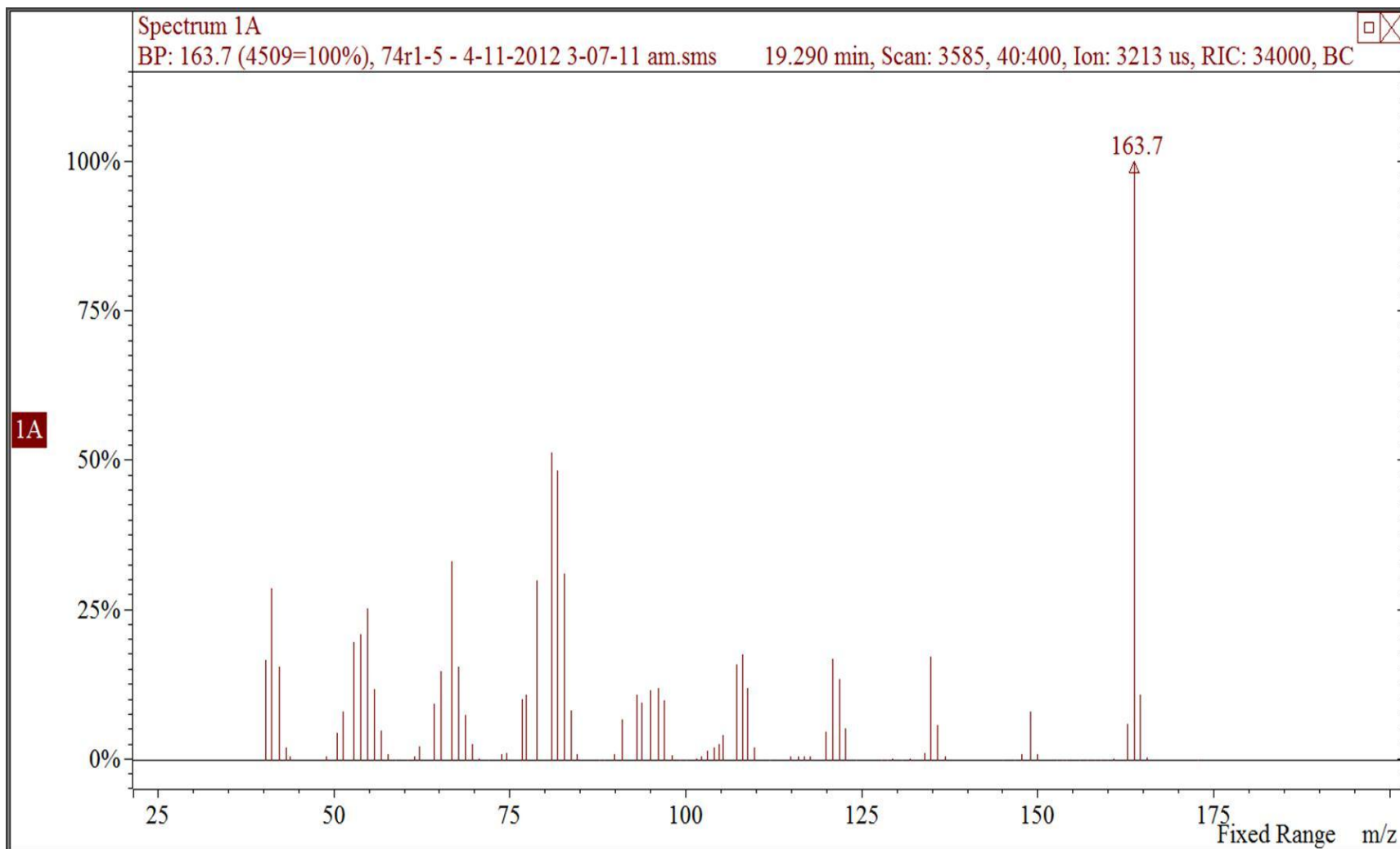


Figure A.4.3: Mass spectra for 3-cyclohexyl cyclohexene

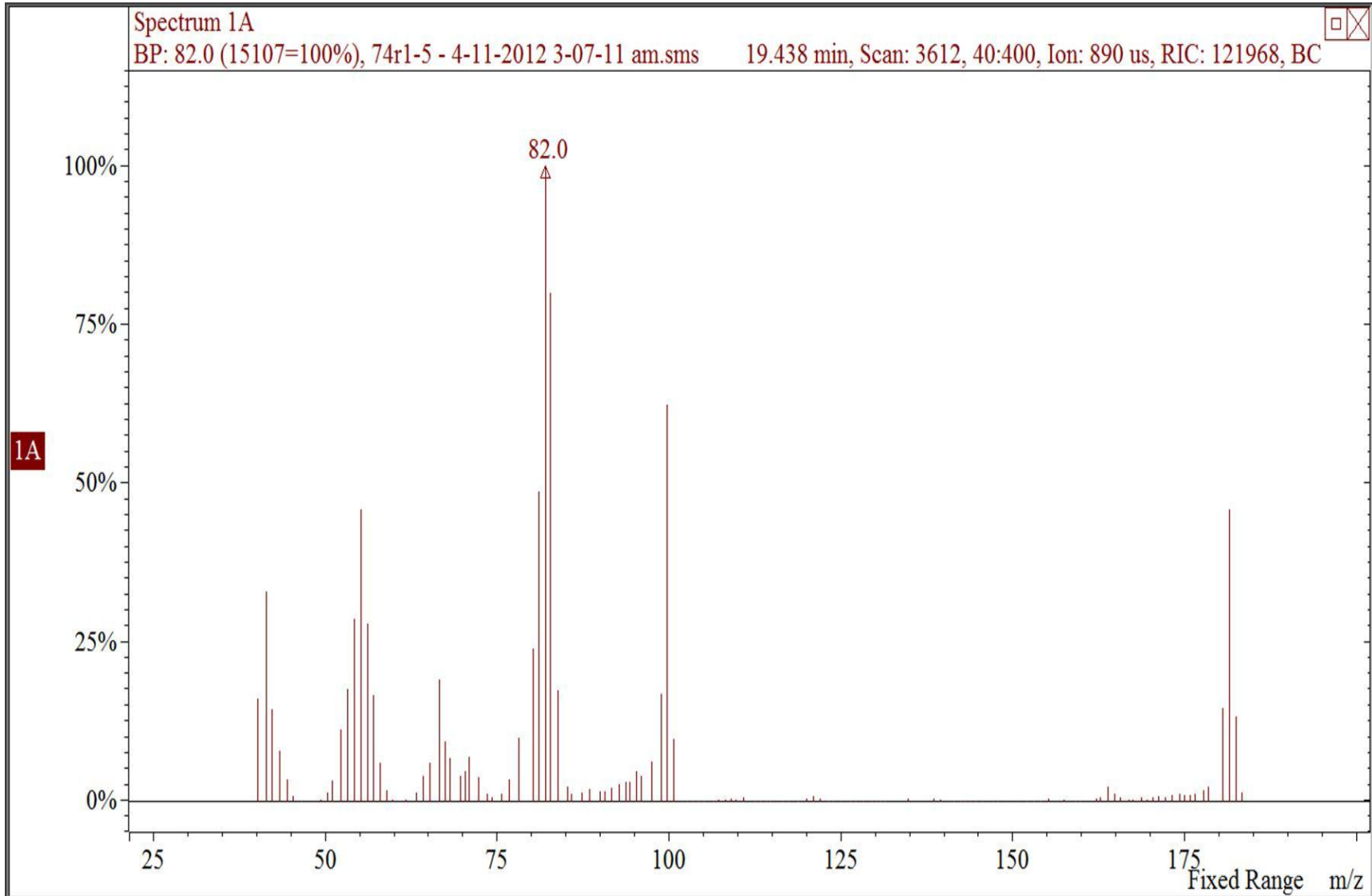


Figure A.4.4: Mass spectra for 1,1'-oxybis cyclohexane

#### *A.5: Calibration plots for sample analysis*

Reaction samples were diluted in 1-Butanol with 5 wt% 1,4 Dioxane (1-BuOH+14D) solvent. To determine the weight of each component in the reaction sample, individual calibrations were carried out. Measured quantity of each component was mixed with known amount of solvent such that the component is 10% by weight in the solution. The calibration samples were made to cover the whole range of mass fraction that is expected in the reaction samples. These samples were analyzed in gas chromatograph as described in Section 2.3. From the chromatograms, area for each component is obtained. From this data, area for a known weight of component and area for fixed amount of 14D is known. The ratio of area of component to that of 14D is plotted against the ratio of known weight of component to that of 14D. This plot is typically a straight line passing through the origin. The slope of this line is the “calibration factor”.

Weight of individual components is unknown in reaction samples. From the chromatograms, area of 14D and areas of individual component are obtained. Weight of 14D is known from the amount solvent used to dilute the reaction sample. Using the calibration factor for each component, weight of the component is obtained. Figures A.5.1 to A.5.3 show the calibration plots used in this study.

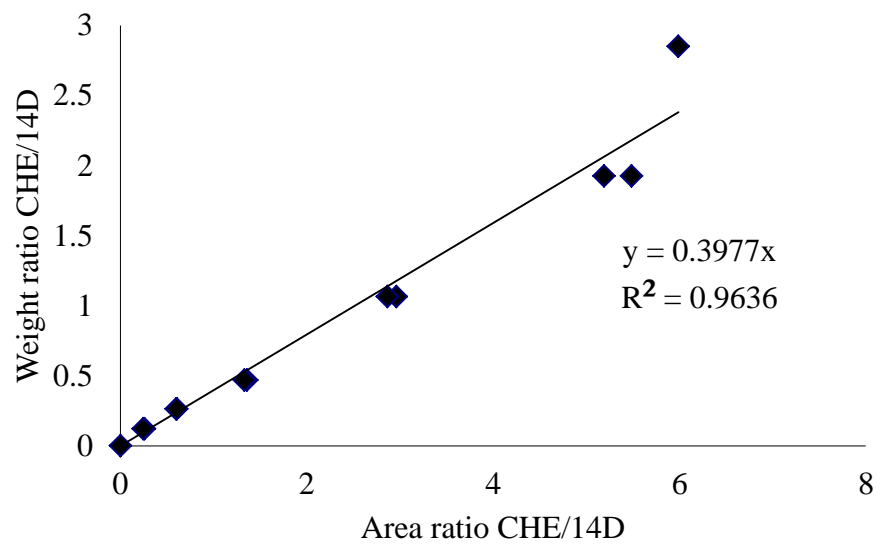


Figure A.5.1: calibration plot for Cyclohexene (CHE)

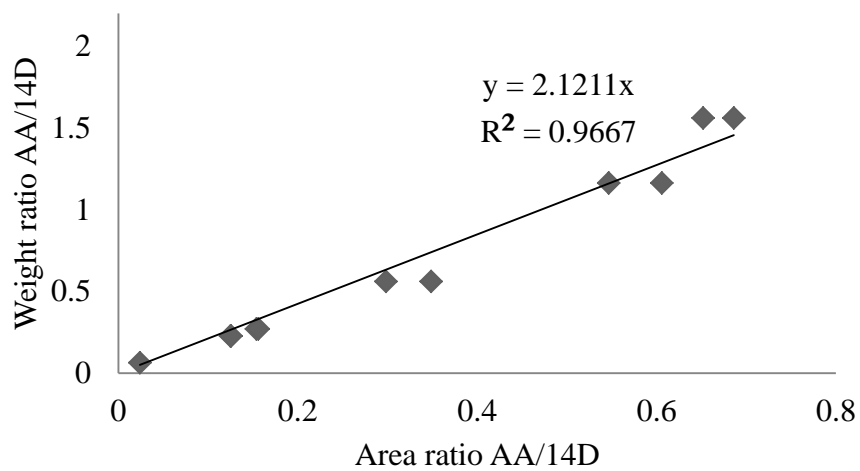


Figure A.5.2: calibration plot for Acetic acid (AA)

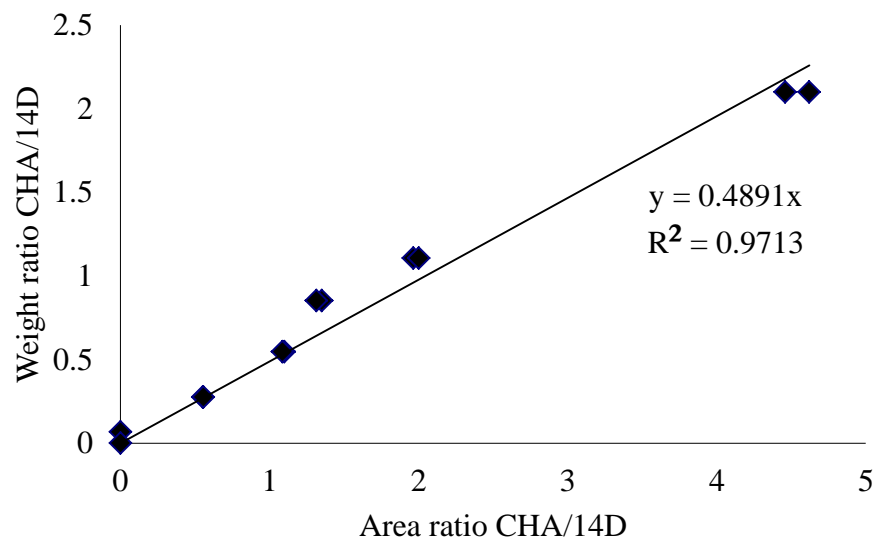


Figure A.5.3: calibration plot for Cyclohexyl acetate (CHA)

*A.6: NRTL parameters*

The NRTL-HOC parameters used in Chapters 2 and 3 to calculate activity coefficients are presented in Tables A.6.1 and A.6.2 [22].

Table A.6.1: HOC parameters used in Aspen simulations

	AA	CHA	CHE	W
AA	4.5	2	0	2.5
CHA	2	0.53	0	
CHE	0	0	0	
W	2.5			1.7

Table A.6.2: NRTL parameters used in Aspen simulations<sup>a</sup>

Component i	CHE	CHA	AA	CHE	AA	CHA	CHE	AA	W	CHX
Component j	AA	CHE	CHA	CHX	CHX	CHX	W	W	CHA	W
Temperature units	K	K	K	K	K	K	K	K	K	K
Source	USER	USER	USER	USER	USER	USER	USER	APV71 VLE-HOC	USER	APV71 LLE- ASPEN
aij	0	- 0.06041	0.62514 6	0	0	2.06657 8	0	-1.9763	6.90004 6	-10.4585
aji	0	10.6828	0.12857	0	0	-2.65123	0	3.3293	3.59808	13.1428
bij	277.36071 2	- 390.093	0	4.2466	601.80	-1334.89	1626.49	609.8886	0	4954.897
bji	584.03308	- 3091.04	0	4386.49	678.993	2029.09	2585.47	-723.888	0	-1066.98
cij	0.3	0.3	1	0.89828	0.5	0.3	0.24319	0.3	0.31077	0.2
Tlower	0	0	0	0	351.95	0	0	293.15	0	283.15
Tupper	1000	1000	1000	1000	391.25	1000	1000	502.9	1000	326.15

a: APV71 refers to Aspen Plus Version 7.1

## **REFERENCES**

## 2.7. References

1. Musser, M.T., Cyclohexanol and Cyclohexanone. Ullmann's Encyclopedia of Industrial Chemistry. 2000: Wiley-VCH Verlag GmbH & Co. KGaA.
2. Steyer, F., H.r. Freund, and K. Sundmacher, *A Novel Reactive Distillation Process for the Indirect Hydration of Cyclohexene to Cyclohexanol Using a Reactive Entrainer*. Industrial & Engineering Chemistry Research, 2008. 47(23): p. 9581-9587.
3. Sharma, M.M., *Some novel aspects of cationic ion-exchange resins as catalysts*. Reactive and Functional Polymers, 1995. 26(1-3): p. 3-23.
4. Saha, B. and M. Mohan Sharma, *Esterification of formic acid, acrylic acid and methacrylic acid with cyclohexene in batch and distillation column reactors: ion-exchange resins as catalysts*. Reactive and Functional Polymers, 1996. 28(3): p. 263-278.
5. Katariya, A., H.r. Freund, and K. Sundmacher, *Two-Step Reactive Distillation Process for Cyclohexanol Production from Cyclohexene*. Industrial & Engineering Chemistry Research, 2009. 48(21): p. 9534-9545.
6. Steyer, F., Z. Qi, and K. Sundmacher, *Synthesis of cyclohexanol by three-phase reactive distillation: influence of kinetics on phase equilibria*. Chemical Engineering Science, 2002. 57(9): p. 1511-1520.
7. Steyer, F. and K. Sundmacher, *VLE and LLE Data for the System Cyclohexane + Cyclohexene + Water + Cyclohexanol*. Journal of Chemical & Engineering Data, 2004. 49(6): p. 1675-1681.
8. Steyer, F. and K. Sundmacher, *VLE and LLE Data Set for the System Cyclohexane + Cyclohexene + Water + Cyclohexanol + Formic Acid + Formic Acid Cyclohexyl Ester*. Journal of Chemical & Engineering Data, 2005. 50(4): p. 1277-1282.
9. Steyer, F. and K. Sundmacher, *Cyclohexanol Production via Esterification of Cyclohexene with Formic Acid and Subsequent Hydration of the Ester Reaction Kinetics*. Industrial & Engineering Chemistry Research, 2007. 46(4): p. 1099-1104.

10. Kumar, R., et al., *Development of a Novel Catalytic Distillation Process for Cyclohexanol Production: Mini Plant Experiments and Complementary Process Simulations*. *Organic Process Research & Development*, 2011. 15(3): p. 527-539.
11. Chakrabarti, A. and M.M. Sharma, *Cyclohexanol from cyclohexene via cyclohexyl acetate - catalysis by ion-exchange resin and acid treated clay*. *Reactive Polymers*, 1992. 18(2): p. 107-115.
12. Verevkin, S.P., et al., *Equilibrium of chemical-transformations in the system of carboxylic acid-olefin-ester*. *Journal of Applied Chemistry of the USSR*, 1992. 65(3): p. 536-541.
13. Siril, P.F., H.E. Cross, and D.R. Brown, *New polystyrene sulfonic acid resin catalysts with enhanced acidic and catalytic properties*. *Journal of Molecular Catalysis A: Chemical*, 2008. 279(1): p. 63-68.
14. Bringué, R., Roger, et al., *Thermally stable ion-exchange resins as catalysts for the liquid-phase dehydration of 1-pentanol to di-n-pentyl ether (DNPE)*. *Journal of Catalysis*, 2006. 244(1): p. 33-42.
15. Bringué, R., et al., *Water effect on the kinetics of 1-pentanol dehydration to di-n-pentyl ether (DNPE) on amberlyst 70*. *Topics in Catalysis*, 2007. 45(1): p. 181-186.
16. Ronchin, L., G. Quartarone, and A. Vavasori, *Kinetics and mechanism of acid catalyzed alkylation of phenol with cyclohexene in the presence of styrene divinylbenzene sulfonic resins*. *Journal of Molecular Catalysis A: Chemical*, 2011. 353-354(0): p. 192-203.
17. Yadav, G.D. and P.K. Goel, *Selective synthesis of perfumery grade cyclohexyl esters from cyclohexene and carboxylic acids over ion exchange resins: an example of 100% atom economy*. *Green Chemistry*, 2000. 2(2): p. 71-78.
18. <http://www.amberlyst.com/literature/a4/70.pdf>. Accessed on 5/22/2012.
19. DIPPRR Data Compilation of Pure Chemical Properties. 2011, Design Institute for Physical Properties, AIChE, New York, NY. 2011.
20. Elliott, R.J. and C.T. Lira, *Introductory Chemical Engineering Thermodynamics*. Second ed. 2009, Boston: Prentice Hall.

21. Helfferich, F.G., Ion exchange. 1st ed. 1962, New York McGraw Hill.
22. Alex Smith, A.K., Carl T.Lira, Dennis J. Miller, *Phase equilibrium data for cyclohexene, acetic acid system*, Manuscript in preparation, Michigan State University.
23. Gates, B.C. and W. Rodriguez, *General and specific acid catalysis in sulfonic acid resin*. *Journal of Catalysis*, 1973. 31(1): p. 27-31.

## **Chapter 3: Cyclohexyl acetate production using reactive distillation: Pilot plant experiments and simulations**

### **3.1. Summary**

Cyclohexyl acetate production using reactive distillation can be an intermediate step during cyclohexanol production by indirect hydration of cyclohexene using acetic acid as reactive entrainer. In this study, pilot scale runs in the MSU reactive distillation facility were conducted to demonstrate technical feasibility of this intermediate step and exemplify the opportunities for external heat integration in a continuous reactive distillation operation. All experiments were conducted at atmospheric pressure in a 6 m tall, 51 mm ID pilot-scale glass column packed with KATAPAK-SP11 structured packing containing Amberlyst 70 cation exchange resin as catalyst. Based on preliminary runs, process configuration and conditions suitable for high conversions of cyclohexene are suggested. The experimental data obtained at steady state were compared with results obtained from simulations performed using RADFRAC column module in Aspen Plus.

### **3.2. Introduction**

Process intensification (PI) uses engineering principles to develop sustainable processing technologies that are simpler, more energy efficient, less waste producing and lower cost [1-3]. PI can be achieved by combining functions or phenomena in an operation, adding or enhancing targeted functions in a process, and/or by using alternative energy sources to enhance performance. One such PI technique is reactive distillation (RD), which integrates chemical reaction and physical separation into one unit operation. The use of RD to produce high purity methyl acetate [4] and the production of methyl tert-butyl ether (MTBE) [5] are perhaps the best

known commercial applications of PI to improve energy efficiency. Freund et al., reviewed the processes that offer an opportunity for application of RD as a PI technique [6, 7]. Cyclohexanol production from benzene by partial hydrogenation to cyclohexene (herein, CHE) and then hydration is one such process where RD can be used to decrease energy consumption and capital expenditures.

Indirect hydration is a novel RD approach to produce cyclohexanol from CHE [8, 9] in high yields. In this process, a carboxylic acid is used as a reactive entrainer. CHE is first esterified with the carboxylic acid to produce a cyclohexyl ester in the first RD column. In a second RD column, the ester is hydrolyzed to liberate the free carboxylic acid, which can be recycled back to the first RD column, and cyclohexanol. Steyer et al and Kumar et al. [10-13] have demonstrated the technical feasibility of producing cyclohexanol from CHE and formic acid using mini plant experiments, and developed a process simulation model that represents steady state experimental data. Apart from safety and energy efficiency, this method offers the additional advantage of separating CHE from cyclohexane, an undesired product of benzene hydrogenation. Cyclohexane does not participate in the esterification reaction and can be isolated and collected as the top product from the first RD column. This eliminates the extractive distillation step required to separate the mixture of CHE and cyclohexane in other approaches employing benzene hydrogenation [14, 15].

To enhance energy efficiency, using the heat of reaction to drive separation must be taken into account during the conceptual stages of designing a particular RD process [16]. This internal heat utilization can be quantified as the thermal effect of a reaction ( $\xi$ ), a dimensional number first introduced by Sundmacher et al. [17]. Thermal effect is defined as the heat of reaction divided by the mean heat of vaporization.

$$\xi = \frac{(\Delta_R H^o)^L}{\sum_{j=1}^N (x_j \Delta H_{v,j})^L} \quad \text{where } j=1,N \text{ number of components in the reaction} \quad (3.1)$$

CHE esterification with acetic acid is an exothermic reaction with a thermal effect of  $\xi = 1.04$  (equilibrium mole fraction data taken from a batch experiment at 90°C was used in this calculation). For reactions with moderate thermal effects ( $0.05 \leq \xi \leq 1.0$ ), feed stage location plays a significant role in determining the energy efficiency of a RD column [18]. For exothermic reactions, it is also important to evaluate heat transfer effects from the section of the column where most of the reaction takes place to sections where energy is most needed (e.g. where there is less reaction).

This study focuses on the first part of the indirect hydration approach using acetic acid (herein, AA) as the reactive entrainer. Pilot scale experiments to evaluate the feasibility of CHE esterification with AA and establish steady state operation were first performed under different process conditions. Further experiments were then conducted to demonstrate the effect of heat loss from a section of the RD column at steady state as a first step in implementing heat integration in the reaction system. Using process simulation, the effect of heat addition or loss from a section of the column and the effect of heat transfer from one of column to another on CHE conversion was studied and compared to the experimental results obtained. Based on the results and challenges encountered during pilot plant runs and simulations, suitable process conditions for RD operation are suggested.

### 3.3. Materials and Methods

Acetic acid (>99.7%, glacial) was purchased from VWR scientific. Cyclohexene (>99%) was obtained from Alfa Aesar. Cyclohexyl acetate (>99%) and 1,4-dioxane (>99%) were

obtained from Sigma-Aldrich. 1-Butanol, which was used as solvent during sample analysis, was obtained from Mallinckrodt-Baker, Inc. Amberlyst 70 resin was purchased from the Dow Chemical Company.

Samples were analyzed using a HP-5890 Series II gas chromatograph equipped with a flame ionization detector (FID). A 30m length, 0.53mm ID, 1.0 $\mu$ m film thickness Aquawax-DA column was used to separate the components. Oven temperature maintained initially at 40°C for 1.0 min, increased at 20°C/min to 250°C, and then maintained at that temperature for an additional 2.0 min. Injector and detector temperatures were maintained at 250°C and 300°C respectively. 1,4-Dioxane was used as internal standard. To identify cyclohexene dimers, a Varian CP-3800 gas chromatograph equipped with Saturn 2000 mass spectrometer was used. A fused silica capillary column SLB™-5ms:30m $\times$  0.25mm  $\times$  0.25 $\mu$ m film thickness was used to separate the components. Water content in the reactants was analyzed using Hydranal-coulomat E solution in a coulometric AQ-2100 Karl-Fisher titrator.

To determine the catalytic activity by titration, catalyst packing was soaked in 1M NaCl solution in water for 2 hours and then titrated using 0.1M NaOH solution. Catalyst reactivation was done by soaking the catalyst packing in 5% by weight sulfuric acid in water for 12 hours and then washing with deionized water till pH of the washed liquid was at least 5.0. A fresh catalyst packing was titrated to obtain an activity value of 2.7 eq/kg.cat.

### **3.3.1 Reactive distillation column configuration and operating procedure**

A schematic of the reactive distillation column for cyclohexyl acetate (herein, CHA) production from CHE and AA is shown in Figure 3.1. The experimental setup comprises a glass column, a total condenser, an accumulator for refluxing the distillate product that works as decanter to separate accumulated water, a reboiler, and a bottom product collector. The glass

column consists of six one-meter long, 51 mm ID removable sections; two noncatalytic sections and four catalytic/reactive sections. The catalytic sections are packed with KATAPAK-SP11 structured packing filled with Amberlyst-70 cationic ion-exchange resin as acid catalyst. Steinigeweg et al., measured separation efficiency of KATAPAK-SP 11 structured packings using water-acetic acid test system and found that number of theoretical stages per meter of the packings is 2 [19]. Therefore in this study, height-equivalent theoretical plate (HETP) of 0.5 was assumed giving the column an equivalent of 12 theoretical stages plus a partial reboiler. Each catalyst packing in the reactive section was 9 cm in length and contained approximately 0.014kg of catalyst. This is equivalent to 11 packings per meter of column i.e., 0.150 kg.cat/1 m of column or 0.075 kg.cat/stage. The catalytic sections are separated by liquid re-distributors that also allow intermediate liquid sample withdrawal. The noncatalytic stripping and enriching sections of the column are packed with structured Sulzer-Mellapak packings. The specifications of the column design are given in Table 3.1.

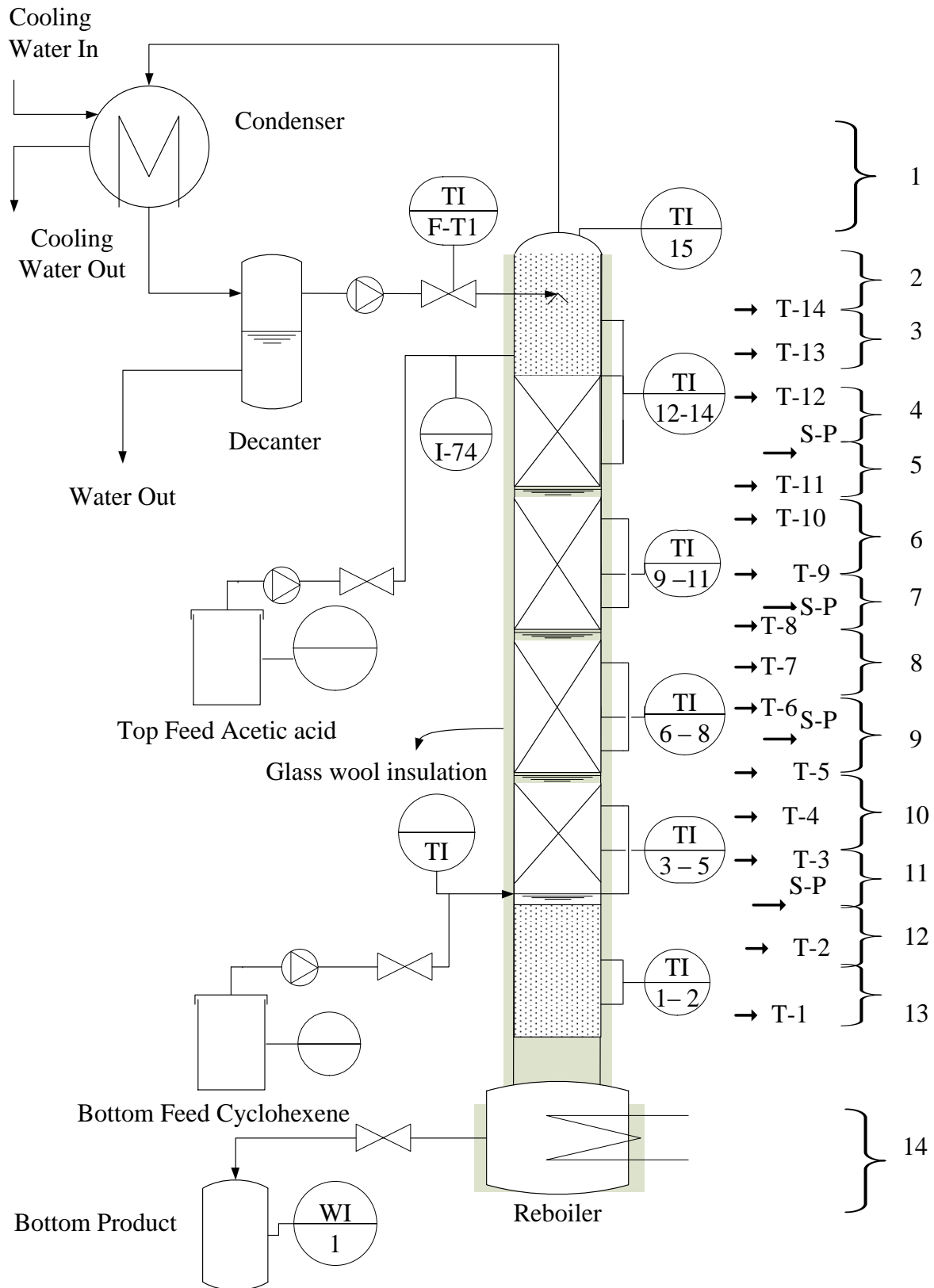


Figure 3.1: A schematic of pilot scale RD column

Table 3.1: Characteristics of pilot plant reactive distillation column

Parameter	Value
height (m)	6
inner diameter (mm)	51
reboiler capacity (L)	2.5
Non-catalytic stripping section height (m)	1
type of packing	Mellapak
catalytic section height (m)	4
Packing type	KATAPAK- SP11
Catalyst	Amberlyst-70
catalyst particle size (mm)	>0.5
catalyst holdup (kg/m <sup>3</sup> )	76
Non-catalytic enriching section height (m)	1
Packing type	Mellapak

The column was wrapped with electric heating tapes and insulated with glass wool bands. Internal and external surface thermocouples were positioned at various points along the column to register temperature profiles inside and outside the column. To imitate adiabatic operation of an industrial scale column, the heating tapes along the column height were individually controlled to match external surface temperature with internal column temperature. To ameliorate the corrosive effects of acetic acid at high temperature, the reboiler was powered by a 1500W, 120V titanium sheath tubular heater obtained from Durex industries (Part No: HB26X-05W-15002-821501). Reboiler power was calculated by measuring current through the heater

using an ammeter. Cooling water was used as coolant in the condenser. To determine condenser duty, the cooling water inlet and outlet temperatures and flow rate were measured during the experiments. By measuring heat input (reboiler power) and output (energy balance over condenser), an overall energy balance across the column was carried out.

During column operation, CHE and AA were fed to the column using diaphragm pumps from feed tanks positioned on electronic balances via insulated pipelines equipped with temperature probes. Both weights and volumes of top and bottom products were measured periodically during the experiments using electronic balance and volumetric flasks. An accurate overall mass balance for each run could be carried out from these measurements.

A typical pilot scale experiment started with CHA in the reboiler. After heating was initiated, AA was fed 1.5 meters below the top of the column (top of Stage 4) at a desired flow rate that was verified periodically by noting the change in weight of the AA feed tank. When the temperature profile across the column reached the boiling point of AA and AA appeared in the condenser, the CHE feed was started at the desired flow rate that was again monitored by noting feed tank weight change. The CHE was fed 0.5 meters from the bottom of the column (top of Stage 12). Temperature set point for heating tapes for the glass column were continuously monitored and changed when necessary to ensure an adiabatic column operation. Experimental steady state was assumed when temperature profile of the column changed by no more than  $\pm 0.5\text{K}$  over one hour, and when inlet and outlet flow rates within 5% of their set points. Typically, steady state was achieved after approximately 3-4 times the volume of liquid holdup in the reboiler was collected as bottom product. As steady state was approached and achieved, multiple sets of distillate and bottoms product samples and intermediate samples from ports along the column were collected for analysis. After the run, the steady state operation of the

column was verified by doing chromatographic analysis of the samples and conducting component mass balances across the column.

### 3.4. Results and Discussion

The complete set of steady state conditions for RD experiments conducted in pilot scale is shown in Table 3.2. In Run 2, CHE mass flow was  $11.9 \pm 0.4$  gm/min and AA flow was maintained such that AA:CHE feed mole ratio was about 1.1. Steady state was achieved in 2.5 hours and from bottom product analysis, it was found that CHE conversion was 100%. To achieve steady state with CHE conversion lower than Run 2, CHE flow was increased to  $25.7 \pm 0.5$  gm/min and AA:CHE feed mole ratio was maintained at 1.9 in Run 3. Steady state was achieved in 2 hours and 100% conversion of CHE was confirmed from bottom product analysis. CHE flow was further increased in Run 4 to  $22.1 \pm 0.5$  gm/min and feed mole ratio of AA:CHE was maintained at 1.1. In this run too, 100% CHE conversion was achieved. When CHE flow was further increased to  $30.9 \pm 0.5$  gm/min, keeping the feed mole ratio of AA:CHE at 1.1, steady state was not achieved even after 4 hours. In Runs 2-5, phase separation of water was observed in intermediate samples collected from the enriching section and from the top of the catalytic section. The AA feed used in the experimental runs was glacial acetic acid with approximately 600 ppm of water. While operating under total reflux conditions, as in Runs 2-5, buildup of water was observed in the column. In Runs 2-4, 100% conversion of CHE resulted in very high bottom temperature as a result of which, unreacted CHE and water were confined to the top part of the column. But when CHE feed rate was further increased in Run 5 such that complete conversion was not achieved, CHE was forced to flow out of the column as bottom product and steady state was not achieved.

Run 6 was discontinued because reboiler heater needed replacement. Similar observation as in Run 5 was made in Runs 7 and 8 during which steady state was not achieved. Under the experimental condition of total reflux in Run 2-8, there was no outlet for accumulated water or unreacted CHE. Therefore, taking CHE as distillate product and using a decanter after the condenser section to remove water was proposed for all further RD runs.

During Runs 2, 3 and 4, 100% CHE conversion resulted in high temperature conditions in the bottom section of the reactive zone that are favorable for CHE oligomerization. Run 4 temperature profile across the column is shown in Figure 3.2 as an example. To test the catalyst for any degradation, a catalyst packing from the bottom of the reactive section was taken out after Runs 2-5. Catalyst was removed by piercing a hole in the packing. This catalyst was washed with ethanol and a sample of the supernatant liquid was analyzed using GC-MS. Cyclohexene dimers (cyclohexene, 1-cyclohexyl and cyclohexene, 3-cyclohexyl) were found to be present in the solution. Catalyst activity by titration was found to be 1.4 eq/kg.cat. Catalyst activity on a packing just above the one that was pierced was 2.3 eq/kg.cat. These findings suggest that the bottom most catalyst packing was affected due to oligomerization of CHE. CHE oligomers can block pores or form new networks inside the pores of Amberlyst 70 catalyst which can be the reason for the observed lower activity. The cause of deactivation and a complete explanation to deactivation phenomenon is beyond the scope of this study. The catalyst packing in the top section of the reactive zone did not lose catalyst activity. The catalyst packings that were removed from the column were replaced in their respective positions before Runs 9a & 9b.

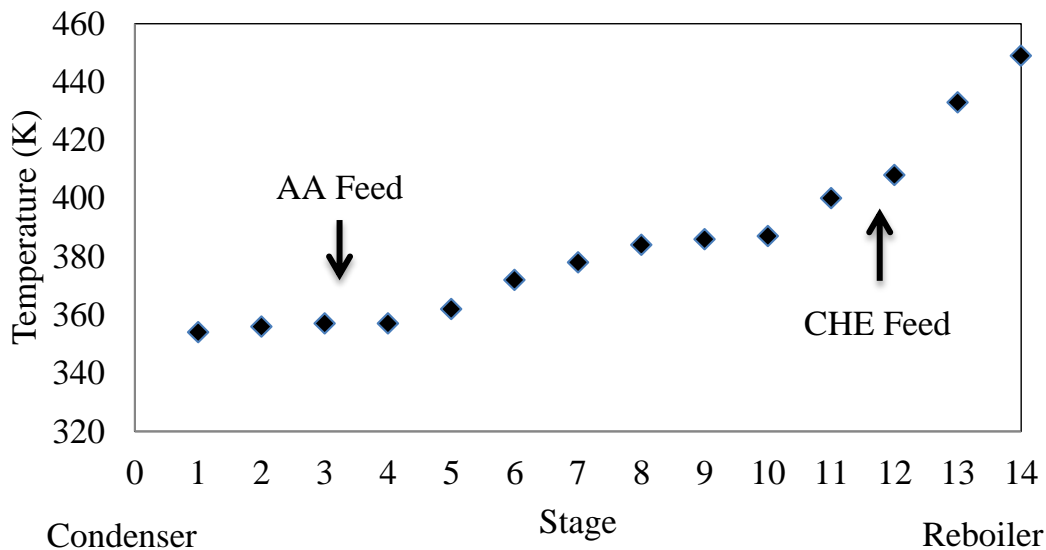


Figure 3.2: Temperature profile for Run 4.

### 3.4.1. Heat Integration Runs

In Runs 9a and 9b, the organic layer collected in the decanter was divided into two streams: top distillate and a reflux stream going back to the column. The bottom aqueous layer from the decanter was periodically drained and discarded. It is to be noted here that phase separation of water might not occur at steady state conditions during a given experimental RD run as water concentration is not high enough to cause phase separation and also because the column is not operated under total reflux conditions. The major function of the decanter during Runs 9a and 9b was to remove accumulated water in the column that was a result of the initial AA wash during column startup as described in the previous section.

Using a decanter to remove accumulated water in the column and distillate flow to accommodate incomplete CHE conversion, steady state was achieved in Run 9a. Details of the steady state operating conditions are given in Table 3.2. To study the effect of heat loss from a section of the column on CHE conversion as a first step in evaluating heat integration, heat insulation from the bottom-most catalytic section (Stages 10 and 11) was removed and a new

steady state was achieved as Run 9b. Distillate flow was adjusted to keep the reflux ratio the same as in Run 9a.

### **3.4.2. Energy balance for Runs 9a & 9b**

Complete energy balances based on 1) experimental material balance and 2) ideal material balance for Runs 9a & 9b are given in Tables 3.3a & 3.3b. Details of energy balance calculations for Runs 9a and 9b are given in Appendix B. It is to be noted here that this energy balance is sensitive to the uncertainties in top and bottom product compositions and also to the uncertainty in feed flow measurement (Table 3.3a). The heat loss using experimental material balance exceeded reboiler input which is unrealistic. An ideal material balance is computed using the experimental CHA yield during Runs 9a and 9b, with all other outlet component flows adjusted to close the material balance. From energy balance based on ideal material balance, shows a reasonable heat loss of 131 W to surroundings which is a reasonable fraction of reboiler input. Also, it was found that there is an extra heat loss of 135 W in Run 9b due to the removal of insulation from the bottom-most reactive zone in the column (stages 10 and 11 in the simulation). Since all the measurements were conducted on the same day and by the same operators using identical procedures, it can be assumed that uncertainty in energy balance of both the runs is the same and that the extra heat loss estimated from the energy balance for Run 9b is the result of insulation removal. These heat loss calculations are important for subsequent process simulations. Ideal vs. experimental material balance data for Runs 9a & 9b is given in Tables 3.4a & 3.4b.

Table 3.2: Summary of reaction conditions in pilot plant runs

Run code	Reboiler power (KW)	Feed flow (gm/min)		Product flow (gm/min)				CHE Conversion <sup>a</sup> %
		Top (AA)	Bottom (CHE)	Configuration	Distillate	Bottom	Bottoms temperature (K)	
2	0.93	8.9±0.4	11.9±0.4	Total reflux		21.6±0.4	446.15	100
3	0.82	25.7±0.5	18.5±0.6	Total reflux		45.2±1.5	416.15	100
4	0.82	16.1±0.4	22.1±0.5	Total reflux		37.7±1.8	451.15	100
5	0.80	24.6±1.2	30.9±0.5	Total reflux		55±2.5	not reached steady state	
7	1.0	25±1.2	29.5±1.5	Total reflux		54.8±2.0	not reached steady state	
8	0.93	18.5±1.5	17.5±1.5	Total reflux		35.5±2.0	not reached steady state	
9a	0.43	25.5±0.9	25.8±1.3	Distillate / decanter	8.7±0.3	45.5±1.5	386.15	46
9b	0.43	25.7±1.5	27.9±1.5	Distillate / decanter	3.44±0.4	48.5±1.5	376.15	40

a. Conversion based on CHA yield using ideal material balance

Table 3.3a: Energy balance from experimental material balance

Run code	Reboiler power (KW)	Condenser heat duty (kW)	CHE feed enthalpy (kW)	AA feed enthalpy (kW)	Distillate enthalpy (kW)	Bottom product enthalpy (kW)	Heat In (kW)	Heat Out (kW)	Heat loss(kW)
9a	0.43	0.29	-0.216	-3.440	-0.308	-3.638	-3.224	-3.658	0.434
9b	0.43	0.14	-0.213	-3.472	-0.127	-3.800	-3.254	-3.784	0.529
								Excess heat loss in Run 9b	0.096

Table 3.3b: Energy balance from ideal material balance

Run code	Reboiler power (KW)	Condenser heat duty (kW)	CHE feed enthalpy (kW)	AA feed enthalpy (kW)	Distillate enthalpy (kW)	Bottom product enthalpy (kW)	Heat In (kW)	Heat Out (kW)	Heat loss(kW)
9a	0.431	0.287	-0.216	-3.440	-0.269	-3.374	-3.224	-3.355	0.131
9b	0.431	0.143	-0.213	-3.472	-0.100	-3.563	-3.254	-3.520	0.266
								Excess heat loss in Run 9b	0.135

Table 3.4a: Ideal vs. Experimental material balance for Run 9a

	Ideal material balance				Experimental material balance	
	Mass flow (gm/min)				Mass flow (gm/min)	
	CHE feed	AA feed	Distillate	Bottoms	Distillate	Bottoms
CHE	28.3		7.865	7.260	6.808	6.416
AA		25.6	1.595	14.353	1.892	16.355
CHA			0	22.808	0	22.794
	Mass fraction				Mass fraction	
CHE	1.0		0.831	0.163	0.782	0.141
AA		1.0	0.169	0.323	0.218	0.358
CHA			0	0.513	0	0.499

Table 3.4b: Ideal vs. Experimental material balance for Run 9b

	Ideal material balance				Experimental material balance	
	Mass flow (gm/min)				Mass flow (gm/min)	
	CHE feed	AA feed	Distillate	Bottoms	Distillate	Bottoms
CHE	27.900		3.962	12.545	3.111	9.906
AA		25.770	0.523	16.918	0.619	18.794
CHA			0.000	19.723	0.000	19.706
	Mass fraction				Mass fraction	
CHE	1.0		0.883	0.255	0.834	0.204
AA		1.0	0.117	0.344	0.166	0.388
CHA			0	0.401	0	0.406

### 3.4.3. Simulation of RD column

Steady state simulations of pilot plant RD operation were performed using the equilibrium stage model in the RADFRAC column module in Aspen Plus (Version 7.1, Aspen Tech). The NRTL model was used to describe liquid phase non-ideality in the column. NRTL parameters were taken from Smith et al.,[20] (Appendix A.6). The column parameters used in simulations were chosen according to the pilot plant set up and are summarized in Table 3.5. Simulations for these pilot plant runs were also conducted. It should be noted that the simulation results for Runs 9a & 9b obtained in this study were compared to results obtained by Dr. John Prindle of Tulane University and were found to be in agreement with each other.

Table 3.5: RD column parameters used in process simulations

Parameter		
Total number of stages (N)		14
HETP – Height equivalent to theoretical plate (m)		0.5
Reactive stages	Catalytic (4-11)	7
	Non-catalytic (12-14)&(2-3)	5
Feed Stages	Acetic acid feed	4 on stage-liquid
	Cyclohexene feed	12 on stage-liquid
Catalyst holdup (kg/stage) (stages 4 to 11)		0.075
Product removal stage	Top	1
	Bottom	14
Properties Base method		NRTL-HOC
Amberlyst 70 Catalyst loading (kg/stage) in structured packings		0.075

### 3.4.3.1 Kinetic parameters for simulations

Experimentally validated pseudo-homogeneous kinetics discussed in Chapter 2 was used to model chemical reactions in the RD column. The units on the pre-exponential factors for forward reaction rates in Chapter 2 were  $\text{kmol.kg soln/kg.cat/min/m}^3 \text{ soln}$ . If the unit for hold-up is chosen as  $\text{kg.cat}$  in simulations for modeling CHE esterification, then the units for pre-exponential factor in Aspen Simulations need to be  $\text{kmol/kg.cat/sec}$ . By dividing units of pre-exponential factor (reported in Chapter 2) with the approximate density of solution ( $950 \text{ kg/m}^3$ ), kinetic parameters with units required for Aspen Plus simulations can be obtained. Modified kinetic parameters used in these simulations are shown in Table 3.6.

Table 3.6: Modified kinetic parameters used in process simulations

Reaction	CHE+AA $\rightarrow$ CHA	CHA $\rightarrow$ CHE+AA	Units
Pre-exponential factor	$5.87 \times 10^7$	$4.34 \times 10^{11}$	$\text{kmol/kg.cat/sec}$
Activation Energy	88100	118410	$\text{kJ/kmol}$

### 3.4.3.2 Algorithm selection

Aspen Plus offers a group of convergence algorithms and initialization methods for distillation problems based on chemical properties of components involved. For the cyclohexene esterification system – which may act as a two phase distillation when water is present in the system, it is apt to use the strongly non-ideal convergence algorithm in simulations. In preliminary simulations using the built-in power law for reaction kinetics, it was observed that two different solutions were obtained by choosing standard algorithm or strongly non-ideal algorithm in the simulation software. However, when a user subroutine was used for kinetics, both the algorithms gave identical result. This observation was sent to AspenTech support for evaluation. AspenTech support indicated that a user subroutine should not force a change in

algorithm contrary to our experience. Therefore, when using the built-in power law for kinetics, both solutions are valid mathematical solutions. The strongly non-ideal algorithm is used in all the simulations presented in this study. It is important to note here that, multiple valid steady-state results are feasible, and caution must be exercised while relying on simulations for design of RD column.

#### **3.4.4. Comparison of simulation and experimental results**

To match steady state temperature and composition profiles from simulations with the experimental profiles, a heat loss of 140 W was assumed on Stage 13 in both the Runs 9a & 9b, in addition to the heat loss due to insulation removal in Run 9b. Figures 3.3a and 3.4a show the experimental and simulated temperature profiles for Runs 9a and 9b. In a separate simulation, this heat loss to surroundings was assumed to be uniform across Stages 2-13 in the column for Run 9a. The resulting temperature profile for Run 9a is shown in Figure 3.3a. It is clear that the assumption of uniform heat loss across Stages 2-13 does not give profiles that match experiments, but the additional heat loss only on stage 13 does give results that agree with experimental results. Therefore, in all further simulations heat loss of 140 W was assumed on only on Stage 13.

CHE conversion obtained from simulations for Runs 9a & 9b were 45.2% and 40.3% respectively, which is very close to the experimentally obtained values. However, reboiler temperatures predicted from simulations for Runs 9a & 9b have an error of 10.1% and 7.6% respectively. The assumption of 140 W heat loss only on Stage 13 affects composition of CHA in the bottoms, resulting in a lower reboiler temperature. To examine this further, heat loss on stage 13 was varied between 90 and 140 W. For a 100 W heat loss on Stage 13 for Run 9a, CHE conversion was 53% and reboiler temperature matched within an error of 5% for Run 9a.

However, the experimentally determined yield for CHA in Run 9a was only 46%. Because it was desired to match the CHA yield in simulations and experiments, the heat loss of 140 W on Stage 13 was retained in all subsequent simulations. This value is very close to the experimental heat loss calculated using ideal material balance.

Composition profiles predicted by simulations for Runs 9a & 9b are presented in Figure 3.3b and 3.4b. The simulated compositions are in good agreement with experimental data except for Stage 1 in Run 9b. For the simulation of Run 9b (insulation removed on Stages 10 and 11), Stage 1 composition depends significantly on heat loss from Stages 10 and 11, because CHE is fed from Stage 12 and any heat loss from bottom sections of catalytic zone will reduce the amount of CHE going to the top of the column. Heat loss on Stages 10 and 11 was varied between 90 W and 140W. At a heat loss of 90 W, predicted stage 1 composition matches with the experimental composition but CHE conversion of 46% is obtained. However, the experimental yield in Run 9b matches closely with simulations when heat loss in Run 9b was set at 140 W. This is the reason for error in simulated Stage 1 compositions in Run 9b.

It is to be noted here that during Runs 9a & 9b, a decanter was used to remove water accumulated in the column. Water separation occurred when CHE feed was started. After a steady state was reached there was no separation of water inside the column or in the decanter. The simulations predicted no phase separation of water with 500 ppm of water in AA feed and 85 ppm of water in CHE feed. Therefore, a decanter unit operation was not used in simulations.

Using this experimentally validated simulation model, additional parametric simulations were conducted to examine, feed stage location, effect of heat loss & addition and effect heat transfer between the stages on CHE conversion and energy requirement. Results are discussed in the following sections.

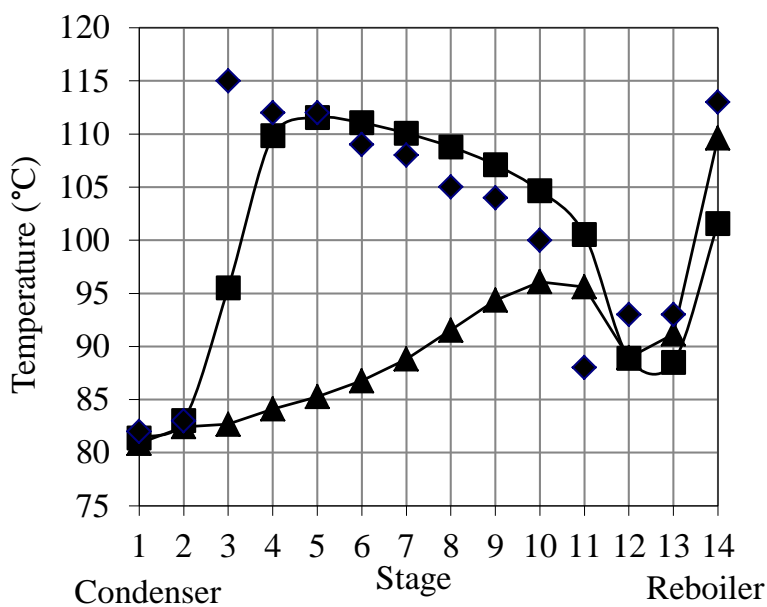


Figure 3.3a: Temperature profile Run 9a. (♦)- Experimental; (■) – simulation assuming heat loss on Stage 13; (▲) – simulation assuming heat loss uniformly across Stages 2-13.

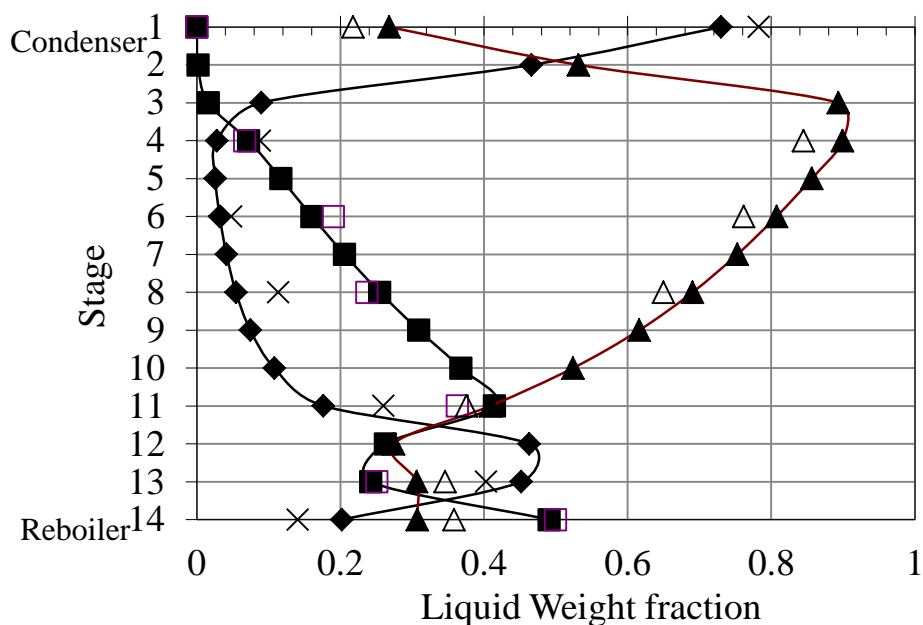


Figure 3.3b: Composition profile of Run 9a. (x)-CHE; (♦)- CHE simulated; (□)- CHA; (■)- CHA simulated; (Δ)-AA; (▲)- AA simulated

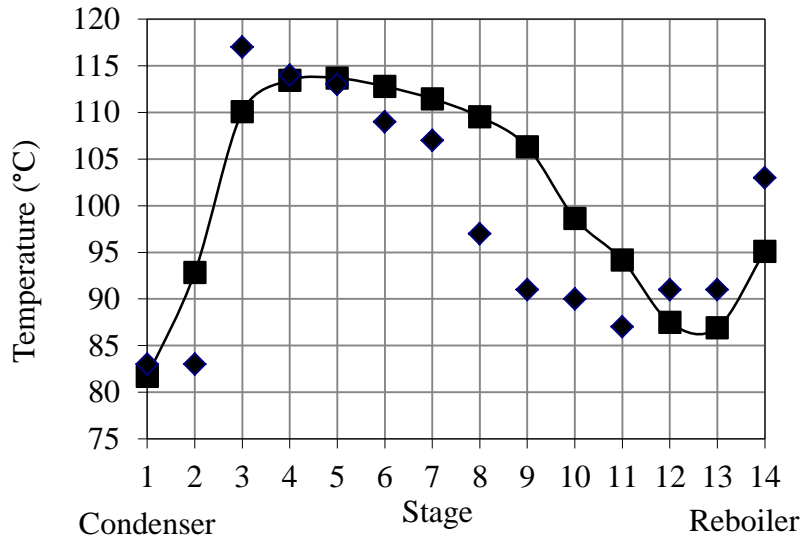


Figure 3.4a: Temperature profile Run 9b. (◆)- Experimental; (■) – simulation.

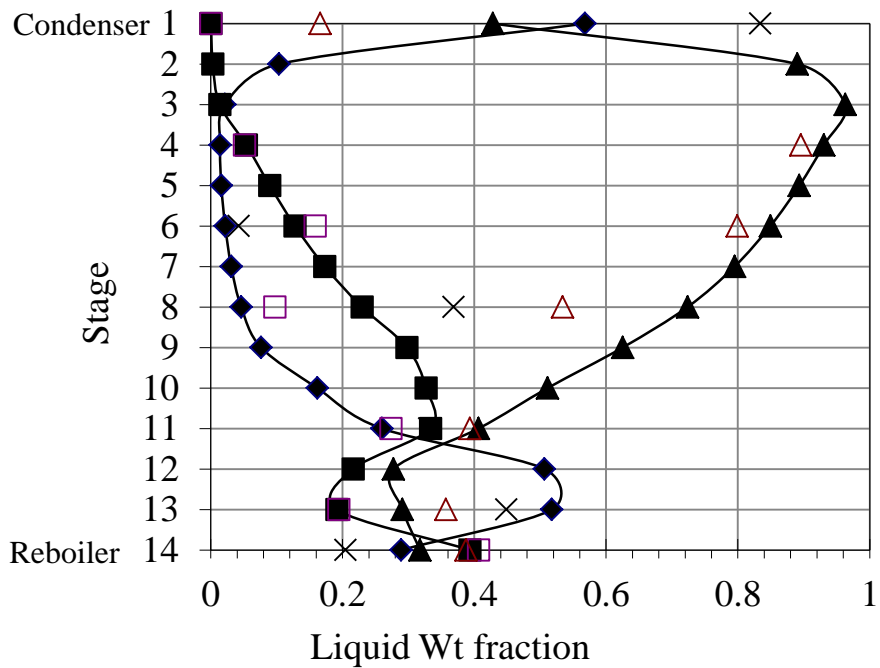


Figure 3.4b: Composition profile of Run 9b. (×)-CHE; (◆)- CHE simulated; (□)- CHA; (■)- CHA simulated; (Δ)- AA; (▲)- AA simulated.

### 3.4.5. Effect of feed stage on CHE conversion

The CHE feed stage was varied between Stages 4 and 12, keeping all other conditions the same as Run 9a to study its effect on CHE conversion. Similarly, CHE feed location was kept constant similar to Run 9a, but AA feed location was varied between stages 2 and 8. The results of these simulations are presented in Figure 3.5. The AA feed stage has no significant effect on CHE conversion. However, by changing CHE feed stage from stage 12 to stage 9, 56% conversion of CHE can be achieved instead of 45% conversion during experimental Run 9a. For CHE conversion of 46% obtained in experimental Run 9a, and with CHE feed on stage 9 simulations show that the reboiler duty can be decreased to 270 W from 430 W. This is an energy saving of approximately 37%, a result that highlights the importance of feed stage location in the RD column for this system.

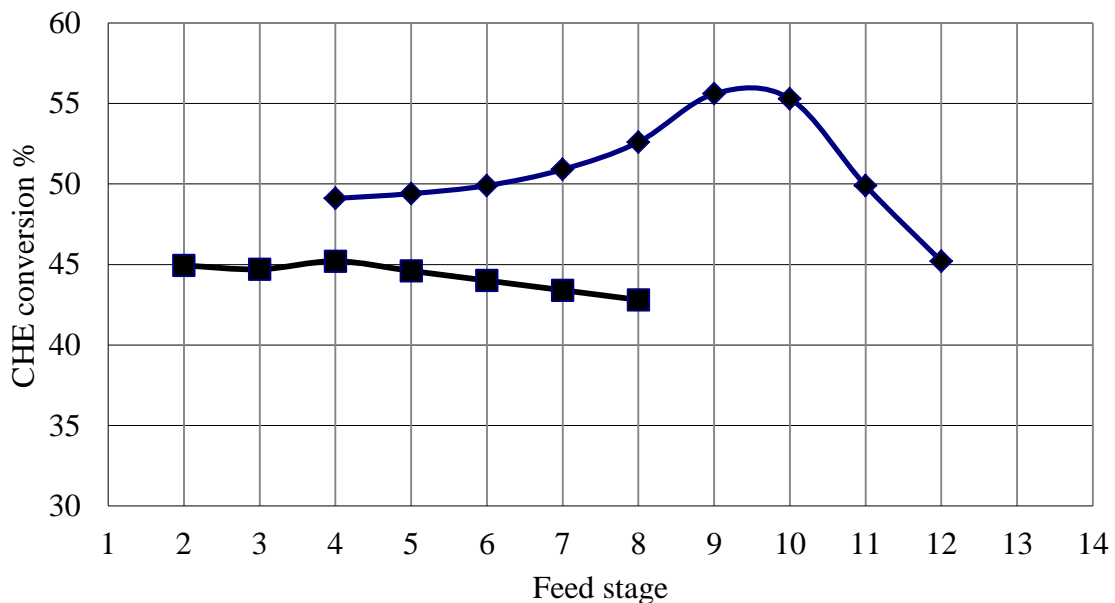


Figure 3.5: Effect of feed stage on CHE conversion for Run 9a. (◆)- Changing CHE feed stage (■) – Changing AA feed stage

### 3.4.6. Effect of heat loss on CHE conversion

Run 9b was conducted to determine the effect of heat loss on CHE conversion. From experiments, it is clear that by removing insulation on Stages 10 and 11, CHE conversion decreases from 46% to 40%. To study the effect of heat loss from all the other reactive stages, simulations were conducted assuming a heat loss of 140 W on pairs of stages (Stage 4&5, Stage 10&11 etc..) from Stage 4 to 11. Effect of heat loss from reactive stages on CHE conversion is shown in Figure 3.6. This heat loss is in addition to the 140 W heat loss assumed for simulations of Runs 9a & 9b on Stage 13. Heat loss from the top three reactive sections result in higher conversion than that achieved in Run 9a. Heat loss from the top reactive stages keeps maximum amount of CHE in the reactive zone which is the reason for this increase in conversion. When heat loss is moved to the lower catalytic zone, driving force for CHE vaporization is decreased and CHE exits as bottom product, thus decreasing CHE conversion.

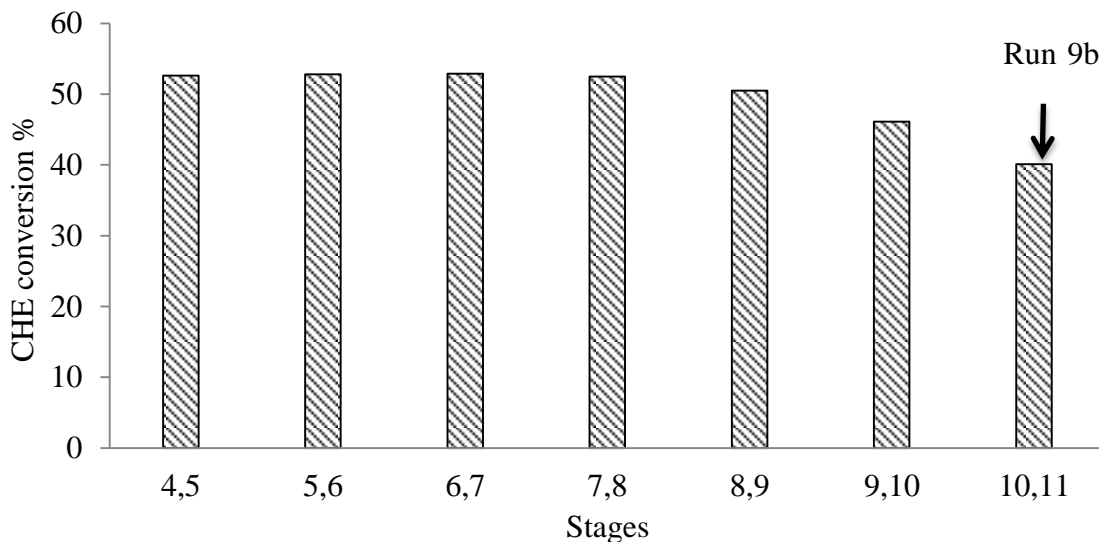


Figure 3.6: Effect of heat loss on CHE conversion for Run 9a.

### **3.4.7. Effect of heat addition on CHE conversion**

In Run 9b, effect of heat loss on CHE conversion was studied and simulated. In order to determine the effect of addition of heat to the catalytic section on CHE conversion, simulations were conducted at Run 9a conditions and adding 140 W heat to a pair of stages. It is clear from the results shown in Figure 3.7 that heat addition alone to any reactive section does not improve CHE conversion.

### **3.4.8. Effect of heat transfer between catalytic sections**

To determine the effect of using heat from one pair of stages on another pair of stages in the same RD column, simulations were conducted with a heat loss 140W on one pair of stages and heat addition of 140 W on another pair of stages in the catalytic section. All the reaction conditions were kept the same as Run 9a. Results are presented in Figure 3.8. When 140 W heat is transferred from Stages 4&5 to 10&11, CHE conversion increases to 51% compared to 46% in Run 9a. In order to achieve 46% conversion, reboiler duty can be decreased to 395 W resulting in an energy savings of 8.1%. Similarly, 140 W heat transfer from top of the catalytic section to bottom catalytic section resulted in improved CHE conversion. This result demonstrates the importance of using exothermic heat of reaction from top catalytic stages to improve energy efficiency of RD column.

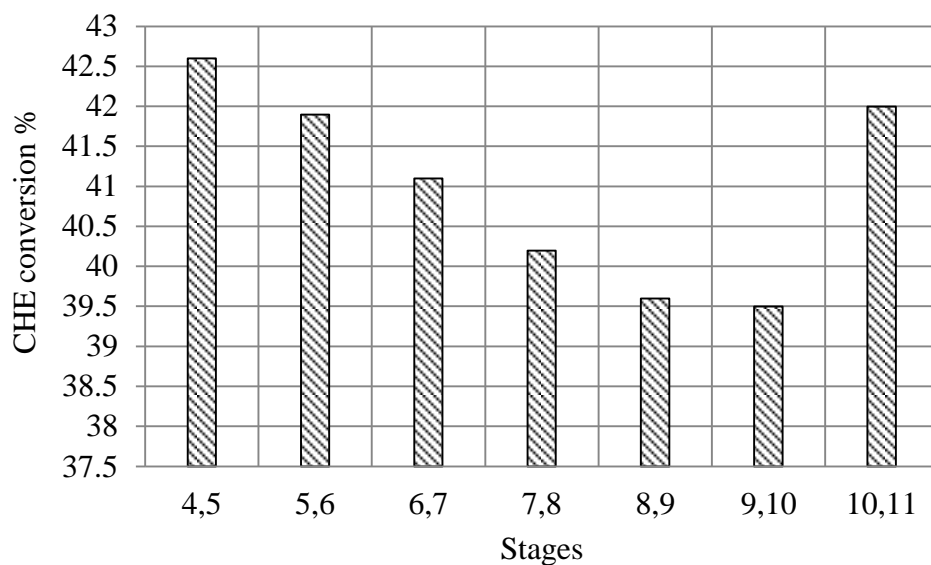


Figure 3.7: Effect of heat addition to stages in catalytic section on CHE conversion for Run 9a.

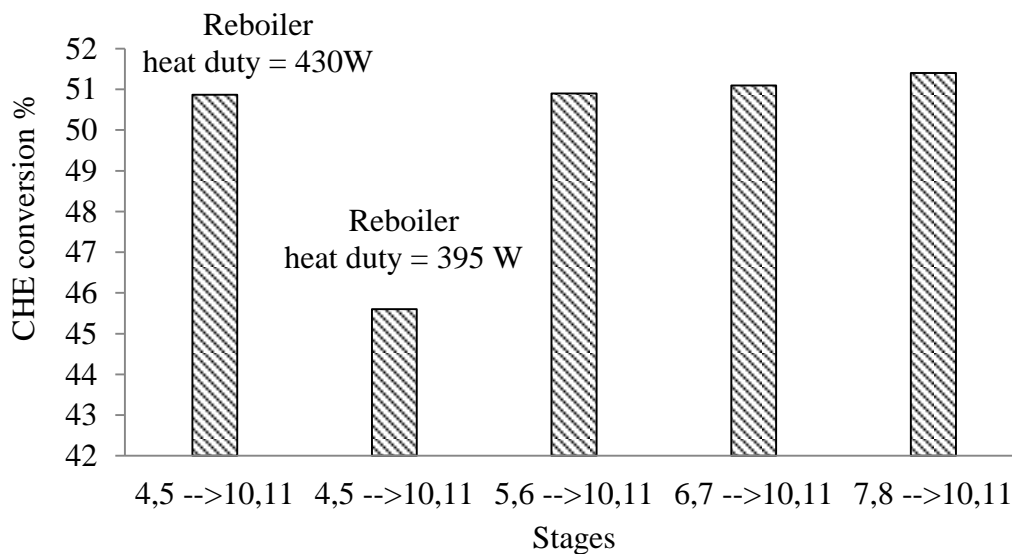


Figure 3.8: Effect of heat transfer between stages in catalytic section on CHE conversion for Run 9a.

### 3.5. Conclusions

The feasibility of producing CHA using RD was demonstrated on a pilot scale using a 6m glass column with Amberlyst 70 catalyst in KATAPAK-SP 11 packings. It was shown that 100% conversion of CHE can be achieved using RD. The effect of high temperature and high catalyst loading conditions that result in CHE oligomerization on the activity of catalyst was studied. It was found that CHE oligomerization decreases the activity of Amberlyst 70 catalyst present in bottom-most part of the catalytic zone. It is beneficial to tag all the catalyst packings so that the packings with decreased catalyst activity can be identified. It is also beneficial to conduct the RD experiments at lower pressure to keep the bottom catalytic zone temperature less than 373 K.

Pilot scale experiments were conducted to study the effect of heat loss from the reactive section of RD column on CHE conversion. Simulations with a simple equilibrium stage model using RADFRAC module in Aspen Plus based on experimentally obtained chemical kinetics, energy balance and vapor-liquid equilibria were performed. Steady-state simulation results were validated by experimental runs in a pilot plant column. This simple simulation model is adequate for an initial approximation of RD column performance for CHA production from CHE and AA.

The effect of feed stage, heat loss, addition and heat transfer between reactive stages was studied using the simulation model. It was found that for reactions with moderate thermal effect such as CHE esterification with AA, heat transfer from top of the catalytic zone to the bottom part of the catalytic zone yields energy efficient results. These simulations can be used as a guideline for designing experiments to determine the effect of external heat integration using RD column for cyclohexanol production from CHE.

## **APPENDIX B**

### 3.6. Appendix B

#### B.1: Reboiler duty calculation

In Runs 9a and 9b, current (I, amps) supplied to reboiler was measured. Resistance (R) of the reboiler specified by the manufacturer was 9.6  $\Omega$ .

$$\text{Power (P)} = I^2 * R \quad (\text{B.1.1})$$

Current measured during Runs 9a and 9b and corresponding power is given in Table

##### B.1.1.

Table B.1.1: Reboiler duty calculation

Run	Current ( Amps)	Power(kW)
9a	6.7	0.43
9b	6.7	0.43

#### B.2: Condenser duty calculation

Condenser heat duty was calculated by measuring temperature of cooling water entering and leaving the condenser and its flow rate. Heat duty ( $Q_c$ ), mass flow rate of water (m) and temperature difference between inlet and outlet temperatures ( $\Delta T$ ) are related as follows:

$$Q_c = m * c_p * \Delta T \text{ where } c_p \text{ is the specific heat capacity of water} = 4.179 \text{kJ/kg/K} \quad (\text{B.2.1})$$

The condenser heat duty calculated using Eq B.2.1 for Runs 9a & 9b are presented in Table B.2.1.

Table B.2.1: Condenser duty calculation

Run	Cooling Water in Temperature °C	Cooling Water out Temperature °C	Flow rate (gm/min)	Condenser duty (kW)
9a	24	32	517.24	0.29
9b	24	28	545.45	0.14

### B.3: Stream enthalpy calculation

The heat capacity for a component at temperature T is calculated as follows:

$$C_p = a + bT + cT^2 + dT^3 \quad (\text{B.3.1})$$

The values for a, b, c and d were obtained for each component from DIPPR database (Table B.3.1). Enthalpy of a stream at temperature T is calculated from the following equation.

$T_R$  is the reference temperature 298K.

$$H_T = \sum_{i=1}^n x_i * \left( \Delta h_{f,i}^o + \int_{T_R}^T \Delta C_{p,i} dT \right) \quad (\text{B.3.2})$$

Where  $x_i$  is the mole fraction of number of components in the stream,  $\Delta h_{f,i}^o$  is the heat of formation at standard state (298 K). Table B.3.1 gives standard heat formation data for components involved in this study. Enthalpy of streams calculated as described above was compared to the enthalpy of streams obtained from Aspen Plus simulations and they were in agreement with each other.

Table B.3.1: Standard heat of formation from DIPPR database

		Heat capacity constants (J/kmol/K)			
	$\Delta h_{f,i}^o$ Standard heat of formation J/kmol	a	b	c	d
CHE	-3.8E+07	105850	-60	0.68	0
AA	-4.8E+08	139640	-320.8	0.8985	0
CHA	-5.5E+08	121460	493.84	0	0

## **REFERENCES**

### 3.7. References

1. Stankiewicz, A.I. and J.A. Moulijn, *Process intensification: Transforming chemical engineering*. Chemical Engineering Progress, 2000. **96**(1): p. 22-34.
2. Schembecker, G. and S. Tlatlik, *Process synthesis for reactive separations*. Chemical Engineering and Processing, 2003. **42**(3): p. 179-189.
3. Lutze, P., R. Gani, and J.M. Woodley, *Process intensification: A perspective on process synthesis*. Chemical Engineering and Processing: Process Intensification, 2010. **49**(6): p. 547-558.
4. Victor H. Agreda; Lee R. Partin, b.o.K., Tenn, *Reactive distillation process for the production of methyl acetate*, U.S. Patent, Editor. 1984, Eastman Kodak Company, Rochester, N.Y.: USA.
5. Sharma, M.M. and S.M. Mahajani, *Industrial Applications of Reactive Distillation*, in *Reactive Distillation*. 2003, Wiley-VCH Verlag GmbH & Co. KGaA. p. 1-29.
6. Freund, H. and K. Sundmacher, *Process Intensification, 1. Fundamentals and Molecular Level*, in *Ullmann's Encyclopedia of Industrial Chemistry*. 2011, Wiley-VCH Verlag GmbH & Co. KGaA.
7. Freund, H. and K. Sundmacher, *Process Intensification, 4. Plant Level*, in *Ullmann's Encyclopedia of Industrial Chemistry*. 2011, Wiley-VCH Verlag GmbH & Co. KGaA.
8. Chakrabarti, A. and M.M. Sharma, *Cyclohexanol from cyclohexene via cyclohexyl acetate - catalysis by ion-exchange resin and acid treated clay*. Reactive Polymers, 1992. **18**(2): p. 107-115.
9. Steyer, F., H.r. Freund, and K. Sundmacher, *A Novel Reactive Distillation Process for the Indirect Hydration of Cyclohexene to Cyclohexanol Using a Reactive Entrainer*. Industrial & Engineering Chemistry Research, 2008. **47**(23): p. 9581-9587.
10. Steyer, F. and K. Sundmacher, *VLE and LLE Data for the System Cyclohexane + Cyclohexene + Water + Cyclohexanol*. Journal of Chemical & Engineering Data, 2004. **49**(6): p. 1675-1681.

11. Steyer, F. and K. Sundmacher, *VLE and LLE Data Set for the System Cyclohexane + Cyclohexene + Water + Cyclohexanol + Formic Acid + Formic Acid Cyclohexyl Ester*. Journal of Chemical & Engineering Data, 2005. **50**(4): p. 1277-1282.
12. Steyer, F. and K. Sundmacher, *Cyclohexanol Production via Esterification of Cyclohexene with Formic Acid and Subsequent Hydration of the Ester Reaction Kinetics*. Industrial & Engineering Chemistry Research, 2007. **46**(4): p. 1099-1104.
13. Kumar, R., et al., *Development of a Novel Catalytic Distillation Process for Cyclohexanol Production: Mini Plant Experiments and Complementary Process Simulations*. Organic Process Research & Development, 2011. **15**(3): p. 527-539.
14. Berg, L., *Separation of benzene from close boiling hydrocarbons by extractive distillation*. 1995, Berg, Lloyd: USA.
15. Osamu Mitsui, Y.F., *Process for producing cyclic alcohol*. 1986, Asahi Kasei Kogyo Kabushiki Kaisha: USA.
16. Huang, K., et al., *Reactive distillation design with considerations of heats of reaction*. AIChE Journal, 2006. **52**(7): p. 2518-2534.
17. Sundmacher, K.A.I., L.K. Rihko, and U. Hoffmann, *Classification of reactive distillation processes by dimensionless numbers*. Chemical Engineering Communications, 1994. **127**(1): p. 151-167.
18. Sun, J., K. Huang, and S. Wang, *Deepening Internal Mass Integration in Design of Reactive Distillation Columns, 1: Principle and Procedure*. Industrial & Engineering Chemistry Research, 2009. **48**(4): p. 2034-2048.
19. Steinigeweg, S. and J.r. Gmehling, *Esterification of a Fatty Acid by Reactive Distillation*. Industrial & Engineering Chemistry Research, 2003. **42**(15): p. 3612-3619.
20. Alex Smith, A.K., Carl T. Lira, Dennis J. Miller, *Phase equilibrium data for cyclohexene, acetic acid system*, Manuscript in preparation, Michigan State University.

## **Chapter 4: A Kinetic Model of the Amberlyst-15 Catalyzed Transesterification of Methyl Stearate with n-Butanol**

### **4.1. Summary**

An attractive approach to improving cold flow properties of biodiesel is to transesterify fatty acid methyl esters with higher alcohols such as n-butanol or with branched alcohols such as isopropanol. In this study, the reaction kinetics of Amberlyst-15 catalyzed transesterification of methyl stearate, a model biodiesel compound, with n-butanol have been examined. After identifying conditions to minimize both internal and external mass transfer resistances, the effects of catalyst loading, temperature, and the mole ratio of n-butanol to methyl stearate in the transesterification reaction were investigated. Experimental data were fit to a pseudo-homogeneous, activity-based kinetic model with inclusion of etherification reactions to appropriately characterize the transesterification system.

### **4.2. Introduction**

Biodiesel, which is composed mainly of fatty acid methyl esters (FAME) produced by transesterification of plant triglycerides, is a renewable fuel with a potential to be used along with or as a replacement for petroleum-based diesel [1]. However, in recent years biodiesel has had an image setback because of high feedstock costs and poor low temperature properties. Cold flow properties of biodiesel can be improved by winterization [2], which affects oxidative stability and cetane value of the fuel, by the alcoholysis of vegetable oils with longer and branched chain alcohols such as isopropanol and n-butanol [2-4], by the addition of cold flow improvers, or by modification of the fatty acid profile of the parent vegetable oils[5].

It is generally understood that biodiesel pour point and cloud point can be improved by using alcohols other than methanol to transesterify plant triglycerides. For example, we have shown that fatty acid butyl esters (FABE) mixed with regular biodiesel reduce cloud point temperature substantially without compromising cetane number [6]. A major difficulty in obtaining fatty acid esters with alcohols other than methanol is that the rate and thermodynamic favorability of base-catalyzed transesterification with higher alcohols is much lower than with methanol, such that reaction does not take place to an appreciable extent in many cases, and in others the advantageous phase separation obtained in methanol transesterification is lost [7].

Because of these challenges, we have developed an approach to producing higher alcohol esters of fatty acids by first making FAME via traditional base catalysis and then transesterifying FAME with other alcohols using heterogeneous catalysts to produce the desired esters. The use of heterogeneous catalysts offers the advantage of easier product purification, a water-free environment, reduced cost, and the potential to implement continuous processes such as reactive distillation.

Because no information is available in the literature describing the kinetics of fatty acid methyl ester transesterification with higher alcohols using heterogeneous catalysts, we have conducted and present here a kinetic study on the transesterification of methyl stearate (MS), a model compound representative of biodiesel and present in some plant oils to a significant degree [1], with n-butanol (BuOH) using Amberlyst 15 strong cationic exchange resin as catalyst. A pseudo-homogeneous, activity-based kinetic model that includes side reactions to form ethers is developed to properly describe the experimental data. This kinetic study lends insight into the use of heterogeneous ion exchange resin catalysts for fatty acid ester transesterification, and is useful for setting the direction of process design in biofuel operations.

### 4.3. Materials and methods

#### 4.3.1. Materials

n-Butanol (BuOH) (99.9%) was obtained from Mallinckrodt-Baker Inc. Methanol (MeOH) (>99.9%), ethyl caprylate (>99%), and methyl stearate (MS) (>96%) were purchased from Sigma-Aldrich. Impurities in methyl stearate included approximately 1.5 wt% non-saponifiable material and 2.5% unsaturated triglycerides, neither of which are expected to have a significant effect on methyl stearate conversion given their low concentration and the large excess of butanol used. For calibration of components in gas chromatography, high purity methyl stearate (>99%) and butyl stearate (BS) (>99%) were purchased from Nucheck-Prep, Inc. 1-Octanol (99%) was purchased from Spectrum Chemical.

Amberlyst 15 cation-exchange resin, which is a copolymer of divinylbenzene and styrene, was purchased from Sigma-Aldrich and washed with de-ionized water and ethanol and vacuum dried at 378K before its use in reaction. The acid site density of the washed resin, as measured by titration with 0.1 M NaOH, is 4.2 meq H<sup>+</sup>/g. Other physical and chemical properties of the resin catalyst are reported in the literature [8].

#### 4.3.2. Reactors

Kinetic experiments were carried out in a Parr 5000 Multi-Reactor system equipped with temperature control ( $\pm 0.2$  K) and stirring speed control (0-1400 rpm). Each of the six batch reactors has a 75-ml capacity with 1.5" internal diameter. Stirring was done using an octagonal, Teflon-coated magnetic stirring bar placed inside the reactor. Samples were taken at specified times during reaction via use of a syringe attached to a sample port. Samples were passed

through a 2  $\mu\text{m}$  filter attached to the end of the sample port to separate the sample solution from catalyst.

#### **4.3.3. Procedure**

In a typical experiment, measured quantities of MS and BuOH totaling approximately 55 mL, along with the Amberlyst-15 catalyst, were charged into the reactor. The reactor was sealed and heating was initiated. Once the desired temperature was reached, stirring was started and that time was taken as the zero reaction time. Typically, five or six 0.8 mL samples were taken at specified time intervals over a period of 24 hours of the reaction; these samples were taken by drawing a 2-3 mL aliquot of reaction solution into the syringe and then flushing it back into the reactor several times to clear the sample line and obtain a representative sample. Withdrawn samples were immediately diluted in 3.0 g of 1-octanol with 5-wt% of ethyl caprylate as the internal standard and refrigerated to ensure no further reaction took place before analysis.

#### **4.3.4. Analysis**

Samples were analyzed using a HP-5890 Series II gas chromatograph with flame ionization detector. Helium was used as carrier gas at a flow rate of 10 ml/min. An Aquawax-DA 30m column with 0.53mmID and 1.0 $\mu\text{m}$  film thickness was used to separate the components. Oven temperature was maintained initially at 313 K for 4.0 min, increased at 293 K/min to 523K, and then maintained at that temperature for an additional 4.0 min. Injector and detector temperatures were maintained at 523 K and 573 K, respectively. To determine MS, BS, DBE, BME compositions, chromatographic data were collected and processed using Peak Simple software. Mole fractions of BuOH, MeOH and water were determined by material balance. Calibration plots used in the sample analysis are presented in Appendix C.1.

## 4.4. Results and Discussion

### 4.4.1. Experimental evaluation of mass transfer resistances

The development of an accurate kinetic model requires that external and internal mass transfer resistances be minimized in reaction. To ensure that there were no external mass transfer resistances in methyl stearate transesterification, the reaction was carried out at several different agitation speeds while keeping all other conditions the same. Figure 4.1 shows that there is no significant effect of speed of agitation on the mole fraction of MS over the entire range of stirring rates. All further reactions were carried out at 1400 rpm.

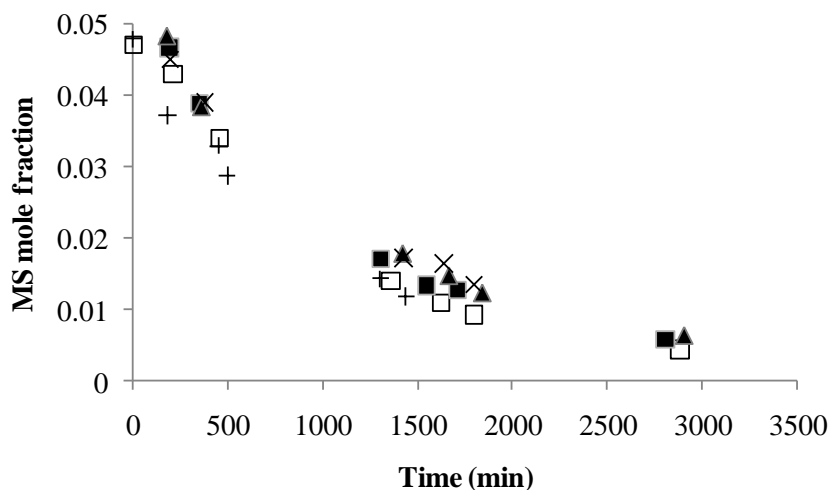


Figure 4.1. Effect of agitation speed on conversion rate of MS. Reaction conditions: BuOH:MS molar feed ratio = 20:1; catalyst loading = 5.6 wt%; reaction temperature = 363 K. ( $\square$  - 300 rpm;  $\blacksquare$  - 900 rpm;  $\blacktriangle$  - 1060;  $\times$  - 1230 rpm;  $+$  - 1460 rpm).

Internal mass transfer resistances were evaluated using different particle sizes of Amberlyst 15, obtained by grinding the resin into finer particles and screening for three different size fractions. These three fractions were evaluated under identical reaction conditions including constant catalyst active site loading. Figure 4.2 shows no significant difference in conversion rate for the different catalyst particle sizes, indicating that intra-particle diffusion resistances are negligible for Amberlyst 15-catalyzed transesterification.

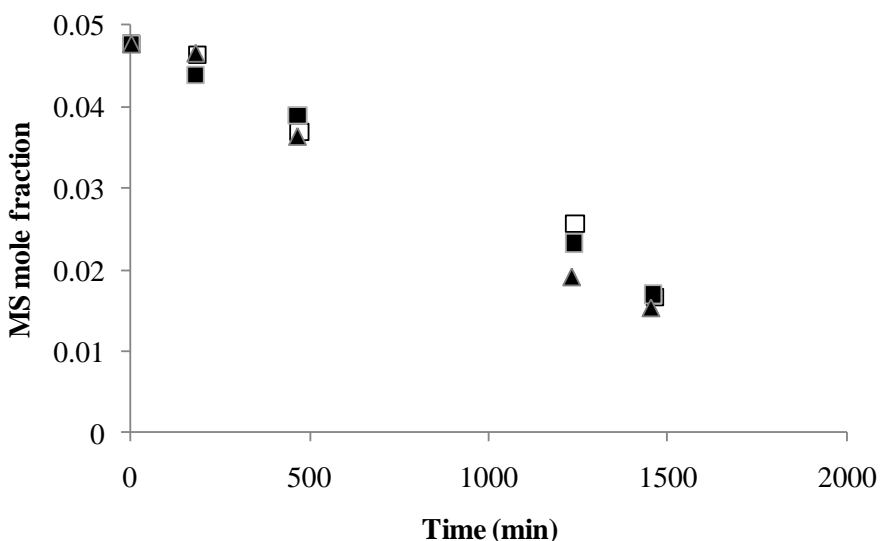


Figure 4.2. Effect of catalyst particle size on conversion rate of MS. Reaction conditions: BuOH:MS molar feed ratio = 20:1; Amberlyst 15 catalyst loading = 5.6 wt% or equivalent of 10.25 meq  $H^+$ ; reaction temperature = 363 K. ( $\square$  - 60-250  $\mu\text{m}$ ;  $\blacksquare$  - 250-500  $\mu\text{m}$ ;  $\blacktriangle$  - > 500  $\mu\text{m}$ ).

This absence of internal mass transport resistances is further corroborated via calculation of the observable modulus ( $\eta\phi^2$ ) for the initial reaction rate at 373 K for the largest resin particle size; the resulting value of  $\eta\phi^2 = 0.03$  is significantly below the range for which internal mass transport limitations are present. In the calculation, a value of the diffusivity of methyl stearate in n-butanol of  $2.3 \times 10^{-10} \text{ m}^2/\text{sec}$  was used from the Wilke-Chang equation. Based on these results, as-received Amberlyst 15 was used without size reduction for the kinetic studies.

#### 4.4.2. Kinetic model

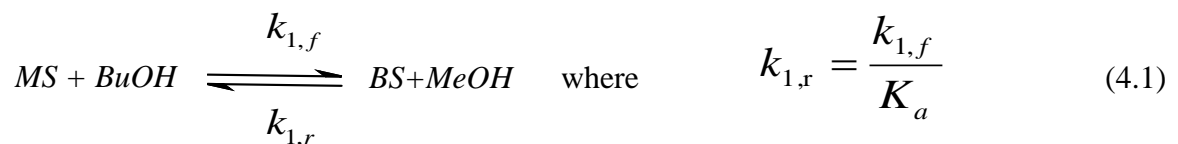
Since the effect of mass transfer resistances is negligible, a pseudo-homogeneous kinetic model can be applied to this system according to Helfferich [9]. To account for the thermodynamic non-ideality of the liquid solution in which reaction takes place, activity is used as a measure of species concentration instead of mole fraction. Although somewhat more complex to develop, the activity-based model generally provides a more accurate representation of species evolution during reaction.

##### 4.4.2.1. Calculation of activity coefficients

The UNIFAC group contribution method was used to calculate activity coefficients of the components present in each product sample taken during methyl stearate transesterification. The UNIFAC group volume ( $R_k$ ) and surface area ( $Q_k$ ) parameters were taken from Rao [10]. Tables C.2.1 and C.2.2 in Appendix C show the splitting of the groups and the UNIFAC group interaction parameters, respectively, used to calculate activity coefficients of each species in solution during reaction.

##### 4.4.2.2. Transesterification reaction

Methyl stearate transesterification with n-butanol can be represented by a single, reversible second order reaction.



The rate constant for the reverse reaction can be represented as

$$k_{1,r} = \frac{k_{1,f}}{K_a} \quad (4.2)$$

where  $K_a$ , the equilibrium constant for transesterification, has been determined experimentally (Section 4.4.2.4 below).

#### 4.4.2.3. Etherification reactions

Although it is always desirable to avoid side reactions [11], preliminary transesterification of MS with BuOH using Amberlyst 15 catalyst showed that dehydration of alcohols to form dibutyl ether (DBE) and butyl methyl ether (BME) was important at high temperatures and high catalyst loadings. The alcohol etherification reactions are given as



In prior studies, Gangadwala et al. [12] report that etherification of BuOH can be neglected at low temperatures (333-363 K). During our experiments, we observed formation of measurable quantities of DBE and BME as low as 353 K, with the quantities formed becoming important at higher temperatures. It is thus necessary to include these two reactions in the kinetic model for MS transesterification to properly describe the system dynamics. Methanol dehydration to dimethyl ether was not observed in reaction because the methanol to butanol mole ratio was low.

Dehydration of n-butanol to dibutyl ether and of n-butanol and methanol to methyl butyl ether can be considered irreversible because of the large equilibrium constant for the reaction [13].

#### 4.4.2.4. Reaction equilibrium

Transesterification reactions are typically characterized by equilibrium constants near unity. For the MS/BuOH system, experiments to measure the equilibrium constant of the reaction were conducted over a temperature range of 353 K to 385 K. The lower temperature range was chosen because side reactions such as irreversible etherification occur at higher temperature and higher catalyst loading, producing water which hydrolyzes the fatty acid ester and prevents the reaction from reaching transesterification equilibrium.

Equilibration reactions were carried out for time periods ranging from 24 to 96 hours, sufficient for the reaction to reach equilibrium. Final product compositions were determined and the activity-based equilibrium constant,  $K_a$  (Eq. 4.5), was calculated via inclusion of activity coefficients of the species in the mixture

$$K_a = \prod a_i^{v_i} = K_x K_\gamma = \prod x_i^{v_i} * \prod \gamma_i^{v_i} \quad (4.5)$$

where  $v_i$  is the stoichiometric coefficient for species  $i$  in the reaction.

The logarithm of the calculated  $K_a$  was plotted vs.  $1/T$  and an enthalpy of transesterification of approximately +2.4 kJ/mol was determined from the best fit of the data. However, the correlation coefficient ( $R^2$ ) was less than 0.1, so for practical purposes the reaction can be considered thermoneutral with a value of  $K_a$  of  $1.3 \pm 0.3$  over the temperature range investigated.

#### 4.4.2.5. Rate equations

The rate of consumption of methyl stearate in the reaction mixture is described by Eq. (4.6):

$$-\frac{dx_{MS}}{dt} = W_{cat} k_{1,f} \left( a_{MS} a_{BuOH} - \frac{a_{BS} a_{MeOH}}{K_a} \right) \quad (4.6)$$

$$a_i = \gamma_i x_i \quad (4.7)$$

Similar differential equations for other species present can be written as follows:

$$\frac{dx_{BS}}{dt} = W_{cat} k_{1,f} \left( a_{MS} a_{BuOH} - \frac{a_{BS} a_{MeOH}}{K_a} \right) \quad (4.8)$$

$$-\frac{dx_{BuOH}}{dt} = W_{cat} k_{1,f} \left( a_{MS} a_{BuOH} - \frac{a_{BS} a_{MeOH}}{K_a} \right) + W_{cat} k_2 a_{BuOH}^2 + W_{cat} k_3 a_{BuOH} a_{MeOH} \quad (4.9)$$

$$\frac{dx_{MeOH}}{dt} = W_{cat} k_{1,f} \left( a_{MS} a_{BuOH} - \frac{a_{BS} a_{MeOH}}{K_a} \right) - W_{cat} k_3 a_{BuOH} a_{MeOH} \quad (4.10)$$

$$\frac{dx_{DBE}}{dt} = W_{cat} k_2 a_{BuOH}^2 \quad (4.11)$$

$$\frac{dx_{BME}}{dt} = W_{cat} k_3 a_{BuOH} a_{MeOH} \quad (4.12)$$

$$\frac{dx_W}{dt} = W_{cat} k_2 a_{BuOH}^2 + W_{cat} k_3 a_{BuOH} a_{MeOH} \quad (4.13)$$

The temperature dependence of the rate constants can be expressed by the Arrhenius equation.

$$k_{1,f} = k_{1,f}^o \exp\left(-\frac{E_{1,f}}{RT}\right) \quad (4.14)$$

$$k_2 = k_2^o \exp\left(-\frac{E_2}{RT}\right) \quad (4.15)$$

$$k_3 = k_3^o \exp\left(-\frac{E_3}{RT}\right) \quad (4.16)$$

#### 4.4.2.6 Parameter identification and determination of rate constants

Six kinetic parameters,  $k_{1,f}^o$ ,  $E_{1,f}$ ,  $k_2^o$ ,  $k_3^o$ ,  $E_2$  and  $E_3$ , have to be determined to describe the reaction system. Values of the equilibrium constant  $K_a$  were calculated using Eq.4.5, giving values for the rate constant and activation energy of the reverse reaction in Eq.4.1.

A second order Runge-Kutta method, ODE23 in MATLAB 7.0, was used to numerically integrate the differential equations (4.6) and (4.8) – (4.13) describing the formation of each species in the system. Liquid phase mole fractions of all species were calculated over the course of each reaction using an initial set of kinetic parameters and were compared to the experimental data. Kinetic parameters were then optimized by minimizing the root mean square error between experimental and calculated mole fractions of all liquid phase components in all experiments according to Eq. (4.17) below. A total of 14 experiments containing more than 80 data points were fitted to the kinetic rate expressions.

$$F^2_{\min} = \frac{\sum_{\text{samples}} (x_{i,\text{cal}} - x_{i,\text{exp}})^2}{n_{\text{samples}}} \quad (4.17)$$

The kinetic parameters that result in the lowest root mean square error are given in Table 4.1. The final value of  $F^2_{\min}$ , determined for the kinetic parameters reported, is 0.166. Mole fraction profiles of components calculated from these kinetic parameters are shown as continuous lines in Figures 4.3 – 4.6 that follow.

Calculated mole fractions of each component were compared to those from experiment by calculating the average of the absolute value of the difference between experimental and calculated mole fractions at all data points within each experiment, represented on both a relative (Eq. 4.18) and an absolute (Eq. 4.19) basis. The F values below give a measure of the fit of the kinetic model to the experimental data.

$$F_{rel} = \frac{\sum_{samples} \left| \frac{x_{i,cal} - x_{i,exp}}{x_{i,exp}} \right|}{n_{samples}} \times 100\% \quad (4.18)$$

$$F_{abs} = \frac{\sum_{samples} |x_{i,cal} - x_{i,exp}|}{n_{samples}} \quad (4.19)$$

Table 4.1: Kinetic model parameters

Parameter	Value	Units
$k_{1,f}^0$	$3.21 \times 10^9$	kg <sub>soln</sub> /(kg <sub>cat</sub> ·min)
$E_{1,f}$	82500	kJ/kmol
$k_2^o$	$1.56 \times 10^{10}$	kg <sub>soln</sub> /(kg <sub>cat</sub> ·min)
$k_3^o$	$3.12 \times 10^{10}$	kg <sub>soln</sub> /(kg <sub>cat</sub> ·min)
$E_2$	98800	kJ/kmol
$E_3$	92500	kJ/kmol

### 4.4.3. Results

Experiments were carried out to study the effect of catalyst loading, temperature, and BuOH:MS mole ratio on the rate of Amberlyst 15-catalyzed transesterification. Table 4.2 summarizes the reaction conditions and the differences between experimental and predicted MS mole fractions in each experiment. Table C.3.1 in Appendix C shows the predicted differences in calculated and experimental mole fractions for BuOH, MeOH and BS. Mole fraction profiles of all kinetic experiments comparing experimental and predicted data are presented in Appendix C.3.

Table 4.2: Summary of experimental conditions and calculated mole fraction differences for MS

Run	Figure number	Molar feed ratio BuOH: MS	Catalyst loading (wt %)	Temperature (K)	$F_{rel}$ for MS (Eq. 4.18)	$F_{abs}$ for MS (Eq. 4.19)
1	C.2.1	20	5.6	343	6	0.0022
2	C.2.2	20	5.6	353	4	0.0014
3	C.2.3	20	5.6	363	4	0.0012
4	C.2.4	20	2.8	363	4	0.0012
5	C.2.5	20	1.4	363	4	0.0017
6	C.2.6	10	4.8	363	2	0.0015
7	C.2.7	10	4.8	363	7	0.0038
8	C.2.8	5	4.8	363	2	0.0027
9	4.4a	20	4.8	363	5	0.0010
10	C.2.9	30	4.8	363	13	0.0018
11	C.2.10	20	4.8	363	6	0.0020

Table 4.2 (cont'd)

12	C.2.11	20	2.8	373	10	0.0022
13	4.4b	20	4.8	373	14	0.0018
14	C.2.12	20	5.6	373	22	0.0036

#### 4.4.3.1. Effect of catalyst loading

A control experiment without Amberlyst 15 catalyst present showed no transesterification over 24 hr reaction time. The effect of catalyst loading from zero to 5.6 wt% of solution on the rate of MS transesterification was examined at 363 K and 373 K with a BuOH:MS initial mole ratio of 20:1. The initial rate of each reaction was determined by taking the slope at  $t=0$  of a curve that best represents the mole fraction vs. time data. The plot of this initial rate ( $dX_{MS}/dt|_{t=0}$ ), versus catalyst loading, given in Figure 4.3a, is linear, showing that external mass transfer resistances are absent and that the catalyst is effectively distributed and active throughout the reaction solution. Figure 4.3b shows the profiles of mole fraction vs. time at 363K for three catalyst loadings; the kinetic model accurately predicts rate as a function of catalyst loading.

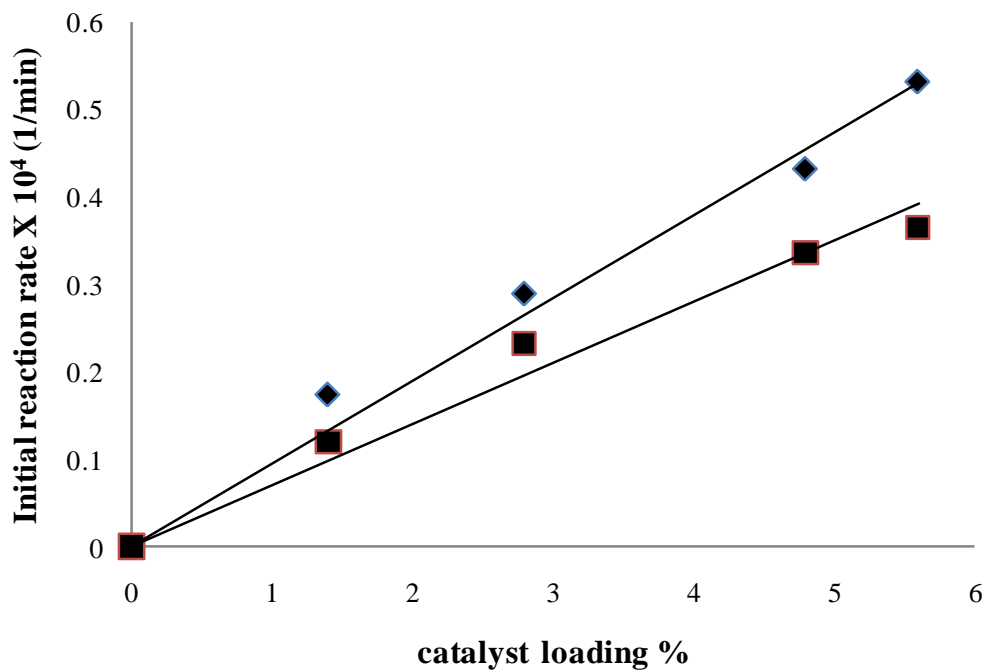


Figure 4.3a. Initial MS transesterification rate vs. catalyst loading (wt%). BuOH:MS molar feed ratio = 20:1. ( $\times$ ) – 373 K; ( $\blacksquare$ ) – 363 K. Solid line represents best fit of the data.

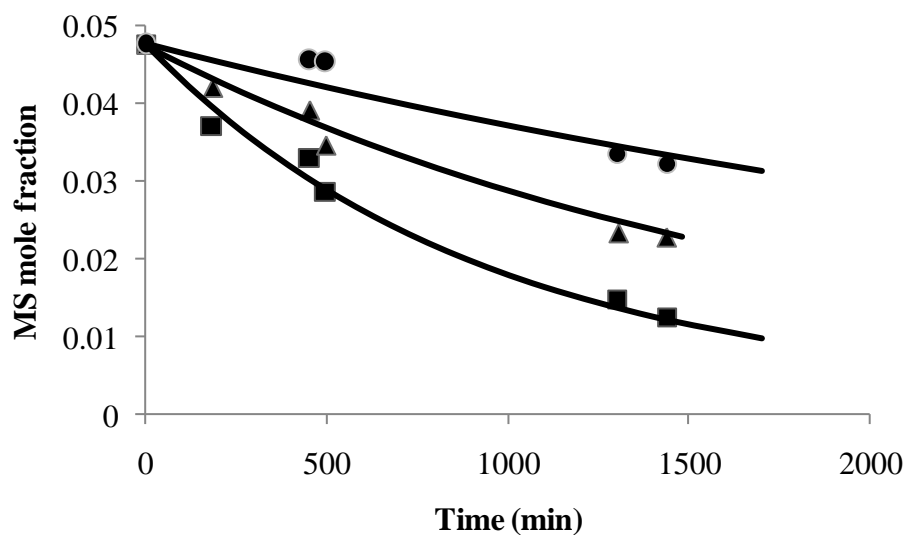


Figure 4.3b. Effect of catalyst loading (wt%) on the conversion rate of MS. Reaction conditions: BuOH:MS molar feed ratio = 20:1; reaction temperature = 363 K. ( $\blacksquare$ ) – 5.6 wt%; ( $\blacktriangle$ ) – 2.8 wt%; ( $\bullet$ ) – 1.4 wt%.

#### 4.4.3.2. *Effect of temperature*

The effect of increasing reaction temperature on the transesterification reaction from 343 K to 373 K at an initial BuOH:MS molar ratio of 20:1 was studied. Etherification of alcohols is slow below 363 K but is important at or above 373 K. Figures 4.4a and 4.4b show the evolution of all species in transesterification over time; etherification of BuOH with MeOH to form BME causes the MeOH mole fraction to fall below that of butyl stearate at longer times and even to decrease at 373 K (Figure 4.4b). Figure 4.5 shows the increasing rate of MS conversion with increasing reaction temperature over the temperature range 343-363 K. The calculated activation energy for methyl stearate transesterification (82,600 kJ/kmol, Table 4.1), is much higher than the value of 40,900 kJ/kmol reported for transesterification of methyl acetate to butyl acetate over Amberlyst 15 [14]. The activation energies for ether formation (98,800 kJ/kmol and 92,500 kJ/kmol) are similar to the value ( $E_a = 102,600$  kJ/kmol) we reported for diethyl ether formation in an earlier publication [15].

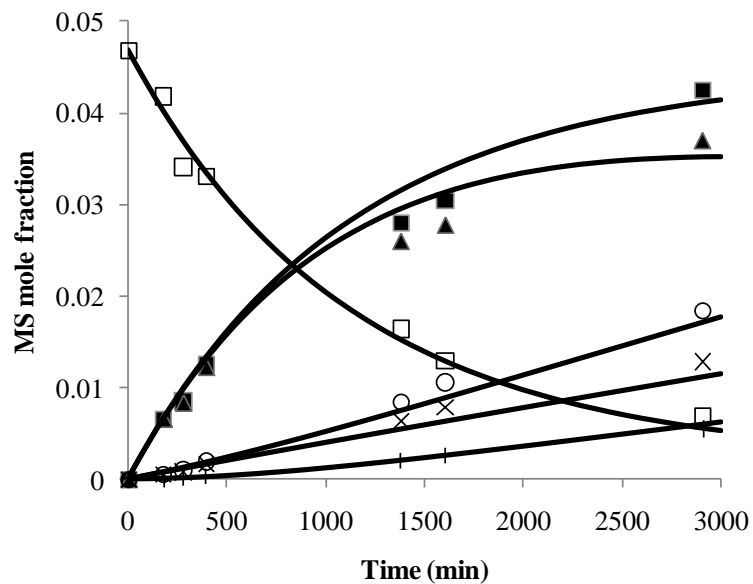


Figure 4.4a. Mole fraction profiles of species present in MS transesterification reactions at 363 K. Reaction conditions: BuOH:MS molar feed ratio = 20:1; catalyst loading = 4.8 wt%. (-□- - MS; -■- - BS; -▲- - MeOH; -×- - DBE; +- - BME; -○- - W).

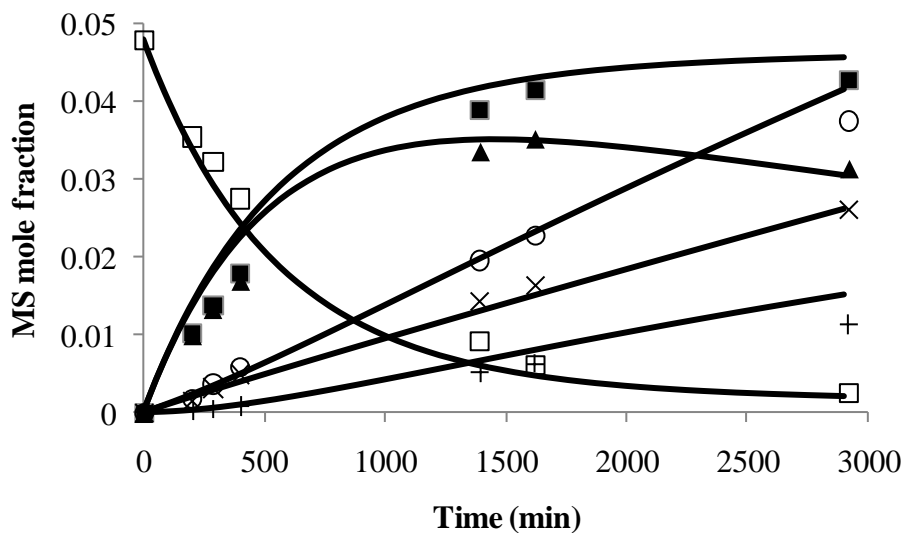


Figure 4.4b. Mole fraction profiles of species present in MS transesterification reactions at 373 K. Reaction conditions: BuOH:MS molar feed ratio = 20:1; catalyst loading = 4.8 wt%; (-□- - MS; -■- - BS; -▲- - MeOH; -×- - DBE; +- - BME; -○- - W).

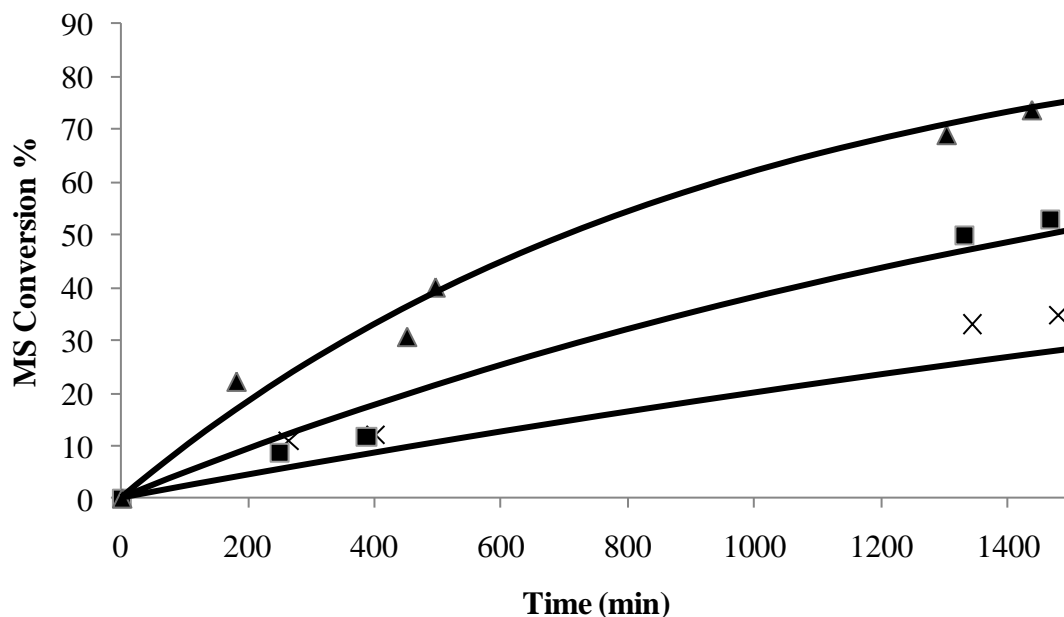


Figure 4.5. Effect of temperature on the conversion rate of MS. Reaction conditions: BuOH:MS molar feed ratio = 20:1; catalyst loading = 5.6 wt%. (x) –343 K ; (■) – 353 K; (▲) –363 K.

#### 4.4.3.3. Effect of initial mole ratio

The results of varying BuOH:MS initial molar ratio from 5:1 to 20:1 at 363 K and 4.8 wt% catalyst loading is shown in Figure 4.6. Both the rate of MS conversion and the ultimate equilibrium conversion increase at higher BuOH:MS molar ratios.

#### 4.4.3.4. Control experiment with $H_2SO_4$ as catalyst

A single control experiment was carried out (363 K, 20:1 BuOH:MS) for MS transesterification with BuOH using 1.2 wt%  $H_2SO_4$  as catalyst; this is the same  $H^+$  loading as 5.6 wt% Amberlyst 15 used in many experiments. The reaction reached 50% conversion after 15 minutes; this corresponds to a rate about 250 times faster than the rate observed with Amberlyst 15 catalyst.

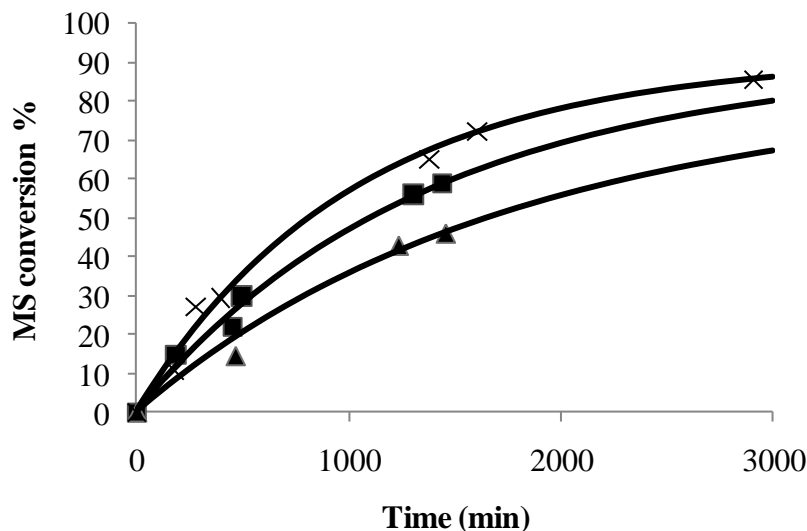


Figure 4.6. Effect of BuOH:MS molar feed ratio on MS conversion. Reaction conditions: Temperature = 363 K; catalyst loading = 4.8 wt%. (-▲- - 5:1; -■- - 10:1; -×- - 20:1).

#### 4.4.4. Discussion

The kinetic model effectively predicts the rate of methyl stearate transesterification and concurrent ether formation over the range of conditions examined. The ether formation reactions add a valuable component to the model in describing loss of BuOH.

We have compared the forward rate constant of MS transesterification with several other BuOH transesterification studies presented in the literature. Results of this comparison, with all rates on a per kmol  $H^+$  (catalyst) basis, are given in Table 4.3. As described above, the  $H_2SO_4$ -catalyzed rate of MS transesterification is about 250 times faster than the Amberlyst 15-catalyzed rate under identical conditions. The transesterification of methyl acetate with butanol over Amberlyst 15, reported by Bozek-Winkler et al., [14] is 60-70 times more rapid than MS transesterification. We also compared our forward transesterification rate constant to that of Friedman et al. [7] for transesterification of soy triglycerides to diglycerides, and monoglycerides to glycerol, with butanol using  $H_2SO_4$ . On the same basis, triglyceride transesterification with

H<sub>2</sub>SO<sub>4</sub> is about 30 times faster than MS transesterification with A-15, but about 1/8 the rate of MS transesterification with H<sub>2</sub>SO<sub>4</sub>.

The difference in rates between the systems reported in Table 3.3 with Amberlyst 15 catalyst is attributable to both the different molecular size and polarity of methyl stearate vs. methyl acetate. Bozek-Winkler et al., [14] state that low polarity molecules can complicate the characterization of kinetics in Amberlyst resins; it is likely that this effect comes into play in our system, yet the pseudo-homogeneous model fits our experimental data adequately.

Our results with Amberlyst 15 and with H<sub>2</sub>SO<sub>4</sub> as catalyst show just how significantly the molecular properties of methyl stearate and butanol influence conversion rate over the heterogeneous catalyst. Even though Amberlyst 15 does not give rates as rapid as H<sub>2</sub>SO<sub>4</sub> for this reaction, the kinetic results presented here do provide an activation energy and a rate expression as well as an insight into byproduct formation. This information should be useful to other researchers in developing advanced biofuel concepts from triglyceride feedstocks.

Table 4.3: Comparison of transesterification forward rate constants at 363 K

Reaction	Catalyst	k <sub>f</sub> (363 K) (kg soln/kmol H <sup>+</sup> /hr)	E <sub>a</sub> (kJ/mol)	Reference
MS + BuOH	Amberlyst 15	6.1 x 10 <sup>1</sup>	82,500	this work
MS + BuOH	H <sub>2</sub> SO <sub>4</sub>	1.6 x 10 <sup>4</sup>	-	this work
Methyl acetate + BuOH	Amberlyst 15	4.0 x 10 <sup>3</sup>	40,890	[14]
Triglyceride + BuOH	H <sub>2</sub> SO <sub>4</sub>	1.9 x 10 <sup>3</sup>	62,000	[7]
Monoglyceride + BuOH	H <sub>2</sub> SO <sub>4</sub>	4.6 x 10 <sup>3</sup>	63,100	

From the forward rate constant, the initial turnover frequency (TOF) of MS transesterification on the acidic Amberlyst 15 sites at 363 K with BuOH:MS at 20:1 is 0.04 kmol MS/kmol H<sup>+</sup>/hr. This low value is another indication that Amberlyst 15 is less than an ideal choice for methyl stearate transesterification.

The experimental data collected in this work has also been fitted to a mole fraction-based model, where activity of each species is replaced by its mole fraction. When this mole fraction model is applied, similar rate constants are obtained and the value of the objective function (Eq. 17) is 0.15, slightly smaller than the value of 0.166 obtained with the activity model. However, the value of  $K\gamma$ , the ratio of product-to-reactant activity coefficients (Eq. 4.5) at the experimental conditions, ranges from 1.3 to 1.5, signifying that there is significant nonideality in this system. Because the value of  $K\gamma$  differs significantly from unity, the activity-based model is preferred and will offer a better fit of data over a range of conditions broader than that investigated here where nonidealities may even more strongly predominate.

#### 4.5. Conclusion

The effect of temperature, reactant molar ratio, and catalyst loading on the rate of Amberlyst 15-catalyzed transesterification of MS with BuOH has been experimentally investigated. The dependence of the transesterification equilibrium constant on temperature was also examined. Based on the experimental results, a second-order, activity-based kinetic model was developed and optimized to fit the data. The model describes the transesterification reasonably well over the range of 343-373 K, including the formation of ethers at higher temperatures. The results clearly show the challenges associated with using Amberlyst 15 catalysts for transesterification of larger fatty acid esters.

## **APPENDIX C**

## 4.6. Appendix C

### *C.3.1 Calibration plots for sample analysis*

Reaction samples were diluted in 1-octanol with 5 wt% ethyl caprylate (1-OC+EC) solvent. To determine the weight of each component in the reaction sample, individual calibrations were carried out. Measured quantity of each component was mixed with a known amount of solvent such that the component is 10% by weight in the solution. The calibration samples were made to cover the whole range of mass fraction that is expected in the reaction samples. These samples were analyzed in a gas chromatograph as described in Section 4.3.4. From the chromatograms, area for each component is obtained. From this data, area for a known weight of component and area for fixed amount of EC is known. The ratio of area of component to that of EC is plotted against the ratio of known weight of component to that of EC. This plot is typically a straight line passing through the origin. The slope of this line is the “calibration factor”.

Weight of individual components is unknown in reaction samples. From chromatograms, area of EC and areas of individual components are obtained. Weight of EC is known from the amount solvent used to dilute the reaction sample. Using the calibration factor for each component, weight of the component is obtained. Figures C.1.1 to C.1.6 show the calibration plots used in this study.

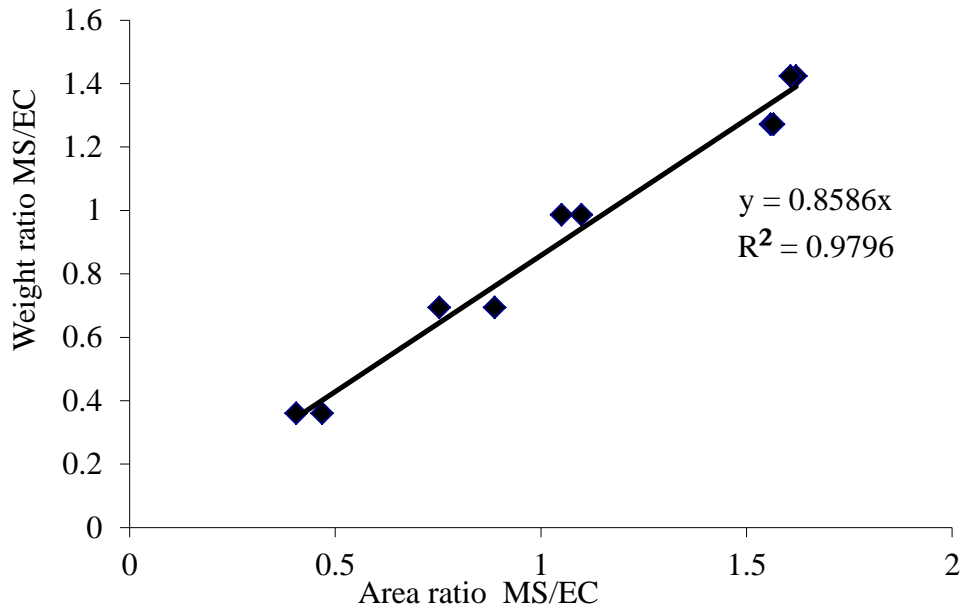


Figure C.1.1: Calibration plot for Methyl stearate (MS)

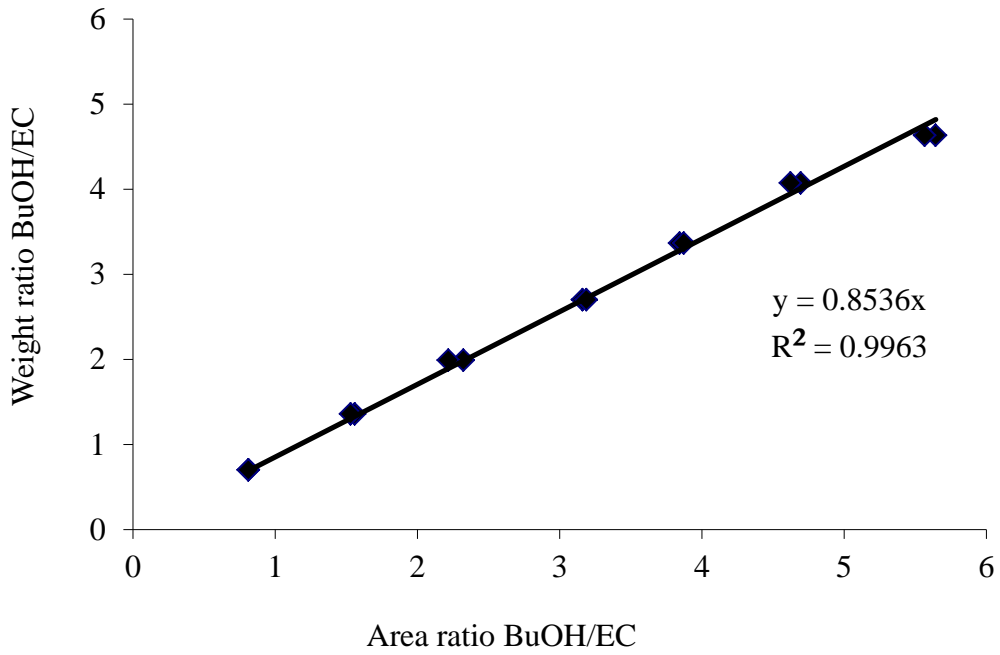


Figure C.1.2: Calibration plot for 1-Butanol (BuOH)

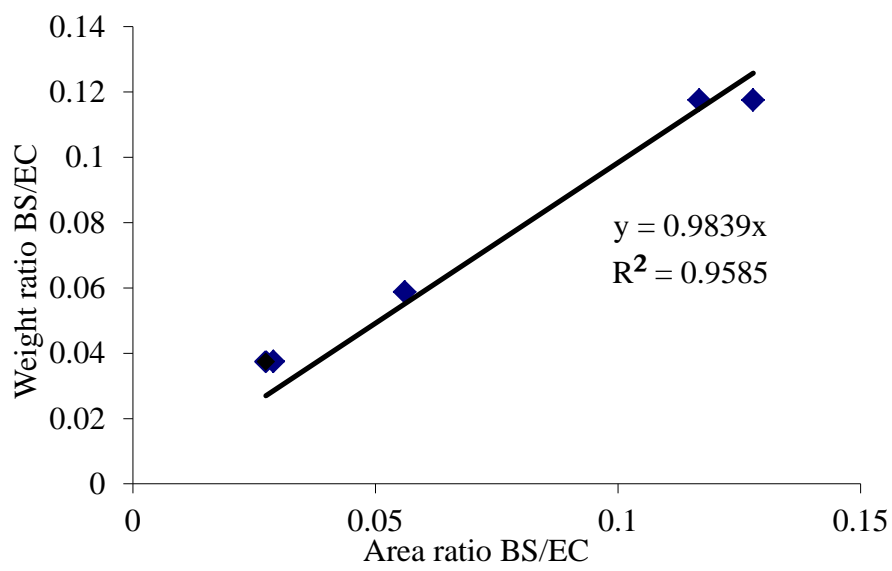


Figure C.1.3: Calibration plot for Butyl stearate (BS)

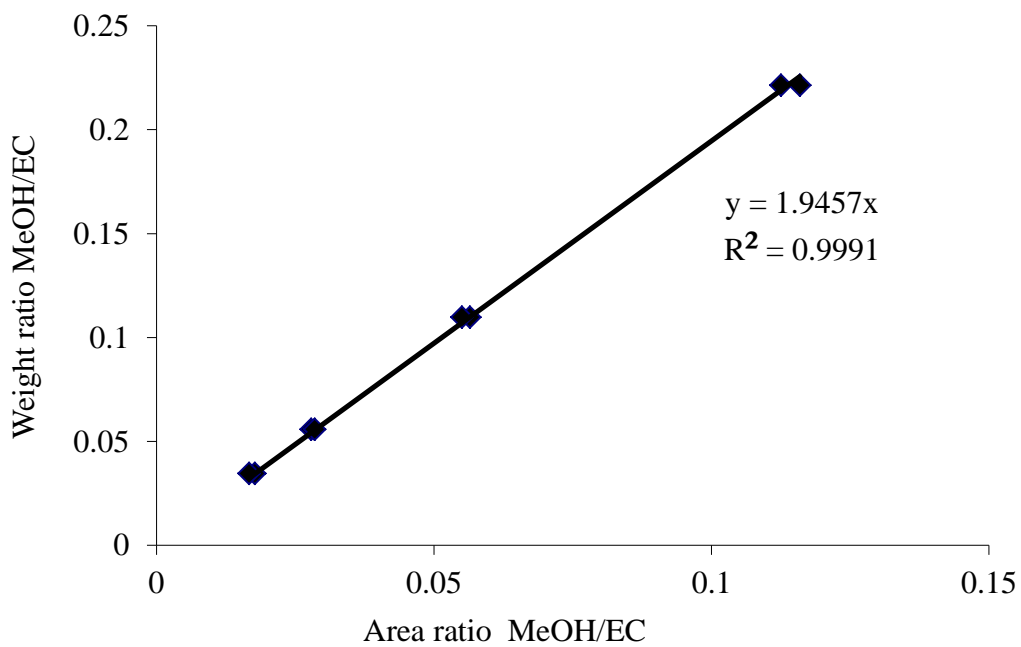


Figure C.1.4: Calibration plot for Methanol (MeOH)

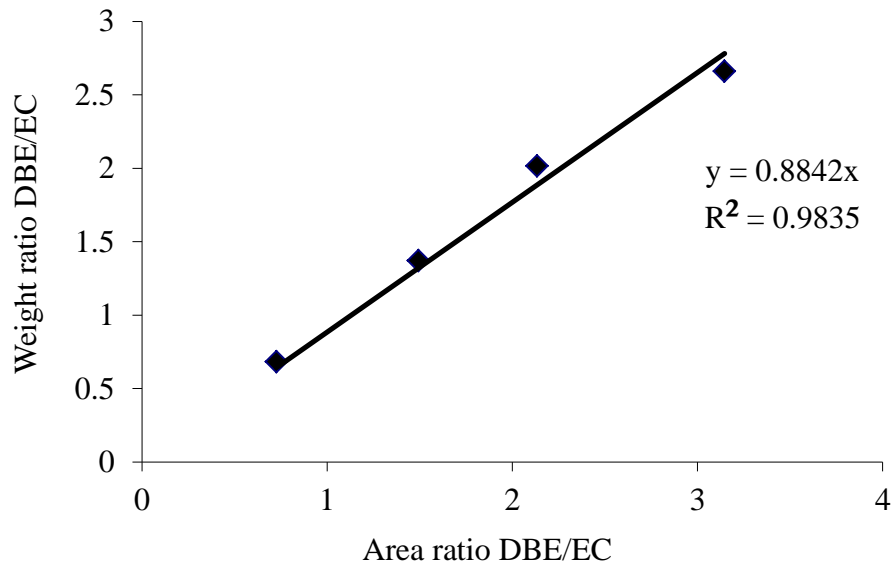


Figure C.1.5: Calibration plot for Dibutyl ether (DBE)

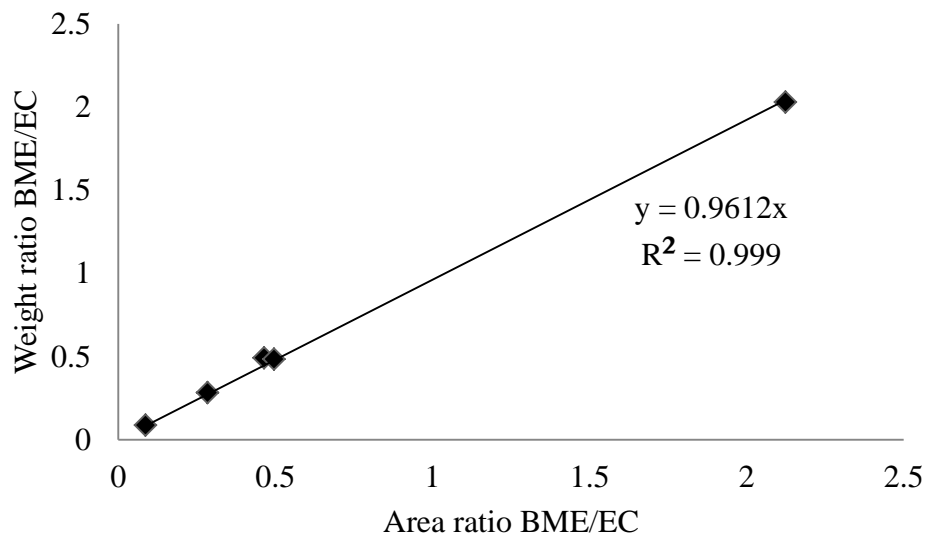


Figure C.1.6.: Calibration plot for Butyl methyl ether (BME)

Table C.2.1: UNIFAC group identification of the components

Component name	Group identification			$v_j$	$R_k$	$Q_k$
	Group name	Main	Secondary			
Methyl Stearate	CH <sub>3</sub>	1	1	2	0.9011	0.848
	CH <sub>2</sub>	1	2	15	0.6754	0.540
	CH <sub>2</sub> COO	11	22	1	1.6764	1.420
n-Butanol	CH <sub>3</sub>	1	1	1	0.9011	0.848
	CH <sub>2</sub>	1	2	3	0.6754	0.540
	OH	5	14	1	1	1.2
Butyl Stearate	CH <sub>3</sub>	1	1	2	0.9011	0.848
	CH <sub>2</sub>	1	2	18	0.6754	0.540
	CH <sub>2</sub> COO	11	22	1	1.6764	1.420
Methanol	CH <sub>3</sub> OH	6	15	1	1.4311	1.432
Di Butyl Ether	CH <sub>3</sub>	1	1	2	0.9011	0.848
	CH <sub>2</sub>	1	2	5	0.6754	0.540
	CH <sub>2</sub> O	13	25	1	0.9183	0.780
Butyl Methyl Ether	CH <sub>3</sub>	1	1	2	0.9011	0.848
	CH <sub>2</sub>	1	2	2	0.6754	0.540
	CH <sub>2</sub> O	13	25	1	0.9183	0.780
Water	H <sub>2</sub> O	7	16	1	0.92	1.4

$v_j$ =number of groups in the component molecule

Table C.2.2: UNIFAC group interaction parameters

	Main Group	1	5	6	7	11	13
Main Group	Name	CH <sub>2</sub>	OH	CH <sub>3</sub> OH	H <sub>2</sub> O	CH <sub>2</sub> COO	CH <sub>2</sub> O
1	CH <sub>2</sub>	0	986.5	697.2	1318	232.1	251.5
5	OH	156.4	0	-137.1	353.5	101.1	28.06
6	CH <sub>3</sub> OH	16.51	249.1	0	-181	-10.72	-128.6
7	H <sub>2</sub> O	300	-229.1	289.6	0	72.87	540.5
11	CH <sub>2</sub> COO	114.8	245.4	249.6	200.8	0	-235.7
13	CH <sub>2</sub> O	83.36	237.7	238.4	-314.7	461.3	0

Table C.3.1: Summary of experimental conditions and calculated errors

Run	Mole ratio BuOH: MS	Catalyst Loading wt%	Temp. (K)	BuOH <sup>1</sup>	BS <sup>1</sup>	MeOH <sup>1</sup>	BuOH <sup>2</sup>	BS <sup>2</sup>	MeOH <sup>2</sup>
1	20	5.6	343	0	3	4	0.0022	0.0003	0.0004
2	20	5.6	353	0	3	3	0.0031	0.0004	0.0004
3	20	5.6	363	1	28	24	0.0120	0.0040	0.0030
4	20	2.8	363	1	32	30	0.0080	0.0027	0.0023
5	20	1.4	363	0	12	11	0.0020	0.0006	0.0005
6	10	4.8	363	1	11	12	0.0052	0.0023	0.0032
7	10	4.8	363	1	6	9	0.0054	0.0027	0.0040
8	5	4.9	363	4	21	23	0.0309	0.0171	0.0195
9	20	4.8	363	0	7	8	0.0041	0.0015	0.0016
10	30	4.8	363	0	8	7	0.0029	0.0013	0.0010
11	20	4.8	363	0	11	10	0.0035	0.0024	0.0020
12	20	2.8	373	1	12	11	0.0065	0.0024	0.0020
13	20	4.8	373	1	17	16	0.0074	0.0031	0.0024
14	20	5.6	373	1	14	16	0.0095	0.0026	0.0031

1-F<sub>rel</sub> - Average relative error % of the species (Eq.4.18)

2-F<sub>abs</sub> - Average absolute error of the species (Eq. 4.19)

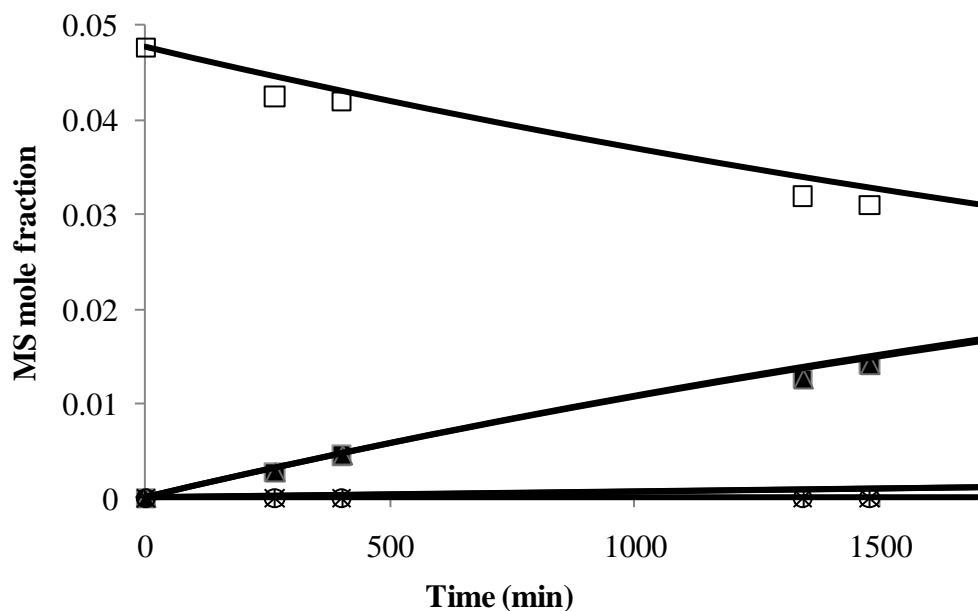


Figure C.3.1: Mole fraction profiles of species present in MS transesterification reactions at 70°C. Reaction conditions: initial mole ratio MS to BuOH = 1:20; catalyst loading = 5.6 wt%; (-□- -MS; -■- -BS; -▲- -MeOH; -×- -DBE; -+- -BME; -○- -W).

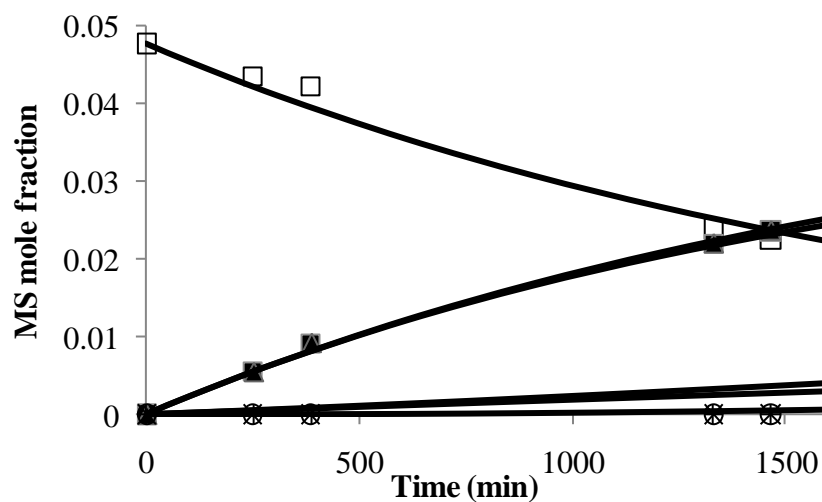


Figure C.3.2: Mole fraction profiles of species present in MS transesterification reactions at 80°C. Reaction conditions: initial mole ratio MS to BuOH = 1:20; catalyst loading = 5.6 wt%; (-□- -MS; -■- -BS; -▲- -MeOH; -×- -DBE; -+- -BME; -○- -W).

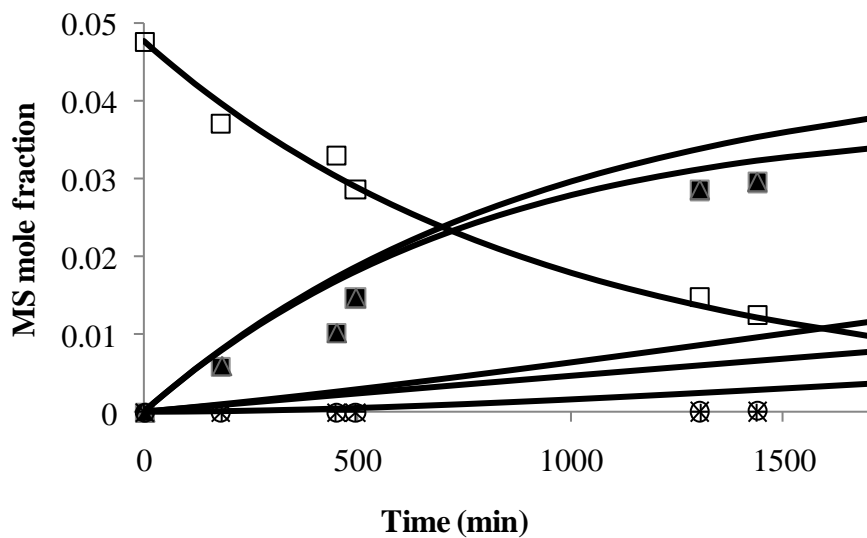


Figure C.3.3: Mole fraction profiles of species present in MS transesterification reactions at 90°C. Reaction conditions: initial mole ratio MS to BuOH = 1:20; catalyst loading = 5.6 wt%; (-□- -MS; -■- -BS; -▲- -MeOH; -×- -DBE; -+- -BME; -○- -W).

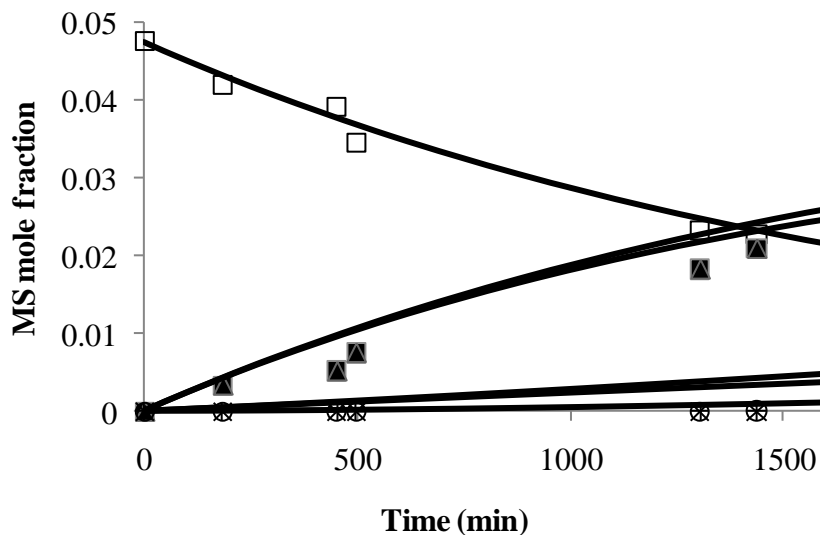


Figure C.3.4: Mole fraction profiles of species present in MS transesterification reactions at 90°C. Reaction conditions: initial mole ratio MS to BuOH = 1:20; catalyst loading = 2.8 wt%; (-□- -MS; -■- -BS; -▲- -MeOH; -×- -DBE; -+- -BME; -○- -W).

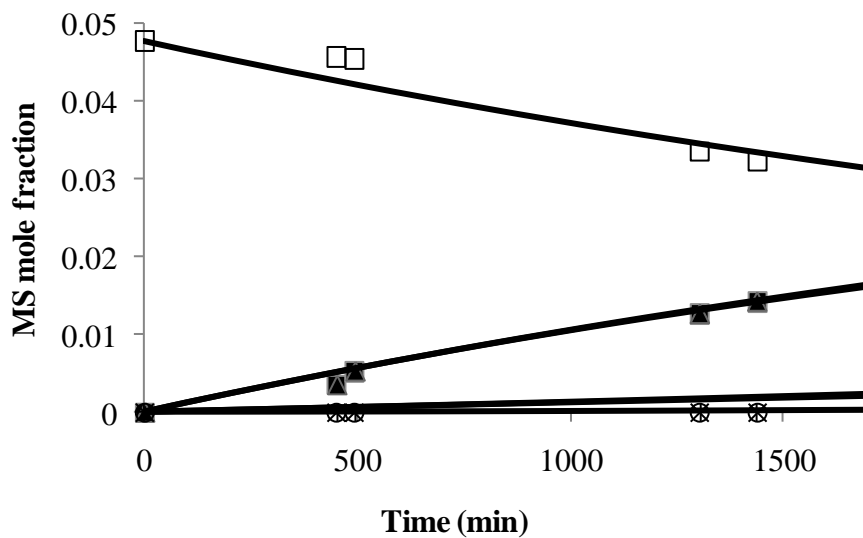


Figure C.3.5: Mole fraction profiles of species present in MS transesterification reactions at 90°C. Reaction conditions: initial mole ratio MS to BuOH = 1:20; catalyst loading = 1.4 wt%; (-□- -MS; -■- -BS; -▲- -MeOH; -×- -DBE; -+- -BME; -○- -W).

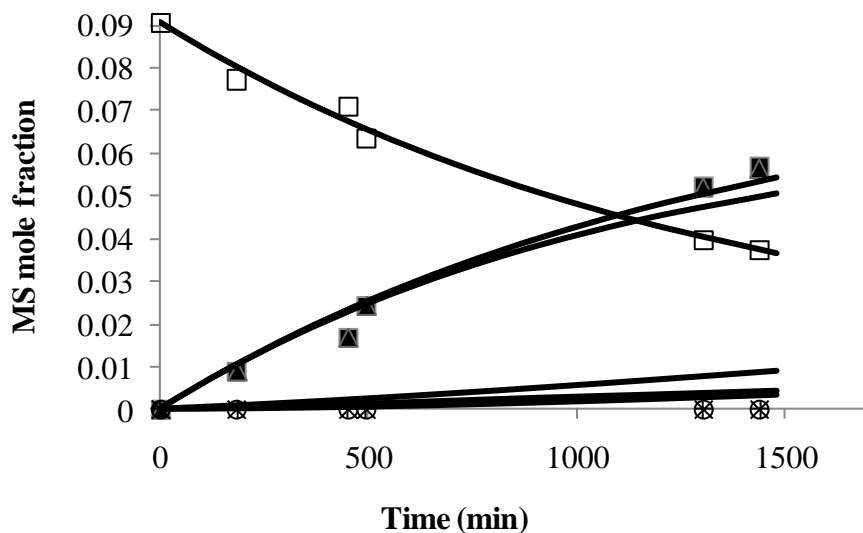


Figure C.3.6: Mole fraction profiles of species present in MS transesterification reactions at 90°C. Reaction conditions: initial mole ratio MS to BuOH = 1:10; catalyst loading = 4.8 wt%; (-□- -MS; -■- -BS; -▲- -MeOH; -×- -DBE; -+- -BME; -○- -W).

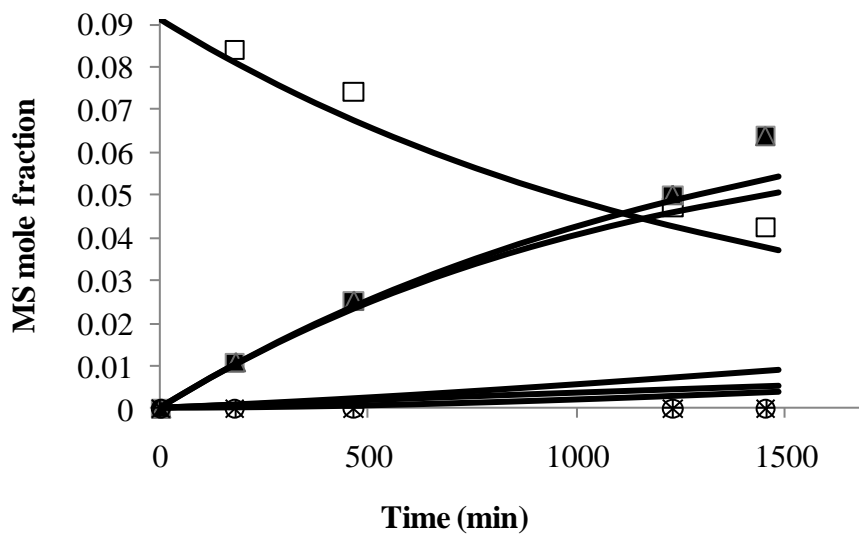


Figure C.3.7: Mole fraction profiles of species present in MS transesterification reactions at 90oC. Reaction conditions: initial mole ratio MS to BuOH = 1:10; catalyst loading = 4.8 wt%; (-□- -MS; -■- -BS; -▲- -MeOH; -×- -DBE; -+- -BME; -○- -W).

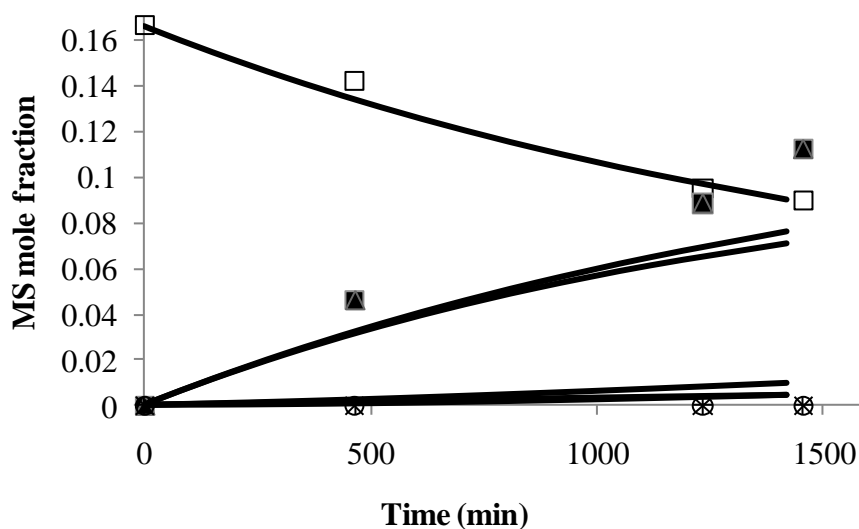


Figure C.3.8: Mole fraction profiles of species present in MS transesterification reactions at 90oC. Reaction conditions: initial mole ratio MS to BuOH = 1:5; catalyst loading = 4.8 wt%; (-□- -MS; -■- -BS; -▲- -MeOH; -×- -DBE; -+- -BME; -○- -W).

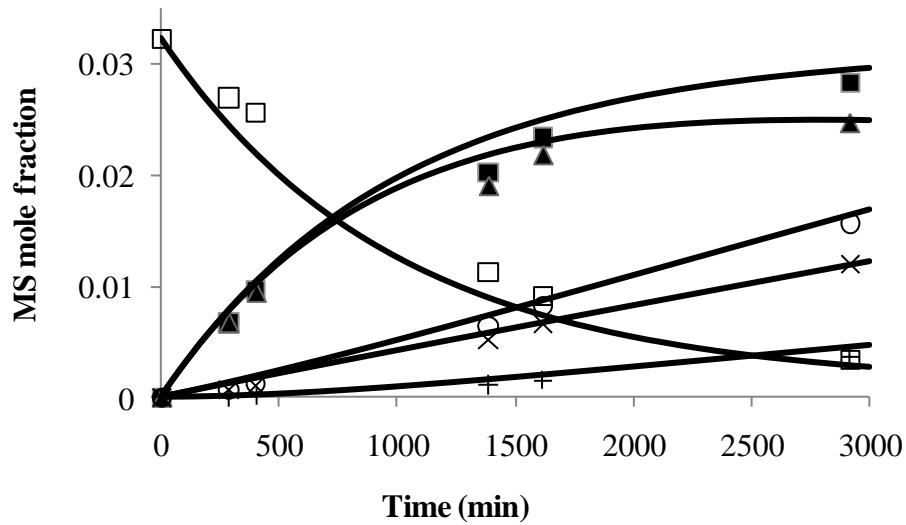


Figure C.3.9: Mole fraction profiles of species present in MS transesterification reactions at 90°C. Reaction conditions: initial mole ratio MS to BuOH = 1:30; catalyst loading = 4.8 wt%; (-□- -MS; -■- -BS; -▲- -MeOH; -×- -DBE; -+- -BME; -○- -W).

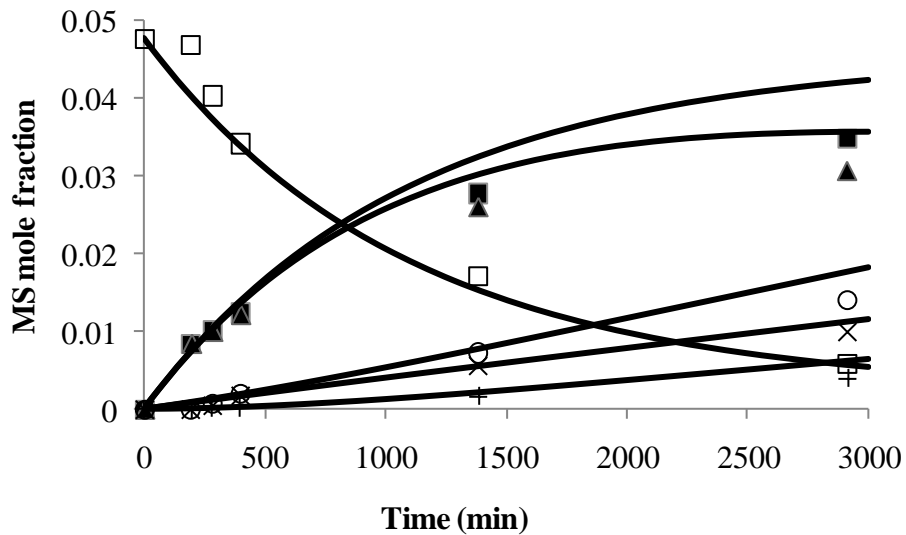


Figure C.3.10: Mole fraction profiles of species present in MS transesterification reactions at 90°C. Reaction conditions: initial mole ratio MS to BuOH = 1:20; catalyst loading = 4.8 wt% (-□- -MS; -■- -BS; -▲- -MeOH; -×- -DBE; -+- -BME; -○- -W).

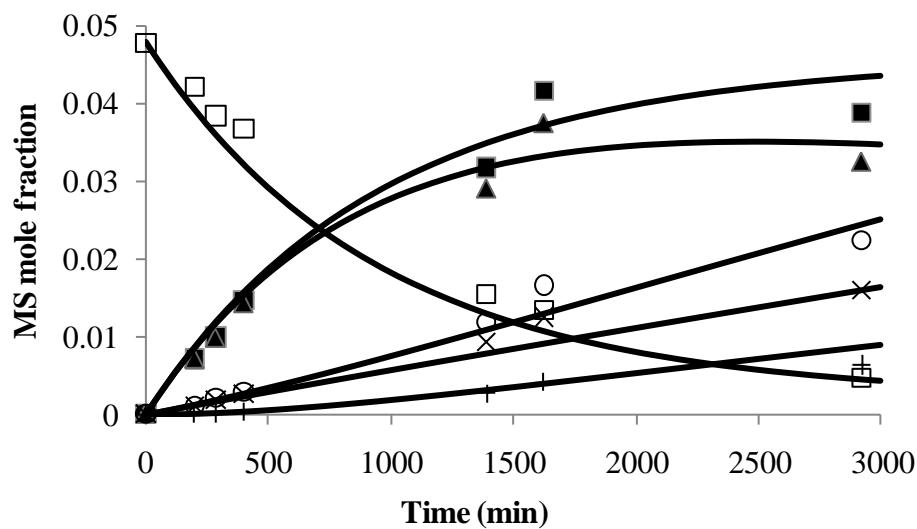


Figure C.3.11: Mole fraction profiles of species present in MS transesterification reactions at 100°C. Reaction conditions: initial mole ratio MS to BuOH = 1:20; catalyst loading = 2.8 wt%; (-□- -MS; -■- -BS; -▲- -MeOH; -×- -DBE; -+- -BME; -○- -W).

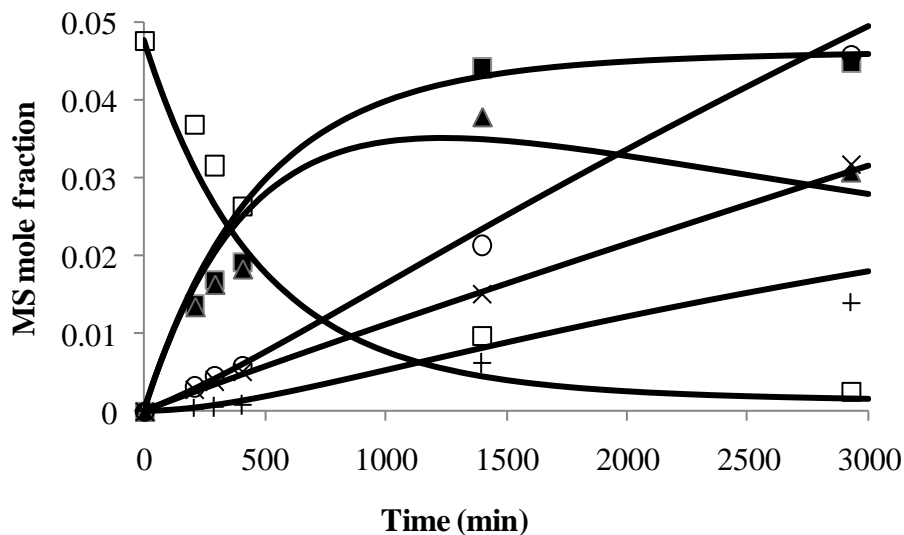


Figure C.3.12: Mole fraction profiles of species present in MS transesterification reactions at 100°C. Reaction conditions: initial mole ratio MS to BuOH = 1:20; catalyst loading = 5.6 wt%; (-□- -MS; -■- -BS; -▲- -MeOH; -×- -DBE; -+- -BME; -○- -W).

## REFERENCES

## 4.7. References

1. Knothe, G., Krahl, J., Van Gerpen, J., Eds., *The Biodiesel Handbook*. 2005, Champaign, IL: AOCS Press: .
2. Lee, I., L.A. Johnson, and E.G. Hammond, *Reducing the crystallization temperature of biodiesel by winterizing methyl soyate*. Journal of the American Oil Chemists Society, 1996. **73**(5): p. 631-636.
3. Wahlen, B.D., B.A. Barney, and L.C. Seefeldt, *Synthesis of Biodiesel from Mixed Feedstocks and Longer Chain Alcohols Using an Acid-Catalyzed Method*. Energy & Fuels, 2008. **22**(6): p. 4223-4228.
4. Wang, P.S., M.E. Tat, and J. Van Gerpen, *The production of fatty acid isopropyl esters and their use as a diesel engine fuel*. Journal of the American Oil Chemists Society, 2005. **82**(11): p. 845-849.
5. Knothe, G., *"Designer" biodiesel: Optimizing fatty ester composition to improve fuel properties*. Energy & Fuels, 2008. **22**(2): p. 1358-1364.
6. Miller, D.J., et al., *Process for producing mixed esters of fatty acids as biofuels*. 2008: Patent application, 12/313,343, USA.
7. Freedman, B., R.O. Butterfield, and E.H. Pryde, *Transesterification kinetics of soybean oil*. Journal of the American Oil Chemists Society, 1986. **63**(10): p. 1375-1380.
8. Bock, H., M. Jimoh, and G. Wozny, *Analysis of reactive distillation using the esterification of acetic acid as an example*. Chemical Engineering & Technology, 1997. **20**(3): p. 182-191.
9. Helfferich, F.G., *Ion exchange*. 1st ed. 1962, New York McGraw Hill.
10. Rao, Y., *Chemical engineering Thermodynamics*. 1st ed. 1997, Hyderabad: Universities Press.

11. Blagov, S., et al., *Influence of ion-exchange resin catalysts on side reactions of the esterification of n-Butanol with acetic acid*. Chemical Engineering Science, 2006. **61**(2): p. 753-765.
12. Gangadwala, J., et al., *Esterification of acetic acid with butanol in the presence of ion-exchange resins as catalysts*. Industrial & Engineering Chemistry Research, 2003. **42**(10): p. 2146-2155.
13. Song, W., et al., *Measurement of Residue Curve Maps and Heterogeneous Kinetics in Methyl Acetate Synthesis*. Industrial & Engineering Chemistry Research, 1998. **37**(5): p. 1917-1928.
14. Bozek-Winkler, E. and J.r. Gmehling, *Transesterification of Methyl Acetate and n-Butanol Catalyzed by Amberlyst 15*. Industrial & Engineering Chemistry Research, 2006. **45**(20): p. 6648-6654.
15. Kolah, A.K., et al., *Reaction Kinetics of the Catalytic Esterification of Citric Acid with Ethanol*. Industrial & Engineering Chemistry Research, 2006. **46**(10): p. 3180-3187.

## **Chapter 5: Butyl stearate production using distillation column with external side reactors: Process concept, simulation and analysis**

### **5.1. Summary**

An alternate approach to direct esterification of fatty acids for producing higher alcohol esters is to first make the fatty acid methyl esters (FAME) via traditional base catalysis and then transesterify FAME with other alcohols using heterogeneous catalysts to produce the desired esters. Conventional reactive distillation will likely be uneconomical for this reaction system because of the slow reaction rate and temperature limitations. Methyl and butyl stearate were chosen as model compounds to represent FAMEs and FABEs respectively. We present here a study that evaluates the potential of carrying out distillation in a column with external side reactors for continuous transesterification of FAME with 1-butanol. Process simulation using Aspen Plus describes column performance as a function of operating conditions, the number of side reactors utilized, requirement for a pre-reactor, location of side draws and re-entry points in the column. The column configuration that maximizes conversion of the methyl ester to its butyl counterpart is presented.

### **5.2. Introduction**

Fatty acid butyl esters (FABE) are commercially important chemicals used in a wide range of applications such as lubricants, emulsifiers and detergents. Recent literature suggests that higher alcohol chain fatty acid esters such as FABE improve cold flow properties of biodiesel and can be used as biodiesel constituents without any modification to the existing diesel engine[1, 2]. Conventional processes to produce higher alcohol fatty acid esters using batch reactors followed by distillation operation is energy intensive. An alternate approach to

direct esterification of fatty acids for producing higher alcohol esters is to first make the fatty acid methyl esters (FAME) via traditional base catalysis and then transesterify FAME with other alcohols using heterogeneous catalysts to produce the desired esters. This work focuses on evaluating techniques that reduce energy consumption in producing higher alcohol fatty acid esters such as FABE. Butyl stearate (here in, BS) was chosen as model compound to represent FABE.

Process intensification (PI) provides an opportunity to use engineering principles to simplify processes, improve energy efficiency, decrease waste production, and lower operational costs. It helps in developing a sustainable processing technology [3-5]. PI can be achieved by combining functions or phenomena into one operation, by adding or enhancing targeted functions in a process, and/or by using alternative energy sources to enhance performance. One such PI technique is reactive distillation (RD), which employs integration of chemical reaction and physical separation into one column.

Reactive distillation has been extensively studied in the literature and is practiced industrially to produce, among other products, organic acid esters and ethers of commercial importance. However, it is not always advantageous to use RD, for example in systems in which temperature favorable for reaction and that for separation based on vapor-liquid equilibrium are not complementary. Another issue that mitigates RD use is limited catalyst life time because of deactivation and the resulting need to change the catalyst in an RD configuration. It is labor intensive to change heterogeneous catalyst packing within an RD column, thus adding to the operational cost of the process. In chemical systems with very low reaction rates, high catalyst hold up is required for achieving high conversion. But high catalyst hold up in RD affects separation operation by minimizing interfacial area between vapor and liquid.

This challenge in operational and hardware configuration for slow reactions can be overcome by using a different PI technique that involves a distillation column with external side reactors (herein D-SRC) [6-9]. This concept has been reported in the literature in simulations of processes for methyl acetate, ethyl acetate, and tertiary amyl ether and benzyl chloride production [10-13]. It holds promise of enhanced reactant-catalyst contact time without increasing size of the distillation column required to purify the products formed.

### **5.3. Distillation with external side reactor concept (D-SRC)**

A schematic of a distillation column with external side reactors is shown in Figure 5.1. The major advantage of D-SRC lies in the operability of interconnected reaction and separation at different process conditions. However, this adds to the complexity of designing distillation columns for separation and of choosing the type of reactors. Along with conventional design variables associated with distillation, additional variables that need to be considered are choice of side reactor- adiabatic or isothermal (if isothermal then temperature of side reactor), choice between similar or different configurations for all side reactors, number of side reactors, catalyst weight in each side reactor, side draw stage, liquid or vapor-liquid mixture of side draw. For the reaction system under examination, a basic simulation methodology accompanied with assumptions and reasons is presented for evaluating D-SRC.

Continuous production of butyl stearate (BS) from methyl stearate (MS) by transesterification with 1-butanol (BuOH) was chosen as a model reaction to evaluate D-SRC using process simulations. Three configurations of distillation operation combined with reaction to produce BS were compared to a base case scenario where three PFRs in series are used to produce BS from MS. All the simulations were carried out in Aspen Plus V7.1 using a RADFRAC column for distillation and a plug flow reactor (PFR) for reaction: results that are

close to highest MS conversion achievable in a given configuration are presented and a simulation methodology is proposed for D-SRC evaluation.

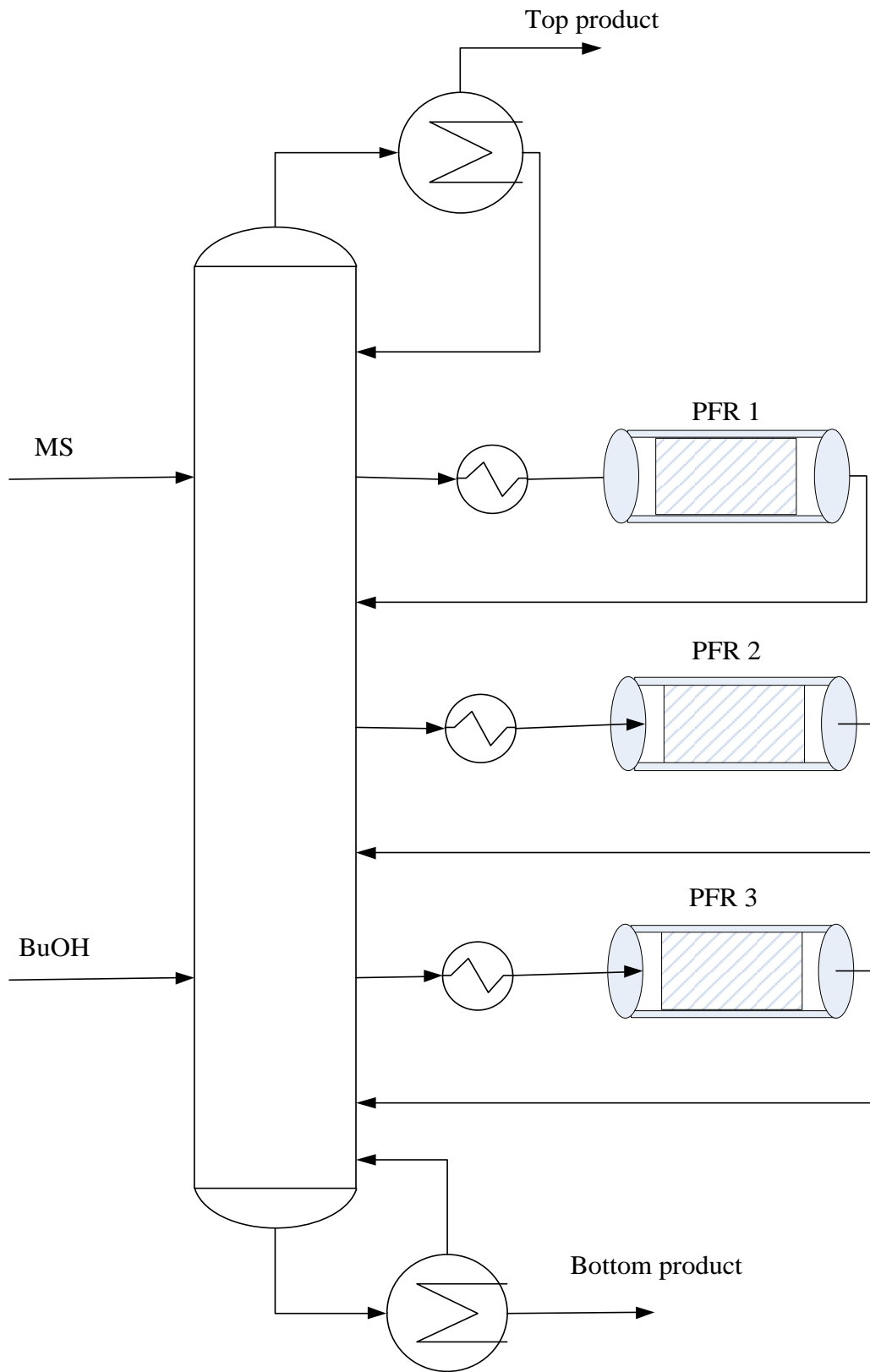
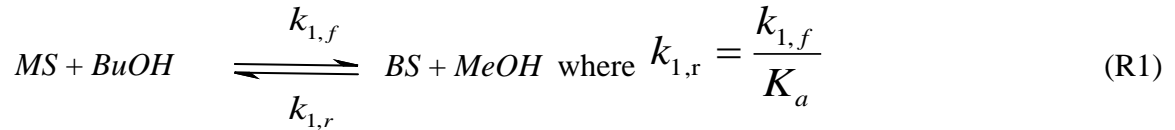


Figure 5.1: Schematic of distillation column with external side reactors and flow diagram for Case 3.

### 5.3.1. MS transesterification reaction

MS transesterification with BuOH can be represented by a single, reversible second order reaction as shown in R1



The alcohol etherification reactions are given as



The components involved in MS transesterification reaction are BuOH, MS, BS, methanol (MeOH), dibutyl ether (DBE), butyl methyl ether (BME) and water (W). Reaction kinetics and chemical equilibrium data for MS transesterification with BuOH catalyzed by Amberlyst 15 is available in literature [14] from our prior study. After making appropriate unit adjustments to kinetic parameters to make them compatible for use in Aspen Plus, these kinetics were used in simulating and evaluating D-SRC. Since MS converts only to BS (R1) and BuOH can convert both to BS and ethers (R2&R3), the four configurations presented in this study are compared in terms of MS conversion and BuOH selectivity towards BS.

### 5.3.2. Boiling point ranking

In order to study the separation using distillation, it is important to determine the boiling point ranking and relative volatilities of components involved in this reaction. The boiling point ranking for this system is BS>MS>DBE>BuOH>W>BME>MeOH. For the desired MS

transesterification reaction in this study, MeOH is the low boiler and stearates are heavy boilers. Methanol can be taken out from top of the column as a product, thus driving the reaction to completion. BuOH is an intermediate boiler, which at first glance allows the column to be operated rich in BuOH and thus makes this reaction ideal for evaluating D-SRC. However, when side reactions are taken into account, DBE is the intermediate boiler. This makes top of the column rich in BuOH and bottom part of the column rich in DBE. These observations help decide the liquid side draw stage that goes to the reactor from the column.

### 5.3.3. Simulation methodology

A simulation methodology to configure D-SRC similar to that proposed by Baur et al.[15] is shown in Figure 5.2. This methodology was used to search for distillation with side reactor configurations that resulted in highest MS conversion and BuOH selectivity to BS. In Case 1, three isothermal PFRs were connected in series. In this scenario, MS conversion is limited by R1 chemical equilibrium. Initial mole ratio of BuOH to MS was increased to improve MS conversion. In Case 2, each PFR is connected to a distillation column and bottom product of the column is sent to the next PFR. In Case 3, a RADFRAC distillation column is connected to three isothermal PFRs. In Case 4, one of the side reactors in Case 3 was used as pre reactor to the distillation column.

BuOH can form azeotrope with water resulting in water build up and phase separation in the column. Since ester hydrolysis is not considered in reaction kinetics in this study, water entering PFRs as a reactant will jeopardize the objective of this study. By decreasing the number of stages in rectifying section and adjusting reflux ratio, water build up in the column can be avoided. This strategy comes with a disadvantage that unreacted BuOH is collected as a top product. Simulations that resulted in high MS conversion with an optimum reflux ratio and total

number of stages without water build up are presented in this study. Assumptions and explanations based on chemical engineering principles that were used as guidelines in selecting side draw stage, side draw return stage and PFR reaction temperature are discussed in the following sections. These guidelines will decrease the design complexity of D-SRC.

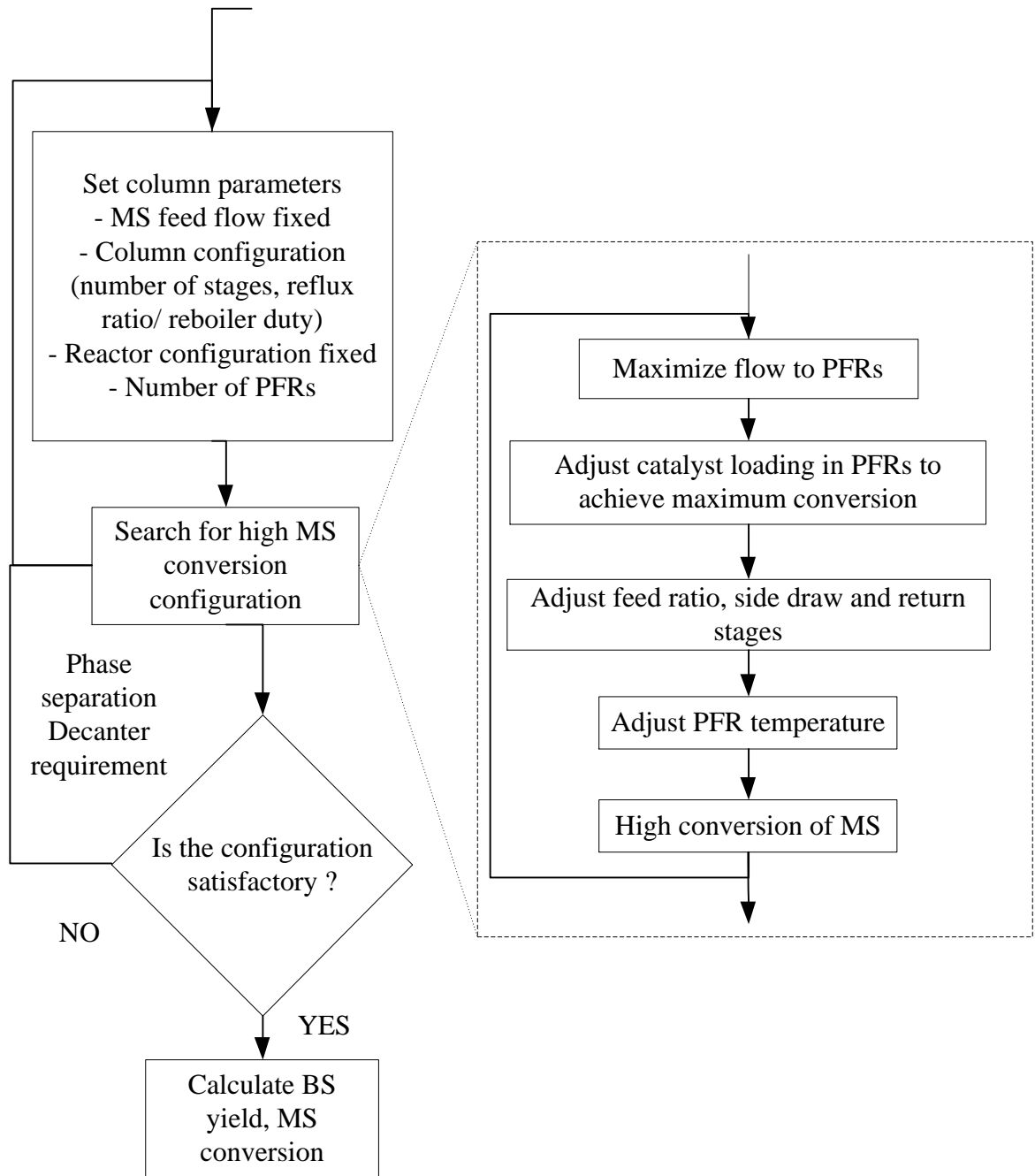


Figure 5.2: Simulation methodology for D-SRC evaluation.

#### *5.3.3.1. Side draw stage*

It is assumed that only liquid is withdrawn from the stages on the column. This eliminates energy required for compression when vapor-liquid mixture is drawn from the column. Liquid return lines from reactors are fed onto the stage directly below the stage from which the side draw was taken. This ensures that BS produced in the reactor will not enter the same reactor again, as it is the heavy key in this system. Methanol, which is the light key, will enter in very small amounts into the reactor because it is predominantly in the vapor phase in the column, and thus etherification reactions (R3) will be minimized. Following these assumptions, the location of the side draw stage is kept as a variable; only the case for which maximum conversion of MS is achieved is reported. In Aspen Plus, side draws increase the number of recycle streams, making convergence of the simulation difficult. Therefore, tear streams are used where appropriate as initial guesses for recycle streams to guide the simulation to convergence. For preliminary simulations, in order to attain simulation convergence, side reactor input flow was started at 0.05 (mol/min) and increased to 0.5 mol/min in small steps. After achieving convergence, the results for side stream outlets from reactors were used as initial guesses for all other simulations.

#### *5.3.3.2. Choice of side reactor: reaction temperature and pressure*

MS transesterification is very slow at lower reaction temperature, necessitating high catalyst loading and higher reaction temperatures. In order to achieve high conversion of MS, all PFRs used in this study are 0.15m dia  $\times$  1.5m long with a catalyst loading of 20 kg, operating at an isothermal reaction temperature of 353 K and at a pressure of 3 atm. The effect of increasing reaction temperature on BS selectivity and yield in a simulated plug flow reactor (PFR) with the same physical configuration as that used in D-SRC simulations is shown in Figure 5.3. It is clear

from these results that BS yield drastically decreases because etherification of BuOH is faster than MS transesterification. This result gives insight into an essential guideline in evaluating D-SRC for MS transesterification, and aids in determining the temperature of the side reactors. As DBE and BuOH are the intermediate boilers in the system, when the column is operated at atmospheric pressure, the column temperature profile will be close to will be 373 K throughout. If liquid is drawn from any stage on the stage at this temperature and reacted in an adiabatic PFR, ether yield will be higher than the desired ester because a) etherification kinetics faster than transesterification b) transesterification is a thermally neutral reaction whereas etherification is an exothermic reaction. Increase in temperature profile along the length of adiabatic PFR will only help etherification and not transesterification. By doing preliminary simulations of distillation with adiabatic side reactors and comparing to that with isothermal PFRs, it was verified that the latter case gave higher MS conversion and selectivity of BuOH towards BS. Therefore, isothermal PFRs at 353 K were used for comparison in all the simulations. To keep MeOH produced in PFRs in the liquid state, all the reactors were operated at 3 atm pressure.

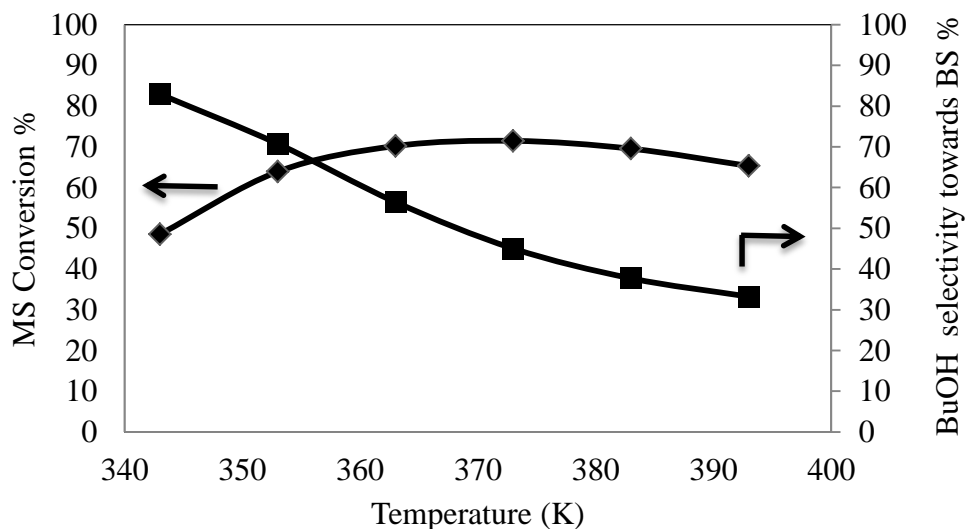


Figure 5.3: Effect of reactor PFR reaction temperature on MS conversion and BuOH selectivity towards BS. (■)- BS selectivity; (◆) - MS conversion. Reaction conditions: Feed mole ratio of BuOH to MS = 2; Catalyst weight in reactor= 20 kg; Pressure = 3 atm.

## 5.4. Results

### 5.4.1. Cases 1&2: Three PFRs in series

Simulation results for producing BS using three PFRs in series (Figure 5.4a) with increasing initial mole ratio are presented in Table 5.1. In Cases 1a and 1b, with increase in mole ratio of BuOH:MS from 1 to 2, MS conversion increases as expected.

Case 2 employs a different configuration that includes distillation columns after each PFR. A block flow diagram for this case is shown in Figure 5.4b. The conversion of MS is higher in Case 2 because of MeoH removal in each distillation column.

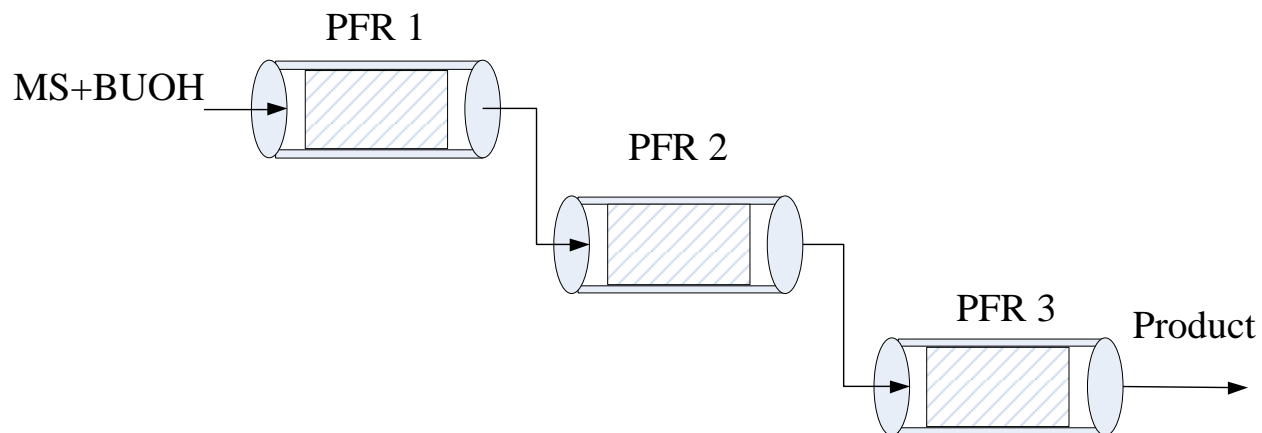


Figure 5.4a: Flow diagram representing cases 1a and 1b.

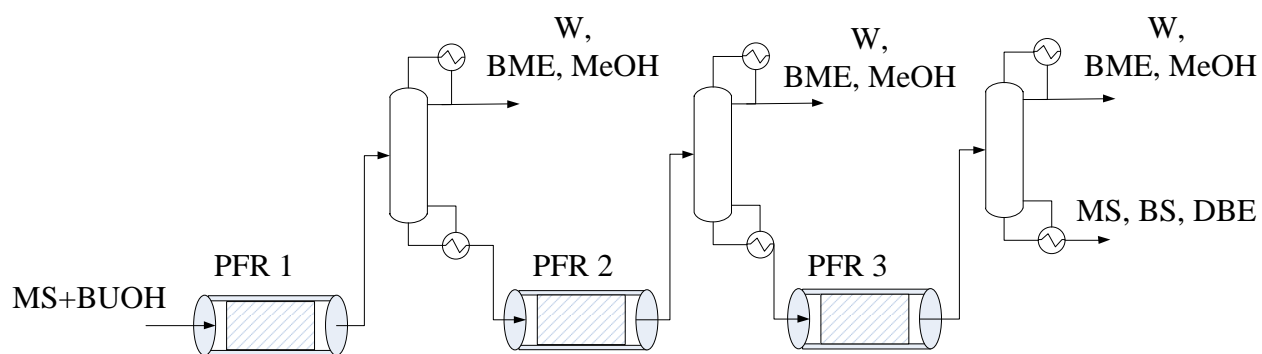


Figure 5.4b: Flow diagram representing case 2.

Table 5.1: Simulation results for cases 1 and 2.

Case	1a	1b	2
MS feed rate [mol/min]	0.1	0.1	0.1
Feed BuOH:MS ratio	1	2	2
PFRs in series	3	3	3
MS conversion	46.9	70.7	85.5
BuOH Selectivity to BS	54.3	52.6	61.0

### 5.4.2. Cases 3: Distillation with three external reactors

Simulation results for BS production using distillation with three external side reactors (see Figure 1) and increasing feed mole ratio of BuOH:MS is presented in Table 2a. MS was fed on stage 4 and BuOH was fed on stage 14 in these cases. Specified and calculated column parameters for the configuration with highest MS conversion in each case are presented in Table 5.2b.

### 5.4.3. Case 4: Distillation with two external reactors and pre-reactor

Following the results from Cases 1, 2 and 3, Case 4 is formulated by adding a PFR pre-reactor to Case 3 to improve MS conversion. An example flow diagram for Case 4 is shown in Figure 5.5. Product from prereactor is fed to the column on stage 7 in the three cases. The number of side reactors and BuOH:MS mole ratio of feed were used as variables. Number of side reactors was changed from 1 to 3, initial feed mole ratio of BuOH:MS was changed from 1 to 3 and temperature of PFRs was changed from 353 K to 373 K. Simulations that resulted in highest MS conversion and BUOH selectivity towards BS are presented in Table 5.2a.

Table 5.2a: Simulation results for cases 3 and 4.

Case	3a	3b	3c	4a	4b	4c
MS feed rate [mol/min]	0.1	0.1	0.1	0.1	0.1	0.1
Feed BuOH:MS ratio	1	2	3	2	3	3
Side reactor PFRs	3	3	3	2	2	1
MS conversion %	50.2	72.6	80.4	90.6	93.3	87.8
BuOH selectivity towards BS	61.8	61.0	53.8	61.0	61.4	67.1
Number of pre- reactors	--	--	--	1	1	1

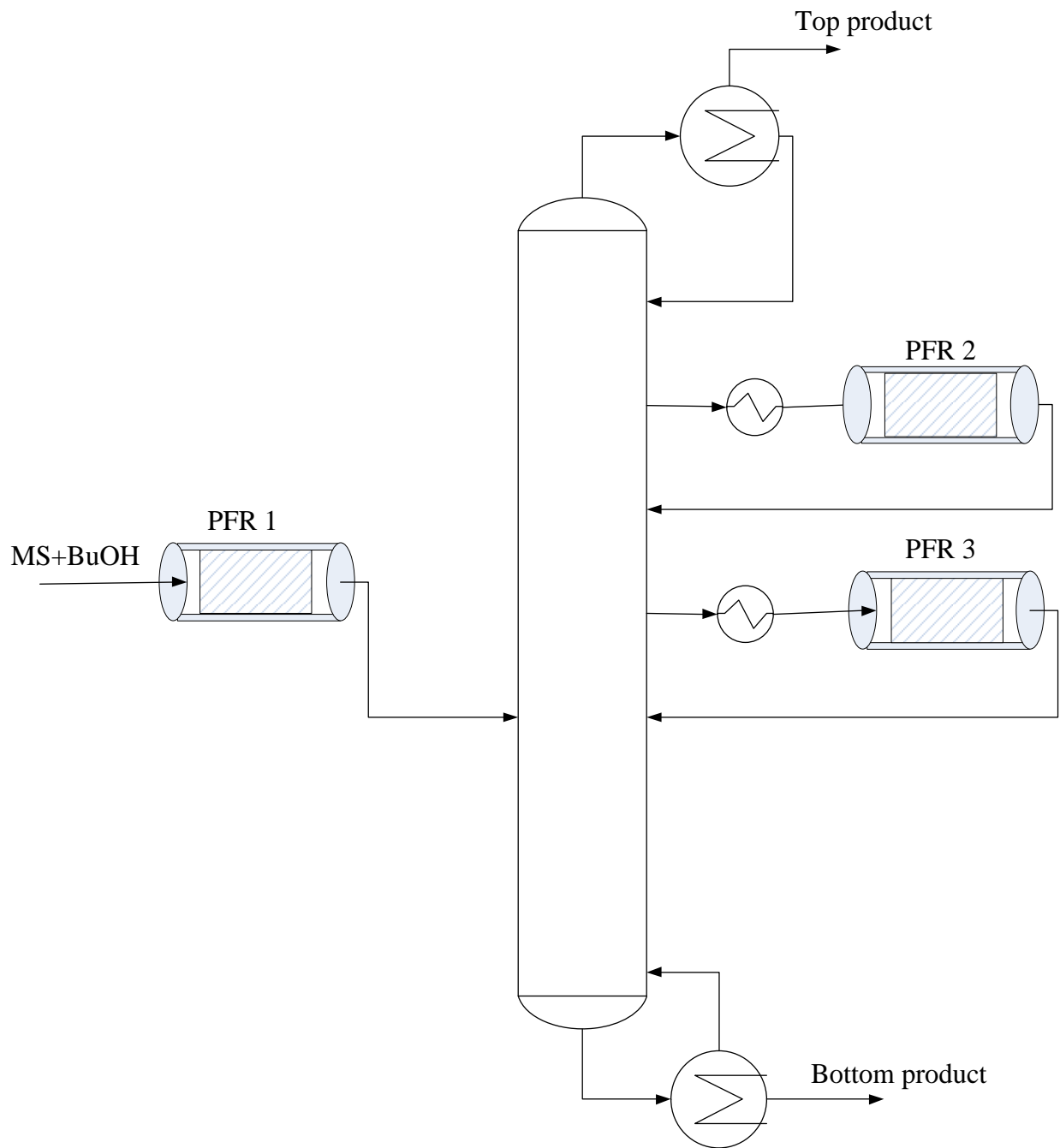


Figure 5.5: Flow diagram representing cases 4a, 4b and 4c.

Table 5.2b: Column properties and conditions from simulation of Cases 3 and 4.

Case	3a	3b	3c	4a	4b	4c
Number of stages	16	16	16	16	16	16
Condenser	Total	Total	Total	Total	Total	Total
Reboiler	Kettle	Kettle	Kettle	Kettle	Kettle	Kettle
Top stage pressure [atm]	1	1	1	1	1	1
Specified reflux ratio	0.85	--	--	--	--	--
Specified distillate rate [mol/min]	0.10	0.20	0.26	0.20	0.26	0.26
Calculated molar reflux ratio	0.85	0.15	0.21	2.61	2.15	2.82
Calculated bottoms rate [mol/min]	0.12	0.12	0.17	0.12	0.17	0.17
Calculated boilup rate [mol/min]	0.48	0.83	1.30	0.76	1.32	1.33
Calculated distillate rate [mol/min]	0.10	0.20	0.26	0.20	0.26	0.26
Condenser / top stage temperature [K]	345	355	357	347	353	355
Condenser / top stage pressure [bar]	1.01	1.01	1.01	1.01	1.01	1.01
Condenser / top stage heat duty [J/sec]	123.22	164.69	228.62	488.73	582.12	714.47
Condenser / top stage reflux rate [mol/min]	0.09	0.03	0.05	0.52	0.56	0.74
Reboiler pressure [bar]	1.01	1.01	1.01	1.01	1.01	1.01
Reboiler temperature [K]	572.82	492.40	413.96	505.44	411.28	409.04
Reboiler heat duty [J/sec]	1048	1000	1020	1020	1020	1020
Side draw to PFR1 stage	7	7	7	7	7	7
Side draw to PFR2 stage	9	9	9	9	9	--
Side draw to PFR3 stage	11	11	11	--	--	--
Return from PFR1 stage	8	8	8	8	8	9
Return from PFR2 stage	10	10	10	10	10	--
Return from PFR3 stage	12	12	12	--	--	--

## 5.5. Conclusion

D-SRC is a useful PI technique for reactions that require different operating conditions for reaction and separation. In this study, D-SRC is evaluated for MS transesterification, characterized by very slow reaction rate at lower temperatures and high side product formation at higher temperatures. The best case scenario identified using D-SRC is with a pre-reactor and one distillation column with two side reactors at stages 7 and 9. Results for this case are superior to the conventional ester production technique involving three PFRs in series with intermediate distillation to remove methanol. Even though this configuration for FAME transesterification with BuOH is better than conventional process, it involves etherification, making this system unsuitable for economic evaluation of D-SRC.

## REFERENCES

## 5.6. References

1. Miller, D.J., et al., *Process for producing mixed esters of fatty acids as biofuels*. 2008: Patent application, 12/313,343, USA.
2. Hellier, P., et al., *The Influence of Fatty Acid Ester Alcohol Moiety Molecular Structure on Diesel Combustion and Emissions*. *Energy & Fuels*, 2012. **26**(3): p. 1912-1927.
3. Stankiewicz, A.I. and J.A. Moulijn, *Process intensification: Transforming chemical engineering*. *Chemical Engineering Progress*, 2000. **96**(1): p. 22-34.
4. Schembecker, G. and S. Tlatlik, *Process synthesis for reactive separations*. *Chemical Engineering and Processing*, 2003. **42**(3): p. 179-189.
5. Lutze, P., R. Gani, and J.M. Woodley, *Process intensification: A perspective on process synthesis*. *Chemical Engineering and Processing: Process Intensification*, 2010. **49**(6): p. 547-558.
6. Baur, R. and R. Krishna, *Distillation column with reactive pump arounds: an alternative to reactive distillation*. *Chemical Engineering and Processing*, 2004. **43**(3): p. 435-445.
7. Kaymak, D.B. and W.L. Luyben, *Design of Distillation Columns with External Side Reactors*. *Industrial & Engineering Chemistry Research*, 2004. **43**(25): p. 8049-8056.
8. Jakobsson, K., et al., *Modelling of a side reactor configuration combining reaction and distillation*. *Chemical Engineering Science*, 2002. **57**(9): p. 1521-1524.
9. Schoenmakers, H. and W. Buehler, *Distillation column with external reactors - an alternative to the reaction column*. *Chem.-Ing.-Tech.*, 1982. **54**(2): p. 163.
10. Ding, L.-H., et al., *Optimum Design and Analysis Based on Independent Reaction Amount for Distillation Column with Side Reactors: Production of Benzyl Chloride*. *Ind. Eng. Chem. Res.*, 2011. **50**(19): p. 11143-11152.
11. Tsai, R.-C., et al., *Design and Control of the Side Reactor Configuration for Production of Ethyl Acetate*. *Industrial & Engineering Chemistry Research*, 2008. **47**(23): p. 9472-9484.

12. Ouni, T., et al., *Enhancing productivity of side reactor configuration through optimizing the reaction conditions*. Chem. Eng. Res. Des., 2004. **82**(A2): p. 167-174.
13. Ojeda Nava, J.A., R. Baur, and R. Krishna, *Combining Distillation and Heterogeneous Catalytic Reactors*. Chemical Engineering Research and Design, 2004. **82**(2): p. 160-166.
14. Pappu, V.K.S., et al., *A kinetic model of the Amberlyst-15 catalyzed transesterification of methyl stearate with n-butanol*. Bioresource Technology, 2011. **102**(5): p. 4270-4272.
15. Baur, R. and R. Krishna, *Distillation column with reactive pump arounds: an alternative to reactive distillation*. Chem. Eng. Process., 2003. **43**(3): p. 435-445.

## **Chapter 6: Butyric acid esterification over solid acid catalysts: The effect of alcohol carbon chain length and a kinetic model for Amberlyst 70 catalyzed esterification with 2-ethylhexanol**

### **6.1. Summary**

Butyric acid esters can improve the cold flow properties of diesel fuels and are thus attractive biofuel constituents. Esters produced from biobutyric acid can also be commercially important renewable chemicals. This study focuses on liquid phase esterification of butyric acid with a series of linear and branched alcohols. The effect of increasing alcohol carbon chain length and branching on esterification rate at 60°C is presented. Four strong cation exchange resins, Amberlyst™ 15, Amberlyst™ 36, Amberlyst™ BD 20, and Amberlyst™ 70, are examined along with p-toluenesulfonic acid as a homogeneous catalyst. For all catalysts, the decrease in turnover number (TON) with increasing carbon chain length of the alcohol is described in terms of steric hindrance and alcohol polarity. Detailed kinetics of butyric acid esterification with 2-ethylhexanol using Amberlyst™ 70 catalyst was studied in a batch reactor. An activity-based, pseudo-homogeneous kinetic model that includes autocatalysis by butyric acid is presented for the Amberlyst 70 ion exchange resin catalyst.

### **6.2. Introduction**

Esterification of carboxylic acids is a widely studied and industrially important reaction [1]. Carboxylic acid esters can be used as plasticizers, industrial solvents, pharmaceuticals, agrochemicals, perfumes, and food flavors [2]. Long chain fatty acid esters can be used as biofuel components [3, 4]. The traditional route for preparing esters is via reaction of the carboxylic acid with an alcohol using a homogeneous catalysts such as sulfuric acid [5] or p-

toluene sulfonic acid [6]. Use of esters as biorenewable chemicals and as “green” solvents has encouraged the study of esterification reactions using heterogeneous catalysts [7-9].

Solid acid catalysts used for esterification include, but are not limited to, Amberlyst 15 [8, 10], Amberlite IR-120 [11], Nafion/silica nanocomposite SAC-13 [12, 13], polymer supported sulfonic acid Smopex-101 [14], heteropoly acid supported on ion exchange resins [7, 15], Amberlyst 36 [16], modified zirconia [17], Dowex 50WX8-400 [18] and Dowex 50WX2 [19].

There is growing interest to produce butyric acid (butanoic acid, herein BA) by fermentation from biorenewable resources [20, 21]. Using BA as a platform molecule, n-butanol can be synthesized by hydrogenolysis (Gaertner et al., 2009); 2-ethylhexanol (herein 2-EHA) can be produced by the Guerbet reaction of n-butanol (Kim et al., 2011), and the secondary alcohol 4-heptanol can be made via ketonization and hydrogenation ([22-24]. Esters of BA made with these alcohols are commercially important renewable chemicals and potential biofuel constituents.

The effect of alcohol chain length and branching on esterification rate of several carboxylic acids is reported in the literature [12, 14, 25]. Erdem and Cebe [25] conducted heterogeneously catalyzed esterification of propanoic acid with different alcohols using dioxane as solvent. They observed that as the chain length and branching increased, esterification rate rapidly decreased because of steric hindrance of alcohols. They described the steric hindrance in terms of the Taft equation [26].

Ju et al. [18] reported esterification kinetics of BA with n-butanol, but little information exists for the behavior of BA in esterification with other alcohols. With the potential of using BA as platform molecule for the production of biofuel constituents, we report here the results of

esterification reactivity of various alcohols with BA using both homogeneous and heterogeneous catalysts. Heterogeneous catalysts include Amberlyst 15, Amberlyst 70, Amberlyst BD 20, and Amberlyst 36 cation exchange resins; esterification rate of different alcohols on these solid acid catalysts is presented and compared to the rate obtained with p-toluene sulfonic acid in solution as a homogeneous catalyst. To further understand BA esterification, a detailed kinetic study of the solid acid-catalyzed esterification of BA with 2-EHA is also presented; the effects of temperature, catalyst loading, and initial mole ratio of 2-EHA to BA in esterification have been examined.

### 6.3. Materials and Methods

Butyric acid ( $\geq 99\%$ ), methanol, ethanol, 1-propanol, 2-propanol, 2-butanol, 3-butanol, iso-butanol (2-methyl-1-propanol), 2-ethylhexanol (2-EHA), 4-heptanone, methyl butyrate, ethyl butyrate, propyl butyrate, butyl butyrate, heptyl butyrate, octyl butyrate and butyryl chloride were purchased from Sigma-Aldrich and used in their as-received states. 1-butanol was obtained from Mallinckrodt-Baker, Inc. Preparation of 4-heptanol and 2-ethylhexyl butyrate is described below.

Ion exchange resin catalyst Amberlyst 15 and Amberlyst 36 were purchased from Sigma Aldrich. Amberlyst 70 and Amberlyst BD 20 were obtained from the Dow Chemical Company. Ion-exchange capacity for the Amberlyst resins was determined by titration using 0.1M NaOH solution in water. The values obtained were 4.3 eq/kg for Amberlyst 15, 5.1 eq/kg for Amberlyst BD 20, 5.4 eq/kg for Amberlyst 36, and 2.7 eq/kg for Amberlyst 70. All ion-exchange resin catalysts were washed with deionized water and ethanol until the supernatant liquid was colorless and then dried overnight at 100°C under vacuum before using in reaction.

### **6.3.1. Preparation of 4-Heptanol**

In a 2L Parr 4520 bench top reactor, 1L of 4-heptanone was hydrogenated at 1000 psi and 180°C using 10 gm of 5% Ru/C as catalyst. Identity of the product 4-heptanol was confirmed by gas chromatography; final purity was >98%. The 4-heptanol obtained was used in esterification of BA.

### **6.3.2. Preparation of 2-ethylhexyl butyrate (2-EHB)**

In a 250 ml three necked glass reactor fitted with a condenser and a thermal probe, 2-EHA (20 ml) was added to Na<sub>2</sub>CO<sub>3</sub> (19.2 gm) and stirred at room temperature. Butyryl chloride (21 ml) was added drop wise over a period of 2 hours. Reactor contents were heated to 55°C, and stirring was continued until no gas bubbles were observed. After cooling, the solution was washed twice with de-ionized water and the organic layer was separated and washed with 0.1M NaOH solution in water to remove any unreacted BA. After decanting the organic layer, magnesium sulfate was added to the product 2-EHB to remove trace amounts of water. Purity of the product was confirmed by gas chromatography as >98%. This material was used as the standard in quantitative analysis of 2-EHB obtained in BA esterification with 2-EHA.

### **6.3.3. Batch experiments**

Batch esterification reactions were performed in a Parr 5000 Multi-Reactor System equipped with temperature control ( $\pm 0.2^\circ\text{C}$ ) and stirring speed control (0-1400 rpm). Experiments were performed under solvent-free conditions. In a typical experiment, a measured quantity of alcohol and catalyst were charged into the reactor. The reactor was sealed and heating was initiated. Once the desired temperature was reached, the required amount of BA was injected into the reactor via syringe and stirring was started - that instant was taken as zero reaction time.

Approximately one-milliliter samples were taken at specified time intervals over the first three hours of reaction via use of a syringe attached to a sample port. Equilibrium samples were collected after 24 hours of reaction. Samples were passed through a 2 $\mu$ m filter attached to the end of the sample port to separate the sample solution from solid catalyst.

#### 6.3.4. Sample analysis

All reaction samples from BA esterification with different alcohols except 2-EHA were analyzed using a HP-5890 Series II gas chromatograph with flame ionization detector. An Aquawax-DA 30m column with 0.53mm ID and 1.0 $\mu$ m film thickness was used to separate the components. Oven temperature maintained initially at 40°C for 1.0 min, increased at 20°C/min to 250°C, and then maintained at that temperature for an additional 2.0 min. Injector and detector temperatures were maintained at 250°C and 300°C respectively. Ethyl caprylate was used as the internal standard. A Varian MSWS 450 with a packed Chromosorb 101 column and a thermal conductivity detector was used for analyzing samples from BA esterification with 2-EHA. Oven temperature was maintained initially at 200°C for 0.5 min, increased at 30°C/min to 300 °C, and then maintained at that temperature for an additional 2.0 min. Injector and detector temperatures were maintained at 250 and 260°C, respectively. Calibration plots used in this study are presented in Section A4.5. To compare BA esterification reactivity among different alcohols, turnover number (TON, kmol BA/kmol H<sup>+</sup>/hr) was calculated from the observed initial reaction rate as follows.

$$TON = \frac{(-r_{BA})_{ini} (MV)_{total}}{W_{cat} \rho_{sol} (IE)_{cat}} \quad (6.1)$$

For heterogeneous catalysts, it is assumed that all acid sites participate in reaction. To determine initial rate, a polynomial curve was fitted to the plot of mole fraction of BA vs. time from experiment; initial reaction rate was taken as the slope of the polynomial at time zero.

## **6.4. Results and Discussion**

### **6.4.1. Esterification of BA with different alcohols**

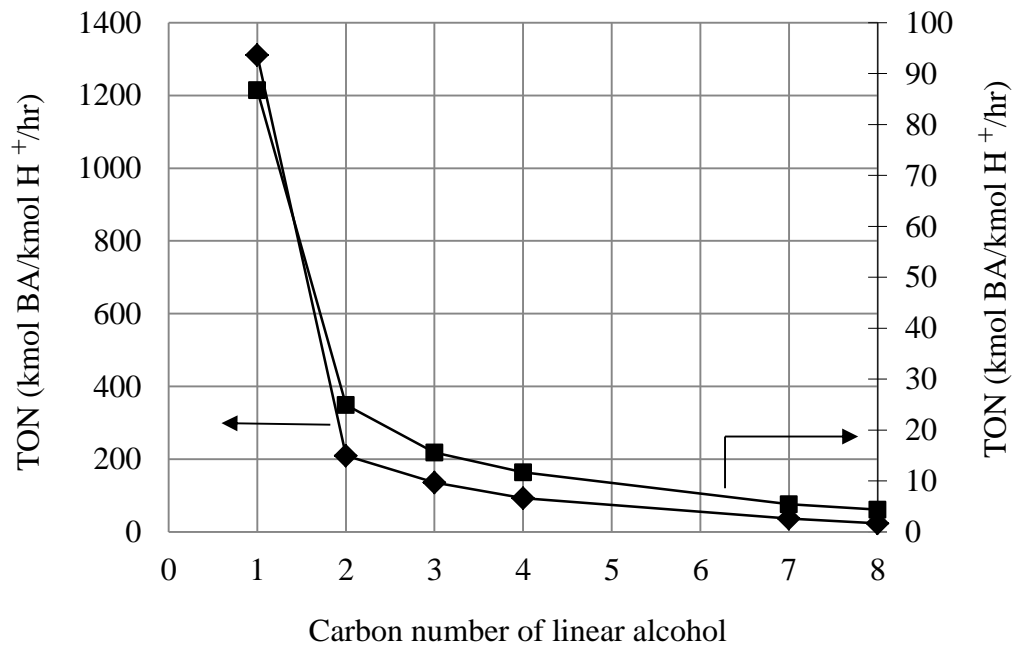
Esterification rate of BA with several alcohols is shown in Figure 6.1a in terms of TON. The trend in reactivity with alcohol carbon number reiterates the observation of Erdem et al. [25]: reactivity decreases significantly from methanol to ethanol, and declines much more slowly as the alcohol carbon number increases from two to eight. This decline in reactivity is observed in both homogeneously and heterogeneously catalyzed reactions. As the number of carbon atoms increases in linear alcohols, the -OH molar concentration decreases logarithmically [27]. This makes the alcohols less polar from methanol to 1-octanol, which affects the esterification reaction rate, and it also lowers the expected reaction rate simply by the presence of fewer hydroxyl groups in solution. The effect of polarity and steric hindrance in BA esterification with this series of primary, linear alcohols was examined using the Taft equation (Appendix D.1).

The plot of the Taft equation (Figures D.1.1 & D.1.2) for the alcohols supports the notion that, for both homogeneously and heterogeneously catalyzed reactions, the decrease in esterification reactivity from methanol to 1-octanol is the result of steric and polar effects. The similarity in reaction trend and in the quality of fit with both homogeneous and heterogeneous catalysts is evidence that the mechanism and overall behavior of esterification is the same for both. Based on this analysis, we conclude that the observed decrease in reactivity with increasing carbon number of the alcohol is the result of steric hindrance and polar effects of the alcohol, and not as a result of differences in affinity of the alcohols for the ion exchange resin catalyst.

It is clear that polar and steric effects of alcohols are essentially the same for both homogeneous and heterogeneous catalysts. The observation that TON for para-toluenesulfonic acid (p-TSA) was 10-12 times higher than Amberlyst 70 (Figure 6.1a) could be attributed to a) some acid sites on Amberlyst 70 are unavailable for reaction or have reduced activity because of resin swelling or hydrophilicity; or b) restricted conformation of intermediate complexes adsorbed on Amberlyst 70 acid sites (as opposed to unrestricted movement in solution with p-TSA). Particular explanation for this observation is beyond the scope of this study. For researchers working on the esterification reaction mechanism under heterogeneous catalysis, a correlation between the structure of alcohols and their reactivity with carboxylic acid presented in this study would give an additional insight. To further investigate the observed rate behavior, the turn over number (TON) for a given alcohol is expressed as a rate constant in terms of molar concentrations of BA and the alcohol.

$$k_{TON} = \frac{TON}{[Acid][Alcohol]} \quad (6.2)$$

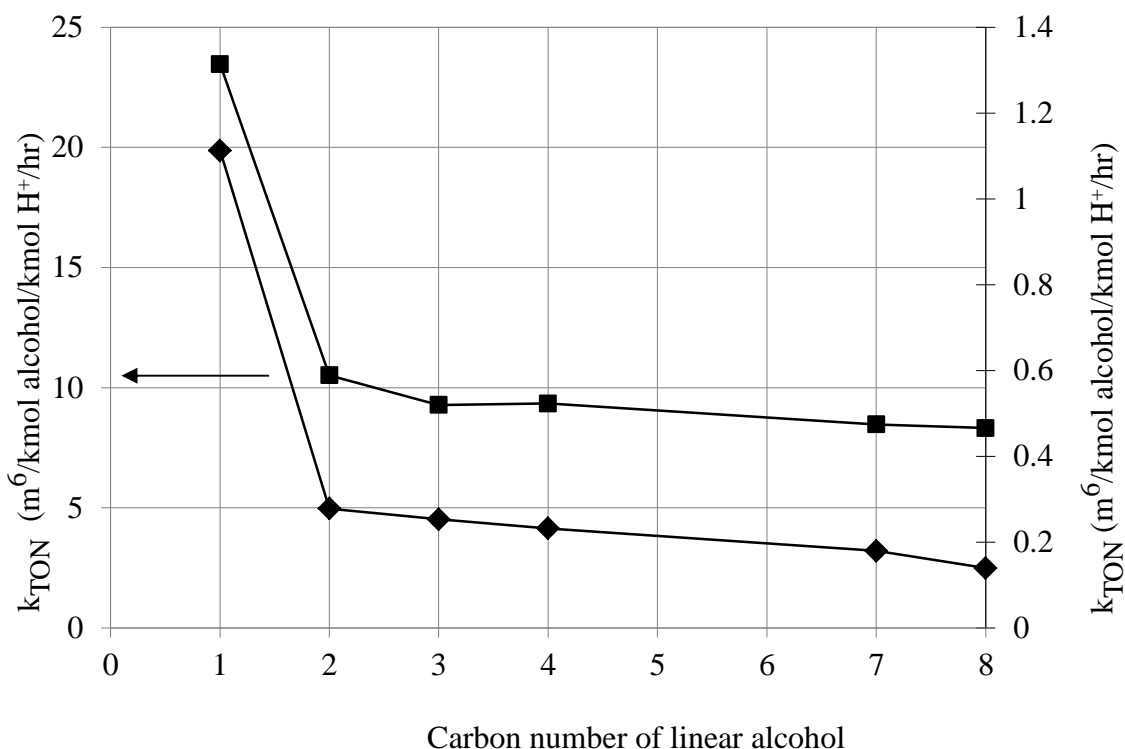
The forward rate constant  $k_{TON}$  in Eq. (6.2) is plotted versus alcohol carbon number in Figure 6.1b. The rate constant decreases sharply from methanol to ethanol, but declines only slightly with increasing carbon number for all other linear, primary alcohols. This common value of  $k_{TON}$  can thus be used to determine the esterification rate of BA with any alcohol or mixture of alcohols from ethanol to 1-octanol under the given range of reaction conditions. For example, an experiment involving mixed alcohol (ethanol and 1-butanol) esterification of BA at an alcohol:acid mole ratio of 3:1 with 1 wt% Amberlyst 70 at 60°C gave a value of  $k_{TON} = 0.48$  [28], close to the value of 0.5 given in Figure 6.1b.



(a)

Figure 6.1. Effect of increasing linear alcohol carbon number on esterification rate of butyric acid. a) (TON); b)  $k_{TON}$  (Eq.6.2). (■) – Amberlyst 70 ;(◆) - p-TSA; Reaction conditions: 3:1 alcohol:acid molar feed ratio, 0.01 kg cat/kg soln, 60°C.

Figure 6.1 (cont'd)



(b)

The TON for BA esterification branched alcohols decreases with increasing branching from 1-butanol to isobutanol, and from 1-octanol to 2-EHA because of steric hindrance (Figure D.2.1, Appendix D). The TON decreases from 11.6 for 1-butanol to 2.6 for 2-butanol, as  $\text{-OH}$  accessibility decreases in secondary alcohols. A similar result was obtained for esterification with 1-heptanol and the secondary alcohol 4-heptanol.

Figure 6.2 compares BA esterification rates with a series of linear alcohols in terms of TON using four ion-exchange resin catalysts. Among heterogeneous catalysts, Amberlyst 70 has high activity per active site ( $\text{H}^+$ ). On a unit mass basis, Amberlyst BD 20 has the highest activity, giving greater conversion of BA with methanol in 1 hour than any other solid acid catalyst. Among the solid catalysts, Amberlyst 15 is commercially available and widely used in industry,

but it suffers the limitation of low thermal stability (<140°C). Amberlyst 70 exhibits high thermal stability because of its halogenated polymer backbone [29]. Therefore, in the following kinetic study of BA esterification with 2-EHA, Amberlyst-70 was used as the catalyst.

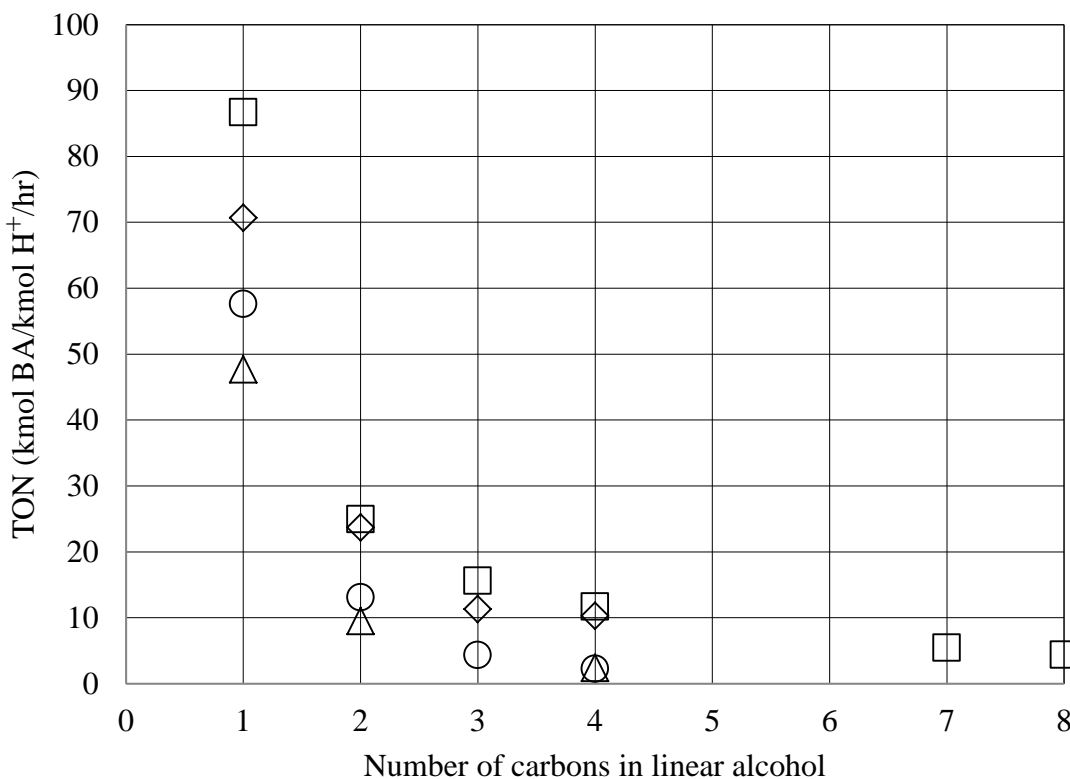
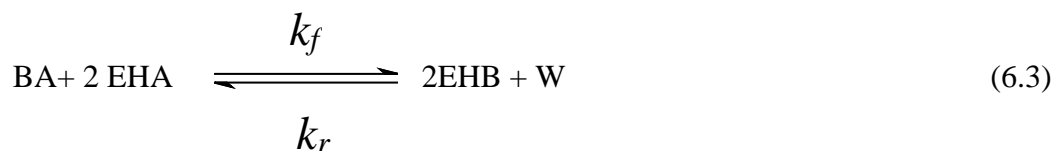


Figure 6.2: Esterification rate of butyric acid with primary alcohols. (□) – Amberlyst 70; (◇) - Amberlyst BD20; (○) – Amberlyst 15; (Δ) - Amberlyst 36; Reaction conditions: 3:1 alcohol:acid feed molar ratio, 0.01 kg cat/kg soln, 60°C.

#### 6.4.2. BA esterification kinetics with 2-EHA

BA esterification with 2-EHA can be represented by a single, reversible second order reaction.



#### 6.4.2.1. Mass transfer resistances

The development of an accurate kinetic model for reactions involving heterogeneous catalysts requires that external and internal mass transfer resistances be minimized in reaction. To ensure that there were no external mass transfer resistances in BA esterification with 2-EHA, the reaction was carried out at several different agitation speeds while keeping all other conditions the same. Over the range of 100 rpm to 850 rpm investigated in this study, no significant effect of the speed of agitation was observed on the rate of esterification. Therefore, all further reactions were carried out at 550 rpm.

To further investigate possible external mass transfer effects and overall catalyst utilization, experiments were conducted at catalyst loadings from 0 to 2 wt% at 120°C and 0.5 to 3 wt% at 130°C. The plot of initial BA esterification rate versus catalyst loading at each temperature is linear (Figure 6.3); this is further evidence that external mass transfer resistances are absent and that the catalyst is effectively distributed and active throughout the reaction solution.

Internal mass transfer resistances were evaluated using different particle sizes of Amberlyst 70, obtained by grinding the resin into fine particles and sieving to obtain three different size fractions. These three fractions were evaluated under identical reaction conditions including constant catalyst loading. No significant difference in conversion rate for the different catalyst particle sizes was observed, indicating that intra-particle diffusion resistances are negligible for Amberlyst 70-catalyzed esterification. Therefore, the resin catalyst was used in its as-received state for all experiments. The effect of stirring rate and the catalyst particle size on rate of esterification is shown in Appendix D (Figures D.3.1a&b).

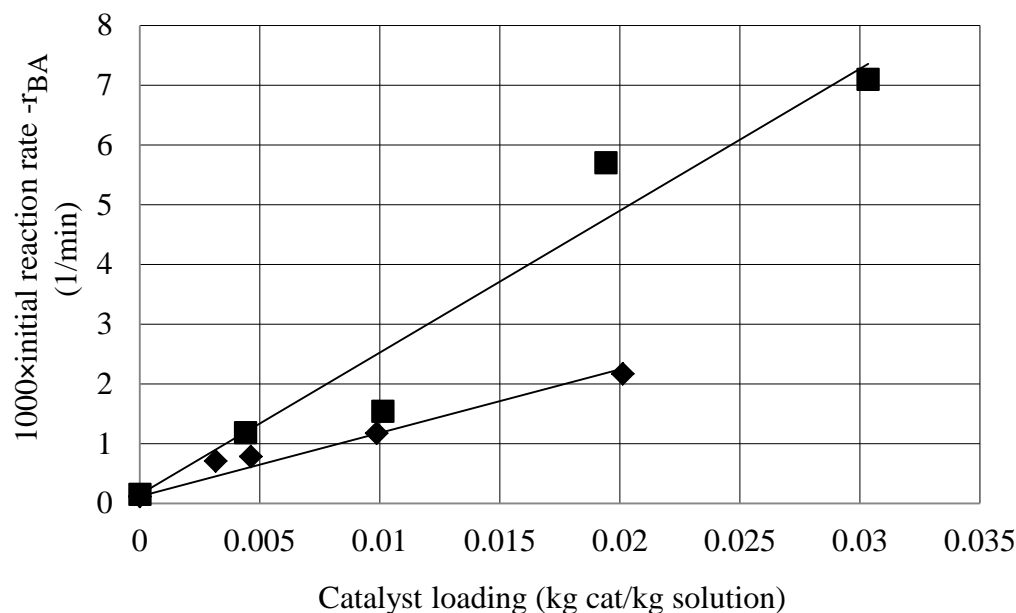


Figure 6.3: Initial BA esterification rate vs. catalyst loading; (◆)-120°C; (■)-130°C; Reaction conditions: 2-EHA:BA feed molar ratio = 6:1. Solid lines represent best fit of the data.

Internal mass transfer resistances were evaluated by estimating the observable modulus  $\Phi$  and implementing the Weisz-Prater criterion:

$$\Phi = r_{\text{obs}} \rho_p R_p^2 / D_e [A_s] \ll 1 \quad (6.4)$$

The observable modulus  $\Phi$ , which represents the ratio of the actual reaction rate to the maximum diffusion rate, can be evaluated from the observed rate of reaction, the catalyst particle radius ( $R_p$ ), effective diffusivity of the limiting reactant ( $D_e$ ), and bulk concentration of the reactant [ $A_s$ ] at the external surface of the particle. When  $\Phi$  is much less than one, the reaction is kinetically controlled and internal mass transfer resistances are absent. For Amberlyst 70,  $R_p = 170 \mu\text{m}$ , catalyst porosity is  $\sim 0.57$ , and the liquid phase diffusion coefficient of BA in 2-EHA,  $D_{AB}$ , calculated using the Wilke-Chang equation, is  $1.5 \times 10^{-5} \text{ cm}^2/\text{sec}$ . For esterification of BA and 2-EHA at 100°C with 1 wt % Amberlyst 70 as catalyst and an initial 2-EHA:BA molar ratio

of 6:1, the value of  $\Phi$  was 0.014. Internal mass transfer resistances can therefore be neglected for this reaction system.

#### 6.4.2.2. Equilibrium constant

The mole fraction-based equilibrium constants ( $K_x$ ) were determined by analysis of reaction samples taken after 24 hrs of reaction time, a sufficient period for the esterification reaction to closely approach equilibrium. The activity-based equilibrium constant,  $K_a$ , was calculated from  $K_x$  via inclusion of activity coefficients of the species in the mixture (Eq. 6.5).

$$K_a = \prod a_i^{v_i} = K_x K_\gamma = \prod x_i^{v_i} * \prod \gamma_i^{v_i} \quad (6.5)$$

The values of  $K_x$  varied only from 1.5 to 5.0 over the range of experimental conditions studied. Therefore, it is assumed that  $K_x$  does not depend on temperature, and an average value for  $K_x$  of 2.6 was determined from all experiments. The activity coefficient ratio  $K_\gamma$ , was calculated using the UNIFAC group contribution method. The UNIFAC group volume ( $R_k$ ) and surface area ( $Q_k$ ) parameters were taken from Rao [30]. Values of  $K_\gamma$  varied from 10.2 to 11.6 over all experiments; an average value of 10.9 was used in the kinetic model.

#### 6.4.2.3. Effect of initial molar feed ratio

A few experiments were carried out initially at low mole ratios of 2EHA:BA (< 4:1). At high conversions of BA under these conditions, the formation of two phases was observed. With this phase separation, even a stirring rate of 1200 rpm did not ensure samples of uniform composition from the batch reactor. This resulted in mass balance errors during sampling and a poor fit of the kinetic data. Therefore, most experiments were carried out at high initial mole

ratio of alcohol to BA (>6:1). As initial alcohol to acid mole ratio increases from six to 15, butyric acid conversion rate increases modestly, but the equilibrium conversion remains close to 93% for all 2-EHA to BA ratios. Figure 6.4 shows the mole fraction profiles reaction of components at 2-EHA:BA molar feed ratio of 6:1. The reactions typically reached the equilibrium composition within 3 hours.

Results from Figure 6.3 at different catalyst loadings show that zero catalyst loading gives a non-zero rate; therefore, several experiments were conducted without catalyst present to facilitate kinetic modeling of auto-catalyzed BA esterification with 2-EHA. The rate at 130°C in Figure 6.3 for zero catalyst loading was extrapolated from uncatalyzed reaction rates at 90°C to 120°C.

#### 6.4.3. Kinetic model for Amberlyst 70-catalyzed and auto-catalyzed esterification

A pseudo-homogeneous kinetic model for esterification, combining auto-catalyzed and resin-catalyzed esterification, has been previously described in the literature [9, 31]. The rate of BA consumption in the reaction mixture is described in terms of activities:

$$-\frac{dx_{BA}}{dt} = -r_{BA} = \left( W_{cat}k_f + x_{BA}k_{f,auto} \right) \left( a_{BA}a_{2EHA} - \frac{a_{2EHB}a_W}{K_a} \right); a_i = \gamma_i x_i \quad (6.6)$$

In Eq. (6.6), the rate constant for the reverse reactions (solid acid catalyzed and auto-catalyzed) is represented as  $k_f/K_a$ , where  $K_a$  is the activity-based equilibrium constant for esterification. Similar differential equations can be written for other species in the reacting system.

The temperature dependence of the rate constants can be expressed by the Arrhenius equation.

$$k_f = k_f^o \exp\left(\frac{-E_f}{RT}\right); k_{f,auto} = k_{f,auto}^o \exp\left(\frac{-E_{f,auto}}{RT}\right) \quad (6.7)$$

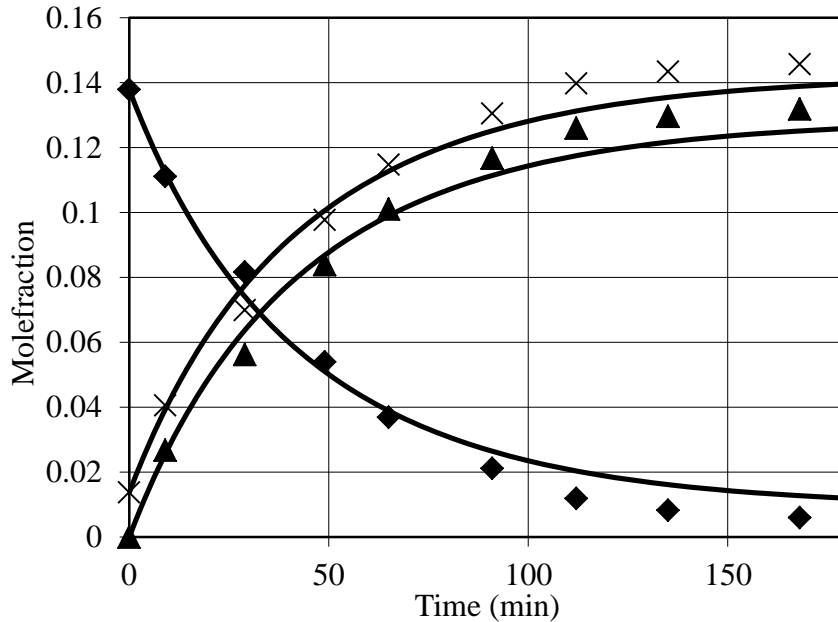


Figure 6.4: Mole fraction profiles of reaction components; (♦) – BA; (▲) – 2EHB; (×) – W; Reaction conditions: 6:1 2-EHA:BA molar feed ratio, 0.01 kg cat/kg soln, 130°C. Continuous lines represent predicted mole fraction profiles from kinetic model.

Four kinetic parameters  $k_f^o$ ,  $k_{f,auto}^o$ ,  $E_f$  and  $E_{f,auto}$  have to be determined to describe the reaction system. Twenty experiments (Appendix D, Table D.4.1) containing 194 data points, at temperatures ranging from 373 K to 423 K, initial molar ratios of 2-EHA:BA from 6:1 to 15:1, and Amberlyst 70 catalyst loading from 0 to 3.0 wt% were fit to the kinetic rate expression. A fourth-order Runge-Kutta method, ODE23 in MATLAB 7.0, was used to numerically integrate the differential equations that describe the formation of each species in the system. Liquid phase mole fractions of all species were calculated over the course of each reaction using an initial set of kinetic parameters and were compared to the experimental data. Kinetic parameters were then

optimized by minimizing the root mean square error between experimental and calculated mole fractions of all liquid phase components in all experiments according to Eq. (8).

$$F^2_{\min} = \frac{\sum (x_{i,cal} - x_{i,exp})^2}{n_{samples}} \quad (6.8)$$

The kinetic parameters that result in the lowest root mean square error, along with their 95% confidence intervals, are given in Table 4.1. The final value of  $F^2_{\min}$ , determined for the kinetic parameters reported is 0.0055, indicating that the model describes the experimental data reasonably well. The predicted and experimental molefraction profiles are given in Appendix D (Section D.4). The calibration plots used in quantification of components using gas chromatography are presented in Section D.5, Appendix D.

#### **6.4.4. Effect of butyrate esters on biodiesel cloud point**

Esters of BA examined in this work were added to canola biodiesel in varying concentrations and their cloud point were measured using Tanaka mini pour/cloud point tester MPC-102L according to ASTM method D2500. As seen in Figure 6.5, addition of butyrate esters decreases the cloud point of canola biodiesel from  $-5^{\circ}\text{C}$  to as low as  $-14^{\circ}\text{C}$ , close to the cloud point of  $-16^{\circ}\text{C}$  for #2 petroleum diesel. This shows the potential of butyrate esters as fuel components to alleviate cold weather limitations of biodiesel.

Table 6.1: Optimized kinetic model parameters with 95% confidence limits

Parameter	Value	Units
$k_{f,auto}^o$	$2.5E6 \pm 5E6$	1/min
$E_{auto}$	$62400 \pm 6400$	kJ/kmol
$k_f^o$	$6820 \pm 4700$	kg <sub>soln</sub> /(kg <sub>cat</sub> ·min)
$E_f$	$41700 \pm 2300$	kJ/kmol

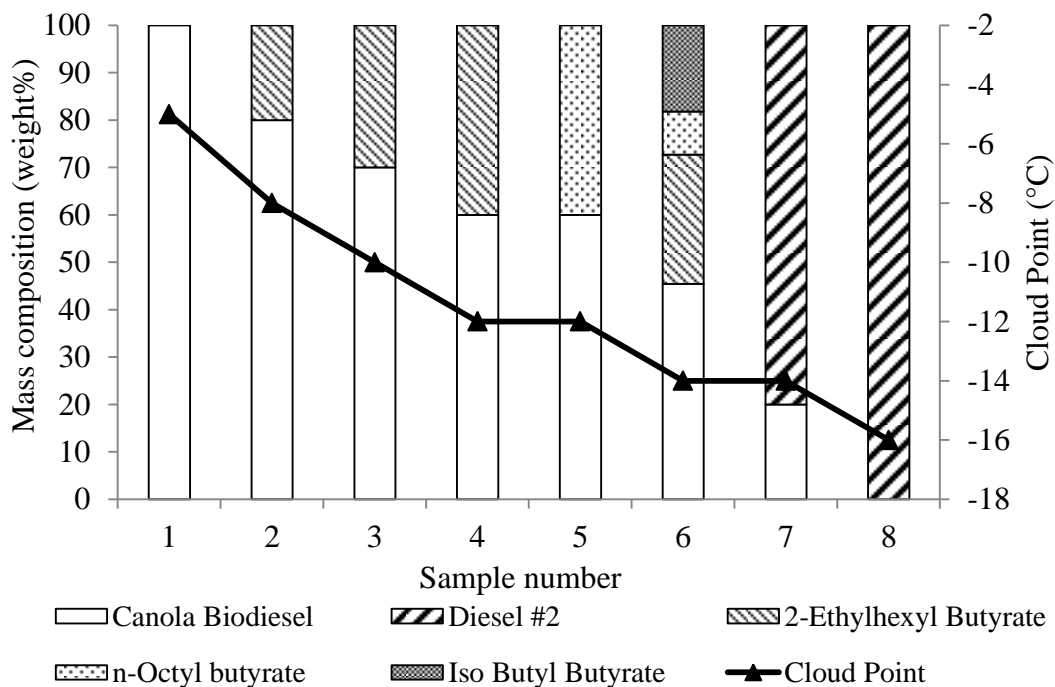


Figure 6.5: Comparison of cloud points between canola biodiesel, #2 Diesel and canola biodiesel with butyric acid esters.

## 6.5. Conclusions

The rate of BA esterification decreases with increasing alcohol carbon chain length because of polarity and steric effects of alcohols and lower molar concentrations of neat alcohols with increasing molecular weight. The forward rate constant for esterification, when the rate is

expressed in terms of molar concentrations of alcohol and acid, is essentially constant for C2 to C8 primary, linear alcohols, but higher for methanol.

The kinetic model developed for Amberlyst-70 catalyzed esterification of BA with 2-EHA predicts esterification rate over the temperature range of 100-150°C reasonably well, making it useful for designing continuous processes for BA esterification.

## **APPENDIX D**

## 6.6. Appendix D

### D.1: Taft equation verification

The correlation between structure of a chemical compound and its reactivity is explained in terms of steric and polar effects using Taft equation. In this section, the substituent effect of different alcohols is discussed in terms of the Taft equation.

For a series of reactants of form R-Y, where for alcohols Y = -OH, the observed kinetic rates should follow an equation analogous to Hammett with respect to the proportionality of polar effects:

$$\log\left(\frac{k}{k_o}\right) = \sigma^* \rho^* \quad (\text{Equation 16, p. 606, Newman[26]} \quad (\text{D.1.1})$$

Here  $\sigma^*$  is the polar substituent constant for the group R relative to the standard -CH<sub>3</sub> group (in methanol) and  $\rho^*$  is a constant giving the susceptibility of a given reaction series to the polar substituent. Values of  $\sigma^*$  are taken from TABLE XII on p. 619 of Newman [26]. Figure D.1.1 is a plot of Eq. D.1.1 using the rate constants for the different linear alcohols studied here normalized to that for methanol. The slope is equal to  $\rho^*$ . An analysis of the Taft relationship of alkyl radicals in alcohols similar to that shown in Figure D.1.1 was conducted by Lilja et al. [14].

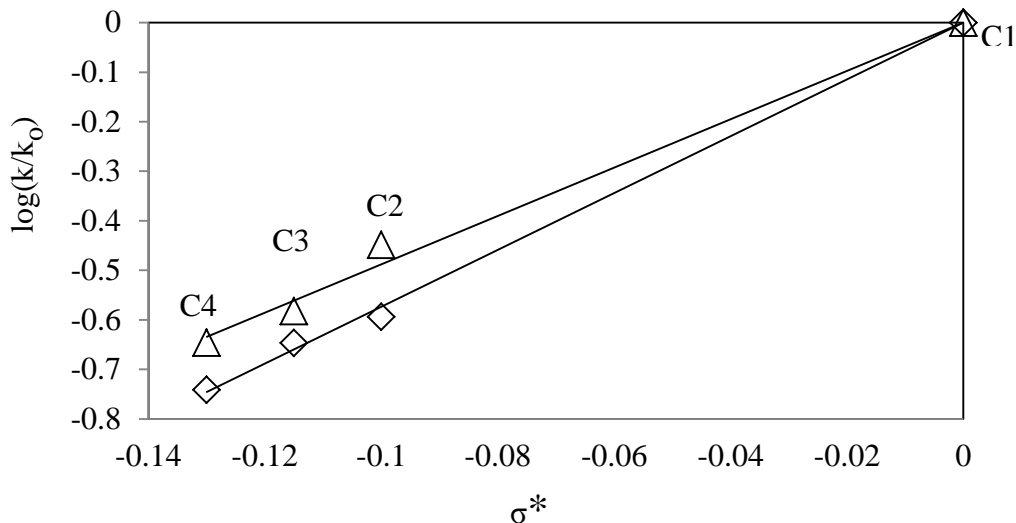


Figure D.1.1: Verification of Taft Equation - polar effect; ( $\diamond$ ) - p-TSA; ( $\Delta$ ) -Amberlyst 70.

In a similar manner, if inductive effects are neglected, the Taft equation can be used to describe steric effects:

$$\log\left(\frac{k}{k_{CH_3}}\right) = \rho E_s ; \text{ Analogous to equation 15 page 597 [26]} \quad (D.1.2)$$

where  $E_s$  is the near-quantitative measure of the total steric effect associated with a given substituent relative to the standard of comparison. In this analysis, the  $-CH_3$  group in ethanol is taken as the standard of comparison, and reaction between ethanol and butyric acid is taken as the standard reaction. Reactions of BA with alcohols only up to n-butanol were evaluated, because values of  $E_s$  for alcohols only up to n-butanol are available. Values given in Table D.1.1 are plotted in Figure D.1.2, showing that the Taft equation is satisfied for steric effects. A similar analysis for propanoic acid esterification with different alcohols was conducted by Erdem et al [25].

Table D.1.1: Data for Figure D.1.2 determined from kinetic rate measurements in this work and corresponding steric substituent constants taken from Newman [26].

	p-TSA	Amberlyst 70	
	$\log(k/k_{\text{CH}_3})$	$\log(k/k_{\text{CH}_3})$	$E_s$
Methanol	0.593	0.448	1.24
Ethanol	0	0	0
n-Propanol	-0.0526	-0.133	-0.07
n-Butanol	-0.1472	-0.197	-0.36

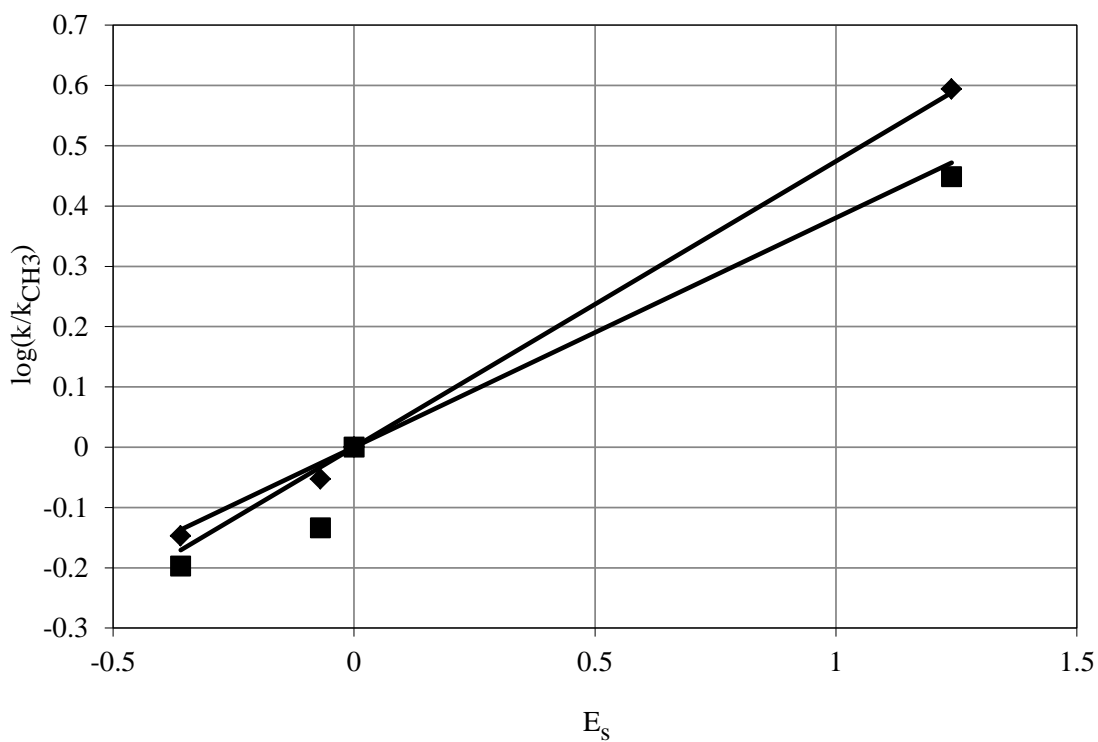


Figure D.1.2: Verification of Taft Equation (steric effect) catalyzed esterification of butyric acid with linear alcohols; (◆) – p-TSA; (■) – Amberlyst 70.

D.2: Effect of alcohol chain branching on butyric acid esterification rate

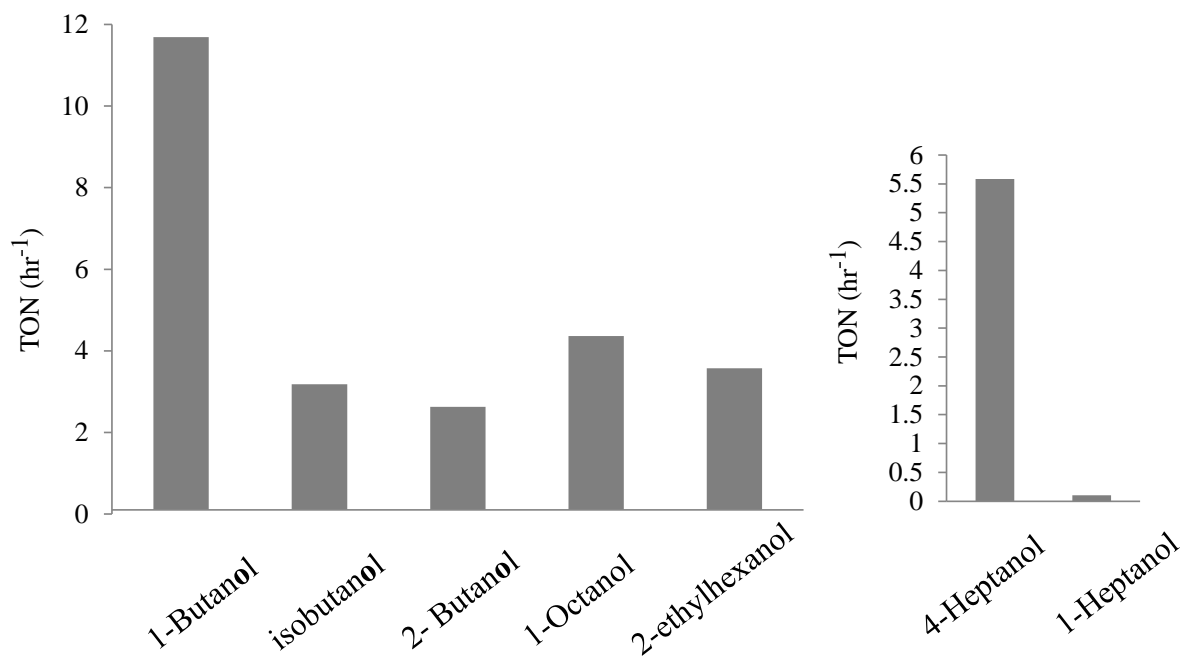
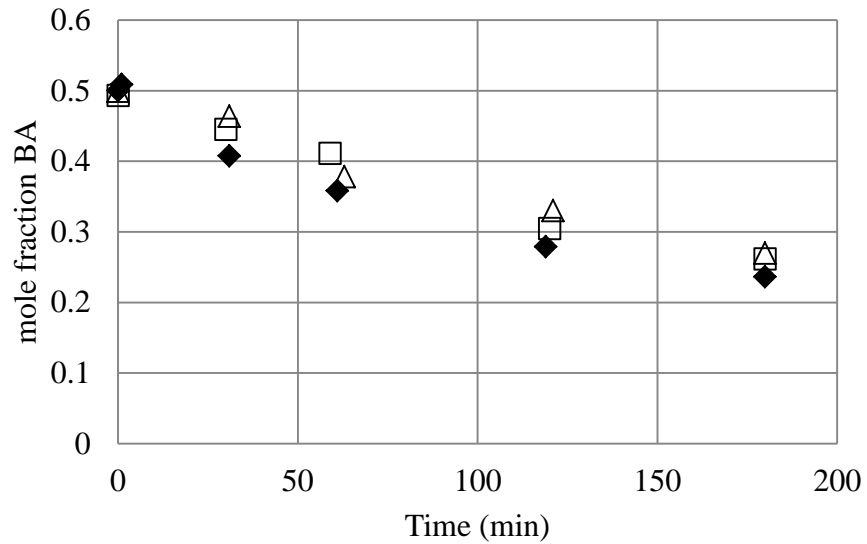
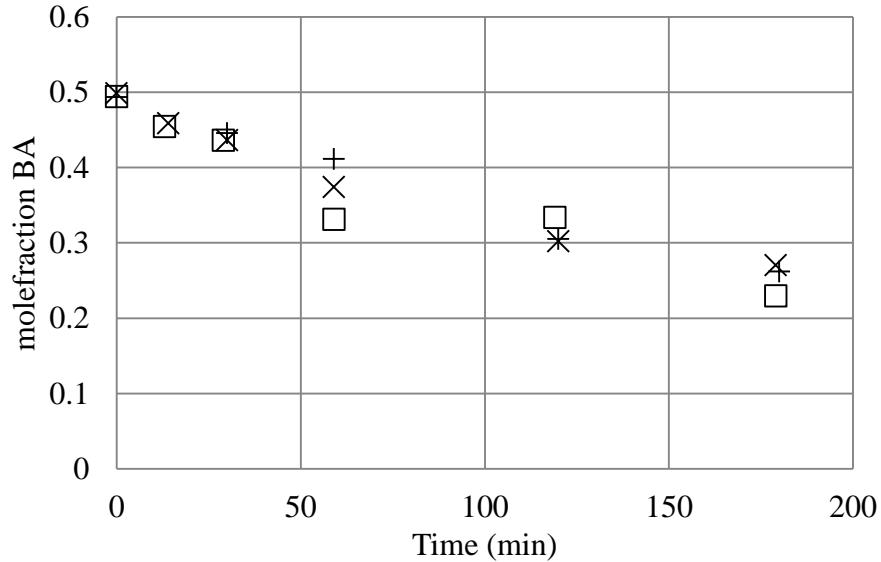


Figure D.2.1: Effect of alcohol chain branching on butyric acid esterification rate. Reaction conditions: 3:1 alcohol:BA feed molar ratio, 0.01 kg Amberlyst 70/kg soln, 60°C.

D.3: Effect of internal and external mass transfer resistance



(a)



(b)

Figure D.3.1: (a) Effect of agitation speed on conversion rate of butyric acid: ( $\Delta$ ) -100rpm; ( $\blacklozenge$ ) - 530 rpm; ( $\square$ ) - 850 rpm. (b) Effect of catalyst particle size on conversion rate of butyric acid: (+) - 300-500 $\mu\text{m}$ ; ( $\times$ ) - 250-500  $\mu\text{m}$ ; ( $\square$ ) - 150-250  $\mu\text{m}$ . Reaction conditions: 1:1 BA:2-EHA molar feed ratio, 0.01 kg Amberlyst 70/kg soln., 110°C.

*D.4: Summary of batch reactor experiments and reaction conditions*

Table D.4.1: Summary of experiments and reaction conditions

Run number	Total Initial moles	Total initial volume (ml)	Reaction temperature °C	$W_{cat}$	Initial mole ratio 2EHA:BA	Figure number
1	0.36	52.78	100	0.01	6	D.4.1
2	0.36	52.74	110	0.01	6	D.4.2
3	0.36	52.75	120	0.01	6.1	D.4.3
4	0.36	52.64	130	0.01	6.2	6.4
5	0.36	52.64	140	0.01	6.2	D.4.4
6	0.36	52.79	150	0.01	6	D.4.5
7	0.34	50.43	130	0.01	12	D.4.6
8	0.34	50.43	140	0.01	12	D.4.7
9	0.35	51.49	130	0.01	8.3	D.4.8
10	0.35	51.47	140	0.01	8.3	D.4.9
11	0.33	49.98	130	0.01	15	D.4.10
12	0.33	49.99	140	0.01	14.9	D.4.11
13	0.36	52.79	120	0.005	6	D.4.12
14	0.36	52.83	130	0.004	6	D.4.13
15	0.36	52.76	130	0.030	5.9	D.4.14
16	0.36	52.82	120	0.003	6	D.4.15
17	0.38	55.09	90	0	5.9	D.4.16
18	0.38	55.09	100	0	5.9	D.4.17
19	0.38	55.09	110	0	5.9	D.4.18
20	0.38	55.09	120	0	5.9	D.4.19

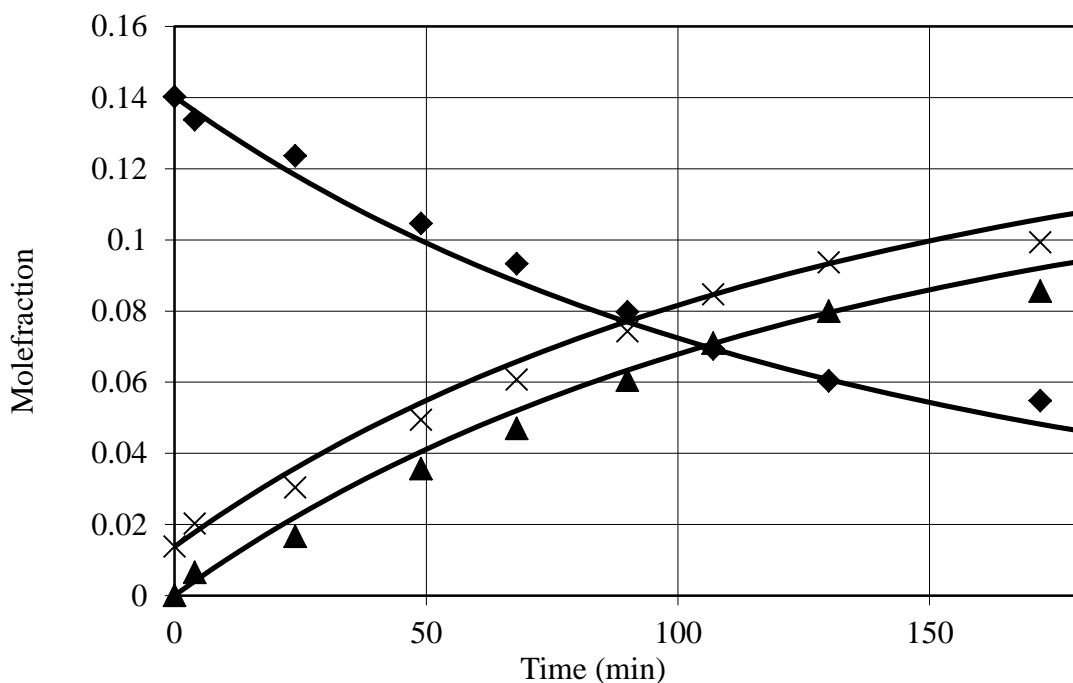


Figure D.4.1: Mole fraction profiles of reaction components for Run 1; (♦) – BA; (▲) – 2EHB; (×) – W. Continuous lines represent predicted mole fraction profiles from kinetic model.

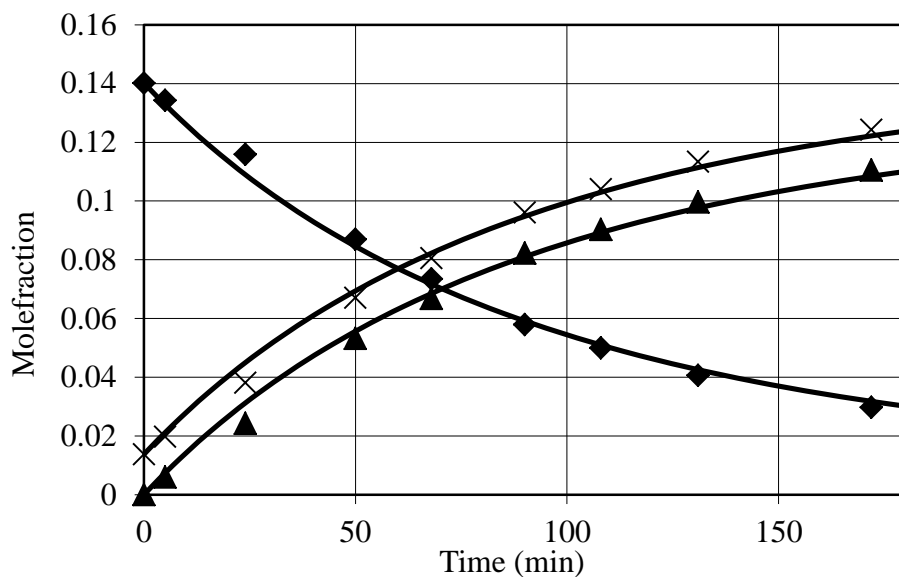


Figure D.4.2: Mole fraction profiles of reaction components for Run 2; (♦) – BA; (▲) – 2EHB; (×) – W. Continuous lines represent predicted mole fraction profiles from kinetic model.

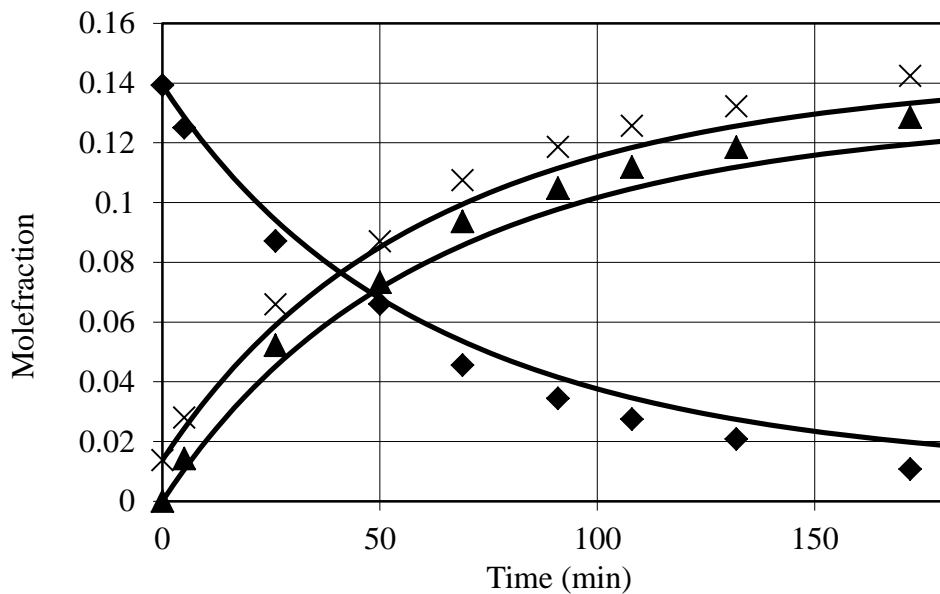


Figure D.4.3: Mole fraction profiles of reaction components for Run 3; (♦) – BA; (▲) – 2EHB; (×) – W. Continuous lines represent predicted mole fraction profiles from kinetic model.

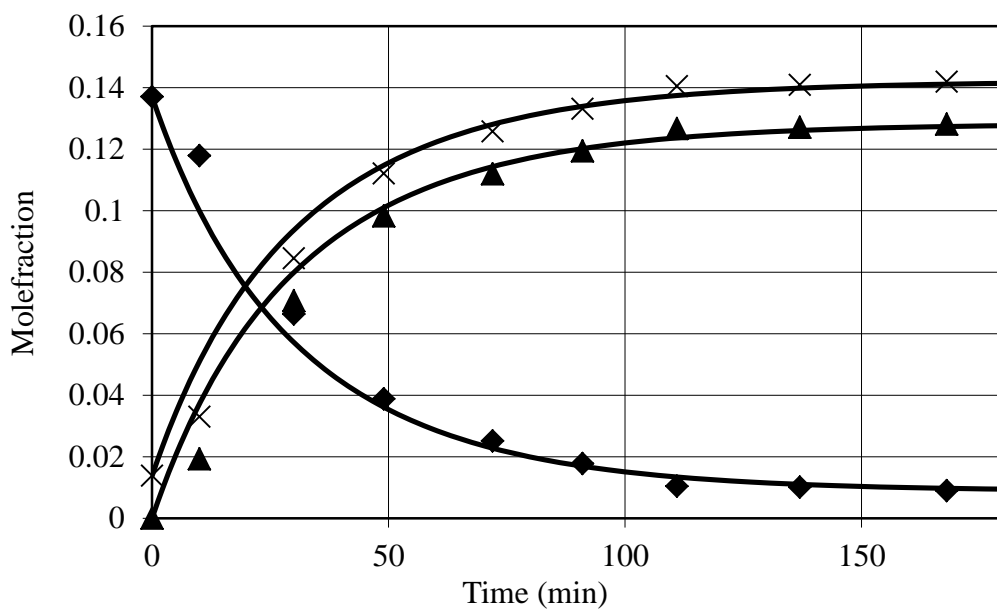


Figure D.4.4: Mole fraction profiles of reaction components for Run 5; (♦) – BA; (▲) – 2EHB; (×) – W. Continuous lines represent predicted mole fraction profiles from kinetic model.

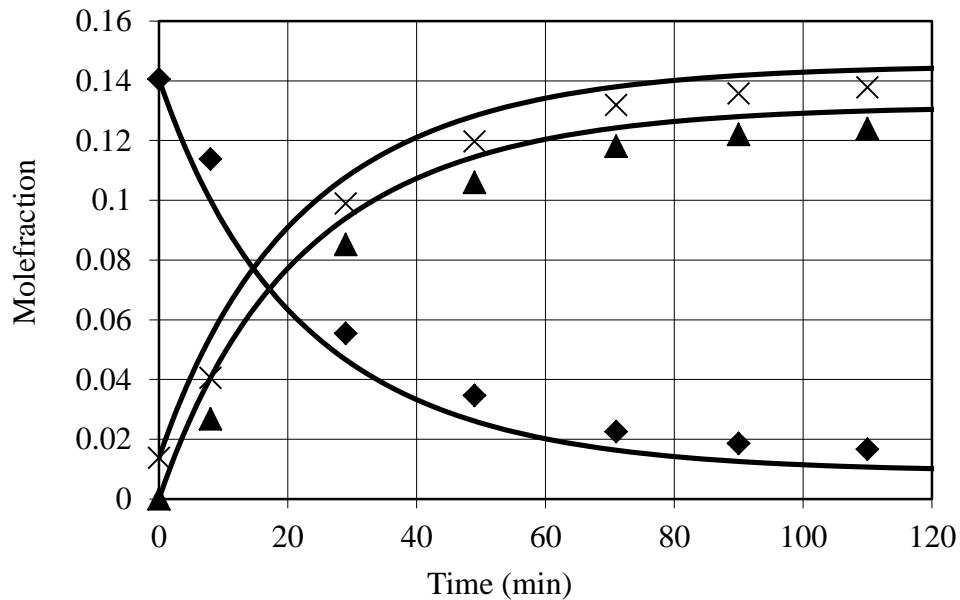


Figure D.4.5: Mole fraction profiles of reaction components for Run 6; (♦) – BA; (▲) – 2EHB; (×) – W. Continuous lines represent predicted mole fraction profiles from kinetic model.

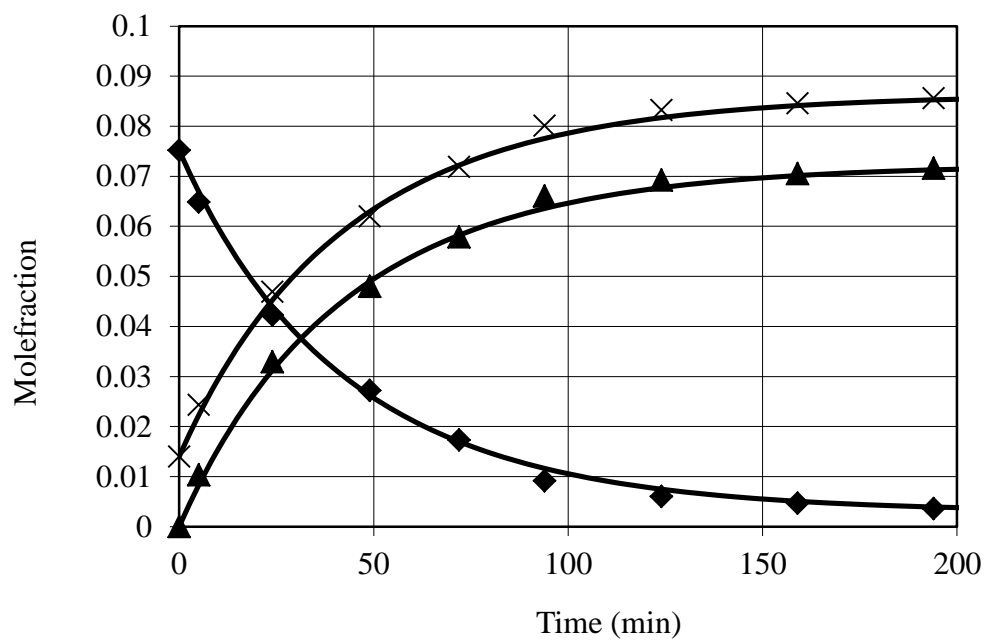


Figure D.4.6: Mole fraction profiles of reaction components for Run 7; (♦) – BA; (▲) – 2EHB; (×) – W. Continuous lines represent predicted mole fraction profiles from kinetic model.

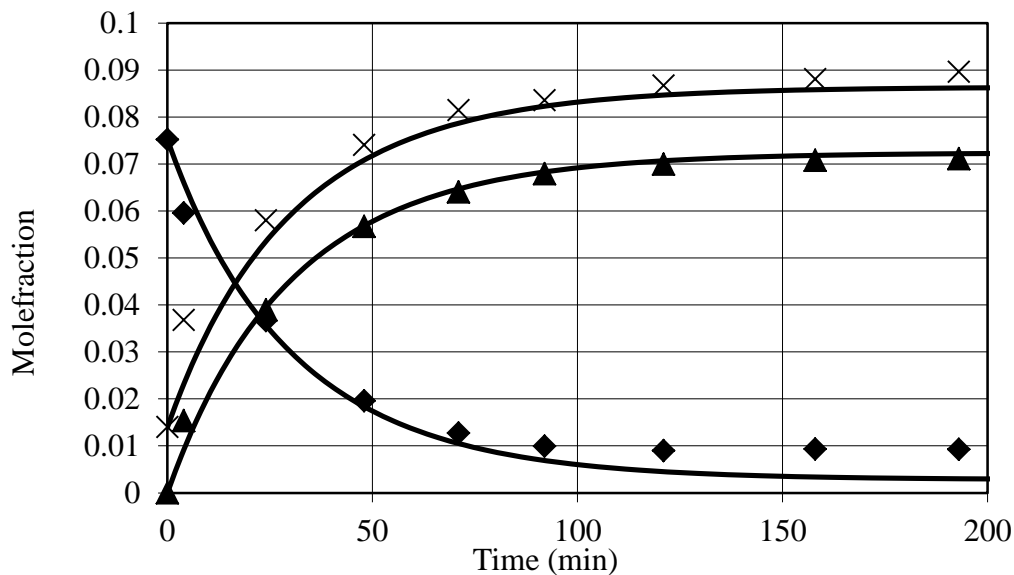


Figure D.4.7: Mole fraction profiles of reaction components for Run 8; (♦) – BA; (▲) – 2EHB; (×) – W. Continuous lines represent predicted mole fraction profiles from kinetic model.

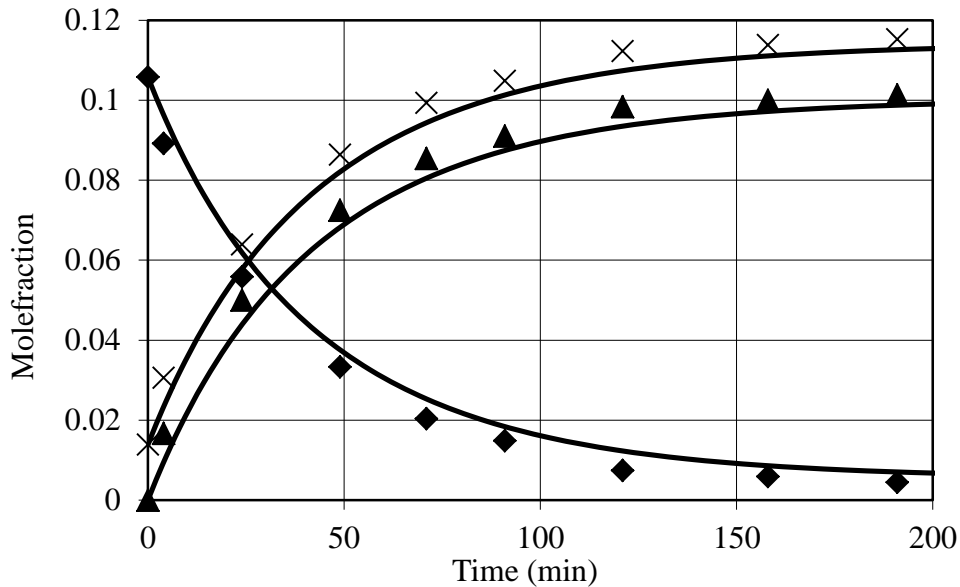


Figure D.4.8: Mole fraction profiles of reaction components for Run 9; (♦) – BA; (▲) – 2EHB; (×) – W. Continuous lines represent predicted mole fraction profiles from kinetic model.

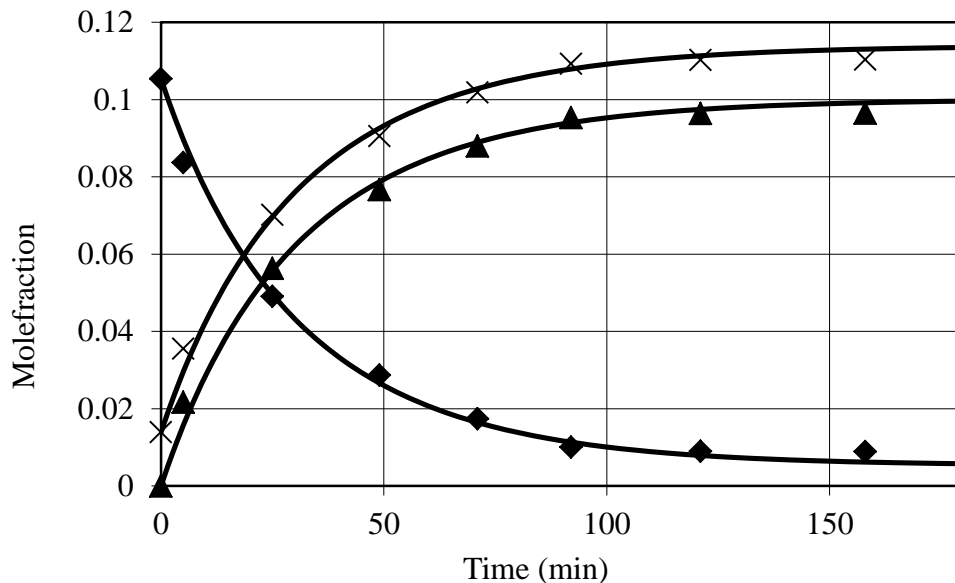


Figure D.4.9: Mole fraction profiles of reaction components for Run 10; (♦) – BA; (▲) – 2EHB; (×) – W. Continuous lines represent predicted mole fraction profiles from kinetic model

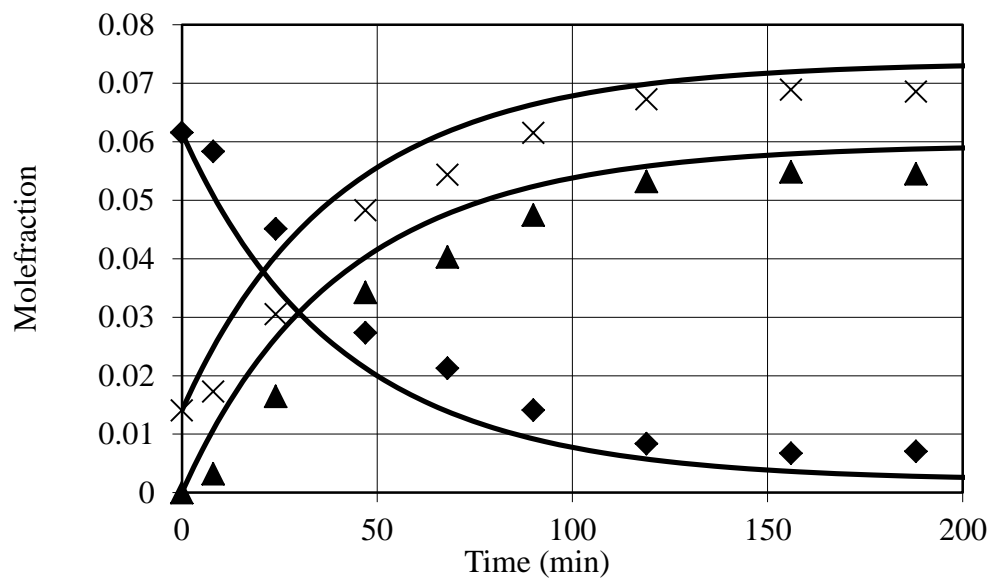


Figure D.4.10: Mole fraction profiles of reaction components for Run 11; (♦) – BA; (▲) – 2EHB; (×) – W. Continuous lines represent predicted mole fraction profiles from kinetic model

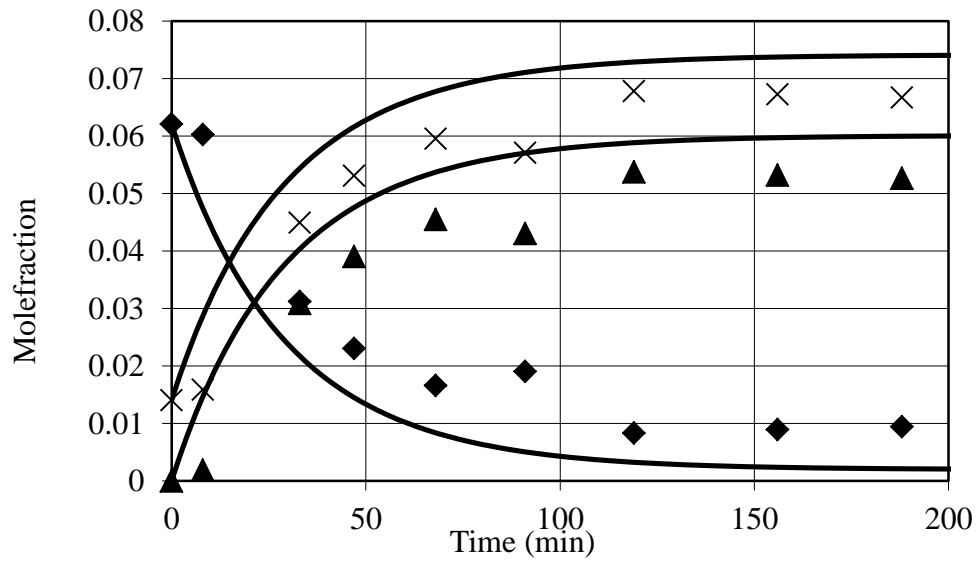


Figure D.4.11: Mole fraction profiles of reaction components for Run 12; (♦) – BA; (▲) – 2EHB; (×) – W. Continuous lines represent predicted mole fraction profiles from kinetic model.

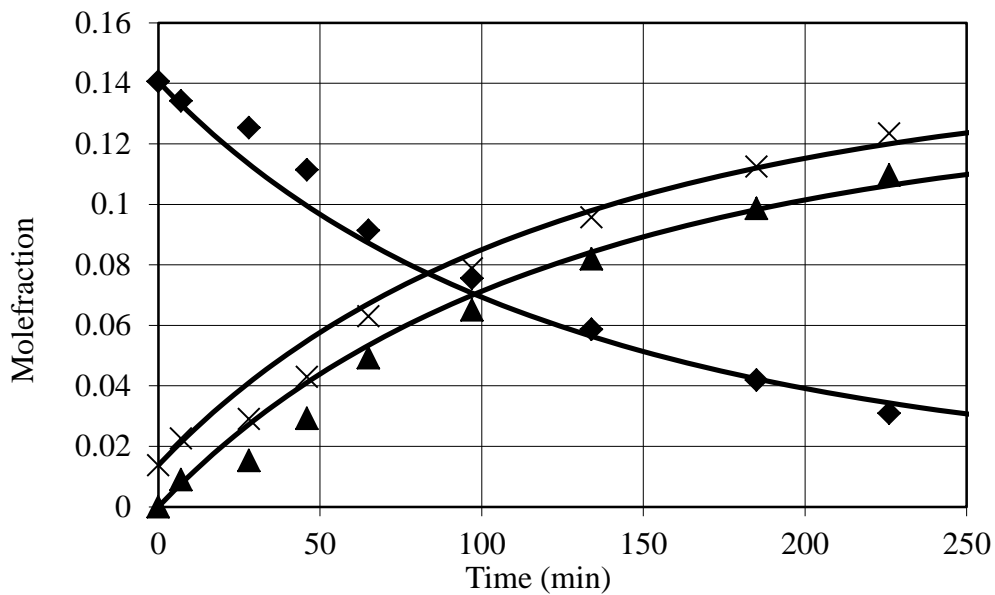


Figure D.4.12: Mole fraction profiles of reaction components for Run 13; (♦) – BA; (▲) – 2EHB; (×) – W. Continuous lines represent predicted mole fraction profiles from kinetic model.

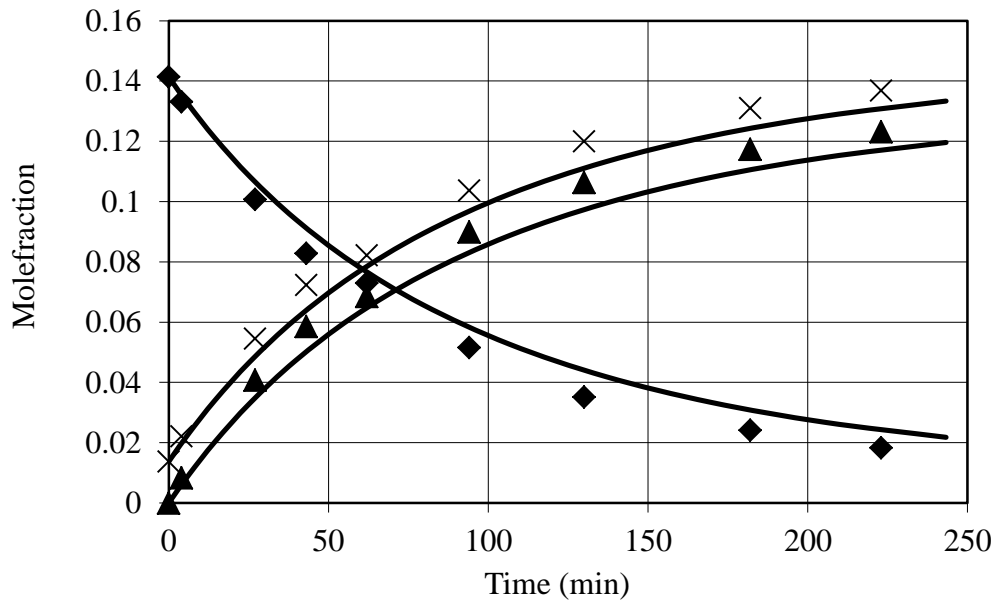


Figure D.4.13: Mole fraction profiles of reaction components for Run 14; (♦) – BA; (▲) – 2EHB; (×) – W. Continuous lines represent predicted mole fraction profiles from kinetic model.

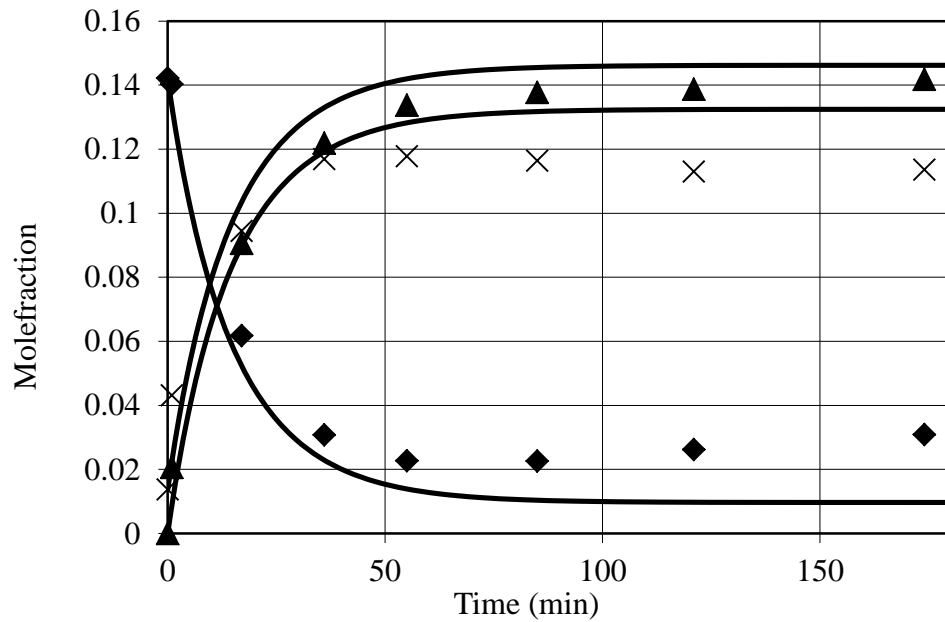


Figure D.4.14: Mole fraction profiles of reaction components for Run 15; (♦) – BA; (▲) – 2EHB; (×) – W. Continuous lines represent predicted mole fraction profiles from kinetic model.

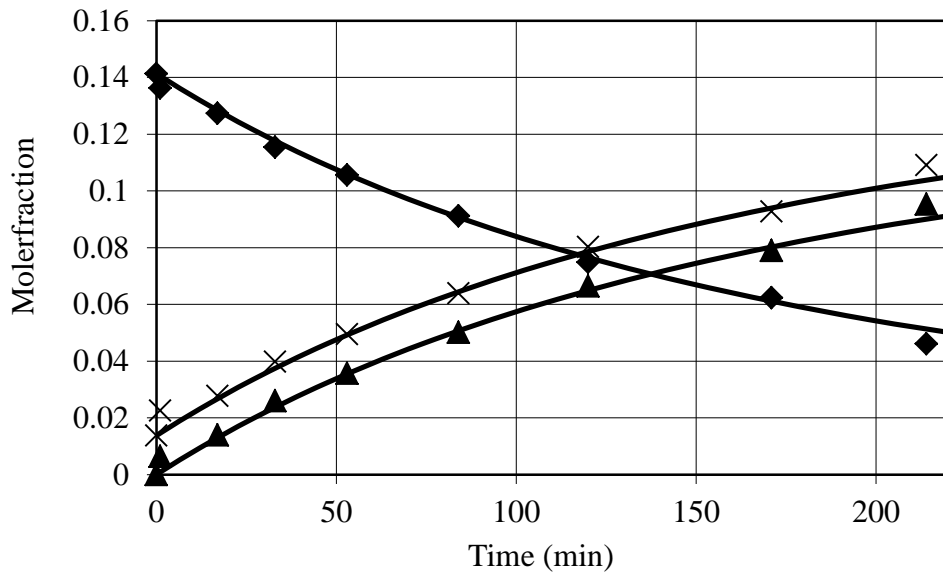


Figure D.4.15: Mole fraction profiles of reaction components for Run 16; (♦) – BA; (▲) – 2EHB; (×) – W. Continuous lines represent predicted mole fraction profiles from kinetic model.

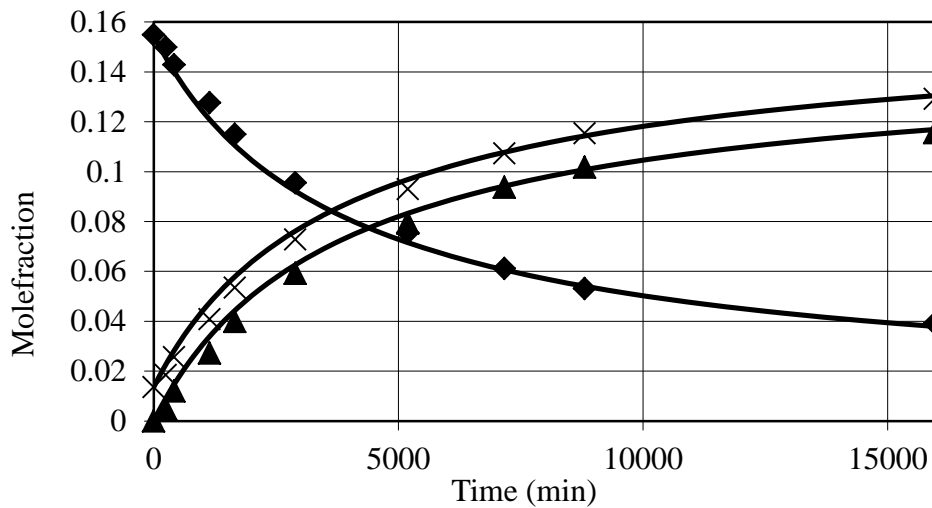


Figure D.4.16: Mole fraction profiles of reaction components for Run 17; (♦) – BA; (▲) – 2EHB; (×) – W. Continuous lines represent predicted mole fraction profiles from kinetic model.

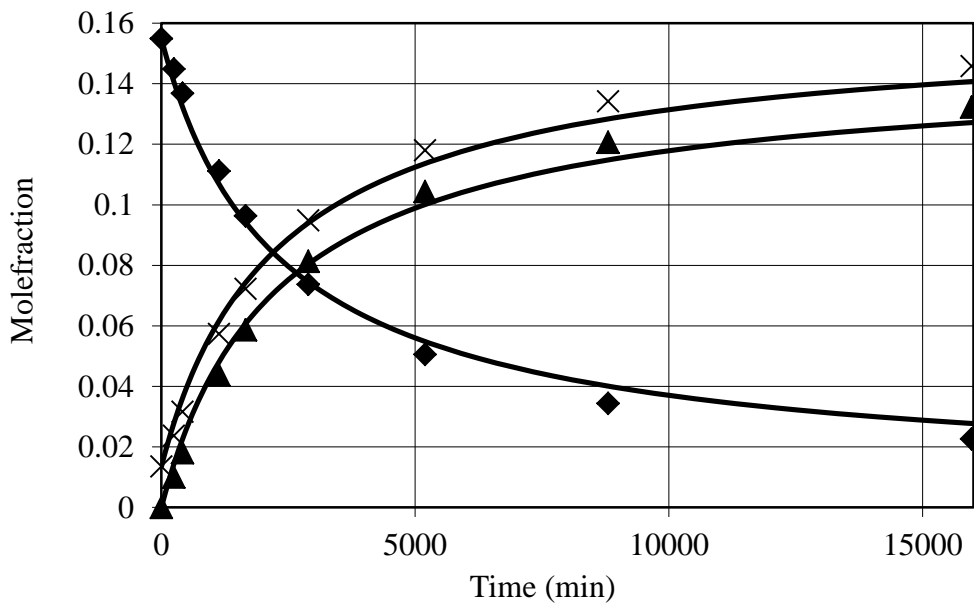


Figure D.4.17: Mole fraction profiles of reaction components for Run 18; (♦) – BA; (▲) – 2EHB; (×) – W. Continuous lines represent predicted mole fraction profiles from kinetic model.

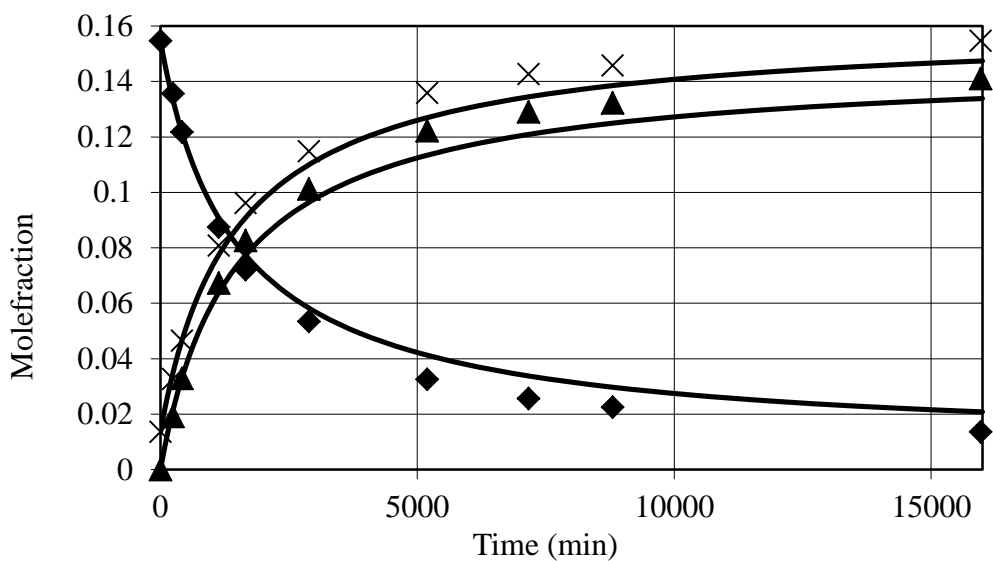


Figure D.4.18: Mole fraction profiles of reaction components for Run 19; (♦) – BA; (▲) – 2EHB; (×) – W. Continuous lines represent predicted mole fraction profiles from kinetic model.

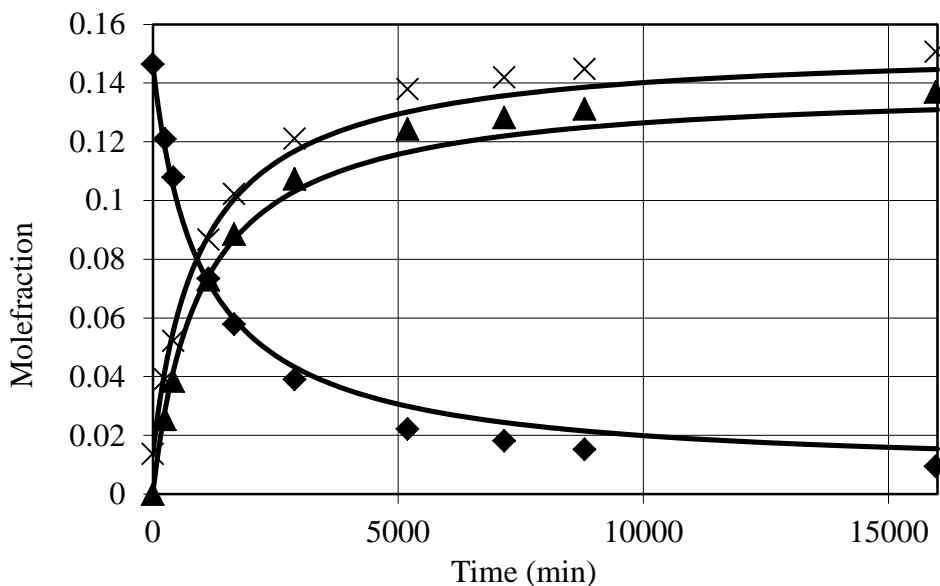


Figure D.4.19: Mole fraction profiles of reaction components for Run 20; (♦) – BA; (▲) – 2EHB; (×) – W. Continuous lines represent predicted mole fraction profiles from kinetic model.

#### *D.5: Calibration plots for sample analysis*

Reaction samples from butyric acid (BA) esterification with methanol (MeOH), ethanol (EtOH) were diluted in 1-Butanol with 5 wt% Ethyl caprylate (1-BuOH+EC) solvent. For all other reaction samples, Isopropanol with 5 wt% Ethyl caprylate (IPA+EC) was used as solvent. To determine the weight of each component in the reaction sample, individual calibrations were carried out. Measured quantity of each component was mixed with known weight of solvent such that the component is 10% by weight in the solution. The calibration samples were made to cover the whole range of mass fraction that is expected in the reaction samples. These samples were analyzed in a gas chromatograph as described in Section 6.3.4. From the chromatograms, area for each component is obtained. From this data, area for a known weight of component and area for a fixed amount of EC is known. The ratio of area of component to that of EC is plotted against the ratio of known weight of component to that of EC. This plot is typically a straight line passing through the origin. The slope of this line is the “calibration factor”.

Weight of individual components is unknown in reaction samples. From the chromatograms, area of EC and areas of individual components are obtained. Weight of EC is known from the amount solvent used to dilute the reaction sample. Using the calibration factor for each component, weight of the component is obtained. Figures D.1.1 to D.1.13 show the calibration plots for BA esterification with different alcohols. Figures D.1.14 to D.1.20 show the calibration plots used for BA esterification with 2-EHA.

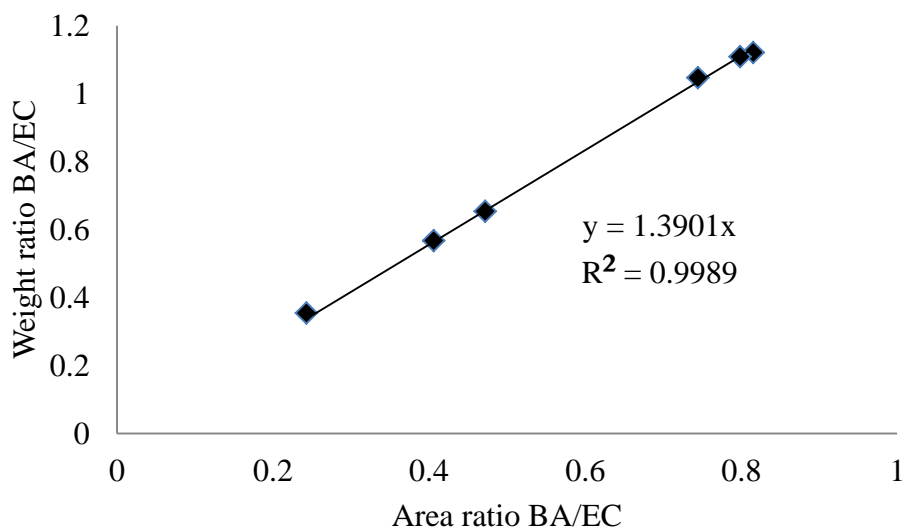


Figure D.5.1: Calibration plot for Butyric acid (BA)

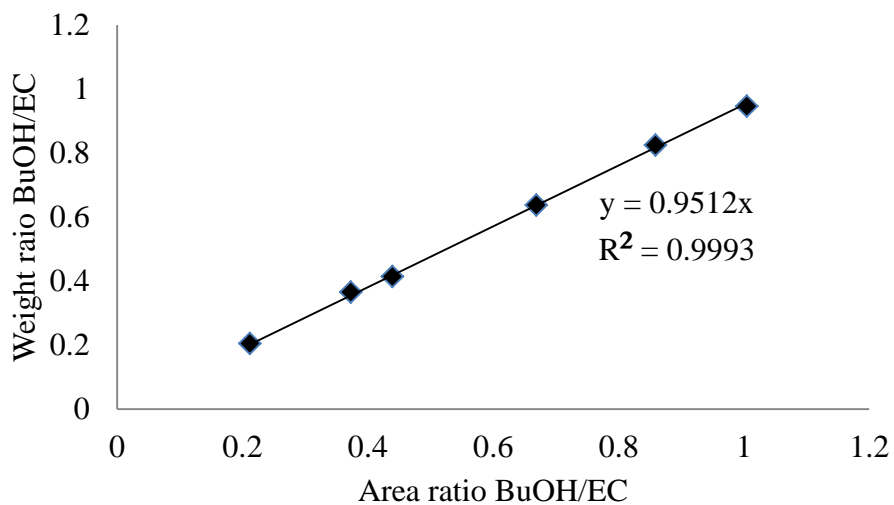


Figure D.5.2: Calibration plot for 1-Butanol (BuOH)

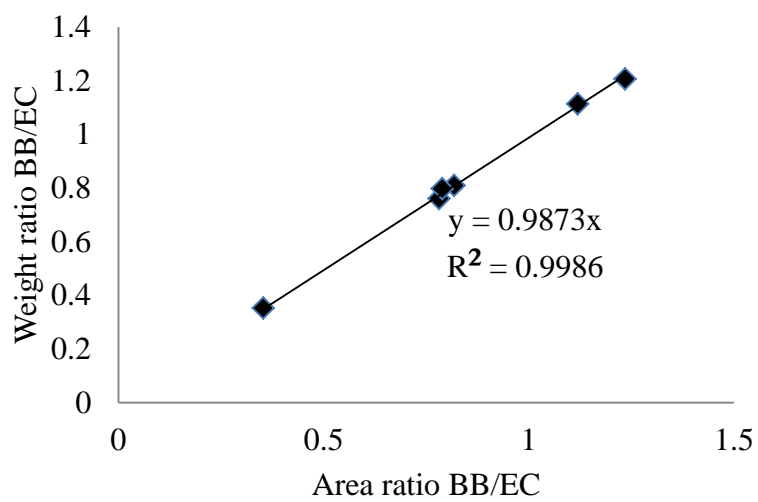


Figure D.5.3: Calibration plot for Butyl butyrate (BB)

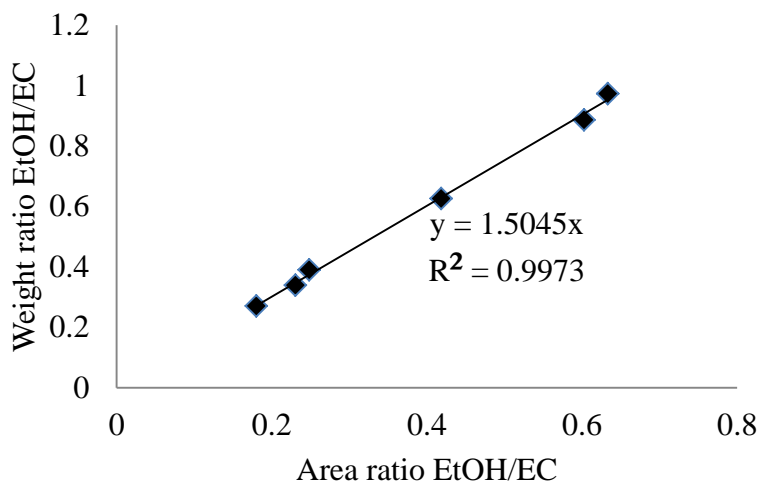


Figure D.5.4: Calibration plot for Ethanol (EtOH).

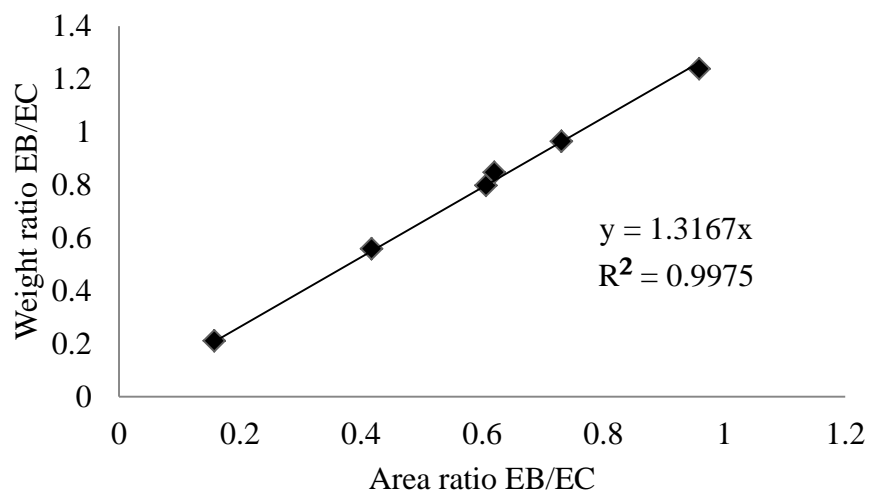


Figure D.5.5: Calibration plot for Ethyl butyrate (EB).

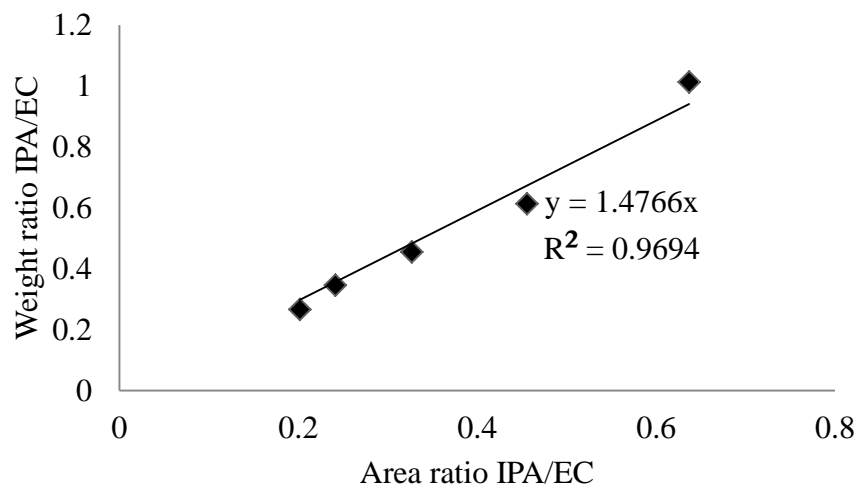


Figure D.5.6: Calibration plot for isopropanol (IPA).

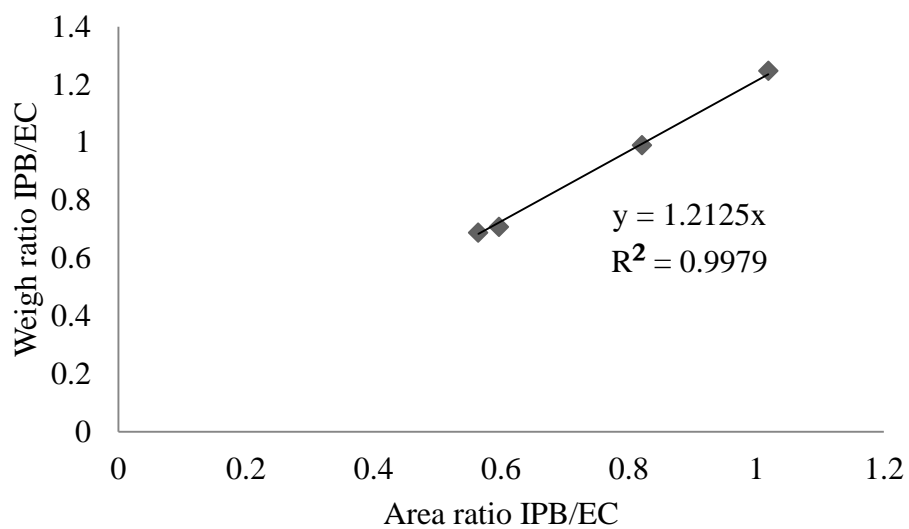


Figure D.5.7: Calibration plot for isopropyl butyrate (IPB).

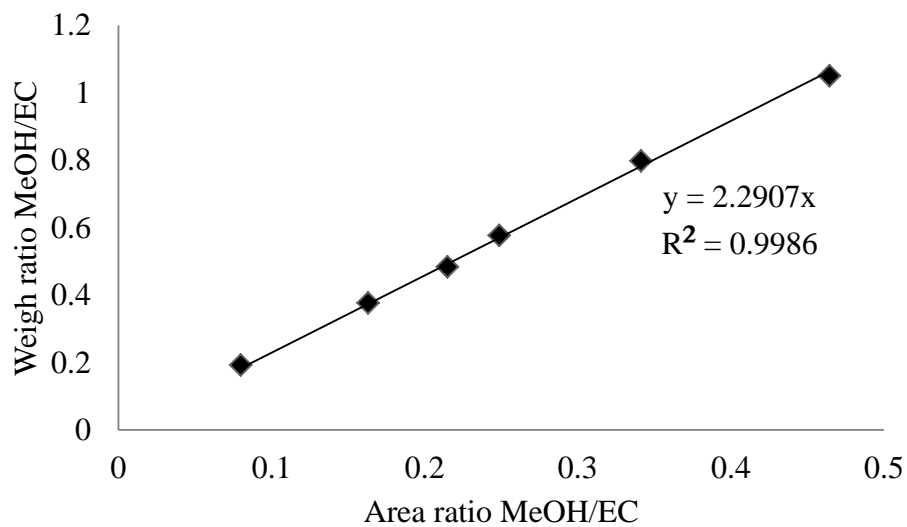


Figure D.5.8: Calibration plot for Methanol (MeOH).

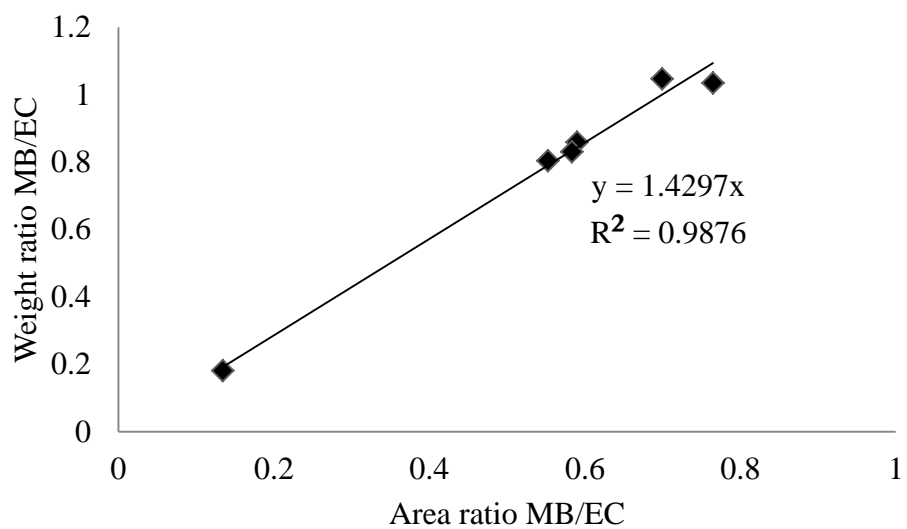


Figure D.5.9: Calibration plot for Methyl butyrate (MB).

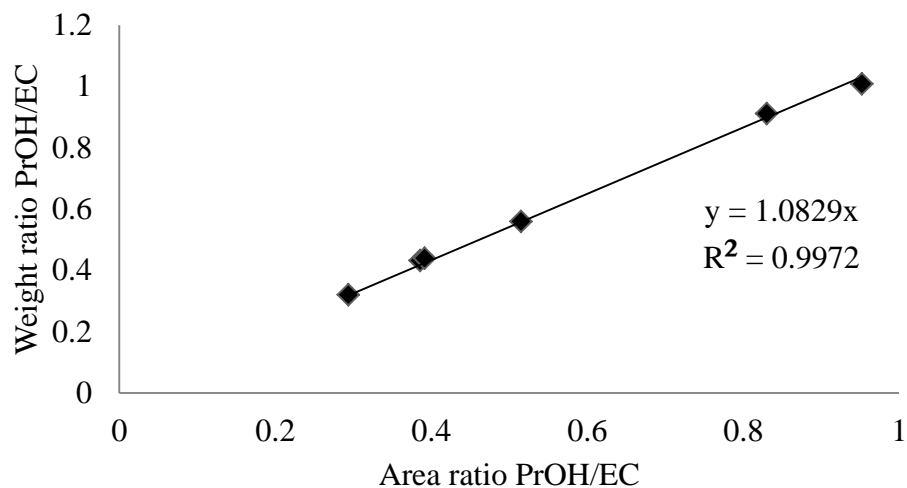


Figure D.5.10: Calibration plot for 1-Propanol (PrOH).

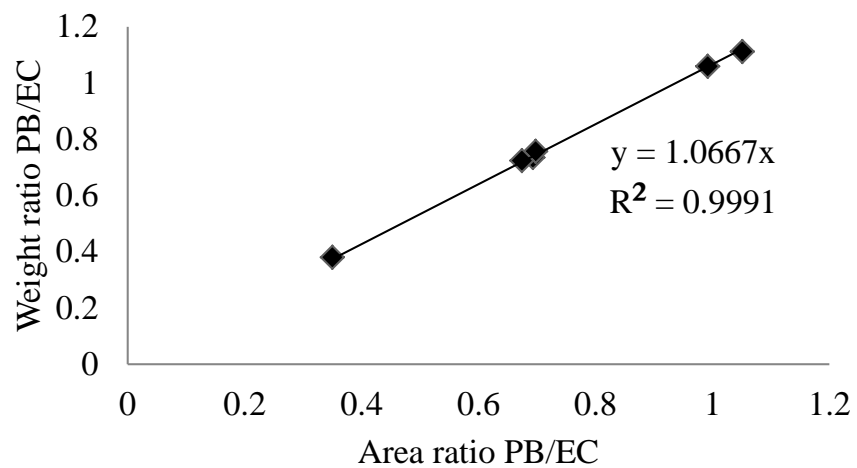


Figure D.5.11: Calibration plot for Propyl butyrate (PB).

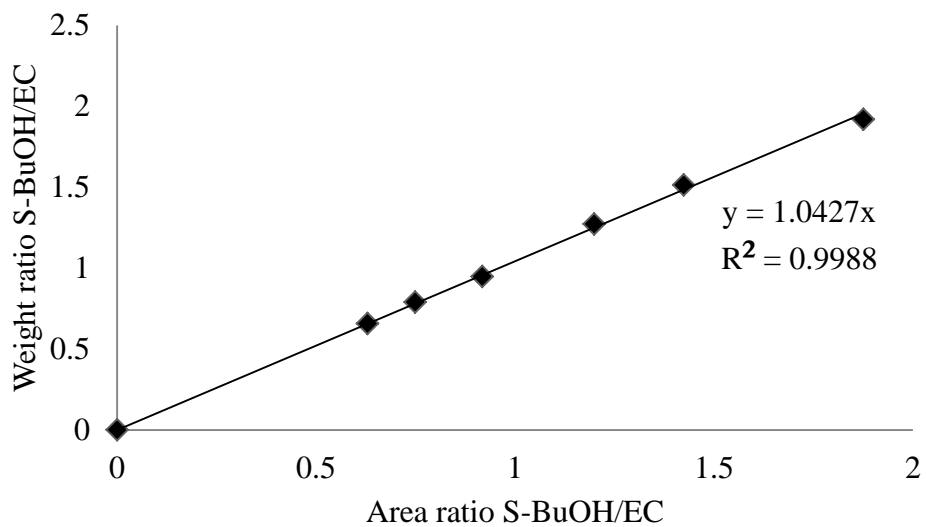


Figure D.5.12: Calibration plot for Sec-Butanol (S-BuOH).

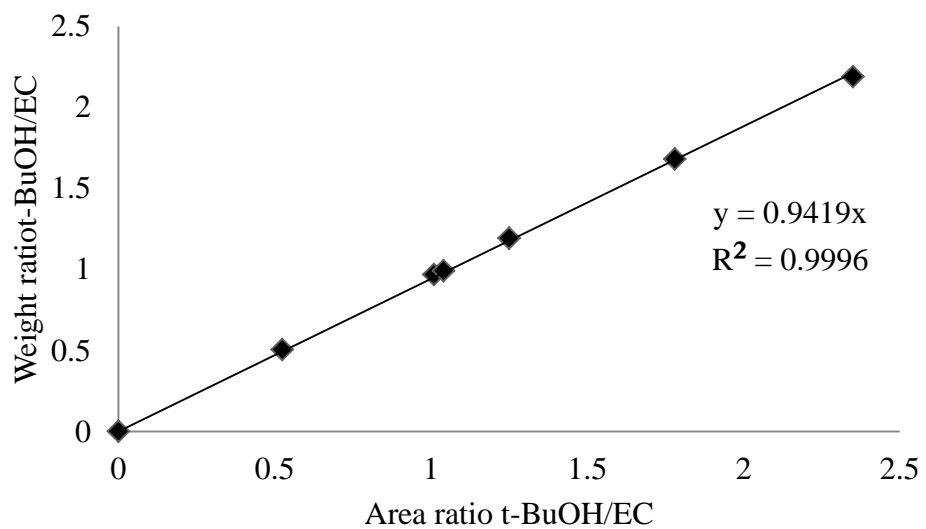


Figure D.5.13: Calibration plot for tert-Butanol (t-BuOH).

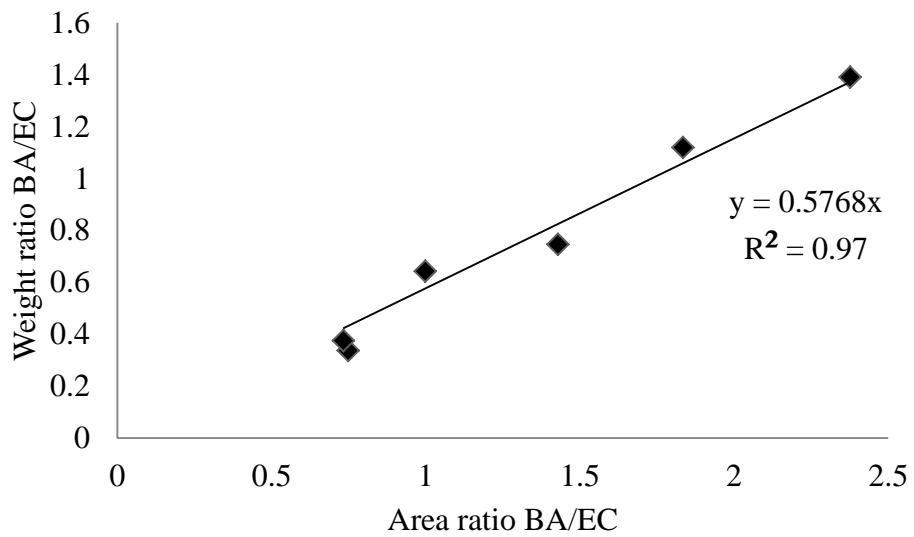


Figure D.5.14: Calibration plot for Butyric acid (BA)

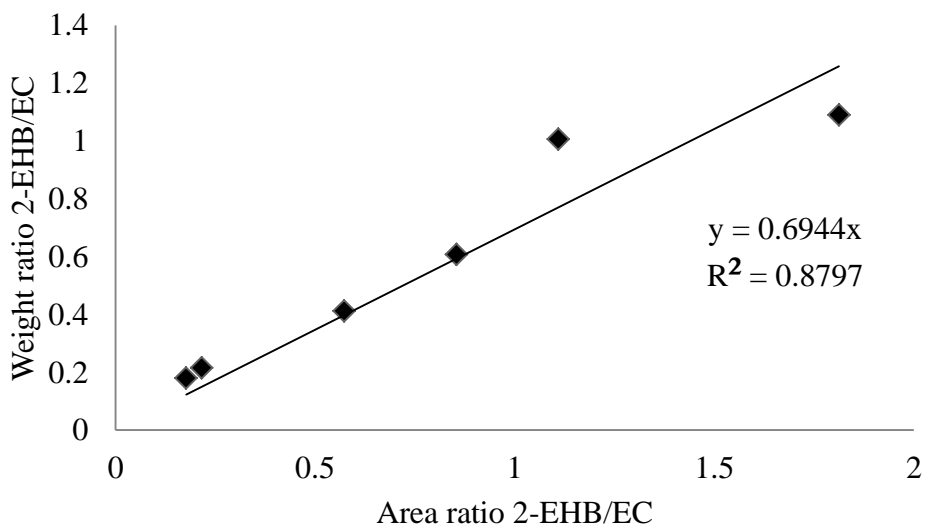


Figure D.5.15: Calibration plot for 2-Ethylhexyl butyrate (2-EHB).

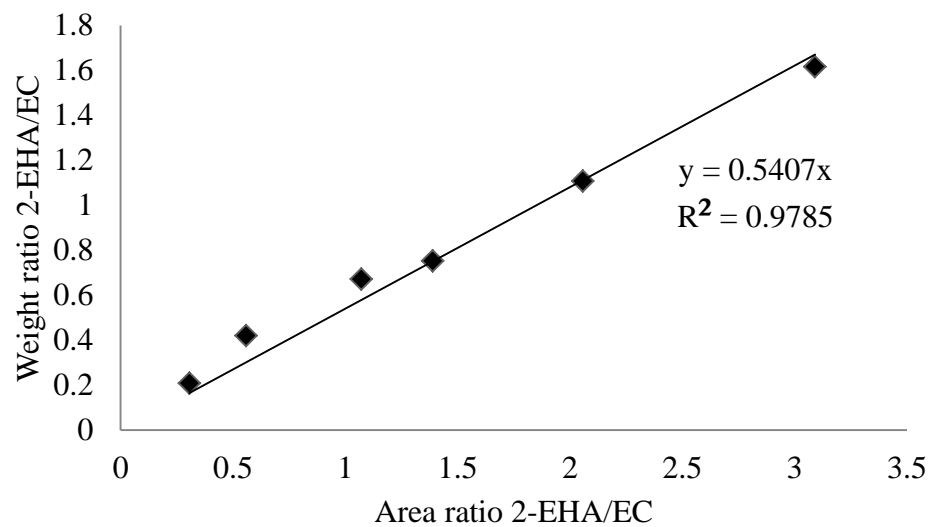


Figure D.5.16: Calibration plot for 2-Ethylhexanol (2-EHA).

## **REFERENCES**

## 6.7. References

1. Yadav, G.D. and P.H. Mehta, *Heterogeneous Catalysis in Esterification Reactions: Preparation of Phenethyl Acetate and Cyclohexyl Acetate by Using a Variety of Solid Acidic Catalysts*. Industrial & Engineering Chemistry Research, 1994. **33**(9): p. 2198-2208.
2. Armstrong, D.W. and H. Yamazaki, *Natural flavours production: a biotechnological approach*. Trends in Biotechnology, 1986. **4**(10): p. 264-268.
3. Mbaraka, I.K., et al., *Organosulfonic acid-functionalized mesoporous silicas for the esterification of fatty acid*. Journal of Catalysis, 2003. **219**(2): p. 329-336.
4. Mbaraka, I.K. and B.H. Shanks, *Design of multifunctionalized mesoporous silicas for esterification of fatty acid*. Journal of Catalysis, 2005. **229**(2): p. 365-373.
5. Grob, S. and H. Hasse, *Reaction Kinetics of the Homogeneously Catalyzed Esterification of 1-Butanol with Acetic Acid in a Wide Range of Initial Compositions*. Industrial & Engineering Chemistry Research, 2006. **45**(6): p. 1869-1874.
6. de Jong, M.C., et al., *Reaction kinetics of the esterification of myristic acid with isopropanol and n-propanol using p-toluene sulphonic acid as catalyst*. Applied Catalysis A: General, 2009. **365**(1): p. 141-147.
7. Engin, A., H. Haluk, and K. Gurkan, *Production of lactic acid esters catalyzed by heteropoly acid supported over ion-exchange resins*. Green Chemistry, 2003. **5**(4): p. 460-466.
8. Kolah, A.K., et al., *Reaction Kinetics for the Heterogeneously Catalyzed Esterification of Succinic Acid with Ethanol*. Industrial & Engineering Chemistry Research, 2008. **47**(15): p. 5313-5317.
9. Kolah, A.K., et al., *Reaction Kinetics of the Catalytic Esterification of Citric Acid with Ethanol*. Industrial & Engineering Chemistry Research, 2006. **46**(10): p. 3180-3187.
10. Gangadwala, J., et al., *Esterification of acetic acid with butanol in the presence of ion-exchange resins as catalysts*. Industrial & Engineering Chemistry Research, 2003. **42**(10): p. 2146-2155.

11. AltIokka, M.R. and A. ÇItak, *Kinetics study of esterification of acetic acid with isobutanol in the presence of amberlite catalyst*. Applied Catalysis A: General, 2003. **239**(1-2): p. 141-148.
12. Liu, Y., E. Lotero, and J.G. Goodwin Jr, *Effect of carbon chain length on esterification of carboxylic acids with methanol using acid catalysis*. Journal of Catalysis, 2006. **243**(2): p. 221-228.
13. Liu, Y., E. Lotero, and J.G. Goodwin Jr, *A comparison of the esterification of acetic acid with methanol using heterogeneous versus homogeneous acid catalysis*. Journal of Catalysis, 2006. **242**(2): p. 278-286.
14. Lilja, J., et al., *Esterification of different acids over heterogeneous and homogeneous catalysts and correlation with the Taft equation*. Journal of Molecular Catalysis A: Chemical, 2002. **182-183**: p. 555-563.
15. Alsalmé, A., E.F. Kozhevnikova, and I.V. Kozhevnikov, *Heteropoly acids as catalysts for liquid-phase esterification and transesterification*. Applied Catalysis A: General, 2008. **349**(1-2): p. 170-176.
16. Schmid, B., M. Doker, and J. Gmehling, *Esterification of Ethylene Glycol with Acetic Acid Catalyzed by Amberlyst 36*. Industrial & Engineering Chemistry Research, 2008. **47**(3): p. 698-703.
17. López, D.E., et al., *Esterification and transesterification using modified-zirconia catalysts*. Applied Catalysis A: General, 2008. **339**(1): p. 76-83.
18. Ju, I.B., et al., *Kinetic study of catalytic esterification of butyric acid and n-butanol over Dowex 50Wx8-400*. Chemical Engineering Journal, 2011. **168**(1): p. 293-302.
19. Vahteristo, K., et al., *Kinetics of Neopentyl Glycol Esterification with Different Carboxylic Acids*. Industrial & Engineering Chemistry Research, 2009. **48**(13): p. 6237-6247.
20. Zhang, C., et al., *Current Progress on Butyric Acid Production by Fermentation*. Current Microbiology, 2009. **59**(6): p. 656-663.

21. Zhu, Y., Z. Wu, and S.-T. Yang, *Butyric acid production from acid hydrolysate of corn fibre by Clostridium tyrobutyricum in a fibrous-bed bioreactor*. *Process Biochemistry*, 2002. **38**(5): p. 657-666.
22. Kim, S.M., et al., *Conversion of biomass-derived butanal into gasoline-range branched hydrocarbon over Pd-supported catalysts*. *Catalysis Communications*, 2011. **16**(1): p. 108-113.
23. Gaertner, C.A., et al., *Catalytic coupling of carboxylic acids by ketonization as a processing step in biomass conversion*. *Journal of Catalysis*, 2009. **266**(1): p. 71-78.
24. Murkute, A.D., J.E. Jackson, and D.J. Miller, *Supported mesoporous solid base catalysts for condensation of carboxylic acids*. *Journal of Catalysis*, 2011. **278**(2): p. 189-199.
25. Erdem, B. and M. Cebe, *Determination of Steric Effect on the Esterification of Different Alcohols with Propanoic Acid over Cation-exchange Resin Catalyst Dowex 50Wx4*. *Zeitschrift für Physikalische Chemie*, 2011. **225**(1): p. 125-136.
26. Newman, M.S., *Steric Effects in Organic Chemistry*. 1956, New York: Wiley.
27. Reichardt, C., *Solvents and Solvent Effects in Organic Chemistry* (3rd edition). 2003, Weinheim: Wiley-VCH.
28. Santhanakrishnan, A., C.T. Lira, and D.J. Miller, *Butyric acid esterification with mixed alcohols catalyzed by Amberlyst 70*, *Personal communication*.
29. Siril, P.F., H.E. Cross, and D.R. Brown, *New polystyrene sulfonic acid resin catalysts with enhanced acidic and catalytic properties*. *Journal of Molecular Catalysis A: Chemical*, 2008. **279**(1): p. 63-68.
30. Rao, Y., *Chemical engineering Thermodynamics*. 1st ed. 1997, Hyderabad: Universities Press.
31. Omota, F., A.C. Dimian, and A. Bliet, *Fatty acid esterification by reactive distillation. Part I: equilibrium-based design*. *Chemical Engineering Science*, 2003. **58**(14): p. 3159-3174.

## **Chapter 7: Conclusions, significance and recommendations for future work**

This chapter is divided into three sections. The use of reactive distillation in cyclohexyl acetate production from cyclohexene is discussed in the first part. The second part involves the evaluation of the concept of distillation with side reactor in butyl stearate production. The third part discusses the significance of butyric acid esterification with a series of alcohols presented in this work.

### **7.1. Reactive distillation in cyclohexyl acetate production**

In this study, the feasibility of producing cyclohexyl acetate using reactive distillation (RD) was demonstrated on a pilot scale glass column. It was shown that 100% conversion of cyclohexene can be achieved using RD. Process simulations were performed with a simple equilibrium stage model using the RADFRAC module in Aspen Plus based on experimentally obtained chemical kinetics, energy balance, and vapor-liquid equilibria.

The reaction kinetics developed in the laboratory included experiments containing cyclohexane, and showed that cyclohexane does not effect cyclohexene esterification kinetics. This simulation model can be used for the design, optimization and process scale-up of cyclohexyl acetate production, as well as for the design of an RD process to separate cyclohexene and cyclohexane.

The availability of pilot scale experimental data with a complete energy balance and studies on the effect of heat loss from reactive on the efficiency of RD are limited in literature. Therefore, in this study it is shown, using experimentally validated simulations that heat transfer between stages can lead to improved energy-efficiency in the operation of the reactive column.

The simulation methodology can be extended to study heat integration effects of any esterification reaction with moderate thermal effect in a RD column.

The challenges in the operation of the RD column described in this work, such as the effect of water on reaction rate and degradation of catalyst due to oligomerization of cyclohexene, offer insights into making modifications to the process (e.g., introduction of a decanter after condenser) and using RD as a potential process intensification technique.

It is recommended that the esterification reactive column be operated under vacuum to keep the column temperature below 373 K. Doing so decreases catalyst degradation due to oligomerization of cyclohexene. All the catalyst packings used in the catalytic zone of the column must be tagged and checked periodically for catalyst activity.

The production of cyclohexyl acetate described in this work is an intermediate step in producing cyclohexanol from cyclohexene (Figure 2.1). During cyclohexyl acetate hydrolysis, it is important to include deacetylation of cyclohexyl acetate into cyclohexene and acetic acid. Since cyclohexene esterification is considered a reversible reaction in this study, the kinetics presented here can be used in cyclohexyl acetate hydration kinetics characterization. This will reduce the number of parameters that need to be regressed.

Preliminary experiments showed that a batch reactor system is not suitable for describing reaction kinetics of cyclohexyl acetate hydrolysis because of the presence of two phases in the sample mixture collected from the reactors. It is recommended that a continuously stirred tank reactor (CSTR) system be used for kinetic model development of this reaction. The gas chromatographic method described in this work can be used to analyze the samples from the organic layer of the cyclohexyl acetate hydrolysis system.

This work is a first step towards a complete study on the advantages of external heat integration in cyclohexanol production from cyclohexene. The primary objective in evaluating external heat integration in cyclohexanol production from cyclohexene is to show that by heat exchange between two RD columns, overall energy efficiency can be improved. The simulation presented in this study can be extended to simulate two RD columns with heat exchange between their reactive stages.

Cyclohexanol can be produced from cyclohexene using formic acid or acetic as reactive entrainer. Because formic acid decomposes at higher temperatures, the formic acid process needs to be operated under vacuum. In this study, it is shown that cyclohexene dimerizes at higher temperatures and affects catalyst activity. So, it is recommended that the acetic acid process be operated under vacuum as well. Therefore, an economic study comparing both the processes is essential.

An experimentally validated simulation model for a process with formic acid as a reactive entrainer has been reported in the literature (Chapter 2, Section 2.2). The simulation model presented here, along with an equilibrium kinetic model for cyclohexyl acetate hydrolysis, can be used to evaluate economic feasibility of cyclohexanol production from cyclohexene using acetic acid as reactive entrainer. Results can be compared with the formic acid process to ascertain feasibility of the acetic acid process.

## **7.2. Distillation with side reactor concept evaluation**

In this study, the concept of distillation with a side reactor is evaluated for methyl stearate transesterification with 1-butanol. This reaction is characterized by very slow reaction rate at lower temperatures and high side product formation at higher temperatures. A distillation column equipped with external side reactors along with a pre-reactor is identified as the best

configuration for this reaction system. It is shown that this configuration is superior to the conventional ester production technique.

It is observed that distillation with a side reactor has both its advantages and additional complexities in terms of design and operation. Before considering this concept, it is recommended that a preliminary study on relative volatilities of components involved be conducted, and that feasible design assumptions that eliminate design variables be formulated. The simulation methodology proposed in this study can be used as a guideline for evaluating the concept of distillation with side reactors for producing bio-renewable chemicals through esterification and transesterification.

### **7.3. Butyric acid esterification with a series of alcohols**

In this study it was found that the rate of butyric acid esterification (mol/volume/time) decreases with increasing alcohol carbon chain length. This is because of the polarity and steric effects of alcohols and lower molar concentrations of neat alcohols with increasing molecular weight. However, the forward rate constant for esterification, when the rate expression is written in terms of molar concentrations of alcohol and acid, is essentially constant for C2 to C8 primary, linear alcohols, but higher for methanol. The result is an important step in predicting the esterification rate in reactions involving carboxylic acid and a mixture of alcohols of known composition (for example, fusel alcohols obtained from ethanol fermentation), because the same rate constant can be used for all C2-C8 alcohols. The detailed kinetics of Amberlyst-70 ion exchange resin – catalyzed esterification of butyric acid with 2-ethylhexanol was presented. This model can be used in process simulations for designing continuous processes for butyric acid esterification.